

Tânia Manuela de Melo Mendonça

Advanced nanoscopic studies in
magneto-electric manganites and high T_C
superconductors



Department of Physics

Faculty of Sciences of the University of Porto

2012

Tânia Manuela de Melo Mendonça



Supervisor: Dr. João Pedro Esteves de Araújo

co-Supervisor: Dr. João Guilherme Martins Correia

*Thesis submitted to the Faculty of Sciences of the
University of Porto in partial fulfillment of the requirements for
the degree of Doctor of Philosophy in Physics*

Department of Physics
Faculty of Sciences of the University of Porto

2012

Resumo

Os avanços tecnológicos na síntese de materiais e em técnicas experimentais conduziram a uma grande variedade de resultados com implicações importantes no estudo das propriedades dos sistemas electrónicos fortemente correlacionados. Este progresso permitiu o estudo de fenómenos exóticos, tais como a supercondutividade de alta temperatura crítica, magneto-resistência colossal ou, mais recentemente, o efeito multiferróico. Estas propriedades são fortemente dependentes da fenomenologia ocorrente à escala nanométrica. Estudos experimentais e teóricos demonstraram que a esta escala estes sistemas não são homogéneos devido a interacções correlacionadas de spin, rede, carga e orbital. Consequentemente, estes sistemas exibem desordem química e electrónica local que está na origem de uma grande variedade de fenómenos à escala macroscópica.

É neste contexto que as técnicas nucleares hiperfinas são introduzidas, as quais são particularmente úteis no estudo da estrutura local e das correlações eléctricas e magnéticas, ao reduzir a escala de observação ao ambiente atómico. Em particular, a técnica de correlações angulares perturbadas, quando combinada com cálculos de primeiros princípios dos observáveis dos gradientes de campo eléctrico e campo magnético hiperfino, proporciona o estudo de fenómenos nanoscópicos que não são observáveis por outras técnicas.

O primeiro tema abordado nesta tese está relacionado com o estudo das interacções hiperfinas numa série de manganites de terras raras (RMnO_3 , $\text{R} = \text{Nd, Sm, Eu, Gd, Tb, Ho, Y, Er, Lu}$), com estruturas hexagonal e ortorrômbica. Os gradientes de campo eléctrico no lugar da sonda (^{111}Cd) foram medidos e comparados com cálculos deste observável obtidos por simulações de densidade de carga através de métodos de primeiros princípios. Todos os compostos revelam dois ambientes locais distintos onde apenas um pode ser atribuído directamente a sítios cristalográficos regulares das terras raras. A existência de um segundo ambiente local, que não pode ser atribuído aos sítios regulares das terras raras ou do manganês, sugere a presença de distorções na vizinhança da terra rara.

A localização e ordenamento de átomos de oxigénio, nos segundo e terceiro membros da família de supercondutores de mercúrio ($\text{HgBa}_2\text{Ca}_{n-1}\text{Cu}_n\text{O}_{2n+2+\delta}$, $n = 2$ e 3) foram estudados no âmbito do segundo tema de estudo desta tese. Os gradientes de campo eléctrico no lugar do mercúrio foram estudados em função da dopagem de oxigénio, acima e abaixo de T_C . Comparando com os

resultados obtidos no primeiro membro desta série de compostos (Hg-1201), a análise mostra que a distribuição de oxigénio nos planos de mercúrio não é uniforme. Os resultados obtidos através de cálculos de primeiros princípios mostram que, a baixas concentrações, regiões sem oxigénio coexistem com regiões onde moléculas de oxigénio ($O_{2\delta}$) ocupam posições intersticiais no centro dos planos de mercúrio. Para altas concentrações, é observada uma competição entre regiões com moléculas de oxigénio e outras onde átomos de oxigénio (O_δ) ocupam posições intersticiais nos planos de mercúrio. Esta competição entre os estados molecular e atómico do oxigénio dopante contribui para clarificar e justificar as diferenças reportadas na literatura entre a concentração do dopante e o número de lacunas criadas nos planos de cobre.

No decorrer deste trabalho várias metodologias para o fabrico de amostras foram desenvolvidos afim de obter materiais de elevada pureza necessária para os estudos à escala atómica.

Summary

Technological advances in materials synthesis and the development of new experimental techniques have created a wealth of information with remarkable implications for understanding the macroscopic properties of systems with strongly correlated electronic properties. These advances allowed the observation of a wide range of exotic phenomena such as high T_C superconductivity, colossal magneto-resistance or, more recently, multiferroic behavior, which are known to be strongly dependent on the nanoscale phenomenology. In fact, several experimental and theoretical studies demonstrated that strongly correlated electron systems are not homogeneous at a local scale due to simultaneously active spin, charge, lattice and/or orbital interactions. Consequently, these systems show nanoscale chemical and electronic disorder, which lead to a rich variety of macroscopic properties.

It is under this scope that the nuclear hyperfine techniques are introduced, being particularly useful to infer the local lattice structure, electric and magnetic correlations in the strongly correlated electron systems by reducing the observation scale to the atomic environment. In particular the perturbed angular correlations technique when combined with powerful first principle simulation techniques of the observables of the electric field gradient provide unique ways to characterize nanoscopic phenomena which would not be unveiled in other ways.

The first theme of this thesis is related to the study of the hyperfine interactions in a series of hexagonal and orthorhombic rare-earth manganites (RMnO_3 , $R = \text{Nd, Sm, Eu, Gd, Tb, Ho, Y, Er, Lu}$). The electric field gradients at the probe sites (^{111}Cd) have been measured and compared with the results obtained with first principle calculations via the augmented plane wave method of the charge densities in the compounds. All studied compounds present two distinct local environments, which only one can be directly attributed to the regular rare-earth crystallographic sites. The existence of a second local environment, which cannot be assigned to the regular rare-earth or manganese sites, suggests for the presence of distortions in the rare-earth local environment.

The lattice sites and collective ordering of oxygen atoms, in the second and third member of Hg-based superconductors family ($\text{HgBa}_2\text{Ca}_{n-1}\text{Cu}_n\text{O}_{2n+2+\delta}$, $n = 2$ and 3), have been studied in the scope of the second theme of this thesis. The electric field gradients at the Hg nuclei have been measured as function of oxygen doping concentration on the Hg planes, above and below T_C . In

comparison with the results obtained for oxygen and fluorine doping in the first member (Hg-1201), the analysis show that, at a local scale, there is non uniform oxygen distribution. A series of first principle electric field gradient calculations allowed to infer that at low concentrations, regions without oxygen coexist with regions where $O_{2\delta}$ dumbbell molecules are located at the centre of the Hg mesh. At high concentrations, $O_{2\delta}$ dumbbell molecules coexist with single O_{δ} atoms occupying the centre of the Hg mesh. The existence of $O_{2\delta}$ molecular dumbbells in competition with single O_{δ} atoms in the Hg planes may provide additional understanding for justifying the systematic differences reported between the measured atomic dopant concentration and the number of holes created in the copper planes of these compounds.

One shall note that to achieve this work several methods for synthesizing high purity samples have been applied and developed.

Résumé

Les progrès technologiques dans la synthèse des matériaux et le développement de nouvelles techniques expérimentales ont fait avancer la compréhension des propriétés macroscopiques des systèmes électroniques fortement corrélés. Ces avancées ont permis l'observation d'une grande variété de phénomènes exotiques, tels que la supraconductivité à haute température, la magnéto-résistance colossale ou, plus récemment, l'effet multiferroïque. Ces propriétés sont connues comme étant fortement dépendantes de la phénoménologie à l'échelle nanométrique. Plusieurs études expérimentales et théoriques ont décrit que ces systèmes ne sont pas homogènes à l'échelle nanométrique en raison de l'interaction simultanée des spin, réseau, charge et orbitale. Par conséquent, ces systèmes présentent un désordre chimique et électronique local différent de la structure moyenne.

Les techniques nucléaires hyperfines, qui réduisent l'observation à l'échelle atomique, peuvent être particulièrement utiles pour l'étude de la structure locale et des corrélations électriques et magnétiques des systèmes électroniques fortement corrélés. Ainsi, la technique des corrélations angulaires perturbées, associée à de puissants outils de simulation, permet l'étude de phénomènes nanoscopiques inobservables par d'autres méthodes.

Dans la série des manganites de terres rares, avec structures hexagonale et orthorhombique, l'étude des interactions hyperfines a été réalisée en utilisant la technique des corrélations angulaires perturbées. Les gradients de champ électrique à la place de la sonde (^{111}Cd) ont été mesurés puis comparés avec les résultats des calculs de premiers principes obtenus par la méthode des ondes plates augmentées. Il en résulte que tous les composés étudiés présentent deux environnements locaux distincts dont un seul peut être attribué directement à des sites cristallographiques réguliers des terres rares. L'existence d'un deuxième environnement local, ne pouvant être attribué ni à des sites réguliers des terres rares ni au manganèse, suggère la présence de distortions autour de la terre rare.

L'ordre des atomes d'oxygène dans les deuxième et troisième membres de la famille des supraconducteurs de mercure a été étudié en utilisant la technique des corrélations angulaires perturbées. Les gradients de champs électriques à la place de la sonde du mercure ont été mesurés en faisant varier l'oxygène dopant dans la maille de mercure, au dessus et en dessous de la T_C .

En comparant ces résultats à ceux obtenus avec de l'oxygène et du fluor dopants dans la série de composés (Hg-1201), l'analyse montre, qu'à l'échelle locale, la distribution de l'oxygène dans la maille de mercure n'est pas uniforme. Les résultats des calculs de premiers principes sur les gradients de champs électriques montrent, qu'à faibles concentrations, des régions sans oxygène coexistent avec des régions où les molécules d'oxygène en *haltère* ($O_{2\delta}$) occupent des positions interstitielles au centre de la maille de Hg. En revanche, à hautes concentrations, on observe au centre de la maille de mercure une coexistence entre des régions occupées par des molécules d'oxygène en *haltère* et des régions occupées par des atomes d'oxygène (O_{δ}). Ces résultats suggèrent que dans les plans de Hg, l'oxygène existe aussi bien sous forme moléculaire que sous forme atomique contrairement à ce qui était connu jusqu'à présent. Cette compétition entre O_{δ} and $O_{2\delta}$ dans les plans de mercure pourrait contribuer à clarifier les différences rapportées entre la concentration de l'atome dopant d'oxygène et le nombre de lacunes créées dans les plans de cuivre.

Acknowledgments

This thesis is the result of a collaboration between Instituto de Física dos Materiais da Universidade do Porto (IFIMUP), Institut Néel (CNRS-Grenoble) and the European Organization for Nuclear Research (CERN/ISOLDE). I acknowledge the Fundação para a Ciência e Tecnologia for the financial support of my PhD (SFRH/BD/29445/2006).

I would like to thank my supervisor Dr. João Pedro Araújo for his dedication, motivation and friendship since I started to work in his group in 2003 and in particular during these four years for my thesis work.

I am very grateful to my co-supervisor Dr. João Guilherme Correia for his support, valuable advises and constant energy.

I am very thankful to a number of people who contributed to the success of this thesis at the professional and personal level:

To Dr. Céline Darie for supporting and supervising my work at Institut Néel.

To Dr. Armandina Lopes for her valuable advises, transmitting the know-how related with the data analysis of the PAC experiments and for her constant energy during the beam time night shifts.

To Dr. Pedro Tavares for transmitting me all his knowledge on sample preparation.

To Dr. Heinz Haas for his support in the electric field gradient calculations used in the interpretation of the experimental results on the superconductors series as also for the fruitful discussions.

To Dr. João Gonçalves for his collaboration in the electric field gradient calculations used in the interpretation of the experimental results in the manganites series.

To Dr. Vítor Amaral for the fruitful discussions on the physics of manganites.

To my colleagues at IFIMUP: André Pereira, Arlete Apolinário, Célia Sousa, Gonçalo Oliveira, João Ventura, José Miguel Teixeira, for their support in several experiments, friendship and good mood.

To the ISOLDE collaboration and to the Porto/Lisbon/Aveiro group that participated in many beam times. In particular, I would like to thank Ana Claudia Marques and Lúgia Amorim for their help in several beam times and for the constant good mood and friendship.

To my dear friends: Sónia Tomás, Sofia Guilherme, Sérgio Marques, Rita Sampaio, Francisco Mota, Filipe Santos, José Couto, Ana Paula Queiroz, Anne-Gaelle Lardeau, Karl Johnston, for their support, presence and for turning my life funnier.

At last but not least, a special thanks to my family for their encouragement and for being always there for me. In particular: to my sisters and nephews, for their support and patience during my long absences at CERN; and to Martin, for his understanding, patience and for staying by my side.

Para a Mímia

Contents

Motivation	5
List of Tables	8
List of Figures	12
1 General Features of Magneto-Electric Manganites and High-T_C Superconductors	23
1.1 The $RMnO_3$ (R=rare-earth) manganites	24
1.1.1 Hexagonal $RMnO_3$	28
1.1.2 Orthorhombic $RMnO_3$	32
1.1.3 Methodology	35
1.2 Hg-based high T_C superconductors	36
1.2.1 Crystal structure	37
1.2.2 Doping questions	39
1.2.3 Methodology	40
2 Experimental Characterization	43
2.1 Structural and magnetic characterization	43
2.1.1 X-ray diffraction	43
2.1.2 Scanning electron microscopy and energy dispersive spectrometry	44
2.1.3 Analytical characterization	44
2.1.4 Magnetic characterization	44
2.2 Sample preparation	45

2.2.1	Synthesis from liquid solutions: sol-gel	45
2.2.2	High pressure-high temperature synthesis	52
2.3	Hyperfine characterization	56
2.3.1	Perturbed angular correlations technique	57
2.3.2	Electric Field Gradients Calculations	66
2.3.3	PAC Experimental Procedure	72
3	Local Probe Studies in Rare-earth Manganites	79
3.1	Hexagonal Rare-Earth Manganites	79
3.1.1	Structural and magnetic characterization	79
3.1.2	EFG dependence on the rare-earth ionic radius	83
3.1.3	EFG dependence on temperature	97
3.1.4	EFG calculations in hexagonal RMnO ₃	108
3.1.5	Discussion	110
3.2	Orthorhombic Rare-Earth Manganites	112
3.2.1	Structural and magnetic characterization	112
3.2.2	EFG dependence on the rare-earth ionic radius	115
3.2.3	EFG dependence on temperature	126
3.2.4	EFG calculations in orthorhombic RMnO ₃	129
3.2.5	Discussion	132
4	Oxygen Ordering in Hg-based Superconductors	137
4.1	Local probe studies in HgBa ₂ CaCu ₂ O _{6+δ}	137
4.1.1	Structural and magnetic characterization	137
4.1.2	Description of the experimental PAC results at room temperature	140
4.1.3	Description of the experimental PAC results in the superconducting state	145
4.2	Local probe studies in HgBa ₂ Ca ₂ Cu ₃ O _{8+δ}	148
4.2.1	Structural and magnetic characterization	148
4.2.2	Description of the PAC experimental results at room temperature	150
4.2.3	Description of the PAC experimental results in the superconducting state	154
4.3	EFG simulations	157

4.4 Discussion 165

5 Conclusions and Perspectives 171

List of Articles 175

Bibliography 176

Motivation

Advances in materials synthesis combined with the development of new experimental techniques have created a wealth of information with important implications for understanding the origin of the macroscopic properties of the transition metal oxides. These materials reveal a broad range of extraordinary phenomena^[1,2] e.g., high-temperature superconductivity (HTSC), colossal magneto-resistance (CMR), metal-insulator transitions and more recently, the rediscovery of the multiferroic effect. Their singularity is due to the existence of several magnetic, electric and structural competing states^[3], which are not fully explained by the long-range crystallographic structure. Furthermore, the basic properties of these systems seem to depend strongly on the nanoscale phenomenology as revealed by experiments sensitive to the local crystallographic and nanoscale electronic structure^[4].

The manganese oxide compounds, commonly known as manganites^[5,6], are a representative class of materials which exhibit several competing states leading to the appearance of interesting effects such as colossal magneto-resistance or the multiferroic/magneto-electric effects. These phenomena are generally dependent on the local electronic structure and on the underlying lattice^[3,7,8]. In the recent years, experimental and theoretical studies have demonstrated that the manganites have dominant states that are not spatially homogeneous^[4], which occurs when spin, charge, lattice and/or orbital interactions are simultaneously active. An interesting example is the rare-earth manganites (RMnO₃) series, where the coexistence of magnetic and electric states has been explained by various microscopic origins which seem to be dependent on the underlying local lattice^[7-11]. Therefore, the knowledge of how the properties evolve at a local scale is expected to contribute to a better understanding of the complex physics of these compounds. The macroscopic properties of these RMnO₃ compounds have been extensively studied contributing to the establishment of their basic physical concepts. Nevertheless, the dependence of these

properties on the local atomic structure evidences the need of nanoscale studies. In this context, nuclear hyperfine techniques, which reduce the observation scale to the atomic environment can be particularly useful to infer the local lattice structure, electric and magnetic correlations^[12]. With this scope, the perturbed angular correlations (PAC) technique has been applied to study the rare-earth local environment in representative samples of the parent RMnO_3 series aiming to contribute to a better understanding of the microscopic phenomenology and their correlation with the origin of multiferroic/magneto-electric effects.

Another outstanding example of strongly correlated electron materials is the high-temperature superconductor cuprates system. Despite their discovery more than 20 years ago by Bednorz and Müller^[13], there is still no unanimously accepted explanation for the phenomena responsible for high-temperature superconductivity. The relationship between charge ordering and doping is still being largely reviewed by the theories attempting to explain HTSC^[14–17]. In the hole-doped cuprate systems (La, Y, Tl, Bi and Hg based families), superconductivity appears when the antiferromagnetic insulating parent is doped with holes^[18], i.e., a distribution of different dopant ions that induces charge transfer to the CuO_2 layers. This distribution leads to chemical and electronic atomic-scale variations, which interfere with the electronic mechanism of superconductivity^[19,20]. Signatures of such local disorder have been reported using different techniques such as scanning tunneling microscopy (STM)^[20,21], angle resolved photoinduced emission spectroscopy (ARPES)^[22], nuclear magnetic resonance^[23,24], among others. Some of these experiments have revealed that the nanoscopic disorder is correlated with the location of interstitial oxygen dopant atoms^[19,20] suggesting a strong interplay between the dopant atoms and the local electronic properties in these materials^[25]. In particular, the Hg-based family (commonly denoted as Hg-12(n-1)n) is a good prototype to study the existence of disorder or inhomogeneities at the atomic scale due to their simple tetragonal structure and the highest T_C 's^[26]. Local disorder at the Hg planes was reported and believed to be associated to Hg deficiencies and/or to non-stoichiometric excess oxygen (O_δ)^[27,28]. Furthermore, the doping level at the CuO_2 planes was found to be considerably lower than expected from the extra O_δ content following ionic models^[29,30]. These discrepancies suggested the presence of single-charged oxygen anions (O^-)^[29,31] or non-oxidizing oxygen atoms although there is no experimental evidence for this fact^[32]. Therefore, the role of O_δ in the formation of charge inhomogeneities and its impact on the local electronic and structural

properties is of great importance. As a contribution to a better understanding of the existence of disorder at the Hg planes, the perturbed angular correlations technique has been applied to study the lattice sites and collective ordering of O_δ in the Hg planes of representative samples of the Hg-based superconductors series.

This manuscript presents the author's contribution for the study of local distortions in rare-earth manganites and in Hg-based high temperature superconductors and its correlation with their macroscopic properties. The thesis is structured in 5 chapters which can be briefly summarized as follows:

General features of magneto-electric manganites and high T_C superconductors

This chapter describes the most relevant aspects of the general properties of two representative classes of highly correlated electron systems (magneto-electric manganites and high temperature superconductor cuprates) in support to understand the subsequent chapters of this thesis.

Experimental techniques

The experimental setups and procedures of the techniques used to perform the synthesis and characterization of the samples are briefly described. Detailed attention is given to the hyperfine characterization via the perturbed angular correlations technique. Reference is given to the institutions where those techniques have been used.

Local probe studies in rare-earth manganites

The evolution of the electric field gradients as a function of the rare-earth ionic radius in a series of hexagonal and orthorhombic rare-earth manganites ($RMnO_3$, $R = Lu, Er, Y, Ho, Tb, Gd, Eu, Sm$ and Nd) has been studied. The electric field gradients at the ^{111}Cd probe atom site have been measured and interpreted with the help of *ab-initio* calculations. The experimental results have been correlated with the average crystalline structure and the magnetic and electric properties of this series of compounds.

Oxygen ordering in Hg-based superconductors

The lattice location and ordering of oxygen in $\text{HgBa}_2\text{Ca}_{n-1}\text{Cu}_n\text{O}_{2n+2+\delta}$ ($n=2$ and 3) system is presented. The electric field gradients at $^{199\text{m}}\text{Hg}$ nuclei have been measured as function of oxygen doping on the Hg planes via the perturbed angular correlations technique, above and below T_C . The data was interpreted with the help of a series of *ab-initio* calculations of charge distributions in $\text{Hg}_m\text{Ba}_{2m}\text{Ca}_{m-1}\text{Cu}_m\text{O}_{4m+n}$ supercells for different oxygen doping configurations.

Conclusions and perspectives

General conclusions of this thesis are presented. The perspectives for future research work are reviewed and highlighted.

List of articles

A list of peer-reviewed articles, obtained with the work of this thesis, which are published, submitted and in preparation is presented.

List of Tables

2.1	List of RMnO_3 samples prepared by the urea method. The last thermal treatment conditions and the final composition obtained by XRD and EDS are also included. .	47
2.2	List of samples of nominal compositions $\text{HgBa}_2\text{CaCu}_2\text{O}_{6+\delta}$ and $\text{HgBa}_2\text{Ca}_2\text{Cu}_3\text{O}_{8+\delta}$ prepared by the HP-HT method with the different pressure and temperature conditions together with the final composition obtained by XRD.	55
2.3	Electrical quadrupole, Q , and magnetic dipole, μ , moments for the intermediate states of $^{111}\text{In} \rightarrow ^{111}\text{Cd}$, $^{111\text{m}}\text{Cd} \rightarrow ^{111}\text{Cd}$ and $^{199\text{m}}\text{Hg} \rightarrow ^{199}\text{Hg}$ decay cascades ^[33]	74
2.4	Annealing conditions used in the post-implantation annealing in the different series of compounds.	75
3.1	Hexagonal RMnO_3 structures and cell parameters obtained from XRD pattern matching.	80
3.2	Néel (T_N) and Curie-Weiss (θ_P) temperatures and $ \theta_P /T_N$ ratio obtained for the hexagonal RMnO_3	82
3.3	Room temperature EFG parameters for the hexagonal RMnO_3 samples. The indexes 1 and 2 refers to the two EFG distributions obtained from the fitting procedure. . . .	86
3.4	Electric field gradient parameters for the hexagonal RMnO_3 samples measured at 573 K. The indexes 1 and 2 refers to the two EFG distributions obtained from the fitting procedure.	90
3.5	Electric field gradient parameters for the hexagonal RMnO_3 samples measured at 77 K. The indexes 1 and 2 refers to the two EFG distributions obtained from the fitting procedure.	93

3.6	Electric field gradient parameters for the hexagonal RMnO_3 samples measured at 10 K. The indexes 1 and 2 refers to the two EFG distributions obtained from the fitting procedure.	95
3.7	Electric field gradient parameters for the hexagonal YMnO_3 sample as a function of temperature.	100
3.8	Electric field gradient parameters for the hexagonal ErMnO_3 sample as a function of temperature.	107
3.9	Augmented plane wave + local orbitals calculated EFG parameters in the rare-earth and manganese sites for the hexagonal RMnO_3 . The first set of columns displays the simulations results with the unrelaxed structures while the second one shows the relaxed values.	108
3.10	APW+lo calculated EFG parameters in the rare-earth and manganese sites with substitutional Cd ($x=1/6$) for the hexagonal RMnO_3 . The first set of columns refers to the simulations with unrelaxed structures while the second one with relaxed crystalline structures.	109
3.11	Calculated EFG parameters in the rare-earth and manganese sites using the APW+lo and PCM methods for the hexagonal RMnO_3	110
3.12	Experimental and calculated EFG parameters in the rare-earth and manganese sites with substitutional Cd for the hexagonal RMnO_3	112
3.13	Orthorhombic RMnO_3 structures and cell parameters obtained from XRD pattern matching.	112
3.14	Néel (T_N) and Curie-Weiss (θ_P) temperatures obtained for the orthorhombic RMnO_3	114
3.15	Electric field gradient parameters for the orthorhombic RMnO_3 samples measured at room temperature. The indexes 1 and 2 refers to the two EFG distributions obtained from the fitting procedure.	117
3.16	Electric field gradient parameters for the orthorhombic RMnO_3 samples measured at 573 K. The indexes 1 and 2 refers to the two EFG distributions obtained from the fitting procedure.	121

3.17	Electric field gradient parameters for the orthorhombic RMnO_3 samples measured at 10 K. The indexes 1 and 2 refers to the two EFG distributions obtained from the fitting procedure.	124
3.18	Electric field gradient parameters for the orthorhombic EuMnO_3 sample as a function of temperature.	129
3.19	APW+lo calculated EFG parameters in the rare-earth and manganese sites for GdMnO_3 and EuMnO_3 . The first set of columns displays the simulations results with the unrelaxed structures while the second one shows the relaxed values.	131
3.20	Calculated EFG parameters in the rare-earth and manganese sites with substitutional Cd ($x=1/4$) using APW+lo for GdMnO_3 and EuMnO_3 . The first set of columns refers to the simulations with unrelaxed structures while the second one with relaxed crystalline structures.	131
3.21	Calculated EFG parameters in the rare-earth and manganese sites using APW+lo and PCM methods for GdMnO_3 and EuMnO_3	132
3.22	Experimental and APW calculated EFG parameters in the rare-earth and manganese sites with substitutional Cd, for GdMnO_3 and EuMnO_3	132
4.1	Preliminary annealing conditions upon oxygen doping of the Hg-1212 as-synthesized samples.	139
4.2	EFG fitting parameters of the experimental $R(t)$ PAC functions measured at room temperature for Hg-1212 samples.	142
4.3	EFG fitting parameters of the experimental $R(t)$ functions for room temperature measurements as function of high oxygen pressure for Hg-1212 samples.	144
4.4	EFG fitting parameters of the experimental $R(t)$ PAC functions measured at 77 K for Hg-1212 samples.	145
4.5	Mean values per EFG triplet, obtained by averaging room temperature and 77 K EFG parameters.	147
4.6	Preliminary annealing conditions upon oxygen doping of the Hg-1223 as-synthesized samples.	149

4.7	EFG fitting parameters of the experimental $R(t)$ PAC functions measured in Hg-1223 samples at room temperature.	153
4.8	EFG fitting parameters of the experimental $R(t)$ functions for room temperature measurements as function of high oxygen pressure for Hg-1223 samples.	155
4.9	EFG fitting parameters of the experimental $R(t)$ PAC functions measured in Hg-1223 samples at 77 K.	155
4.10	Calculated EFG parameters for all atoms on the relaxed Hg-1212+ single O_δ supercells. The inserted figures show the Hg planes of different supercells, presented as shadowed regions. Light/dark symbols represent Hg/O atoms.	161
4.11	Calculated EFG parameters for all atoms on the relaxed Hg-1212+ $O_{2\delta}$ dumbbells supercells. The inserted figures show the Hg planes of different supercells, presented as shadowed regions. Light/dark symbols represent Hg/O atoms.	162

List of Figures

1.1	The crystal structures of RMnO ₃ manganites: a) hexagonal structure (space group $P6_3cm$) and its local MnO ₅ and RO ₈ environments; and b) orthorhombic structure (space group $Pnma$) and its local MnO ₆ and RO ₁₂ environments.	26
1.2	The crystal field in: a) trigonal bipyramidal environment, and b) octahedral environment.	26
1.3	Structural, T _{struct} (stars), ferroelectric, T _{FE} (open dots), and magnetic, T _N (closed dots) transition temperatures as function of the rare-earth ionic radius (R ³⁺) for hexagonal and orthorhombic RMnO ₃	27
1.4	Sketch view of the hexagonal RMnO ₃ crystal structure: a) the room temperature $P6_3cm$ space group, and b) the high temperature $P6_3/mmc$ paraelectric space group.	29
1.5	Sketch view of the orthorhombic RMnO ₃ crystal structure. On the right side, the local MnO ₆ and RO ₁₂ local environments.	33
1.6	The Jahn Teller effect for Mn ³⁺ ($3d^4$): the MnO ₆ octahedra (left) can distort (right), leading to the splitting of the t_{2g} and e_g orbitals. This distortion lowers the overall energy by lowering the energy of the singly occupied e_g orbital. The saving in energy from the lowering of the d_{xz} and d_{yz} orbitals is balanced by the raising of the d_{xy} one. Adapted from ^[34]	34
1.7	a) Magnetic phase diagram for orthorhombic RMnO ₃ as function of the rare-earth ionic radius (R _I ³⁺). The data has been taken from ^[35,36] . b) Different possible spin arrangements. The circles represent the position of the Mn ions and the sign of their spin projections along the z -axis. Adapted from ^[6]	35

1.8	Schematic representation of the time line of discovery of the different superconducting families and respective superconducting transition temperatures, T_C	36
1.9	Schematic view of the Hg-1201, Hg-1212 and Hg-1223 crystalline structures.	38
1.10	T_C dependence on the extra oxygen content, δ , for the 2 nd (Hg-1212) and 3 rd (Hg-1223) members of the Hg-based superconductors series ^[37–40]	40
2.1	Schematic representation of the sol-gel process.	46
2.2	Representative room temperature XRD patterns of hexagonal (left panel) and orthorhombic (right panel) RMnO_3 samples. The experimental patterns (dots), calculated (solid lines), reflections of the corresponding phases (tick marks) and fit deviation (solid line in the bottom) are presented.	48
2.3	SEM micrographs of representative samples of RMnO_3 series: a) LuMO, b) YMO, c) HMO, d) GMO, e) EuMO and f) SMO.	49
2.4	a) SEM micrograph of $\text{Ba}_2\text{Ca}_2\text{Cu}_3\text{O}_x$ calcined precursor powder obtained via the urea route. b) TGA curves for the nominal $\text{Ba}_2\text{Ca}_2\text{Cu}_3\text{O}_x$ calcined precursor powders obtained via the urea (U) and acrylamide (AA) routes.	51
2.5	XRD pattern obtained for the $\text{Ba}_2\text{Ca}_2\text{Cu}_3\text{O}_x$ precursor produced using urea and acrylamide routes: a) after annealing at 1093 K, in air for 20 hrs; b) after annealing at 1093 K, under vacuum for 10 hrs for the urea powder and 24 hrs for the acrylamide powder. The main reflections of $\text{Ba}_2\text{Cu}_3\text{O}_6$, CaCuO_2 and $\text{Ba}_2\text{Ca}_2\text{Cu}_3\text{O}_7$ are noted by 1, 2 and 3, respectively.	52
2.6	Schematic diagram of the Conac type high-pressure cell: (5) Anvil (tungsten carbide); (6) Gasket; (7) CaCO_3 cell; (8) Pyrophyllite; (9) Electrical contact; (10) Insulator in CaCO_3 ; (11) Furnace (graphite, Mo); (12) Capsule (Au, Pt) ^[41]	54
2.7	Representative room temperature XRD patterns of Hg-1212 (top) and Hg-1223 (bottom) samples. The experimental patterns (dots), calculated (solid line), reflections of the corresponding phases (tick marks) and fit deviation (solid line in the bottom) are presented.	56

2.8	a) Schematic representation of a $\gamma-\gamma$ cascade, with indication of the energies (E) and quantum numbers (i and f indexes refer to the initial and final states respectively). b) Representation of the alignment of the spin I of the intermediate state ($m=0$ is not populated), which is achieved by choosing the γ_1 emission direction as quantization axis.	58
2.9	a) Electric quadrupole energy splitting and b) magnetic splitting, for spin $I=5/2$ of the intermediate state, originated by an interaction with an EFG and a magnetic hyperfine field, respectively.	61
2.10	a) Schematic representation of an in-plane four detector $\gamma-\gamma$ PAC experimental setup. b) Illustrative representation of the count rate at 90° and 180°	64
2.11	Schematic representation of the Hg planes of $\text{HgBa}_2\text{CaCu}_2\text{O}_{6+\delta}$ and $\text{HgBa}_2\text{Ca}_2\text{Cu}_3\text{O}_{8+\delta}$ as viewed along the c axis. Shaded regions represent supercells with different O_δ concentrations ($\delta=0$ to 0.66).	71
2.12	Schematic representation of the ISOLDE hall with the general purpose separator (GPS), high resolution separator (HRS) and its different beam lines. The implantation chamber used in this work is located at the end of the GLM beam line.	72
2.13	Periodic table with the elements produced at ISOLDE (in blue). The elements suitable for solid state experiments are surrounded by circles.	73
2.14	a) ^{111}In decay to ^{111}Cd by electronic capture and b) $^{199\text{m}}\text{Hg}$ to ^{199}Hg decay cascade, with indication of the PAC cascades used in the PAC measurements.	74
2.15	a) Picture of the system used for annealings under oxygen pressure. b) Picture of the six detector $\gamma-\gamma$ PAC spectrometer equipped with a refrigerator mounted in the centre of the detectors.	76
3.1	a) a and c cell parameters, and b) respective unit cell volumes as a function of the rare-earth ionic radius (R_{I}^{3+}) for the hexagonal RMnO_3 ($R= \text{Lu, Er, Y and Ho}$). The closed dots represent the values obtained in this work. For comparison unit cell values for polycrystalline (hexagons) and single-crystal (stars) samples taken from the literature are also included ^[9,42-46] . Dashed lines are guides to the eye. The ionic radii have been taken from ^[47]	80

- 3.2 Field cooling magnetic susceptibilities as a function of temperature for the samples (nominal composition): a) LuMO (LuMnO₃), b) ErMO (ErMnO₃), c) YMO (YMnO₃) and HMO (HoMnO₃). Right side scale: inverse magnetic susceptibility for the same samples. 82
- 3.3 (Left) Representative room temperature R(t) experimental functions and correspondent fits (represented as thicker lines over the R(t) spectra) for the hexagonal RMnO₃ samples : a) LuMO (LuMnO₃), b) ErMO (ErMnO₃), c) YMO (YMnO₃) and d) HMO (HoMnO₃). (Right): Corresponding Fourier transforms. 84
- 3.4 EFG parameters for measurements at room temperature: a) EFG principal component, V_{zz} , b) asymmetry parameter, η , c) fractions of probes interacting with each EFG distribution, f , and d) static attenuation parameter, δ , for EFG₁ (closed dots) and EFG₂ (open dots). The vertical lines indicate the ionic radius of each rare-earth element, which have been taken from^[47]. The dashed lines are guides to the eye. . . 85
- 3.5 (Left) Representative R(t) experimental functions and correspondent fits (thicker lines over the R(t) spectra) measured at 573 K, for the hexagonal RMnO₃ samples: a) LuMO (LuMnO₃), b) ErMO (ErMnO₃), c) YMO (YMnO₃) and d) HMO (HoMnO₃). (Right) Corresponding Fourier transforms. 88
- 3.6 EFG parameters for measurements at 573 K: a) EFG principal component, V_{zz} , and b) asymmetry parameter. η , c) fractions of probes interacting with each EFG distribution, f , and d) static attenuation parameter, δ , for EFG₁ (closed dots) and EFG₂ (open dots). The vertical lines indicate the ionic radius of each rare-earth ion, which have been taken from^[47]. The dashed lines are guides to the eye. 89
- 3.7 (Left) Representative R(t) experimental functions and correspondent fits (thicker lines over the R(t) spectra) measured at 77 K, for the hexagonal RMnO₃ samples: a) LuMO (LuMnO₃), b) ErMO (ErMnO₃), c) YMO (YMnO₃) and d) HMO (HoMnO₃). (Right) Corresponding Fourier transforms. 91

- 3.8 EFG parameters for measurements at 77 K: a) EFG principal component, V_{zz} , b) asymmetry parameter, η , c) fractions of probes interacting with each EFG distribution, f , and d) static attenuation parameter, δ , for EFG₁ (closed dots) and EFG₂ (open dots). The vertical lines indicate the ionic radius of each rare-earth element, which have been taken from^[47]. The dashed lines are guides to the eye. 92
- 3.9 (Left) Representative $R(t)$ experimental functions and correspondent fits (thicker lines over the $R(t)$ spectra) measured at 10 K, for the hexagonal RMnO₃ samples: a) LuMO (LuMnO₃), b) ErMO (ErMnO₃), c) YMO (YMnO₃) and d) HMO (HoMnO₃). (Right): Corresponding Fourier transforms. 94
- 3.10 EFG parameters for measurements at 10 K: a) EFG principal component, V_{zz} , b) asymmetry parameters, η , c) fractions of probes interacting with each EFG distribution, f , and d) static attenuation parameter, δ , for EFG₁ (closed dots) and EFG₂ (open dots). The vertical lines indicate the ionic radius of each rare-earth element, which have been taken from^[47]. Dashed lines are guides to the eye. 96
- 3.11 (Left) Representative $R(t)$ experimental functions and correspondent fits (thicker lines over the $R(t)$ spectra) measured from room temperature (293 K) up to 1296 K, for YMnO₃. (Right) corresponding Fourier transforms. 98
- 3.12 (Left) Representative $R(t)$ experimental functions and correspondent fits (thicker lines over the $R(t)$ spectra) measured from 14 K up to 286 K, for YMnO₃. (Right) corresponding Fourier transforms. 99
- 3.13 EFG parameters dependence with temperature for YMnO₃: a) EFG principal component, V_{zz} , b) asymmetry parameter, η , c) fractions of probes interacting with each EFG distribution, f , and d) static attenuation parameter, δ . The vertical dashed lines indicate the ferroelectric (T_{FE}) and magnetic (T_N) transition temperatures. 101
- 3.14 (Left) Representative $R(t)$ experimental functions and correspondent fits (thicker lines over the $R(t)$ spectra) measured from 373 K up to 1296 K, for ErMnO₃. (Right) Corresponding Fourier transforms. 104

- 3.15 (Left) Representative $R(t)$ experimental functions and correspondent fits (thicker lines over the $R(t)$ spectra) measured from 10 K up to 292 K, for ErMnO_3 . (Right) Corresponding Fourier transforms. 105
- 3.16 EFG parameters evolution with temperature for ErMnO_3 : a) EFG principal component, V_{zz} , b) asymmetry parameter, η , c) fraction of probes interacting with each EFG distribution, f , and d) static attenuation parameter, δ . The vertical dashed lines indicate the ferroelectric (T_{FE}) and magnetic (T_{N}) transition temperatures. 106
- 3.17 EFG parameters evolution with the rare-earth ionic radius: a) EFG principal component, V_{zz} , and b) asymmetry parameter, η , for the experimental EFG₁ (closed dots) and EFG₂ (open dots). The APW calculated EFG parameters for R1 (stars), R2 (hexagons) and Mn (triangles) sites are included for comparison. 111
- 3.18 RMnO_3 (R= Tb, Gd, Eu, Sm and Nd) cell parameters as a function of the rare-earth ionic radius (R_{I}^{3+}). The closed dots represent the values obtained in this work. For comparison cell parameter values for polycrystalline (hexagons) samples taken from the literature are also included^[44,48-50]. Dashed lines are guides to the eye. The ionic radii have been taken from^[47]. 113
- 3.19 Field cooling magnetic susceptibilities as a function of temperature for the samples: a) TMO (TbMnO_3), b) GMO (GdMnO_3), c) SMO (SmMnO_3) and d) NMO (NdMnO_3). Right side scale: reciprocal magnetic susceptibility for the same samples. 115
- 3.20 (Left) Representative room temperature $R(t)$ experimental functions and correspondent fits (thicker lines over the $R(t)$ spectra) for the orthorhombic RMnO_3 samples: a) TMO (TbMnO_3), b) GMO (GdMnO_3), c) EuMO (EuMnO_3), d) SMO (SmMnO_3) and e) NMO (NdMnO_3). (Right) Corresponding Fourier transforms. 116
- 3.21 Room temperature EFG parameters for the orthorhombic RMnO_3 series: a) EFG principal component, V_{zz} , b) asymmetry parameter, η , c) fractions of probes interacting with each EFG, f , and d) static attenuation parameters, δ , for EFG₁ (closed dots) and EFG₂ (open dots). The vertical lines indicate the ionic radius of each rare-earth element, which has been taken from^[47]. The dashed lines are guides to the eye. 118

- 3.22 (Left) Representative $R(t)$ experimental functions and correspondent fits (represented as thicker lines over the $R(t)$ spectra) measured at 573 K, for the orthorhombic RMnO_3 samples: a) TMO (TbMnO_3), b) GMO (GdMnO_3), c) EuMO (EuMnO_3), d) SMO (SmMnO_3) and e) NMO (NdMnO_3). (Right) Corresponding Fourier transforms. 120
- 3.23 EFG parameters obtained at 573 K: a) EFG principal component, V_{zz} , b) asymmetry parameter, η , c) fractions of probes interacting with EFG distribution, f , and d) static attenuation parameter, δ , for EFG₁ (closed dots) and EFG₂ (open dots). The vertical lines indicate the ionic radius of each rare-earth element, which have been taken from^[47]. The dashed lines are guides to the eye. 122
- 3.24 (Left) Representative $R(t)$ experimental functions and correspondent fits (thicker lines over the $R(t)$ spectra) measured at 10 K, for the orthorhombic RMnO_3 samples: a) TMO (TbMnO_3), b) GMO (GdMnO_3), c) EuMO (EuMnO_3), d) SMO (SmMnO_3) and e) NMO (NdMnO_3). (Right) Corresponding Fourier transforms. 123
- 3.25 EFG parameters obtained at 10 K: a) EFG principal component, V_{zz} , b) asymmetry parameter, η , c) fractions of probes interacting with EFG distribution, f , and d) static attenuation parameter, δ , for EFG₁ (closed dots) and EFG₂ (open dots). The vertical lines indicate the ionic radius of each rare-earth element, which have been taken from^[47]. The dashed lines are guides to the eye. 125
- 3.26 (Left) Representative $R(t)$ experimental functions and correspondent fits (thicker lines over the $R(t)$ spectra) for EuMnO_3 measured from room temperature up to 968 K. (Right) Corresponding Fourier transforms. 127
- 3.27 (Left) Representative $R(t)$ experimental functions and correspondent fits (thicker lines over the $R(t)$ spectra) for EuMnO_3 measured from 10 K up to 292 K. (Right) Corresponding Fourier transforms. 128
- 3.28 EFG parameters as a function of temperature for EuMnO_3 : a) EFG principal component, V_{zz} , b) asymmetry parameter, η , c) fractions of probes interacting with each EFG, f , and d) static attenuation parameter, δ , for EFG₁ (closed dots) and EFG₂ (open dots). The vertical lines indicate the magnetic transition temperature, T_N . The dashed lines are guides to the eye. 130

3.29	EFG parameters evolution with the rare-earth ionic radius at room temperature: a) EFG principal component, V_{zz} , and b) asymmetry parameter, η , for the experimental EFG ₁ (closed dots) and EFG ₂ (open dots). The APW calculated EFG parameters for the rare-earth (hexagons) and manganese (triangles) sites are included for comparison. The dashed lines are guides to the eye.	133
3.30	EFG parameters evolution with the rare-earth ionic radius for the hexagonal and orthorhombic RMnO ₃ series: a) EFG principal component, V_{zz} , and b) asymmetry parameter, η , for the experimental EFG ₁ (closed dots) and EFG ₂ (open dots). . . .	134
4.1	Temperature dependence of the magnetic susceptibility, χ , for the Hg-1212.	138
4.2	a) a and c cell parameters, and b) superconducting transition temperature, T_C , dependence on the extra oxygen content, O_δ , for Hg-1212 samples. The experimental values obtained in this work are represented by closed dots and the values taken from the literature ^[37,38,51-54] by open dots. The vertical line indicate the values obtained per sample.	140
4.3	a)-f) (Left) Room temperature experimental perturbation functions, $R(t)$, and (Right) corresponding Fourier transforms for Hg-1212 samples. The thicker lines over the spectra are the fitting functions.	141
4.4	(Left) Room temperature experimental perturbation functions, $R(t)$, and (Right) corresponding Fourier transforms, for measurements performed at: a) atmospheric pressure and b) under 152 bar pressurized oxygen. The thicker lines over the spectra are the fitting functions.	144
4.5	a)-d) (Left) Experimental perturbation functions, $R(t)$, and (Right) corresponding Fourier transforms for measurements performed at 77 K in Hg-1212 samples. The thicker lines over the spectra are the fitting functions.	146
4.6	a) Principal component of each EFG tensor, V_{zz} , and b) asymmetry parameter, η , as a function of the preliminary annealing atmosphere. The obtained EFG are represented by open dots (E1), closed dots (E2) and closed squares (E3).	147
4.7	Temperature dependence of the magnetic susceptibility, χ , for Hg-1223.	149

- 4.8 a) a and c cell parameters, and b) superconducting transition temperature, T_C , dependence on the extra oxygen content, δO , for Hg-1223 samples. The experimental values obtained in this work are represented by closed dots while the literature values by open dots^[26,39,40,55,56]. The vertical lines represent the experimental values per sample. The dashed lines are guides to the eye. 150
- 4.9 a)-e) (Left) Room temperature experimental perturbation functions, $R(t)$, and (Right) corresponding Fourier transforms as a function of the annealing atmospheres for Hg-1223. The thicker lines over the spectra are the fitting functions. 151
- 4.10 (Left) Room temperature experimental perturbation functions, $R(t)$, and (Right) corresponding Fourier transforms for measurements performed in Hg-1223 at: a) atmospheric pressure and b) under 152 bar pressurized oxygen. The thicker lines over the spectra are the fitting functions. 154
- 4.11 a)-c) (Left) Experimental perturbation functions, $R(t)$, and (Right) corresponding Fourier transforms as a function of the annealing atmospheres for Hg-1223 as measured at 77 K. The thicker lines over the spectra are the fitting functions. . . . 156
- 4.12 a) Principal component of the EFG tensor, V_{zz} , and b) asymmetry parameter, η , as a function of the annealing atmosphere for Hg-1223. The obtained EFG are represented by open dots (E1), closed dots (E2) and closed squares (E3). 157
- 4.13 Representation of the Hg planes of Hg-1212 as viewed along the c axis. Shaded regions represent the different supercells used into the FLAPW simulations with different O_δ concentrations ($\delta= 0$ to 0.66). 158
- 4.14 Artistic view of the Hg-1212 supercell structures C2, C3 and C4, as obtained from the FLAPW calculations, which were used to calculate the EFGs: (Left) projections of the lattice along the c axis and (Right) projections along the plane perpendicular to the c axis. 160
- 4.15 Plot of relative z coordinates for: a) barium and b) apical oxygen as a function of dopant oxygen, δ . The data includes values reported in the literature^[37,52,55] (dark symbols) and from FLAPW calculations for different supercells with single O_δ (open dots) and with $O_{2\delta}$ dumbbell molecules (open squares). The calculated values are normalized to the neutron powder diffraction ones for the undoped case. 163

- 4.16 a) Evolution of the principal component of the EFG tensor, V_{zz} , and b) asymmetry parameter, η , with oxygen doping obtained from FLAPW calculation for different Hg-1201 supercells. The closed dots refer to unrelaxed structures^[57,58] and the open dots to the relaxed structures. 164
- 4.17 Experimental and simulated EFG parameters: a), c) principal component of the EFG tensor, V_{zz} ; and b), d): asymmetry parameter, η . The calculated EFG parameters for (top) Hg-1212+single O_δ and (bottom) Hg-1212+dumbbells $O_{2\delta}$ supercells are represented by the horizontal lines. 166
- 4.18 Neutron powder diffraction simulated spectra for: a) relaxed structure according to C2 configuration, and b) relaxed structure according to C2* configuration. The open dots represent the experimental data taken from^[59] and the line at the bottom represents the difference. 169

Chapter 1

General Features of Magneto-Electric Manganites and High- T_C Superconductors

This chapter presents introductory remarks about the general characteristics of two representative families of strongly correlated electron systems: the rare-earth manganites and Hg-based superconductors. Despite some distinct properties exhibited by these two systems, both fall into the same category since they reveal several fundamental aspects in common^[2]. Their crystal structures derive from the perovskite one, being strongly coupled to the electric and magnetic properties, through a complex interplay of charge, spin and lattice degrees of freedom. Moreover these systems are near a metal-insulator instability: the parent compounds are antiferromagnetic insulators which upon suitable doping exhibit anomalous metallic properties such as metal-insulator transitions accompanied by huge resistivity changes^[2].

The basic physical concepts ruling the properties of these systems have been established. Nonetheless, general theories are still lacking and long range order studies are yet not sufficient to fully explain their anomalous phenomena. In fact, their basic properties seem to depend strongly on the nanoscale and local atomic structure^[3,4]. For a better understanding of the work presented in this thesis, introductory remarks addressing the general features of these systems will be presented in the next sections.

1.1 The RMnO_3 (R=rare-earth) manganites

The manganese oxides, commonly called manganites^[5,6], are a very important group of compounds belonging to the strongly correlated electron systems. Numerous studies revealed several interesting properties such as colossal magneto resistance^[60], metal insulator transitions^[2] or more recently multiferroic/magnetoelectric effects^[35,61]. In particular, the parent compounds RMnO_3 (R=rare earth) have attracted considerable attention due to the complex electric and magnetic phase diagrams^[62] and the rich variety of unusual electronic states, which are known to be strongly dependent on the underlying lattice.

In the last decade, additional interest has been created by the rediscovery of coupling between ferroelectric and magnetic orders in the RMnO_3 manganites leading to the inclusion of these materials in the multiferroic magnetoelectric^[61,63] class of compounds. Multiferroic materials are those which exhibit at least two of the three, ferroic orders: ferroelectric, ferromagnetic or ferroelastic^[63]. The subclass of compounds where electric and magnetic orders are coupled are known as magnetoelectrics^[61,63]. This coupling is revealed by the change of electric polarization through external magnetic fields or, vice versa, the change of the magnetic order due to the application of an external electric field. Such multifunctionality is of great importance due to possible technological applications such as the design of ferroelectric memories which can be magnetically read/written^[64–66] or electrically tune barriers in magnetic tunnel junctions^[67]. In fact, this great potential for practical applications has led to an extremely rapid development in this field as pointed out by the numerous reports and reviews available in the literature (e.g.^[61,68–72]).

From the physical point of view these materials are extremely appealing as they can be used as a playground to study the coupling between charge, spin, orbital and lattice degrees of freedom^[73]. Their properties have been extensively studied and several microscopic mechanisms have been proposed^[74,75], which led to a classification of the multiferroic/magnetoelectric materials in two types. In the so-called type I multiferroics, ferroelectricity and magnetism have different sources and appear independently of one another although some coupling between them is observed. The ordered ferroelectric state appears at significantly higher temperatures than the ordering of the magnetic states and its spontaneous polarization, P , is rather large ($\sim 10\text{-}100 \mu\text{C}/\text{cm}^2$ ^[76,77]). Nevertheless, the ferroelectric order breaks the spatial inversion symmetry while the magnetic

order breaks the time-reversal symmetry leading to a weak magnetoelectric coupling. On the other hand, in type II multiferroics the ferroelectric order is magnetically induced. The magnetic order breaks both spatial and time inversion symmetry leading to a ferroelectric order and to a magnetoelectric coupling that is typically larger than the one exhibited by type I multiferroics. Though, the polarization in these materials is small being in the order of $10^{-2} \mu\text{C}/\text{cm}^2$ ^[78].

The rare-earth RMnO_3 manganites are included in both types of multiferroics since these compounds show two different crystalline structures: hexagonal or orthorhombic. Consequently, the electric and magnetic properties are distinct and are known to be strongly dependent on the underlying lattice. Most manganites form perovskite derived crystalline structures although the hexagonal layered ones can be also obtained for particular rare-earth substitutions. In fact, depending on the rare-earth ionic radius (R_I), the two structures can be obtained. For rare-earth ions (R^{3+}) with a smaller ionic radius than the Tb one (R=Ho-Lu, Y), the hexagonal structure is obtained whereas the orthorhombic perovskite structure is stabilized for larger rare-earth ions (R=La-Tb). Furthermore, the compounds with smaller rare-earth ions can be also synthesized as a metastable phase in the orthorhombic structure by either special chemical procedures^[48,79,80] or high pressure methods^[36,81].

Figure 1.1 shows a representation of the hexagonal (left) and orthorhombic (right) RMnO_3 crystalline structures where one can see the respective manganese and rare-earth environments. The crystalline structure of the hexagonal manganites has one major difference when compared to the orthorhombic structure: the manganese ions are located at the center of a trigonal bipyramid (MnO_5) whereas in the orthorhombic structure the Mn ions are octahedrally coordinated forming MnO_6 blocks. As a consequence of these differences in the Mn coordination, the corresponding crystal field is distinct, as schematically represented in fig. 1.2. In the trigonal bipyramid symmetry, the crystal field splits the $3d$ orbitals of Mn into two doublets (e_{1g} and e_{2g}) and one singlet (a_{1g}). The Mn^{3+} ground state configuration becomes $e_{1g}^2 e_{2g}^2$ with no partially filled degenerate level. On the other hand, in the octahedral symmetry the crystal field divides the $3d$ orbitals into one triplet (t_{2g}) and one doublet (e_g).

As a consequence of the different manganese local environments, these compounds show different electric and magnetic properties. Figure 1.3 shows the evolution of the structural (T_{struct}), ferroelectric (T_{FE}) and magnetic transition temperatures (T_{N}) as function of the rare-earth ionic

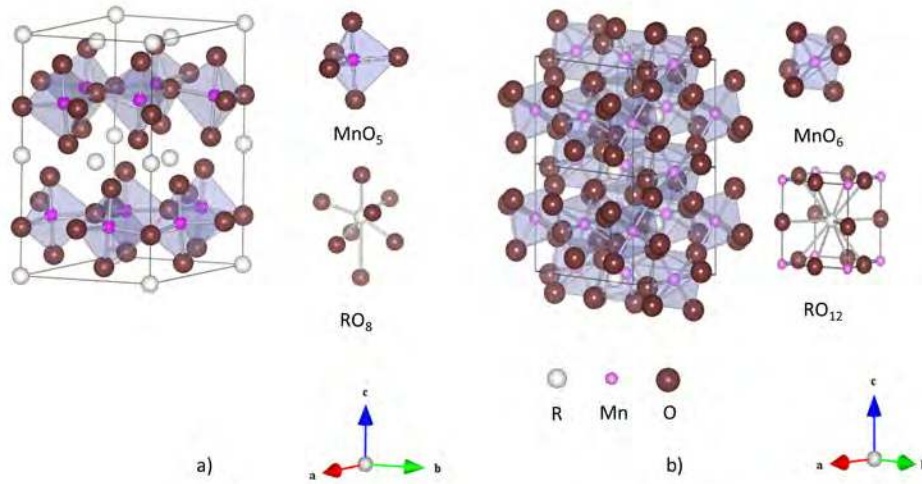


Figure 1.1: The crystal structures of RMnO_3 manganites: a) hexagonal structure (space group $P6_3cm$) and its local MnO_5 and RO_8 environments; and b) orthorhombic structure (space group $Pnma$) and its local MnO_6 and RO_{12} environments.

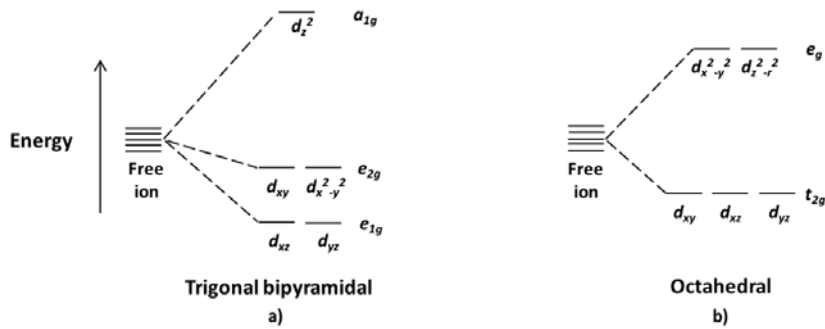


Figure 1.2: The crystal field in: a) trigonal bipyramidal environment, and b) octahedral environment.

radius for both hexagonal and orthorhombic structures. The ferroelectric order in these compounds is found to be very distinct in the two crystalline structures. The hexagonal manganites exhibit a distinct ferroelectric transition at high temperatures ($T_{\text{FE}} \sim 600\text{-}1000 \text{ K}$ ^[82,83]) and spontaneous polarizations of about $P \sim 5 \mu\text{C}/\text{cm}^2$ ^[76] leading to the inclusion of these compounds on type I multiferroics. Moreover, the hexagonal compounds show a structural transition given by the change in the space group typically $\sim 200 \text{ K}$ above T_{FE} . On the other hand, the orthorhombic RMnO_3 ,

that are included on type II multiferroics, exhibit ferroelectric ordering induced by the magnetic transition with $T_{\text{FE}} \sim 20\text{-}40\text{ K}$ ^[35,84]. Here, the spontaneous polarization is much smaller than for the hexagonal compound being in the order of $\sim 10^{-2}\text{ }\mu\text{C}/\text{cm}^2$ ^[78] although the magnetoelectric coupling is rather strong.

Concerning the magnetic properties, in the hexagonal structure, the MnO_5 bipyramids are linked in a two dimensional (2D) Mn-O-Mn superexchange interaction in the ab plane, which leads to an antiferromagnetic (AFM) ordering of the Mn spins at temperatures below $T_{\text{N}} \sim 90\text{ K}$ ^[85,86]. In contrast, the MnO_6 form a three dimensional (3D) magnetic structure with Mn-O-Mn interplane superexchange interaction leading to an AFM ordering of the Mn spins with T_{N} ranging between 30 and 140 K^[35]. Furthermore, these compounds exhibit a complex magnetic phase diagram with the appearance of different magnetic structures below T_{N} ^[35].

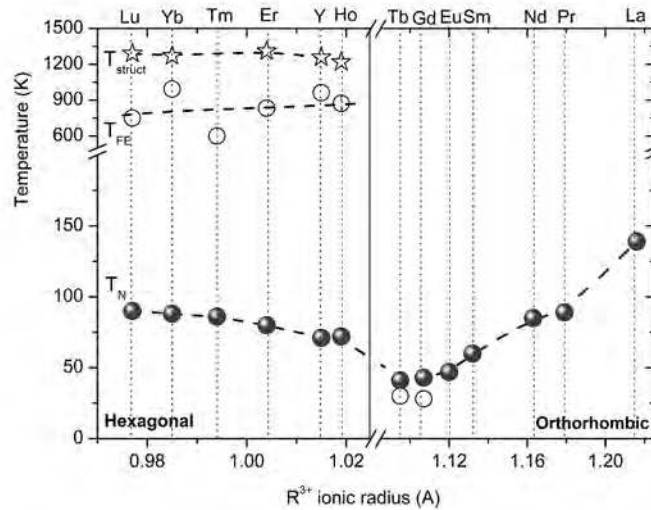


Figure 1.3: Structural, T_{struct} (stars), ferroelectric, T_{FE} (open dots), and magnetic, T_{N} (closed dots) transition temperatures as function of the rare-earth ionic radius (R^{3+}) for hexagonal and orthorhombic RMnO_3 .

These properties are strongly dependent on the underlying lattice and detailed knowledge on how the properties and structure evolve with the rare-earth ionic radius is thus expected to provide significant insights into the complex physics of the rare-earth manganites series. For a better understanding of the most relevant structural, magnetic and electric features of this series of compounds, the further descriptions will be performed addressing the different crystalline structures

and their properties.

1.1.1 Hexagonal RMnO_3

Crystal structure and ferroelectricity

RMnO_3 manganites with rare-earths with ionic radius smaller than that of terbium have the hexagonal layered structure as the thermodynamically stable state. Nevertheless, by varying the synthesis technique these compounds can be also obtained as a metastable phase in the orthorhombic structure^[36,48,79–81]. These compounds have been extensively studied due their multiferroic behavior^[68,73] and its crystalline structure has been precisely determined by X-ray and neutron diffraction techniques^[42,43,87–90].

Figure 1.4(a) shows a view along the c -axis of the room temperature hexagonal structure of RMnO_3 . This crystalline structure consists of layers of MnO_5 polyhedra that are separated by layers of R^{3+} along the c -axis. The manganese ions are surrounded by two apical oxygen ions (denoted as O1 and O2) and three in plane O ions (one O3 and two O4) while R is surrounded by eight oxygen ions. At room temperature, the hexagonal RMnO_3 crystallize in the non-centrosymmetric $P6_3cm$ space group where two non equivalent rare-earth sites are allowed (denoted as R1 and R2)^[91].

Changes in the hexagonal crystalline structure are known to occur with temperature. At high temperatures (typically above 1200 K^[82,83,92]), these compounds show a centrosymmetric structure (space group $P6_3/mmc$, shown in fig. 1.4(b)) where all atoms are constrained to planes parallel to ab . This high temperature structure can be seen as the undistorted form of the room temperature one. Lowering temperature, the structure loses its mirror planes parallel to ab and undergoes a transition from the centrosymmetric to the non-centrosymmetric structure (space group $P6_3cm$). Furthermore, this transition results in the tilting of the MnO_5 polyhedra, unequal apical R-O bond lengths and tripling of the unit cell volume with low temperature unit-cell parameters $a = \sqrt{3}a'$ and $c = c'$ ^[90,93].

The change to non-centrosymmetric space group would be expected to originate ferroelectricity since the removal of the center of symmetry allows the appearance of electric polarization. However, the ferroelectric ordering is found to be several hundreds kelvin lower than the structural transition. Furthermore, discrepancies in the values of the ferroelectric ordering temperature, T_{FE} , have been

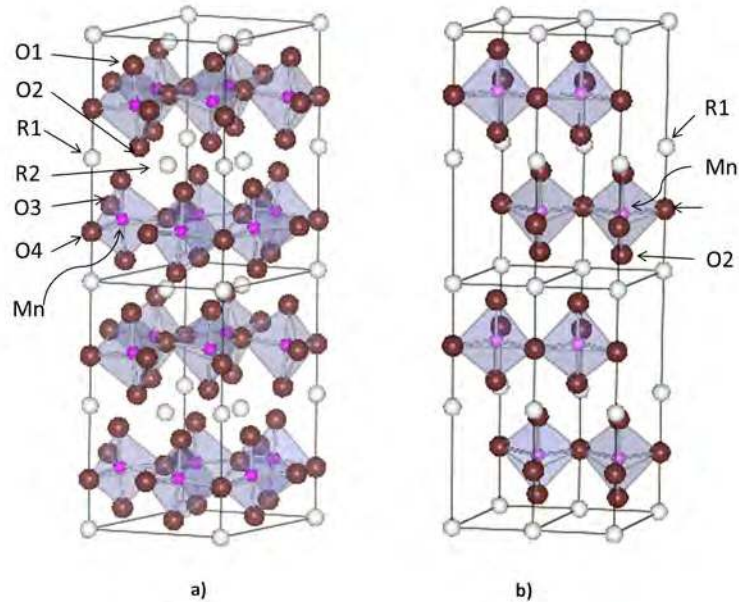


Figure 1.4: Sketch view of the hexagonal RMnO_3 crystal structure: a) the room temperature $P6_3cm$ space group, and b) the high temperature $P6_3/mmc$ paraelectric space group.

reported leading to ambiguity about the mechanism and exact nature of the polar ordering. Some authors attributed these discrepancies to impurities introduced by the synthesis method^[94]. One shall note that the subtle nature of the transitions and experimental difficulties in measuring physical properties at high temperatures make the transition temperatures difficult to define.

Different mechanisms for the occurrence of ferroelectricity have been proposed. The unusual electronic structure of the MnO_5 bipyramids has been suspected to be relevant for ferroelectricity in the hexagonal RMnO_3 . First principle calculations^[95] suggested one dimensional Mn d^0 -ness as the origin of ferroelectricity in these compounds. Since under the trigonal symmetry (shown in fig. 1.2(a)) the $\text{Mn}^{3+} d^4$ ground state configuration becomes $e_{1g}^2 e_{2g}^2$, the a_{1g} orbital is empty and can hybridize with the O $2p$ orbitals along the hexagonal c axis. Nevertheless, x-ray and neutron powder diffraction studies^[96,97] found no off center displacement of the Mn ions within the MnO_5 polyhedra, contradicting the one dimensional Mn d^0 -ness scenario. Moreover, these results^[96] showed that the polarization in the hexagonal RMnO_3 is a geometric effect rather than hybridization. Here, ferroelectricity is presented as a consequence of the unusual rare-earth site coordination and layered MnO_5 network whereas long range dipole interactions and oxygen rotations both cooperate leading

the system to the ferroelectric order. In fact, the two non-equivalent rare-earth sites (R1 and R2) allowed by the $P6_3cm$ space group are responsible for the appearance of ferroelectricity in these compounds. The dipolar ordering in these compounds is due to opposing dipoles caused by opposite but unequal displacements of the two rare-earth sites^[73] (which leads to a net polarization) and the associated tilting and distortion of the MnO_5 bipyramids^[96,98] resulting in a ferrielectric-like ordering. This unusual driving mechanism has been termed geometric ferroelectricity^[96] as it seems to depend purely on ionic size effects.

Although there is a general agreement regarding the importance of the rare-earth off center movements at the origin of ferroelectricity in the hexagonal $RMnO_3$, the existence of two transitions at high temperatures is not fully understood. The existence of an intermediate phase between the structural and ferroelectric transitions has been noted by several authors. Abrahams^[83,99] reported an atomic coordinate analysis study of the $YMnO_3$ system where a paraelectric and paramagnetic phase ($P6_3/mcm$) is found between T_{FE} and T_{struct} . At T_{struct} , the phase transition to $P6_3/mmc$ space group with reduction of the cell volume is reported. Lonkai et al.^[82] have calculated irreducible representations of the distortions from the high to the low temperature structures suggesting a two step phase transition at temperatures $T > T_{FE}$. These results have been further confirmed by other authors^[98]. High temperature x-ray synchrotron diffraction measurements performed by Nénert et al.^[94] also revealed the existence of an intermediate phase in the same temperature range, based on the slow changes in the a and c lattice parameters between the structural and ferroelectric transitions.

Recent neutron powder diffraction studies^[90] in $YMnO_3$ found no intermediate phase between the paraelectric $P6_3/mmc$ phase and the polar $P6_3cm$ one. Although these authors did not observe a defined intermediate phase of differing crystallographic symmetry, their results show evidence of a secondary isosymmetric transition in the $P6_3cm$ phase, simultaneous with T_{FE} , being attributed to an electronic transition involving the Y-O3 bonds.

The existence of two high temperature transitions in the hexagonal $RMnO_3$ is still ambiguous and the knowledge of the long range crystallographic structure may be not sufficient to explain these differences. The use of local probe techniques can give an important contribution to a better understanding of the existence of two high temperature transitions and its relation with the appearance of ferroelectricity in the hexagonal compounds. One shall note that most of the

studies reported on the literature are concerned to YMnO_3 and studies on the full RMnO_3 hexagonal series are expected to give further insights on the mechanism responsible for ferroelectricity.

Magnetic properties

The magnetic properties of the hexagonal RMnO_3 have been investigated using neutron powder diffraction^[7,9,76,88,100,101], second harmonic generation^[102], magnetic and heat capacity measurements^[85,86,103–105]. The magnetic structure of these compounds is formed by Mn^{3+} ions in a two dimensional triangular network in the ab plane coupled by antiferromagnetic (AFM) exchange, where the Mn^{3+} ions occupy the $6c$ positions in the $P6_3cm$ space group of the hexagonal structure. Each Mn^{3+} has trigonal symmetry and it is connected to two apical (O1 and O2) and three in plane (two O3 and O4) oxygens. The magnetic order of the Mn moments is dominated by antiferromagnetic (AFM) in plane Mn-O-Mn superexchange interactions, which are stronger than the interplane Mn-O-O-Mn interactions. This two dimensional (2D) triangular lattice gives rise to geometrically frustrated magnetism^[106] leading to spin frustration effects and an AFM spin arrangement with neighboring spins rotated by 120° . The Mn^{3+} spins order below T_N , which ranges from 70 to 100 K upon changing the rare-earth^[85,86,107]. In some cases, these temperatures can be much lower than the Curie-Weiss temperature (θ_P). These large differences between T_N and $|\theta_P|$ are attributed to the strong geometrical frustration of the triangular lattice of the Mn ions. Furthermore, in the hexagonal RMnO_3 with R^{3+} with partially filled $4f$ shell (R=Ho, Er, Tm, Yb) there is an additional contribution to the magnetic properties due to the R^{3+} spin ordering at much lower temperatures than those of Mn, typically below 10 K^[107].

One shall note that in addition to the magnetic ordering of the Mn spins, spin-reorientational phase transitions (T_{SR}) have been observed particularly in HoMnO_3 ^[11,88,101]. Heat capacity and magnetic susceptibility measurements observed that the position of T_N is independent of external magnetic fields whereas T_{SR} is strongly field dependent and moves to lower temperature with increasing magnetic fields^[108]. Furthermore, anomalies in the dielectric constants and heat capacity measurements suggest a strong coupling between the magnetic and ferroelectric order.

To understand the unique coexistence of magnetism and ferroelectricity and their interplay in these compounds, it is essential to know how various parameters change under the variation of R.

1.1.2 Orthorhombic RMnO_3

Crystal structures

The RMnO_3 compounds with R larger than Ho crystallize in the perovskite-like orthorhombic structure within the $Pbnm$ space group. Ideally, the RMnO_3 perovskite structure can be visualized as a three-dimensional network of corner-sharing MnO_6 octahedra, with the Mn ions in the middle. Eight octahedra form a cube with the R ion placed in its centre being twelfefold surrounded by oxygen ions. The insertion of R ions with smaller ionic radius leads to a deviation from the cubic structure leading to the so-called orthorhombic distortion, as depicted in figure 1.5, which arises from two sources. One is the mismatch of the R-O and Mn-O equilibrium lengths with a lattice adjustment by a cooperative rotation (tilting) of the MnO_6 octahedra, which further increases with decreasing ionic radius of the rare-earth^[109]. The deviation from the ideal cubic structure is given by the tolerance factor, t , , proposed by Goldschmidt^[110]:

$$t = \frac{r_A + r_O}{\sqrt{2}(r_B + r_O)} \quad (1.1)$$

where r_A , r_B and r_O are the ionic radius of A, B and oxygen ions respectively. For a purely cubic structure the tolerance factor is equal to unity. Large deviations from the unity will indicate the formation of distorted perovskite structures such as orthorhombic, rhombohedral or tetragonal. The tolerance factor can be also expressed using the interatomic distances between the A and B ions and oxygen (d_{A-O} and d_{B-O} , respectively)^[110]:

$$t = \frac{d_{A-O}}{\sqrt{2}d_{B-O}} \quad (1.2)$$

In addition, the lattice is further distorted by the Jahn-Teller (JT) deformation. These distortions appear in the presence of certain ions (Mn^{3+} , Cr^{2+} or Cu^{2+}) due to their particular electronic configuration. In the free Mn^{3+} ion ($3d^4$), its d orbitals (d_{xy} , d_{zx} , d_{yz} , $d_{x^2-y^2}$ and d_{z^2} , as depicted in fig. 1.2(b)) will be degenerated in energy. In the MnO_6 environment, the crystal field potential blocks the *free – rotation* of the electrons by introducing the crystal field splitting of the d orbitals. This partial removal of the orbital degeneracy splits the orbitals into two states: e_g ($d_{x^2-y^2}$ and d_{z^2}) and t_{2g} (d_{xy} , d_{xz} and d_{yz}). This crystal field splitting does not introduce any distortion in the MnO_6 octahedra, unless one of the high energy e_g states is occupied as observed for Mn^{3+} . The four electrons in Mn^{3+} will occupy the three t_{2g} and one of the high energy e_g orbitals.

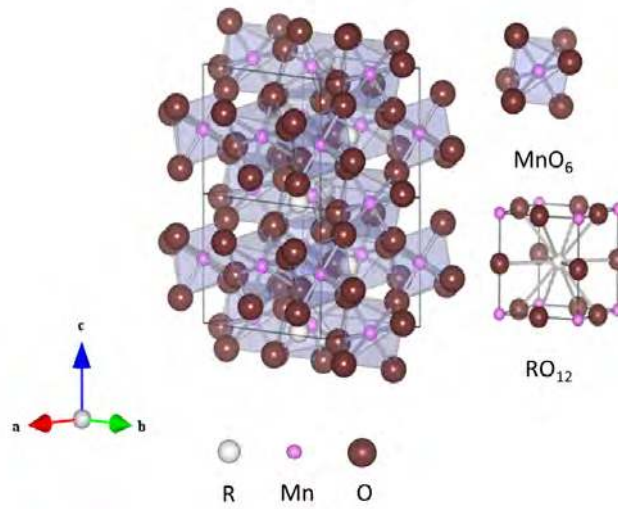


Figure 1.5: Sketch view of the orthorhombic RMnO_3 crystal structure. On the right side, the local MnO_6 and RO_{12} local environments.

The electronic energy of the singly occupied e_g state can be lowered if the double degeneracy of the e_g orbitals is lifted through a distortion of the MnO_6 octahedra, as shown in fig. 1.6. This distortion becomes long range ordered below T_{JT} and increases with the rare-earth ionic radius from ~ 750 K for La to ~ 1500 K for Dy^[48,111].

At room temperature, the RMnO_3 series (R= Tb, Gd, Eu, Sm, and Nd) presented in this work crystallize in the orthorhombic structure, within the $Pbnm$ space group where only one non-equivalent rare-earth site is allowed.

Magnetic properties and ferroelectricity

The orthorhombic RMnO_3 show a complex magnetic phase diagram with changes in the ground state while varying the rare-earth ionic radius. Figure 1.7(a) shows the magnetic phase diagram for a series of orthorhombic RMnO_3 following results reported in the literature^[35,36]. In fig. 1.7(b) the most common types of spin arrangements are presented.

Looking at fig. 1.7(a), one can observe that with decreasing R_{I}^{3+} , the magnetic ground state of the RMnO_3 compounds changes from the A-type antiferromagnetic ordering (A-AFM) (for the large ionic radius elements such as LaMnO_3) to a spiral spin state (like TbMnO_3 and DyMnO_3) and

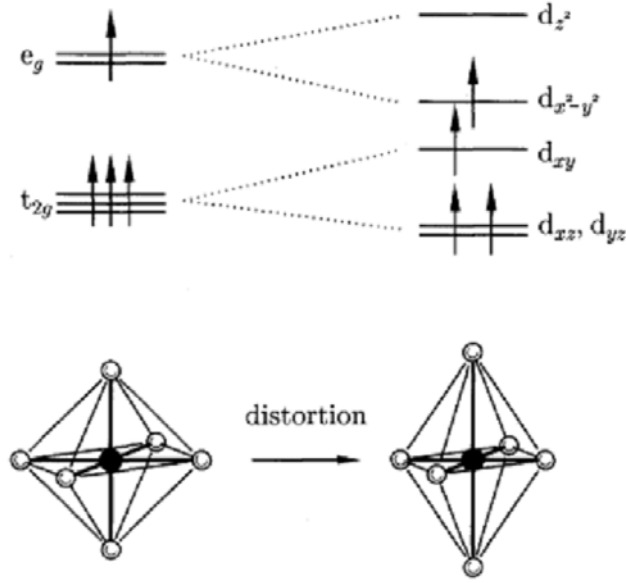


Figure 1.6: The Jahn Teller effect for Mn^{3+} ($3d^4$): the MnO_6 octahedra (left) can distort (right), leading to the splitting of the t_{2g} and e_g orbitals. This distortion lowers the overall energy by lowering the energy of the singly occupied e_g orbital. The saving in energy from the lowering of the d_{xz} and d_{yz} orbitals is balanced by the raising of the d_{xy} one. Adapted from [34].

to the E-AFM (displayed by the orthorhombic HoMnO_3) [35,36]. A continuous decrease on T_N with decreasing ionic radius for La to Gd is observed, as expected from the increased structural distortion. For Eu and Gd, a sinusoidal incommensurate (IC) magnetic structure is observed before the A-type ordering. Furthermore, for Tb and Dy the A-type AFM structure is no longer the stable ground-state structure where the IC structure undergoes a transition to a transverse spiral structure [112,113]. This spiral structure is reported to be responsible for the appearance of ferroelectricity and magneto-electric effects due to the break of the spatial inversion symmetry [35,114]. For Ho and the smaller rare-earths, the spin structure presents similar changes with a transition from the IC structure to an E-type AFM arrangement [101]. In particular, the orthorhombic HoMnO_3 is also reported to be ferroelectric [35,101].

The appearance of ferroelectricity in the orthorhombic manganites is not expected following structural considerations. In fact, contrarily to the hexagonal manganites, the origin of ferroelectricity is not due to structural displacements but due to the appearance of an incommensurate

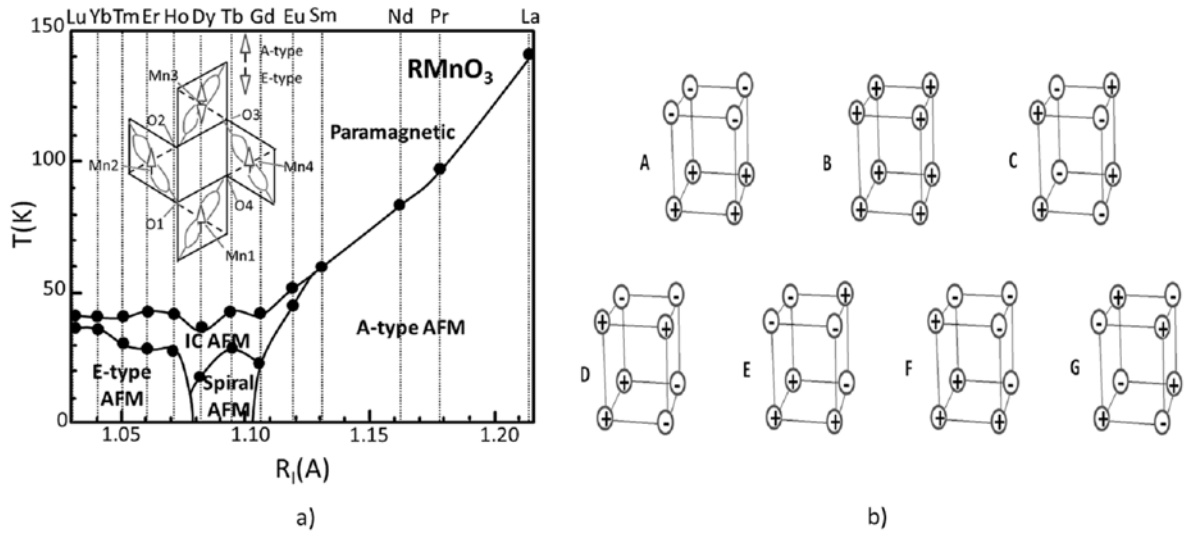


Figure 1.7: a) Magnetic phase diagram for orthorhombic RMnO_3 as function of the rare-earth ionic radius (R_1^{3+}). The data has been taken from [35,36]. b) Different possible spin arrangements. The circles represent the position of the Mn ions and the sign of their spin projections along the z -axis. Adapted from [6].

order, which breaks the inversion symmetry of the space group $Pbnm$ [35]. One shall note that although EuMnO_3 shows an IC ordering no evidences for the appearance of ferroelectricity have been reported. Nonetheless, in the $\text{Eu}_{1-x}\text{Y}_x\text{MnO}_3$ system, a ferroelectric polarization was observed coexisting with a spiral magnetic phase for concentrations $x \geq 0.3$ [115].

1.1.3 Methodology

The study of local distortions at the rare-earth site in a series of hexagonal and orthorhombic RMnO_3 has been performed using the perturbed angular correlations (PAC) technique. With this aim, polycrystalline samples of the RMnO_3 series have been synthesized via sol-gel methods at ambient pressure. The quality control of the samples has been performed using x-ray diffraction and magnetic measurements.

The PAC measurements have been performed after implanting the samples with ^{111}mCd or ^{111}In , to a small dose of 10^{11} atoms, followed by suitable annealing to recover from remaining implantation damage. To perform the measurements, a six detector PAC spectrometer has been used in a temperature range from 10 up to 1300 K, covering both magnetic and ferroelectric transitions. The PAC experimental data has been interpreted with the help of first principle full

potential augmented plane wave (FLAPW) calculations.

1.2 Hg-based high T_C superconductors

The discovery of superconductivity in the system La-Ba-Cu-O in 1986 by Bednorz and Müller^[13] led to a flurry of research in this field. As a consequence, several families of cuprates, and recently iron-based compounds^[116–118], were found to display superconductivity. Figure 1.8 shows a schematic representation of the time line of the discovery of the different superconductor families together with the respective superconducting transition temperatures, T_C . In particular, the discovery of high temperature superconductivity contributed to the findings of new areas of the materials behavior as well as to the development and optimization of new techniques allowing the study of microscopic phenomena responsible for superconductivity. Regardless of these progresses, more than 20 years after the discovery of superconductivity in cuprates, there is yet no theoretical understanding nor unanimously accepted explanation for the mechanism responsible for superconductivity in these materials.

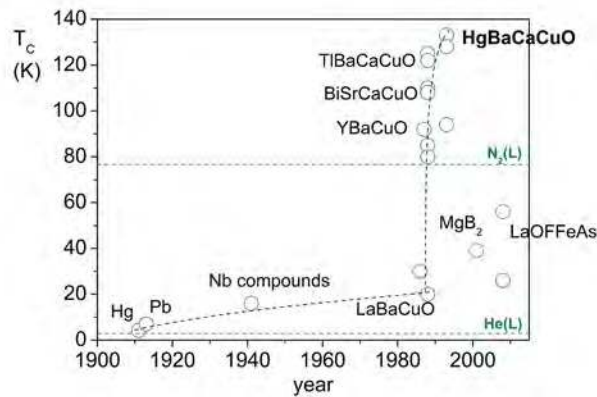


Figure 1.8: Schematic representation of the time line of discovery of the different superconducting families and respective superconducting transition temperatures, T_C .

The presence of dopants in high T_C superconductors (HTSC) is a crucial parameter that determines its critical temperature. Moreover, it is well established that the presence of dopants in these compounds strongly affect their behavior causing structural and electronic inhomogeneities^[20,25]. The existence of intrinsic inhomogeneities inherent to doping and how is the relationship between charge ordering and doping became open questions of the physics of the

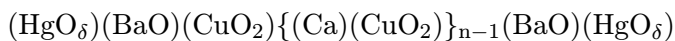
HTSC materials^[14-17].

In contrast to conventional superconductors, cuprates are randomly doped systems leading to atomic scale variations in their chemical and electronic structure. The most remarkable examples are the hole-doped cuprates (La, Y, Bi, Tl and Hg based families, with the highest T_C 's) where superconductivity appears when the antiferromagnetic insulating compound is doped with holes^[18]. This mechanism is generally related with a distribution of different dopant ions inducing charge transfer to the CuO_2 layers. This distribution leads to a chemical and electronic local inhomogeneity, diverging from the average structure that definitely trigger the electronic mechanism of superconductivity in these materials^[19,20]. Local disorder has been observed experimentally using techniques such as Scanning Tunneling Microscopy^[20,21], Angle Resolved Photoinduced Emission Spectroscopy^[22], Nuclear Magnetic Resonance^[23,24], among others. Some of these experiments have revealed that the nanoscopic disorder is correlated with the location of interstitial oxygen dopant atoms^[19,20] suggesting a strong interplay between the dopant atoms and the local electronic properties in these materials.

Among the cuprate superconductors, the mercury-based family ($\text{HgBa}_2\text{Ca}_{n-1}\text{Cu}_n\text{O}_{2n+2+\delta}$) is a good prototype to study the existence of disorder or inhomogeneities at the atomic scale due to its simple tetragonal structure and the highest T_C 's (132 K for the 3rd member of the series^[26]). A description of the crystalline structures and doping questions of the Hg-based superconductors will be addressed in the next subsections.

1.2.1 Crystal structure

The crystalline structures of the mercury-based homologous series (also denoted as Hg-12(n-1)n) can be described in the frame of layered structures. Figure 1.9 shows a schematic view of the layered crystalline structures of the first three members of the Hg-based homologous series. This structure can be seen as a continuous stacking of perovskite-type layers of $(\text{CuO}_2)\text{Ca}(\text{CuO}_2)_{n-1}$ and rock-salt layers of $(\text{BaO})(\text{HgO}_\delta)(\text{BaO})$. The perovskite-like blocks contain the main structural unit of these compounds, the superconducting Cu-O planes, and the thickness of this block may vary by the insertion of $(\text{Ca})(\text{CuO}_2)$ fragments resulting in the formation of the sequence of layers alternating along the c -axis of the unit cell:



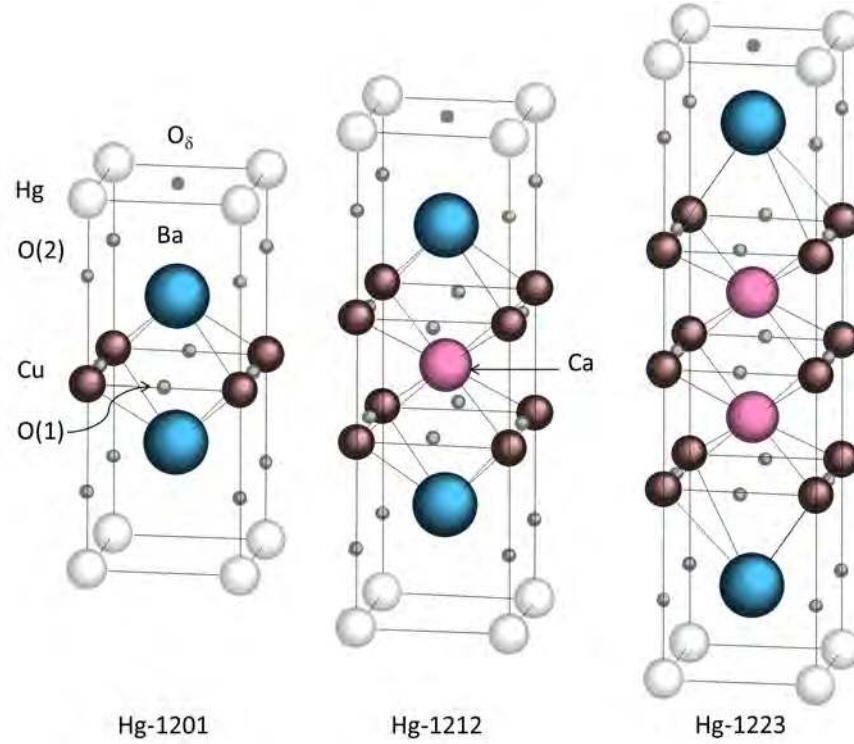


Figure 1.9: Schematic view of the Hg-1201, Hg-1212 and Hg-1223 crystalline structures.

These compounds crystallize in the tetragonal crystalline structure (space group $P4/mmm$) with close a parameters whereas c increases with the thickness of the perovskite block, following the formula: $c(\text{\AA}) \approx 9.5 + 3.2 \times (n - 1)^{[119]}$. Furthermore, the insertion of $(\text{Ca})(\text{CuO}_2)$ layers leads to different copper coordination environment, which changes from octahedral, CuO_6 , in the first member (Hg-1201) to square pyramid, CuO_5 , in the second one (Hg-1212)^[119]. In the 3rd member of this series, Hg-1223, two different types of Cu-O planes are found: one consisting of corner shared CuO_4 squares without apical oxygen atoms and square-planar coordination in addition to two CuO_5 pyramids with fivefold pyramidal coordination^[39]. The increase of the number of copper planes (n) results in an increase of the number of layers where the copper atoms have only square-planar environment. The CuO_6 octahedra and the CuO_5 pyramids are apically elongated due to the Jahn-Teller distortion, exhibiting much longer Cu-O interatomic distances along the c -axis than in the ab -plane^[119], being this apical distance much longer for the Hg-based homologous series when compared with other cuprate superconductors. As an example, the Cu-O apical distance in Hg-1201 ranges between 2.75-2.8 \AA while for the first member of the Y-based series ($\text{YBa}_2\text{Cu}_3\text{O}_7$) it equals

to 2.32 \AA [32,120].

The Cu-O planes are linked by O-Hg-O chains involving the apical oxygen atoms in a stable dumbbell coordination, which leads to the formation of two strong covalent Hg-O bonds. Thus, the interaction with the non-stoichiometric oxygen atoms (O_δ) located at the middle of Hg square mesh is very weak. One shall note that the insertion of O_δ does not result in the appearance of a superstructure or long range distortions due to their positioning in the middle of the Hg square and weak bonding to cations. Therefore, the non stoichiometric oxygen atoms can be easily removed without significant structural changes.

The simple tetragonal crystalline structure exhibited by the Hg-based series makes these compounds promising for systematic experimental investigations. Furthermore, the record transition temperatures and the property of confining chemical disorder to the Hg layers makes this system extremely appealing for the study of local inhomogeneities. Nonetheless, these compounds have received little attention when compared to other cuprates series due to the difficulties inherent to the synthesis of single phase bulk samples and to the lack of sizeable high quality single crystals. Recently, Hg-1201 single crystals have been growth successfully and have been used in x-ray and neutron scattering, optical conductivity and specific heat measurements^[27,121] opening the possibility of performing new studies.

1.2.2 Doping questions

The existence of non-stoichiometric excess oxygen (O_δ) in the Hg planes has been reported in early x-ray and neutron diffraction studies^[32,37,119] and its influence on T_C has been carefully studied. Figure 1.10 shows the dependence of T_C on oxygen doping for Hg-1212 and Hg-1223 where a cupola-like dependence is observed. The experimental T_C values reported by several authors^[37-40] have been correlated with oxygen doping contents, which have been determined by x-ray and neutron powder diffraction techniques^[30,31,39,51,55,122].

The comparison of δ obtained from refinement of neutron diffraction data with the hole concentration estimated by thermoelectric power measurements^[31] or iodometric titration^[32] showed differences on the doping values for samples with similar T_C 's. Moreover, the doping level at the Cu-O planes was found to be considerably lower than the expected following formal ionic considerations^[29,30]. These differences suggested the presence of single charged oxygen anions^[29,31]

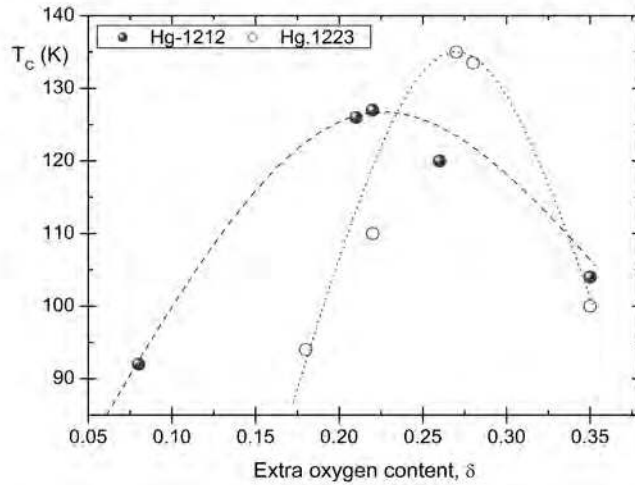


Figure 1.10: T_C dependence on the extra oxygen content, δ , for the 2nd (Hg-1212) and 3rd (Hg-1223) members of the Hg-based superconductors series^[37–40].

or different oxygen species at the Hg planes, as suggested for $\text{La}_2\text{CuO}_{4+\delta}$ ^[123].

The role of O_δ in the formation of charge inhomogeneities and local disorder in Hg-based superconductors is not yet fully understood and its impact on the local electronic and structural properties is of great importance. Systematic studies on doping efficiency lead to different results, which are attributed to the existence of point defects and impurities^[124]. In this context, the nuclear techniques, and in particular the perturbed angular correlation technique, can give an important contribution by measuring the local amount of dopant atoms in the Hg vicinity as demonstrated by previous works performed in Hg-1201^[57,58].

1.2.3 Methodology

The study of oxygen ordering at the Hg planes in the 2nd and 3rd members of the Hg-based superconductor family (denoted as Hg-1212 and Hg-1223) has been performed using the perturbed angular correlation (PAC) technique.

Hg-1212 and Hg-1223 polycrystalline samples have been synthesized via the high pressure - high temperature (HP-HT) technique. The control of quality of the synthesized samples has been performed using X-ray diffraction and magnetic measurements

To perform the PAC experiments, the samples have been implanted with $^{199\text{m}}\text{Hg}$ to a small dose

of 10^{11} atoms followed by annealing. Several different annealings have been performed to change the oxygen content of the synthesized samples. After annealing, the PAC spectra have been measured using a six detector spectrometer at room temperature and 77 K, allowing to study possible changes upon the superconducting transition. The experimental results have been interpreted with the help of first principle full potential linearized augmented plane wave (FLAPW) calculations for different supercells accounting for different oxygen concentrations and configurations.

Chapter 2

Experimental Characterization

In this chapter a general outline of the experimental techniques used in this work is given to the essential of our use, with appropriate reference to the extensive number of publications with a comprehensive explanation of those techniques. In the first section, the structural and chemical characterization techniques are briefly introduced followed by a simple description of the magnetic methods. The second section is dedicated to the overview of the methods employed to produce the samples used in this work with focus to the developments achieved on the preparation techniques. The last section is dedicated to the hyperfine characterization techniques.

2.1 Structural and magnetic characterization

2.1.1 X-ray diffraction

The crystalline structure of the polycrystalline samples was characterized using a Siemens D-5000 x-ray diffractometer, installed at Institut Néel (CNRS/Grenoble). This diffractometer is equipped with a Ge monochromator at the primary beam (with Cu K_α radiation, $\lambda=1.54056\text{\AA}$). The diffractograms have been obtained in a 2θ range between 10° and 90° and depending on the desired precision of the measurement the 2θ steps ranged between 0.01° and 0.05° . The measurements have been performed in powder samples permitting that the distribution and orientation of the small crystals would be sufficient to allow the observation of a maximum number of reflections. For more detailed explanation of this experimental technique and measurement procedures see references^[125,126]. The lattice parameters were refined using the Le Bail method^[127] with the

program Full Prof Suite^[128].

2.1.2 Scanning electron microscopy and energy dispersive spectrometry

The samples morphology and chemical composition were evaluated using a JEOL scanning electron microscope (SEM), model 840A. This microscope is equipped with an energy dispersive spectrometer (EDS) and is available at Institut Néel (CNRS/Grenoble). The average grain size and grain size distribution have been obtained via the SEM measurements, which have been complemented with information about the chemical composition obtained via EDS analysis.

2.1.3 Analytical characterization

Thermo gravimetric (TGA) analyses were performed to control the thermal stability of the synthesized samples with a Perkin-Elmer thermo-gravimetric apparatus using air as carrier gas. The TGA curves provide information concerning the thermal stability of the initial materials, intermediate compounds that may be formed and of the final products. The measurements were recorded from room temperature up to 1100° in rates ranging between 5 and 10°/min.

2.1.4 Magnetic characterization

Magnetic measurements have been performed using a SQUID (superconducting quantum interference device) magnetometer from Quantum Design (sensitivity 10^{-7} emu) installed at IFIMUP (University of Porto). This magnetometer is equipped with a 5.5 T superconducting coil and an EverCool dewar. The system allows accurate magnetization measurements in a 1.7 to 380 K temperature range.

Magnetization as function of temperature, $M(T)$, was performed via two experimental procedures: in zero field cooling (ZFC) procedure, the samples are cooled, with $H=0$, down to the desired temperature, after what the magnetic field is applied and the subsequent magnetization measurements are performed upon heating. In the field cooling (FC) procedure, the samples are cooled down to the lowest temperature under a preset magnetic field. Then the measurements are performed during heating.

Following the ZFC and FC procedures, described above, the magnetic parameters such as Curie (T_C) or Néel (T_N) temperatures have been obtained. To compare the magnetization curves at

different fields, the magnetic susceptibility in the paramagnetic phases, χ , has been calculated as $\chi = M/H$. In the present experiments, the samples were mounted in plastic straws glued with a special non magnetic kapton tape for low temperatures. A detailed description of the experimental apparatus, technical specifications and measurement procedures can be found in references^[129,130].

2.2 Sample preparation

The quality of the synthesized samples is of great importance. Particularly, the presence of secondary crystalline phases may result in loss of the desired properties and/or ambiguity in the interpretation of the results. Hence, considerable effort has been performed in this work in order to develop and optimize the synthesis parameters of the studied systems.

The synthesis techniques used in this work were mainly chemical although in specific cases the use of mechanical induced reactions via high pressure methods has been also employed. For convenience, among the wide variety of chemical methods available to produce ceramic powders only syntheses from liquid solutions will be described while accounting for the details needed to obtain single phase samples. A description of high pressure methods will be also performed.

2.2.1 Synthesis from liquid solutions: sol-gel

The potential of the synthesis using liquid solutions in achieving very high levels of chemical homogeneity was recognized in the 1950s and 1960s where a large number of novel ceramic oxide compositions have been obtained^[131–133]. Since this time, numerous sol-gel routes have been developed and applied in diverse materials such as polycrystalline fibers, glasses, coatings and films^[134,135], among others.

The term sol-gel is used to refer to the production of powders by a process that involves the preparation of a solution (*sol*), its gelation (*gel*) and further removal of the solvent. A *sol* is a suspension of colloidal particles (particles with diameters of 1-100 nm) in a liquid. A *gel* is a semirigid mass formed when the link between colloidal particles is established forming a 3D network. When the solvent is removed by thermal evaporation, the resulting product is termed as *xerogel*, which is a porous solid network. The heat treatment of the *xerogel* at elevated temperatures reduces the number of pores and their connectivity due to viscous-phase sintering, termed as densification.

A schematic general representation of the process is shown in Fig. 2.1. Detailed information on sol-gel science can be found on references^[133,136–138] and references herein.

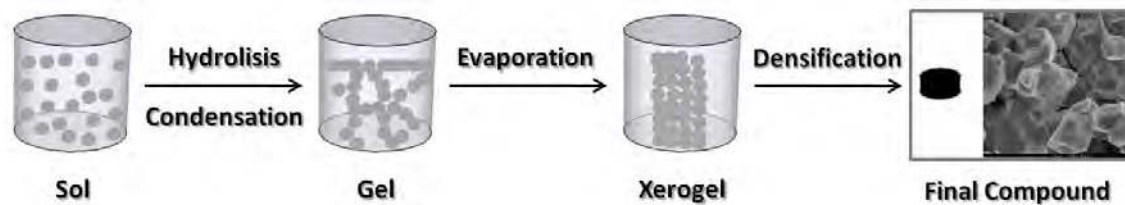


Figure 2.1: Schematic representation of the sol-gel process.

The starting materials for the preparation of the *sol* consist generally of inorganic salts or metal-organic compounds. The chemical reactions that occur during the conversion of the solution to the *gel* have significant influence on its structure and chemical homogeneity. Consequently, the control of several processing variables such as chemical composition of the starting materials, concentration of the reactants, pH of the solution and/or temperature are of great importance.

This process has proven to be adequate to produce high quality samples at low sintering temperatures. Also it has the potential advantage over other methods not only for achieving homogeneous mixing of all components at the atomic scale, but also the possibility of forming films and fibers from gels for technological purposes. Other goals are lower processing temperatures and short annealing times, high purity of the materials, particle sizes well below 100 nm at the lower processing temperatures.

A wide range of different sol-gel routes have been developed in the last years for the production of ferrites^[139,140], manganites^[141–144], among others, using different gelificant agents.

The urea route in the synthesis of rare-earth manganites

For the synthesis of RMnO_3 system ($\text{R}=\text{Lu}, \text{Er}, \text{Y}, \text{Ho}, \text{Tb}, \text{Gd}, \text{Eu}, \text{Sm}$ and Nd), urea was used as a gelificant agent following the recommendations of Vazqu ez-Vazqu ez^[143] that applied this gelificant agent in the preparation of colossal magneto-resistive manganites. In this work, the same route was optimized with changes in urea ratio and thermal treatment temperatures to obtain single phase

RMnO₃ samples.

Stoichiometric quantities of rare-earth oxides (R₂O₃, Sigma Aldrich) and manganese carbonate (MnCO₃, Sigma Aldrich) were dissolved separately in nitric acid and distilled water. When the complete dissolution was obtained, the nitrate solutions were mixed and urea (CH₄N₂O, Acros Organic) was added in a quantity calculated according to:

$$\psi = \frac{[Urea]}{[R][Mn]} = 3 \quad (2.1)$$

The complete dissolution of the solution containing the metal and the urea was achieved by changing its concentration by means of adding water. After this, the pH was adjusted by adding ammonia. The optimal pH was attained in the interval 5.0-5.4.

The obtained solution was heated, with continuous stirring, and evaporated. When a gel was obtained, the beaker was kept in the heating plate promoting the combustion of the gel. The resulting black powder was fast calcinated at 873 K, in air, for two hours. Subsequent thermal treatments were performed up to 1623 K, followed by quenching to room temperature. Between each thermal treatment the samples were grounded, sieved and pressed into pellets.

Table 2.1: List of RMnO₃ samples prepared by the urea method. The last thermal treatment conditions and the final composition obtained by XRD and EDS are also included.

Sample Reference	Nominal Composition	Last thermal treatment T (K)/t (hrs)	XRD results (% vol.) Crystalline phase	EDS results (% atomic)
LuMO	LuMnO ₃	1623 K/40 hrs	92(2)%LuMnO ₃ +8(2)%Lu ₂ O ₃	Lu _{1.15} Mn ₁
ErMO	ErMnO ₃	1623 K/24 hrs	single phase ErMnO ₃	Er _{0.92} Mn ₁
YMO	YMnO ₃	1623 K/72 hrs	single phase YMnO ₃	Y _{0.74} Mn ₁
HMO	HoMnO ₃	1623 K/72 hrs	single phase HoMnO ₃	Ho _{1.31} Mn ₁
TMO	TbMnO ₃	1623 K/60 hrs	single phase TbMnO ₃	-
GMO	GdMnO ₃	1623 K/72 hrs	single phase GdMnO ₃	Gd _{1.24} Mn ₁
EuMO	EuMnO ₃	1623 K/72 hrs	single phase EuMnO ₃	Eu _{0.87} Mn ₁
SMO	SmMnO ₃	1623 K/60 hrs	single phase SmMnO ₃	Sm _{0.99} Mn ₁
NMO	NdMnO ₃	1623 K/60 hrs	single phase NdMnO ₃	Nd _{0.95} Mn ₁

The purity of the samples has been controlled by XRD and EDS analyses. Table 2.1 summarizes the series of samples prepared via the urea route together with the last thermal treatment and the composition obtained by XRD and EDS.

Figure 2.2 shows representative XRD patterns for hexagonal (left panel) and orthorhombic (right panel) samples. All samples were found to be single phase with exception of LuMnO₃. This sample presented an impurity phase of 8(2)% vol. of Lu₂O₃.

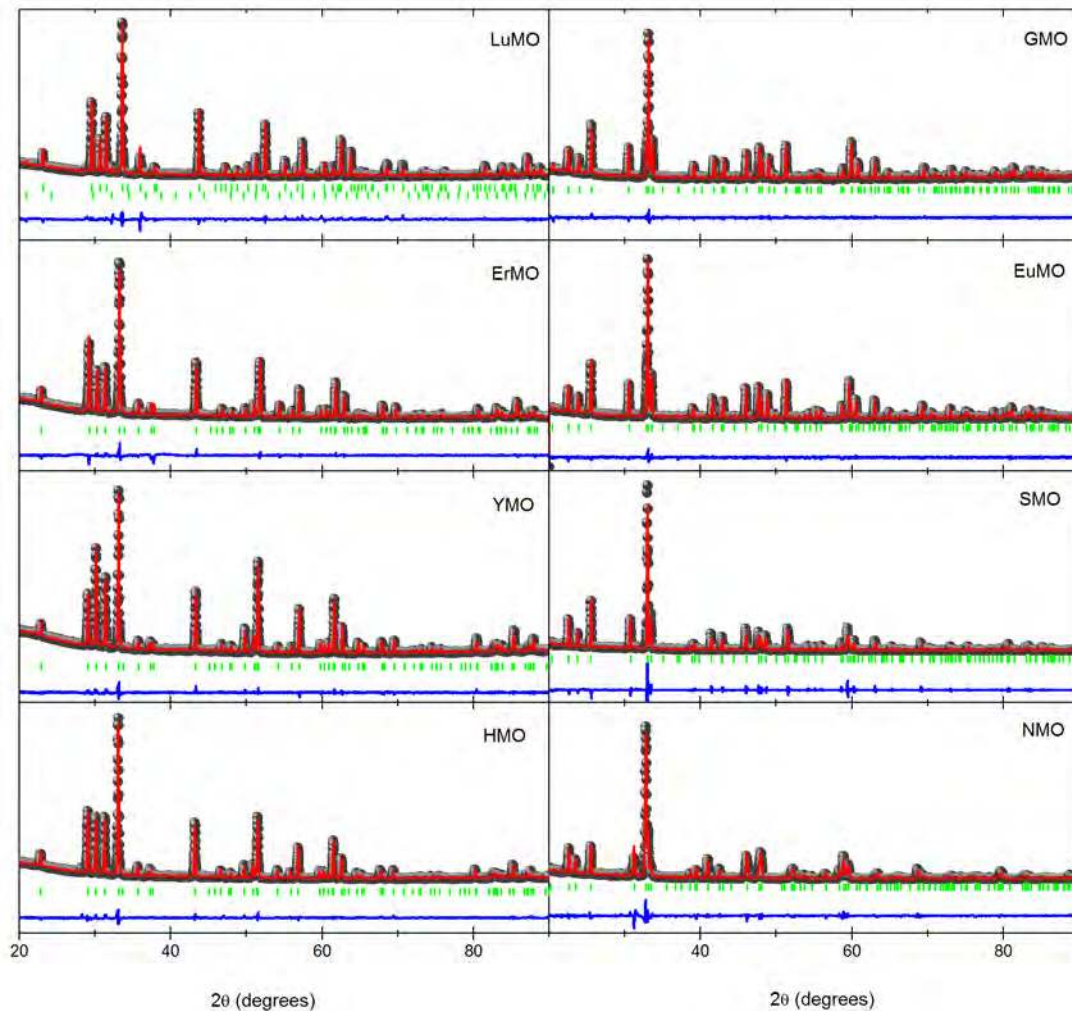


Figure 2.2: Representative room temperature XRD patterns of hexagonal (left panel) and orthorhombic (right panel) RMnO₃ samples. The experimental patterns (dots), calculated (solid lines), reflections of the corresponding phases (tick marks) and fit deviation (solid line in the bottom) are presented.

Also the metal compositions obtained by EDS show a good agreement with the nominal compositions. Scanning electron microscopy was performed to verify the samples morphology and homogeneity at the μm scale. In figure 2.3, representative SEM micrographs of the final RMnO₃ sample's are presented where one can visualize the samples homogeneity through a narrow grain

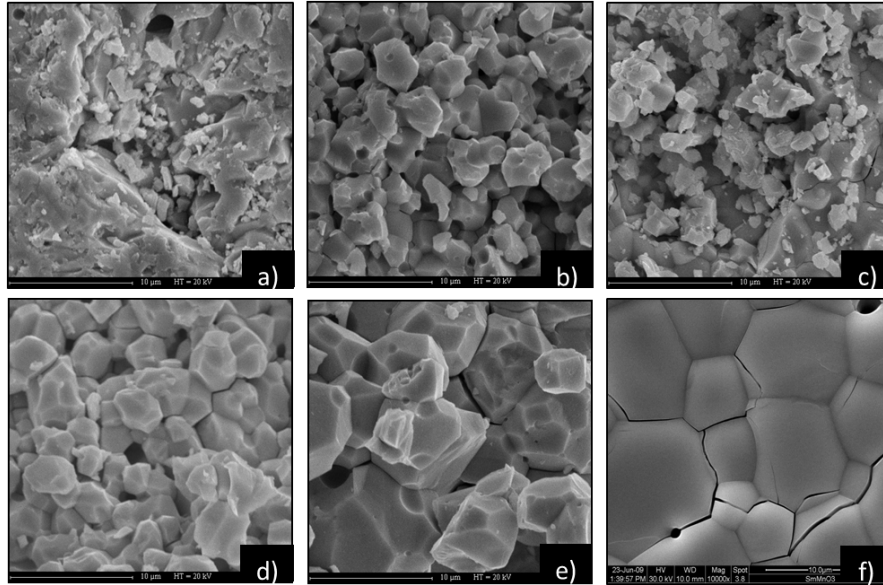


Figure 2.3: SEM micrographs of representative samples of RMnO_3 series: a) LuMO, b) YMO, c) HMO, d) GMO, e) EuMO and f) SMO.

size distribution.

The urea combustion method in the synthesis of Ba-Ca-Cu-O system

Polycrystalline precursor powders with nominal composition $\text{Ba}_2\text{CaCu}_2\text{O}_5$ and $\text{Ba}_2\text{Ca}_2\text{Cu}_3\text{O}_7$ were synthesized using stoichiometric quantities of BaCO_3 (Acros Organic), CaCO_3 (Acros Organic) and CuO (Sigma Aldrich), which were dissolved individually in nitric acid. When the complete dissolution was achieved, the solutions were mixed and the urea (H_2NCONH_2 , Acros Organic) was added. The amount of urea was fixed at $\psi = 3$, with $\psi = \frac{[\text{urea}]}{[\text{Ba}][\text{Ca}][\text{Cu}]}$. The pH was adjusted with addition of ammonia to be in the range where the solution was perfectly clear (pH \sim 3). Then the solvent was evaporated directly in a hot plate with continuous stirring. When the temperature reached 463-473 K, the auto-ignition took place. The result was a porous black powder, which was grounded in an agate mortar. To evaluate the influence of the precursor preparation in the synthesis of Hg-based superconductor samples, precursor powders with the same nominal composition were prepared using acrylamide ($\text{C}_3\text{H}_5\text{NO}$, Sigma Aldrich) as complexing agent. Details on the experimental procedure used in this sol-gel route can be found elsewhere^[145].

After, both urea and acrylamide (denoted here as AA) powders were calcined at 973 K in air with

a heating rate of 10 K/min, for 10 hours. SEM analysis showed that the urea calcined powders are very thin (0.5-1 μm)^[146] although they are agglomerated in aggregates of few μm as also observed in precursor powders prepared via the AA method^[145]. A representative micrograph of the urea calcined $\text{Ba}_2\text{Ca}_2\text{Cu}_3\text{O}_x$ powders is presented in figure 2.4(a).

To control the decomposition mechanism and determine the synthesis temperatures of the intermediate precursors, thermo-gravimetric (TGA) measurements have been performed after the calcination. Figure 2.4(b) shows TGA curves for $\text{Ba}_2\text{Ca}_2\text{Cu}_3\text{O}_x$ calcined powders, obtained via the urea (U) and acrylamide (AA) routes, using air as a carrier gas. A weight decrease is observed for both cases being the urea powder more reactive in air with a total weight loss of about 8% regarding the 5% loss of the AA powder. A shoulder is observed in the temperature interval 630-680 K, which is probably attributed to an incomplete nitrate decomposition during the calcination process. Here, the reduction of Cu(II) to Cu(I), which occurs in the same temperature range, is excluded since the measurement was not performed in a reductive atmosphere^[147]. After this temperature range, there is a continuous weight loss with a small kink in each curve. For the urea powder, the kink starts at 1000 K while for the AA powder this reaction takes place only at 1180 K. This kink in the curves indicates the beginning of carbonates decomposition reactions, which reveals a better efficiency of urea in the formation of the precursor powders allowing a complete decarbonation at lower temperatures regarding acrylamide. The better efficiency of the urea can be attributed to a better complexing ability, which results in a better mixing at the molecular level leading to lower decarbonation temperatures. One shall note that this temperature range is in good agreement with the reported values for carbonate decomposition in powders synthesized using different polymeric agents^[145,147]. Nevertheless, the length of this reaction was found to be shorter when using the urea route^[146].

Following the TGA results, the calcined powders were subjected to two thermal treatments: at 1093 K in air, for 20 hours, and the last treatment at the same temperature using dynamic vacuum (10^{-3} mbar), for 10 hours for total removal of carbonates, with intermediated grindings. Fig. 2.5 shows the XRD patterns obtained after the annealing steps at 1093 K in air and in dynamic vacuum. The resulting powders, after the two annealing steps, consisted of a mixture of crystallographic phases, typically found in this type of compounds: $\text{Ba}_2\text{Ca}_2\text{Cu}_3\text{O}_7$, $\text{Ba}_2\text{Cu}_3\text{O}_6$, CaCuO_2 and some traces of CaO and CuO. While the carbon impurities were eliminated after

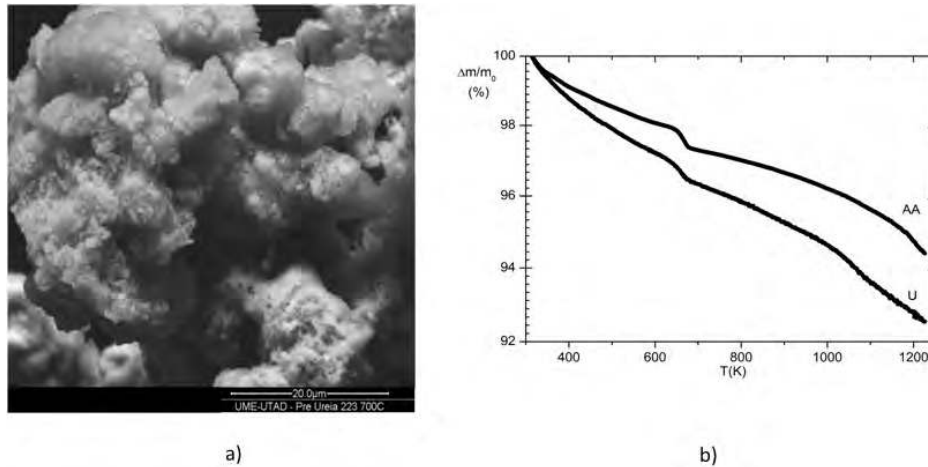


Figure 2.4: a) SEM micrograph of $\text{Ba}_2\text{Ca}_2\text{Cu}_3\text{O}_x$ calcined precursor powder obtained via the urea route. b) TGA curves for the nominal $\text{Ba}_2\text{Ca}_2\text{Cu}_3\text{O}_x$ calcined precursor powders obtained via the urea (U) and acrylamide (AA) routes.

the 1st annealing step in the urea method, in the AA route this was only achieved after annealing in dynamic vacuum. In both cases, the annealing step in vacuum showed an improvement of the crystallinity of the formed phases.

The powders obtained via the urea route have been obtained with high purity (any carbonate contaminations) in shorter processing times and without the need of special atmosphere^[146] when compared with powders prepared using acrylamide as complexing agent. The use of urea in the formation of precursor powders allowed a complete decarbonation in the same temperature range as the needed for other polymeric agents in shorter times and without the need of special annealing atmospheres. Some points shall be mentioned regarding the influence of the complexing agent on the synthesis of Ba-Ca-Cu-O precursor powders. Clearly the urea route appears as advantageous alternative to other sol-gel routes. Urea was found to play a crucial role since it coordinates the metal cations through the carbonyl-amino groups^[148], promoting the bonds between the metals still in the solution, and allows obtaining the desired phases at lower temperatures. Using polymeric agent routes, such as acrylamide, these precursor powders can be also obtained though it is only possible by annealing it in vacuum. In addition, the total time needed to stabilize the precursor phases was found to be higher than the needed by using the urea route. Moreover, the polymeric routes may present several limitations since its monomers can react with the Cu cations. To avoid

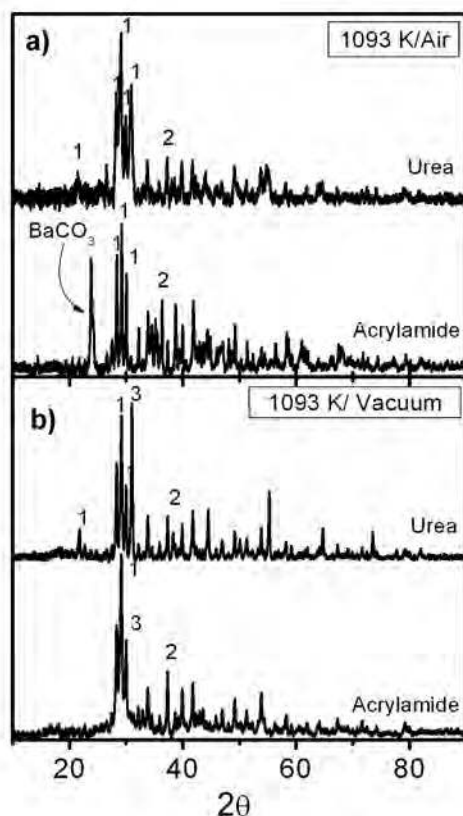


Figure 2.5: XRD pattern obtained for the $\text{Ba}_2\text{Ca}_2\text{Cu}_3\text{O}_x$ precursor produced using urea and acrylamide routes: a) after annealing at 1093 K, in air for 20 hrs; b) after annealing at 1093 K, under vacuum for 10 hrs for the urea powder and 24 hrs for the acrylamide powder. The main reflections of $\text{Ba}_2\text{Cu}_3\text{O}_6$, CaCuO_2 and $\text{Ba}_2\text{Ca}_2\text{Cu}_3\text{O}_7$ are noted by 1, 2 and 3, respectively.

these reactions, a chelating agent (e.g. EDTA) is used although small changes in its concentration can lead to partial complexing reaction of Cu^{2+} , inhibiting the correct formation of the precursor.

One shall note that the urea combustion method has been applied for the first time in the synthesis of precursor powders of the system Ba-Ca-Cu-O during the work of this thesis. The development here reported has been published^[146].

2.2.2 High pressure-high temperature synthesis

As a thermodynamic variable, pressure is one of the most significant parameters to explore and modify materials. In particular, high pressure combined with high temperature is an important tool for the synthesis of new solid state phases or for studying existing phases allowing the access

to unusual states of matter. The extreme changes induced by pressure in the chemical bonding and in the distribution and dispersion of the electronic energy levels of atoms allows otherwise incompatible elements combine to form new compounds^[149]. Moreover, pressure is an important parameter for the discovery of unexpected properties, e.g. the appearance of a spin liquid state in YMnO_3 ^[150] or to induce the increase on T_C on HTSC superconductors^[26].

In the recent decades, there were great advances on high pressure technology leading to the development of a multitude of high pressure systems working in different pressure domains and reaction media. Several equipments are currently in use for the synthesis of novel materials: the reaction vessel-type, the piston-cylinder, the belt-type apparatus and the cubo-octahedral multi-anvils for lower pressures (up to 20 GPa), and the diamond anvil cell (DAC) opening new limits to the highest pressures (up to 100 GPa).

In Institut Néel, Grenoble, two high pressure systems are available: a belt-type apparatus and a Conac type system^[41] being the latter the equipment used in this work. Fig. 2.6 displays a schematic view of this system with details on the the different parts composing this press. For syntheses using these systems, the starting mixture is inserted in a closed capsule (in gold or platinum), which is heated by a graphite or metal (e.g. Mo) furnace. The pressure transmission is ensured by materials having plastic deformation (such as calcite, CaCO_3). To isolate the furnace from the mechanical metallic pieces and to prevent electric shortcuts, insulating pieces in pyrophyllite are also added. The piston and anvil have been designed enabling to treat samples up to 1 cm^3 volume. The pressure is applied by uniaxial presses, which are monitored and controlled by an electronically regulated system enabling the programming of reproducible cycles. The thermal treatments are performed using a power supply (600 A and 7.5 V), which is also electronically regulated. Both internal pressure and temperature are known from calibration curves. The present systems allow the production of polycrystalline samples with good pressure and temperature stability as also the development of crystal growth under high pressure^[151].

Although HP-HT synthesis allows the production of novel compounds, the reaction processes are difficult to establish and the phase diagrams and reaction paths are not well understood. To help in understanding these reactions and to optimize the synthesis conditions, in situ x-ray studies of the reactions under pressure are commonly performed using synchrotron radiation^[151]. One shall stress that operating in closed systems may be an advantage because one can control the amount

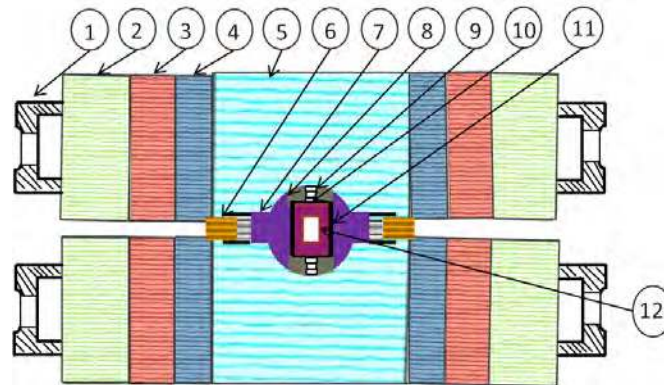


Figure 2.6: Schematic diagram of the Conac type high-pressure cell: (5) Anvil (tungsten carbide); (6) Gasket; (7) CaCO_3 cell; (8) Pyrophyllite; (9) Electrical contact; (10) Insulator in CaCO_3 ; (11) Furnace (graphite, Mo); (12) Capsule (Au, Pt)^[41].

of volatile species present in the samples.

Synthesis of $\text{HgBa}_2\text{Ca}_{n-1}\text{Cu}_n\text{O}_{2n+2+\delta}$ superconductors via the HP-HT technique

$\text{HgBa}_2\text{CaCu}_2\text{O}_{6+\delta}$ (Hg-1212) and $\text{HgBa}_2\text{Ca}_2\text{Cu}_3\text{O}_{8+\delta}$ (Hg-1223) polycrystalline samples have been synthesized using the HP-HT technique. Stoichiometric quantities of HgO and Ba-Ca-Cu-O precursor powders, which were previously prepared by the urea combustion method^[146], have been mixed, grounded and inserted in a Au capsule. In the particular case of this series of compounds, the use of Pt capsules shall be avoided due to the high reactivity of barium compounds with platinum. The mixtures have been subjected to different pressure, temperature and dwell times. Several samples have been synthesized by this method^[152] and a list of representative samples is presented in table 2.2.

Figure 2.7 (top) shows the XRD pattern obtained for Hg-1212, synthesized at 1.8 GPa, 1068 K for a 2.5 hours dwell, conditions found to be optimal. For all listed cases, the Hg-1212 phase has been obtained although traces of impurity phases such as CaHgO_2 and BaCuO_2 were also found. The synthesis of the Hg-1212 phase seems to not depend strongly on the applied pressure though the number of experiments performed at different pressures does not allow to conclude about the influence of this parameter. For the syntheses at 1.8 GPa, the increase on both temperature and dwell times promote the formation of the Hg-1212 phase.

Figure 2.7 (bottom) shows the XRD diffraction obtained for Hg-1223, synthesized at 1.8 GPa,

Table 2.2: List of samples of nominal compositions $\text{HgBa}_2\text{CaCu}_2\text{O}_{6+\delta}$ and $\text{HgBa}_2\text{Ca}_2\text{Cu}_3\text{O}_{8+\delta}$ prepared by the HP-HT method with the different pressure and temperature conditions together with the final composition obtained by XRD.

Sample Reference	Nominal Composition	Pressure (GPa)	Temperature/dwell time K/min	XRD composition (% vol.) Crystalline phase
Hg12a	Hg-1212	1.6	1123 K/60 min	96(1)% Hg-1212
Hg12b	Hg-1212	1.8	973 K/96 min	84(2)% Hg-1212
Hg12c	Hg-1212	1.8	1063 K/120 min	86(2)% Hg-1212
Hg12d	Hg-1212	1.8	1086 K/60 min	73(2)% Hg-1212
Hg12e	Hg-1212	1.8	1086 K/96 min	85(1)% Hg-1212
Hg12f	Hg-1212	1.8	1086 K/120 min	95(1)% Hg-1212
Hg12g	Hg-1212	1.8	1086 K/150 min	98(1)% Hg-1212
Hg23a	Hg-1223	1.8	1086 K/60 min	82(1)% Hg-1223
Hg23b	Hg-1223	1.8	1086 K/96 min	63(1)% Hg-1223
Hg23c	Hg-1223	1.8	1143 K/150 min	90(2)% Hg-1223
Hg23d	Hg-1223	1.8	1173 K/60 min	86(2)% Hg-1223
Hg23e	Hg-1223	1.8	1173 K/150 min	99(1)% Hg-1223
Hg23f	Hg-1223	1.9	1086 K/60 min	15(1)% Hg-1223
Hg23g	Hg-1223	5.2	1086 K/60 min	10(1)% Hg-1223
Hg23h	Hg-1223	5.2	1086 K/90 min	10(1)%Hg-1223

1173 K for 2.5 hours dwell time^[146]. In this case, all synthesis parameters were found to have a strong effect on the formation of the Hg-1223 phase. For temperatures below the optimal, the Hg-1223 phase was always obtained even though other crystalline phases such as CaHgO_2 and BaCuO_2 are also present. The increase on dwell times seems to promote the formation of the Hg-1223 phase. On the other hand, the effect of pressure seems to be stronger and for higher pressures only traces of the Hg-1223 phase were found, which was decomposed in the precursor phases Hg-1212 , CaHgO_2 and BaCuO_2 .

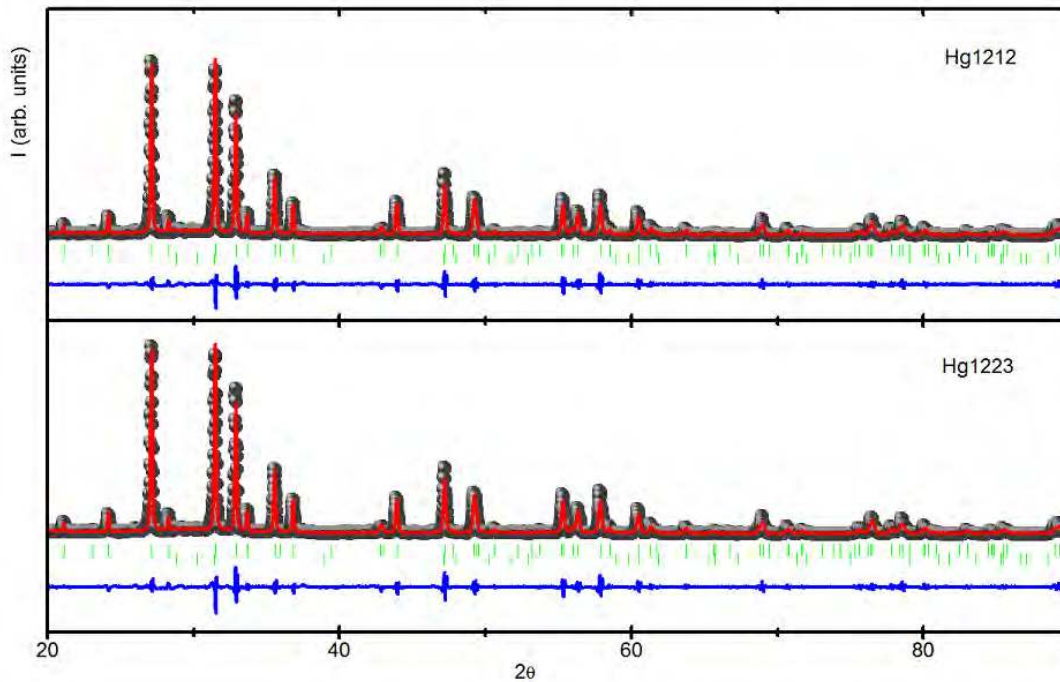


Figure 2.7: Representative room temperature XRD patterns of Hg-1212 (top) and Hg-1223 (bottom) samples. The experimental patterns (dots), calculated (solid line), reflections of the corresponding phases (tick marks) and fit deviation (solid line in the bottom) are presented.

2.3 Hyperfine characterization

Nuclear hyperfine interactions are defined as the interactions between the nuclear moments (electric and magnetic) and extranuclear electromagnetic fields. These electromagnetic fields interact with the nuclear moments leading to a rearrangement in the nuclear level structure. The measurement of these interactions provides an accurate method to investigate condensed matter phenomena yielding direct information of the local charge distribution and magnetic hyperfine fields. In highly correlated electron systems subtle differences in microscopic phenomena originate very distinct macroscopic properties. Therefore the use of nuclear hyperfine methods is of great importance in solid state physics studies.

There are numerous experimental techniques that allow the study of microscopic properties of materials. Among these, the non-radioactive: nuclear magnetic resonance (NMR), nuclear

quadrupole interactions (NQI), and the radioactive: Mössbauer effect (ME), β -NMR or perturbed angular correlations (PAC) are good examples. As mentioned above, these experimental methods make use of the hyperfine interactions established between the nuclear moments of a specific probe nucleus and the external electromagnetic fields induced in its neighborhood by, e.g., neighboring elements, point defects, distortions, localized charges. In the particular case of the radioactive techniques, the high sensitivity combined with a smaller number of required probe atoms make them ideal for the atomic scale studies of structural, electronic and dynamical properties of solids. Moreover, the information obtained by these techniques is of particular interest in highly correlated materials, where intrinsic disorder requires real lattice atomic scale studies.

In this section the most relevant aspects of the Perturbed Angular Correlations (PAC) technique will be presented. The mathematic formalism of PAC is complex and can be found on detail in several textbooks, PhD thesis and review articles^[153–159]. Therefore, only a brief description of the theoretical and experimental aspects of the PAC technique will be presented.

2.3.1 Perturbed angular correlations technique

The PAC spectroscopy method makes use of radioactive isotopes, which will act as probes, to extract both electric field gradient and magnetic hyperfine field. It shows several advantages over other nuclear techniques since its sensitivity is essentially temperature independent, does not require external magnetic fields and only a small number of radioactive nuclei is sufficient to perform an experiment (10^{10} - 10^{11} PAC probe atoms). As a result, the PAC technique is being used successfully not only in condensed matter physics but as well in chemistry, biology and medicine^[160–162]. On the other hand, a potential difficulty is the fact that it is necessary to introduce inside the material a radioactive isotope, which will act as probe.

The basic principle of the γ - γ PAC spectroscopy arises from the emission of two consecutive γ rays from the internal decay of a probe nucleus. The probability of emission of two consecutive γ -rays from a radioactive nucleus depends on the angle between the directions of emission and of the nuclear spins of the cascade transitions. In general, the spins of a nuclei are randomly distributed being the emitted radiation the same in every direction, i.e., isotropic. An anisotropic emission is observed when a set of nuclei have some degree of orientation. An oriented set of nuclei can be selected upon defining a detection direction for the first γ -ray on a decay cascade. In a radioactive

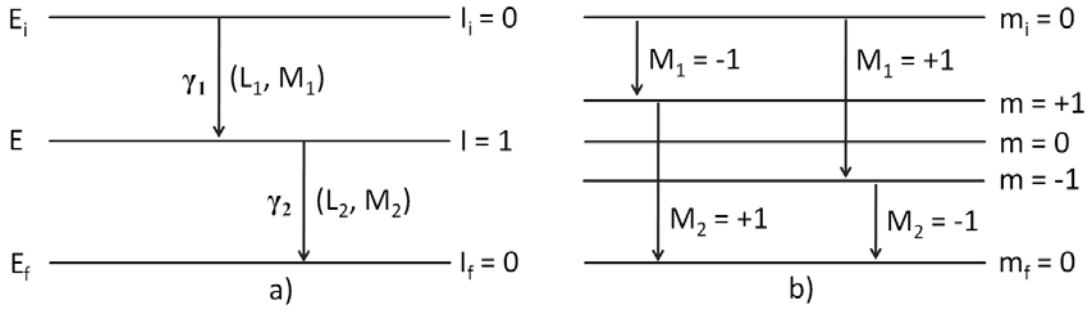


Figure 2.8: a) Schematic representation of a γ - γ cascade, with indication of the energies (E) and quantum numbers (i and f indexes refer to the initial and final states respectively). b) Representation of the alignment of the spin I of the intermediate state ($m=0$ is not populated), which is achieved by choosing the γ_1 emission direction as quantization axis.

decay cascade with an intermediate decay, as represented in the example of fig. 2.8(a), the selection of the detection direction of γ_1 (k_1) as quantization axis only allows photon states with $M_1 = \pm 1$. Due to conservation of spin angular momentum the condition $m + M_1 = m_i$ must be fulfilled (fig. 2.8(b)) and only the states with $m = \pm 1$ in the cascade's intermediate state will be populated, while $m = 0$ cannot be populated by this transition. This means that the direction of γ_1 defines an alignment of the nuclear spin I of the intermediate state with respect to k_1 . The second photon, γ_2 , connects the nuclear states with spin $I=1$ and $I_f=0$. However, the decay from the state with $m = 0$ cannot occur due to the preceding detection of γ_1 . Furthermore, because of $m_f + M_2 = m$, γ_2 is restricted to $M_2 = \pm 1$. Consequently, the detection of γ_2 will reveal an anisotropic emission pattern showing an angular correlation with the direction of emission of γ_1 .

The probability $W(\theta)$ of finding γ_2 in a certain direction k_2 at an angle θ relatively to k_1 and in coincidence with γ_1 can be described by^[163]:

$$W(k_1, k_2) = W(\theta) = \sum_{k=0}^{k=k_{max}} A_k(\gamma_1) A_k(\gamma_2) P_k(\cos(\theta)) \quad (2.2)$$

where the sum runs over for even values of k as a result of parity conservation of the electromagnetic radiation. The upper limit, k_{max} is determined by the smallest of $2I$, $L_1 + L'_1$ and $L_2 + L'_2$ where $L_{1,2}$ and $L'_{1,2}$ are the multiplicities of the electromagnetic transitions. The two γ quanta coincidence probability follows a general dependence on the Legendre polynomials, $P_k(\cos\theta)$, weighted by the cascade dependent $A_k(\gamma_1)$ and $A_k(\gamma_2)$ terms. These coefficients depend on the correspondent

angular momentum of the involved levels, on the mixing of multipolarities of the emitted radiation and can be calculated from ref.^[164]. One shall note that although the described situation refers to angular correlations between two emitted γ -rays, those can be also found between other type of emitted particles, e.g. conversion electrons and α particles, where in particular for conversion electrons, the A_k parameters strongly depend on the electron energy multipolarity and of the atomic shells from where these were converted.

When the nuclei are in the presence of external atomic fields, the quadrupole, Q_I , and magnetic, μ_I nuclear moments of the intermediate state will interact with the electric field gradients (EFG) and/or with magnetic hyperfine fields (MHF) generated by the charge distribution surrounding the probe nucleus. This interaction will perturb the angular correlation function causing the splitting on the nuclear magnetic sub-levels. The latter is dimensioned by the coupling between the nuclear quadrupole moment (Q) with an electric field gradient (EFG) and/or with the nuclear magnetic moment (μ) coupling with a magnetic hyperfine field (B_{hf}). During the time t when a nucleus remains at the intermediate state (time delay between the emission of γ_1 and γ_2) a hyperfine interaction will promote a change in the occupation of the different magnetic sub-levels ($m - m'$ transitions). Therefore, the emission probability of γ_2 , in a certain direction, becomes time dependent. Taking into account this effect, the induced perturbation in the angular correlation, equation 2.2 shall be modified according the changes in the sub-level occupation during the elapsed time of the two γ -rays. Moreover, the PAC observable function depends on the crystalline nature of the material being the simplest case found for polycrystalline samples where the function is obtained by averaging the angular correlation over all possible orientations of the EFG/MHF fields. In this case only the relative angle between the two emission directions becomes relevant and the angular correlation function is reduced to^[163]:

$$W(\theta, t) = \sum_{k=0}^{k=k_{max}} A_k(\gamma_1)A_k(\gamma_2)G_{kk}(t)P_k(\cos(\theta)) \quad (2.3)$$

where $G_{kk}(t)$ is the perturbation factor, which contains all information about the hyperfine fields interaction with the probe nuclei. The shape of $G_{kk}(t)$ depends on the interaction type (electric quadrupolar and/or magnetic), which will be described in the next sub-sections.

Electrical quadrupole interaction

The electrical quadrupole interaction stems from the coupling between the probe nuclei quadrupole moment with the EFG. The quadrupole energy is frequently written as:

$$E_Q = \frac{e}{6} \sum_{ij} Q_{ij} V_{ij} \quad (2.4)$$

where e is the magnitude of the electron charge, Q_{ij} is the electric quadrupole moment tensor as defined by:

$$Q_{ij} = \int \rho_N(x_1, x_2, x_3) (3x_i x_j - r^2 \delta_{ij}) dx_1 dx_2 dx_3 \quad (2.5)$$

being ρ_N the nuclear charge density. The EFG tensor, V_{ij} , is a consequence of the external charge distribution in the neighborhood of the probe nuclei and is defined as the traceless part of the second partial derivative tensor of the external electrical potential ($\Phi_{ij} = \frac{\partial^2 \Phi}{\partial x_i \partial x_j}$) created by the charge distribution around the nucleus:

$$V_{ij} = \Phi_{ij} - \frac{1}{3} \text{Tr}(\Phi_{ij}) \delta_{ij} \quad (2.6)$$

V_{ij} is a symmetric tensor and thus, it is possible to find an eigenvector basis where the tensor is diagonal. Also, since this tensor is traceless, once diagonalized, it can be described by only two of its components. Commonly, the eigenvalue with largest magnitude and the axial asymmetry parameter η are chosen to describe it. After choosing the eigenvector basis, the eigenvalues are arranged in such a way that $|V_{zz}| \geq |V_{yy}| \geq |V_{xx}|$. The asymmetry parameter, η , measures the deviation of the local charge distribution from axial symmetry and can be defined by:

$$\eta = \frac{V_{xx} - V_{yy}}{V_{zz}} \quad (2.7)$$

Tetragonal or hexagonal lattices are examples of axially symmetric structures with nil asymmetry parameters. Non-axial symmetric charge distributions resulting either from the lattice structure itself or from the presence of point defects result in $0 < \eta \leq 1$.

The quadrupole energy can be also written using the asymmetry parameter, η , and EFG principal component, V_{zz} :

$$E_Q = \frac{eV_{zz}}{12} [3Q_{zz} + \eta(Q_{xx} - Q_{yy})] \quad (2.8)$$

The EFG interaction lifts off the m states degeneracy of the intermediate level originating an energy splitting ΔE_n , as represented in fig. 2.9(a) for the case of a nuclear spin $I=5/2$. The

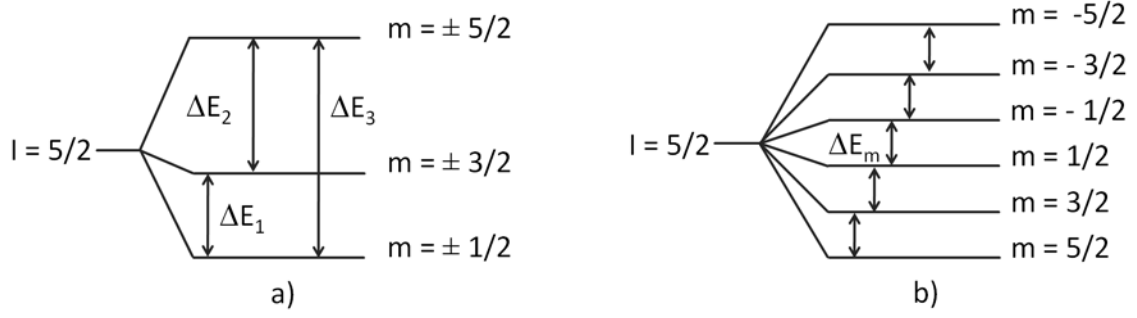


Figure 2.9: a) Electric quadrupole energy splitting and b) magnetic splitting, for spin $I=5/2$ of the intermediate state, originated by an interaction with an EFG and a magnetic hyperfine field, respectively.

transitions between the m sub-levels result in different spin precession-like frequencies ω_n , which can be observed experimentally.

If the interaction is axially symmetric and if the principal EFG axis, V_{zz} , is defined as the quantization axis, the electric quadrupole Hamiltonian is given by

$$E_Q = \hbar\omega_Q [3m^2 - I(I + 1)] \quad (2.9)$$

where ω_Q is the quadrupole frequency, which is defined by:

$$\omega_Q = \frac{eQV_{zz}}{4I(2I - 1)\hbar} \quad (2.10)$$

The energy splitting between two sub-levels m and m' is given by:

$$\Delta E_Q = 3\hbar\omega_Q |m^2 - m'^2| \quad (2.11)$$

$|m^2 - m'^2|$ is always integer so all transition frequencies are multiples of ω_Q and of the fundamental observable frequency ω_0 , the lowest transition frequency is:

$$\omega_0 = k\omega_Q$$

with $k=6$ for I half-integer and $k=3$ for I integer

Is also usual to define another quantity, the fundamental frequency:

$$\nu = \frac{eQV_{zz}}{h} = \omega_0 \frac{4I(2I - 1)}{2\pi k} \quad (2.12)$$

The number of frequencies observed experimentally depends on the spin of the intermediate level. As depicted in fig. 2.9, an intermediate state with $I = 5/2$ is split by a pure electric quadrupole

interaction into three different energy levels leading to three different observable frequencies in the PAC spectrum (ω_1 , ω_2 and $\omega_3 = \omega_1 + \omega_2$). The perturbation factor G_{kk} for the electric quadrupole interaction is then given by,

$$G_{kk}(t) = \sum_{n=0}^{n_{max}} s_{kn} \cos(n\omega_0 t) \quad (2.13)$$

where s_{kn} are the frequency amplitudes, $n = |m^2 - m'^2|/2$ for I half integer and $n = |m^2 - m'^2|$ for I integer. Hence, the angular correlation *precesses* with a superposition of several harmonics of the fundamental frequency ω_0 , which is related to the hyperfine fields.

Magnetic interaction

Alike the electric quadrupole interaction, the magnetic hyperfine results from the interaction of the magnetic dipole moment μ of the probe nucleus with the magnetic hyperfine field B in its surroundings. The magnetic dipolar energy is defined as

$$E_m = -\mu \cdot B \quad (2.14)$$

where the nuclear dipole moment μ of the nuclear charge distribution is proportional to its angular momentum $\hbar I$:

$$\mu = \gamma \hbar I \quad (2.15)$$

Here, γ is the gyromagnetic ratio, which is often expressed by the nuclear magneton μ and the dimensionless g -factor: $\gamma = g\mu_N/\hbar$.

The hamiltonian of a magnetic interaction is diagonal in the $|I, m\rangle$ basis, assuming that the magnetic field is applied parallel to the z axis, resulting in the expression

$$E_m = -\gamma \hbar B_z m \quad (2.16)$$

The magnetic dipole interaction also lifts the m states degeneracy of the intermediate state, as depicted in fig. 2.9(b). In this case the splitting is energetically equidistant (Zeeman splitting) and the degeneracy is lifted off with respect of the signal of m . Since only transitions between any two adjacent sub-levels are allowed, the energy splitting is given by

$$\Delta E_m = E_{m+1} - E_m = -\gamma \hbar B_z = \hbar \omega_L \quad (2.17)$$

where $\omega_L = \gamma B_z$ is the Larmor frequency.

The perturbation factor for a pure magnetic dipole interaction in polycrystalline samples, with magnetic domains randomly oriented, is described by:

$$G_{kk}(t) = \frac{1 + 2 \sum_{n=1}^k \cos(n\omega_L t)}{2k + 1} \quad (2.18)$$

When both magnetic and electric interactions are present the hamiltonian for such combined static interactions is given by^[159]

$$\mathcal{H} = \hbar\omega_Q \left[3I_z^2 - I(I + 1) + \frac{1}{2}\eta(I_+^2 + I_-^2) \right] - \mu \cdot B \quad (2.19)$$

where, for the quadrupole part, the identity $I_x^2 - I_y^2 = \frac{1}{2}(I_+^2 + I_-^2)$ has been used. In general, if combined interactions are present the hamiltonian cannot be diagonalized analytically and its eigenvalues and eigenvectors shall be calculated numerically.

PAC experimental function and data analysis

The perturbation function $G_{kk}(t)$ contains all information concerning the hyperfine fields. To determine experimentally $G_{kk}(t)$ the coincidence count rates, $N(\theta, t)$, as function of time between the emission of the two γ -rays, γ_1 and γ_2 , at a fixed detector angle, θ , is measured. The experimental coincidence count rate for a (i, j) pair of detectors is then given by:

$$N_{i,j}(\theta, t) = N_0 e^{-t/\tau} W(\theta, t) + B \quad (2.20)$$

where $t = t_{\gamma_2} - t_{\gamma_1}$ is the time delay between detection of the two γ -rays, θ is the angle between the i and j detectors and $W(\theta, t)$ is the perturbed angular correlation (equation 2.3). N_0 is proportional to the number of coincident start(γ_1) - stop(γ_2) events registered during the measurement. B is proportional to the uncorrelated chance coincidence rate ($\gamma_1 - \gamma_2$ coincidences arising from different nuclei). Generally, B is referred as the spectra background.

The coincidence count rate is measured with a PAC apparatus, which consist of a group of gamma scintillator detectors geometrically arranged in such way that the angles between detector pairs are 90° and 180° , taking as an example the detector arrangement shown in fig. 2.10(a). By considering one i, j pair of detectors, if a γ -ray strikes a detector, two signals are generated in the detector's photomultiplier. A sharp negative anode signal will be used as a mark for the γ arrival, t_γ , and a dynode signal from where the energy information, E_γ , will be determined. If a γ -ray

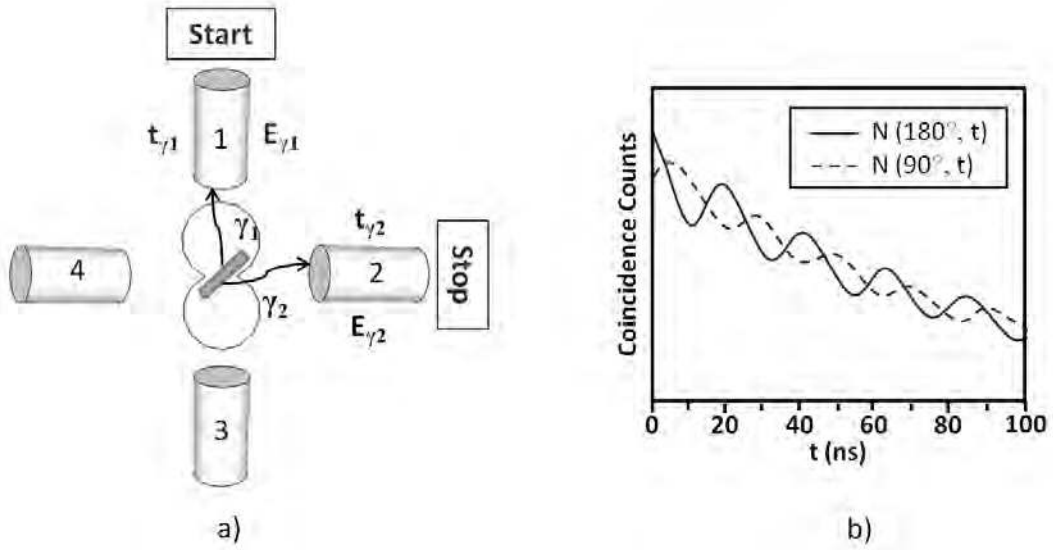


Figure 2.10: a) Schematic representation of an in-plane four detector γ - γ PAC experimental setup. b) Illustrative representation of the count rate at 90° and 180° .

is detected in a detector, with the right energy, $E_{\gamma 1}$, the clock is started. When a second γ -ray, with the correct energy, $E_{\gamma 2}$, reaches another detector then the clock will stop. This event will be stored in the coincidence counter of the i, j pair of detectors. Fig. 2.10(b) shows examples of such histograms for detectors with $\theta=90^\circ$ and $\theta=180^\circ$.

Depending on the type of setup, several spectra, taken for $\theta=90^\circ$ and $\theta=180^\circ$, are combined and the experimental perturbation function $R(t)$ is constructed. $R(t)$ is a quantity that provides the relevant information and is usually defined by:

$$R_{exp}(t) = 2 \frac{N(180^\circ, t) - N(90^\circ, t)}{N(180^\circ, t) + 2N(90^\circ, t)} \quad (2.21)$$

where $N(\theta, t)$ is calculated by appropriate average for correction of different efficiencies after chance coincidence background subtraction between the detectors made from all $N_{ij}(\theta, t)$ taken at the same angle (180° or 90°), after background subtraction, $N(\theta, t) = N_0 \sqrt{\prod_{ij} N_{ij}(\theta, t)}$. Here N_0 is the total number of spectra at a certain angle θ . One shall note that equation 2.21 eliminates the exponential component due to the half-life contribution of the intermediate state of the cascade. Also, one shall point that the measurable experimental quantity, $R_{exp}(t)$, is proportional to $G_{kk}(t)$ that contains the information about the hyperfine fields to study.

Data analysis

The PAC experimental spectra analysis is performed via a theoretical fit of the experimental data. The procedure is based on the construction of a theoretical function, $R_{fit}(t)$, containing the perturbation function (equation 2.13), which is calculated numerically by taking into account the full hamiltonian for the nuclear electric quadrupole and/or magnetic dipole hyperfine interactions. This procedure is carried out using a computer software^[165,166] which calculates numerically the eigenvalues and eigenstates of the hamiltonian expressed in equation 2.19. To account for the finite time resolution of the PAC setup the $G_{kk}(t)$ is modified multiplying each frequency term in the sum by $P(F_{whm}^*, \omega_n)$ (assumed as Gaussian-like).

$$P(F_{whm}^*, \omega_n) = \exp\left(-\frac{\omega_n^2 F_{whm}^{*2}}{16 \ln 2}\right) \quad (2.22)$$

where F_{whm}^* is the full width half maximum associated with the time resolution distribution function of the spectrometer. Furthermore, possible EFG distributions are considered by multiplying the $G_{kk}(t)$ terms by the distribution's Fourier transform $D(F_{whm}, t)$.

$$G_{kk}^{fit}(t) = \sum_{n=0} S_{kn} \cos(\omega_n t) D(F_{whm}, t) P(F_{whm}^*, \omega_n) \quad (2.23)$$

The corresponding PAC functions $W_{fit}(\theta, t)$ are then calculated for $\theta=90^\circ$ and $\theta=180^\circ$. The fit function, whose parameters are changed to fit the $R_{exp}(t)$ function, is described as

$$R_{fit}(t) = 2 \frac{W_{fit}(180^\circ, t) - W_{fit}(90^\circ, t)}{W_{fit}(180^\circ, t) + 2W_{fit}(90^\circ, t)} \quad (2.24)$$

One shall note that often distinct fractions of probes are subjected to distinct EFGs or MHFs and the effective fit function becomes in this case

$$\overline{W_{fit}(\theta, t)} = \sum_i f_i W_i^{fit}(\theta, t) \quad (2.25)$$

where f_i is the relative intensity of each $W_i^{fit}(\theta, t)$ angular correlation function characterizing the i th fraction of probe atoms interacting with a particular EFG _{i} /MHF _{i} .

Static attenuation due to EFG distributions

The presence of lattice defects (e.g. implantation defects) or chemical disorder in long range can lead to slightly different hyperfine fields in the probe's neighborhood. These subtle differences

in the hyperfine fields originate a distribution of frequencies around a central value instead of a characteristic unique value. Such distributions in the frequency space (usually represented by Gaussian or Lorentzian distributions) induce a time dependent attenuation of the PAC spectra amplitude^[167]. This attenuation is considered during the fitting procedure, as mentioned above, by multiplying each frequency dependent term of the calculated perturbation function by the Fourier transform of the frequency distribution. For a Gaussian frequency distribution, the attenuation function, in time space, can be defined as:

$$D_{gauss}(F_{whm}, t) = e^{-\frac{F_{whm}^2}{16ln2}t^2} \quad (2.26)$$

where the standard deviation σ is defined as $\sigma = F_{whm}/\sqrt{8ln2}$ and F_{whm} stands for the frequency distribution full width at half maximum. The standard deviation is often described as a fraction (δ) of the fundamental frequency $\delta = \sigma/\omega_0$.

For a Lorentzian frequency distribution, the attenuation is given by:

$$D_{lorentz}(F_{whm}, t) = e^{-\frac{F_{whm}}{2}t} \quad (2.27)$$

with $\delta = \sigma/\omega_0$ where σ is now defined as $\sigma = F_{whm}/2$.

The frequency amplitudes, s_{kn} , are attenuated by the finite time resolution of the spectrometer τ_{setup} . When $\omega_n\tau_{setup} > 2\pi$ the attenuation becomes important and a correction to the s_{kn} coefficients is necessary. As referred previously, this correction is performed by multiplying each coefficient by the term $P(F_{whm}^*, \omega_n)$, which was defined in equation 2.22.

2.3.2 Electric Field Gradients Calculations

The information obtained from the analysis of PAC data allows the determination of the electric field gradient parameters: the principal component of the EFG tensor, V_{zz} , and the asymmetry parameter, η , which are defined in equations 2.6 and 2.7, respectively. The EFG is non-zero if the charges surrounding the nucleus do not possess cubic symmetry. Therefore, the deviation of charge distribution from cubic symmetry is characterized by measuring the EFG, which is highly sensitive to the electronic density in the immediate vicinity of a nucleus.

For a long time, the use of phenomenological models was the only approach to estimate EFGs in solids. These models assumed the EFG as sum of two contributions: one due to the charge

asymmetry originated in the neighboring ion cores, V_{zz}^{latt} , and a second one due to electrons, V_{zz}^{el} . Summing up these contributions, the EFG is given by^[159,168,169]

$$V_{zz} = (1 - \gamma_{\infty})V_{zz}^{latt} + (1 - R)V_{zz}^{el} \quad (2.28)$$

The contribution of the probe core-electrons results from a polarization effect leading to an amplification of the lattice EFG, being γ_{∞} the Sternheimer antishielding coefficient. This coefficient ranges from -100 to -10 depending on the element and ion charge state and can be found tabulated in^[170-173]. The term $(1 - R)$ is included to account for the amplification of the conduction electrons contribution.

For the case of ionic insulators, with non overlapping ion cores, the EFG can be approximated as

$$V_{zz} = (1 - \gamma_{\infty})V_{zz}^{latt} \quad (2.29)$$

In metals the computation of V_{zz}^{el} is particularly difficult, due to the fact that the electrons in a metal cannot be treated as uniformly distributed, requiring accurate band-structure calculations. Nevertheless, a relation between the electronic and lattice contributions to the EFG has been suggested^[33]:

$$V_{zz}^{el} = -KV_{zz}^{latt}(1 - \gamma_{\infty}) \quad (\text{with } K = 3) \quad (2.30)$$

This expression, known as "universal EFG systematics", states that the measured V_{zz} is also proportional to the lattice EFG, in the absence of point defects.

$$V_{zz} = V_{zz}^{latt}(1 - \gamma_{\infty})(1 - K) \quad (2.31)$$

This phenomenological model allows an estimation of the lattice EFG independently of the probing atom.

By using phenomenological models, the theoretical estimation of the EFG was limited to point charge models using Sternheimer antishielding factors. The point charge models (PCM) can provide fair estimations in the case of ionic solids although in covalent solids large deviations are observed. Still, in the absence of more sophisticated techniques, this method has been used extensively e.g. to estimate EFGs at the A site in perovskite oxides^[174].

In the recent years EFG calculations based on the full potential augmented plane wave (FLAPW)^[175] or projected augmented wave (PAW)^[176] first principle methods are widely used and

proved to be accurate and reliable^[177,178]. Starting from the crystal charge density (requiring only the lattice constants as input) the EFG is obtained numerically without further approximations.

In the next sub-sections, both point charge model (PCM) and FLAPW methods will be presented, including details needed for the calculations performed in RMnO₃ and Hg-based superconductors systems.

Point charge model calculations

In this method the crystalline solid is regarded as an array of point ionic charges, $Z_i e$, located at the ion sites thus being an approximation for the lattice contribution to the EFG, V_{ij}^{latt} , since it considers only its nominal charge. This calculation allows an easy estimation of the EFG making use of the second partial derivatives of the potential ϕ at the probe site created by the external charges $z_i e$ at the position r_i from the origin. Since the electrons are assumed to be uniformly distributed, no contribution to the EFG arises from them and the computation is reduced to the sum of individual contributions from the lattice atoms, except from the probe itself, resulting in

$$V_{ij}^{PCM} = \sum_i \frac{z_i e}{4\pi\epsilon_0 r_i^5} \begin{pmatrix} 3x_i^2 - r_i^2 & 3x_i y_i & 3x_i z_i \\ 3y_i x_i & 3y_i^2 - r_i^2 & 3y_i z_i \\ 3z_i x_i & 3z_i y_i & 3z_i^2 - r_i^2 \end{pmatrix} \quad (2.32)$$

As referred previously, after diagonalization the eigenvalues are chosen in such a way that $|V_{xx}| \leq |V_{yy}| \leq |V_{zz}|$ and the asymmetry parameter η can be obtained.

Due to its simplicity, this method has been used extensively providing a first estimation in EFG calculations in particular for ionic solids where a fair agreement has been reported. However, as mentioned above, in covalent solids and large molecules this approach is not a good approximation and it is difficult to implement because it neglects as well the effect of distant ions on the charge distribution around the nuclei.

PCM calculations in RMnO₃ In this work, PCM calculations have been performed to obtain an estimation of the EFG at the rare-earth and manganese sites in the magneto-electric RMnO₃ system. These results were later compared with FLAPW calculations performed in the same system, which will be described in the next sub-section. The experimental lattice parameters, for the different crystalline structures, were taken from literature^[42-44,73] and the formal charges

of +3, +3 and -2 were assigned to R, Mn and O, respectively. The different atoms have been differentiated by the Sternheimer coefficients γ_∞ ^[170–173]. The lattice sum was performed up to a distance of 25 Å from the probe nucleus. The direct comparison with the experimental results has been performed accounting for the location of the probe atom at the rare-earth or manganese sites.

EFG first principle calculations

The FLAPW method proved to be accurate and reliable in energy band structure calculations requiring only the lattice parameters as input^[175,177,178]. This method divides the unit cell into non overlapping spheres centered at the atoms, where its basis are atomic-like functions, and the interstitial region are described by plane waves functions. Inside the atomic spheres a linear combination of radial functions times spherical harmonics is employed. The EFG is calculated from the total charge of the system without additional Sternheimer coefficients nor other corrections/approximations. The charge density and potential have no shape restrictions and exchange-correlation effects are treated within density functional theory, via the local density approximation (LDA) or the generalized gradient approximation (GGA)^[179].

FLAPW calculations in RMnO₃ The FLAPW approach has been used to calculate the EFG at the rare-earth and manganese sites in the RMnO₃ magneto-electric system. These calculations have been performed in collaboration with Dr. João Nuno Gonçalves (University of Aveiro). The calculations have been performed using the code Wien2K^[180] considering spin-polarized atoms and the GGA approximation, with the Perdew-Burke-Ernzerhof (PBE) parametrization of the exchange-correlation potential^[179]. In the first step of the calculations, the supercells represent pure RMnO₃ compounds with the set of lattice parameters taken from the literature^[42–44,73]. The crystallographic parameters were fixed during this first step of the simulation. The sphere radii used were 2.2, 1.8 and 1.6 atomic units (a.u.) for the rare-earths, manganese and oxygen, respectively. The basis size allows plane waves with $K_{\max}=6/R_0=3.75$ a.u.⁻¹ for one unit cell of 30 atoms (6 formula units). Later, on a second phase, the simulations have been performed allowing the relaxation of the internal atomic positions, by minimizing the atomic forces to a value less than 5 mRy/a.u. (i.e., the atoms can move along the free coordinates: z_{R_1} , z_{R_2} , x_{Mn} , z_{Mn} , x_{O_1} , z_{O_1} , x_{O_2} , z_{O_2} , z_{O_3} , z_{O_4}). For simplicity, the antiferromagnetic (AFM) order

of the low temperature compound has been neglected, using instead ferromagnetic calculations. Additional simulations in YMnO_3 , assuming the AFM order, have been also performed showing differences in the EFG values below 2% for all atoms, relative to the ferromagnetic case after relaxation of the internal parameters.

The second part of the simulations aimed a realistic interpretation of the PAC experiments. With this aim, substitutional cadmium atoms, used as probe atoms in the experiment, were inserted into the simulated structure. The radius of the Cd APW sphere is the same of the substituted atom. For each EFG calculation per crystallographic site (R_1 , R_2 or Mn), the Cd was included in the structure by substitution at one of the sites in the unit cell, giving the formulae $\text{R}_{5/6}\text{Cd}_{1/6}\text{MnO}_3$ or $\text{RCd}_{1/6}\text{Mn}_{5/6}\text{O}_3$. The subsequent steps in the simulation procedure followed the description presented previously. An important factor to take into account in these calculations is the Cd concentration, since in principle a supercell calculation with a more diluted Cd probe would give a more accurate result. Nevertheless, detailed calculations as a function of dilution on orthorhombic Ca-based manganites did not reveal large changes already at concentrations below $x(\text{Cd})=1/4$ ^[181].

FLAPW calculations in Hg-based superconductors The FLAPW approach has been used to calculate the EFG at the mercury site in $\text{HgBa}_2\text{CaCu}_2\text{O}_{6+\delta}$ and $\text{HgBa}_2\text{Ca}_2\text{Cu}_3\text{O}_{8+\delta}$ superconductors. The calculations have been performed in a collaboration with Dr. Heiz Haas, using the code Wien2K^[175] with the generalized gradient approximation^[179] (GGA) for the density functional. The lattice parameters have been taken from published neutron diffraction experiments^[51,182] accounting for different oxygen dopings. The calculations have been performed considering both unrelaxed and relaxed supercells. The relaxation of the atomic positions was done in a self-consistent way by minimizing atomic forces, as already described.

To illustrate different O_δ doping configurations, various supercells have been constructed assuming the composition $\text{Hg}_m\text{Ba}_{2m}\text{Ca}_m\text{Cu}_{2m}\text{O}_{6m+n}$. Following earlier works^[57,58], the simulations implemented here describe different configurations of single O_δ atoms all sitting within the Hg planes, including new models representing a dumbbell $\text{O}_{2\delta}$ dopant molecule with the symmetry axis parallel to c -axis at the centre of the Hg mesh. One shall stress that the aim of the different supercells is to provide the understanding of which local configurations of O_δ or $\text{O}_{2\delta}$ can originate

the measured EFGs at the Hg site.

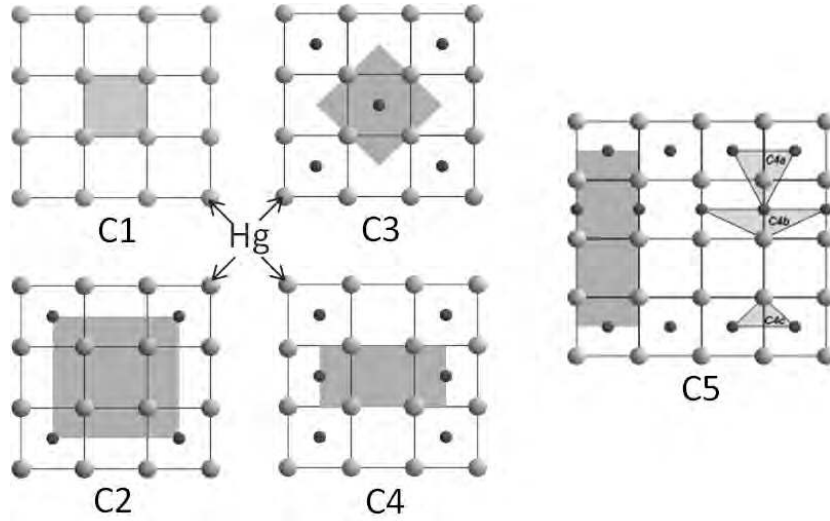


Figure 2.11: Schematic representation of the Hg planes of $\text{HgBa}_2\text{CaCu}_2\text{O}_{6+\delta}$ and $\text{HgBa}_2\text{Ca}_2\text{Cu}_3\text{O}_{8+\delta}$ as viewed along the c axis. Shaded regions represent supercells with different O_δ concentrations ($\delta=0$ to 0.66).

Fig. 2.11 illustrates a schematic view of the implemented supercells, projected along the c axis onto the mercury planes. The shaded regions represent the ab plane of the supercells. Since similar configurations were used for both O_δ and $\text{O}_{2\delta}$ cases, only one set of pictures is presented. Fig. 2.11-C1 shows the undoped supercell with $m=1$ and $n=0$. The effect of oxygen doping has been calculated by constructing four doped supercells (C2, C3, C4 and C5 configurations). The supercell with $m=4$ and $n=1$, depicted in fig. 2.11-C2, represents the case where the mercury atoms interact one single dopant oxygen, which is located at the centre of the Hg mesh. Figs. 2.11-C3 and 2.11-C4 display two local configurations ($m=2$ and $n=1$ supercells) existing for Hg atoms interacting with two oxygen dopants, both having the same nominal concentration $\delta=0.50$. Although these two configurations have the same nominal δ , one expects that the different oxygen rearrangement causes changes in the EFG parameters. The supercell C3 represents a checkerboard-like arrangement of the oxygen dopant where the $\text{Hg-O}_\delta\text{-Hg}$ make 180° . The simulation represented by the supercell C4 corresponds to the situation where the dopant is distributed along interstitial rows parallel to the b axis and the $\text{Hg-O}_\delta\text{-Hg}$ bonds make 90° . A highly doped supercell ($\delta=0.66$) is depicted in fig. 2.11-C5 ($m=3$, $n=3$) with three non equivalent Hg atoms. This supercell was created to understand if under high O_δ concentrations, interstitial Hg-Hg bonds could be occupied by O_δ atoms.

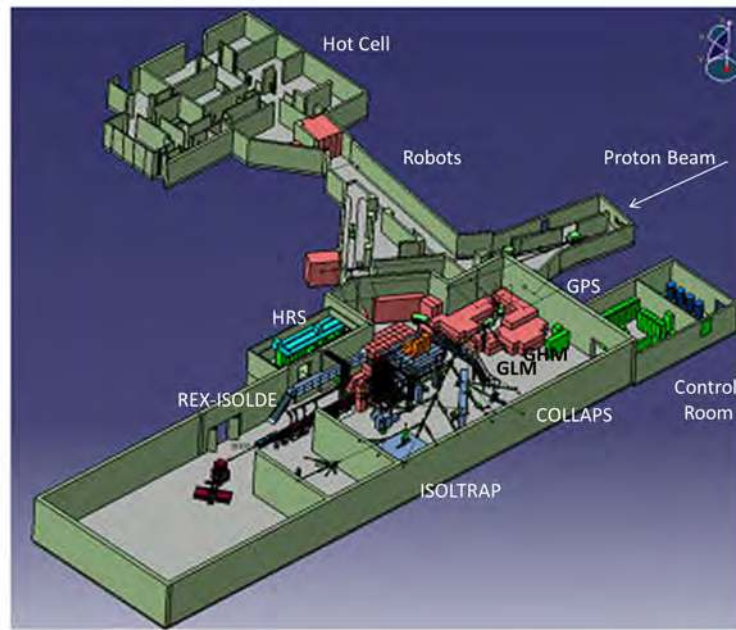


Figure 2.12: Schematic representation of the ISOLDE hall with the general purpose separator (GPS), high resolution separator (HRS) and its different beam lines. The implantation chamber used in this work is located at the end of the GLM beam line.

2.3.3 PAC Experimental Procedure

Sample Implantation

The first step to perform a PAC experiment is to introduce a radioactive isotope, which will act as a probe, inside the material under study. This is generally done either by diffusion of a solution containing the desired isotope or via ion implantation. In this work, all samples have been implanted at the On-Line Isotope Mass Separator (ISOLDE) facility at CERN^[183], shown in the schematic view of figure 2.12. This facility, situated at the Proton-Synchrotron Booster (PSB) at CERN, is dedicated to the production of a large number of radioactive ion beams for many different experiments in the fields of nuclear, atomic and condensed matter physics and biophysics.

At ISOLDE radioactive nuclides are produced via spallation, fission or fragmentation reactions in a thick target, which is irradiated with a proton beam from the PSB at an energy of 1.4 GeV and an intensity up to $2 \mu\text{A}$. The nuclear reaction products are released from the target, which is heated, into an ion source via chemically selective processes and are extracted as a radioactive low energy

The figure shows a periodic table where elements produced at ISOLDE are highlighted in blue. Elements suitable for solid state experiments are circled in black. The circled elements include: H, He, Li, Be, Na, Mg, B, C, N, O, F, Ne, Al, Si, P, S, Cl, Ar, K, Ca, Sc, Ti, V, Cr, Mn, Fe, Co, Ni, Cu, Zn, Ga, Ge, As, Se, Br, Kr, Rb, Sr, Y, Zr, Nb, Mo, Tc, Ru, Rh, Pd, Ag, Cd, In, Sn, Sb, Te, I, Xe, Cs, Ba, La, Hf, Ta, W, Re, Os, Ir, Pt, Au, Hg, Tl, Pb, Bi, Po, At, Rn, Fr, Ra, Ac, Ce, Pr, Nd, Pm, Sm, Eu, Gd, Tb, Dy, Ho, Er, Tm, Yb, Lu, Th, Pa, U, Np, Pu, Am, Cm, Bk, Cf, Es, Fm, Md, No, Lr.

Figure 2.13: Periodic table with the elements produced at ISOLDE (in blue). The elements suitable for solid state experiments are surrounded by circles.

beam (5-60 keV). The beam is then magnetically mass separated via two isotope separators on-line: the general purpose separator (GPS) with one bending magnet and a electrostatic switchyard permitting the simultaneous delivery of three mass separated beams; and the high resolution separator (HRS) that has two bending magnets with a more elaborate ion-optical system and better mass resolution. Additionally, an off-line mass separator is available for target tests and calibrations. Both separators are connected to a common beam-line system and feed the major experimental installations for nuclear spectroscopy, nuclear orientation, laser spectroscopy, mass measurements, solid state and surface studies. The high proton energy combined with the target and ion-source knowledge allows the production of more than 700 isotopes of more than 70 elements ($z=2$ to 88) including the ones suitable for nuclear solid state physics techniques. Figure 2.13 shows a periodic table with the elements produced at ISOLDE, where the elements with suitable radioactive isotopes for solid state experiments are highlighted with circles.

Implantations for solid state physics are usually performed at the chamber mounted on line at the GLM beam line. The chamber is equipped with a multi sample holder allowing the implantation of several samples in a row without breaking vacuum, through a choice of different diameters and shape beam collimators. During the sample implantation, the beam is swept to produce homogeneous implanted area and the current at the samples is measured and integrated in order to control the

implanted dose.

In this work, ^{111}mCd , ^{111}In and $^{199\text{m}}\text{Hg}$ have been selected as radioactive probe atoms to perform the PAC experiments. The decay cascades for the referred isotopes are depicted in fig. 2.14 with the respective nuclear data parameters summarized in table 2.3.

Table 2.3: Electrical quadrupole, Q , and magnetic dipole, μ , moments for the intermediate states of $^{111}\text{In} \rightarrow ^{111}\text{Cd}$, $^{111\text{m}}\text{Cd} \rightarrow ^{111}\text{Cd}$ and $^{199\text{m}}\text{Hg} \rightarrow ^{199}\text{Hg}$ decay cascades^[33].

Isotope	Q (b)	μ (μ_N)	Implanted compounds
$^{111}\text{In} \rightarrow ^{111}\text{Cd}$	0.83(13)	-0.766(3)	RMnO ₃
$^{111\text{m}}\text{Cd} \rightarrow ^{111}\text{Cd}$			
$^{199\text{m}}\text{Hg} \rightarrow ^{199}\text{Hg}$	0.674(77)	0.873(28)	HgBa ₂ Ca _{n-1} Cu _n O _{2n+2+δ}

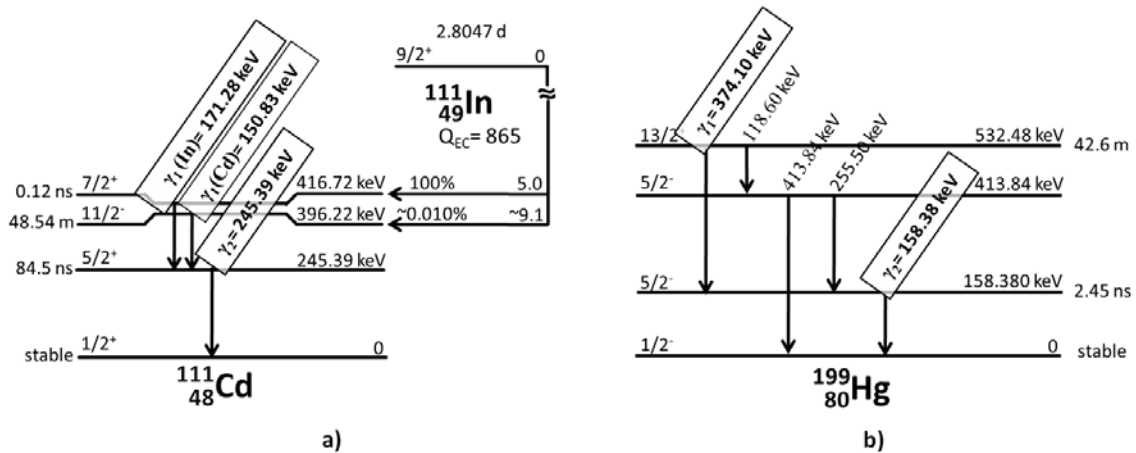


Figure 2.14: a) ^{111}In decay to ^{111}Cd by electronic capture and b) $^{199\text{m}}\text{Hg}$ to ^{199}Hg decay cascade, with indication of the PAC cascades used in the PAC measurements.

After implantation the samples are annealed to remove remaining implantation damage. The laboratory for sample preparation includes three different tubular furnaces allowing the annealing of different samples under different atmospheres (vacuum, gas flux or air). The temperature of the furnaces is electronically controlled and the thermal treatments can be performed up to 1773 K.

Table 2.4: Annealing conditions used in the post-implantation annealing in the different series of compounds.

Sample Composition	Implanted Isotope	Atmosphere	Temperature (°K)	Dwell time (min)
RMnO ₃ R=rare-earth	^{111m} Cd ¹¹¹ In	air	973	20
HgBa ₂ Ca _{n-1} Cu _n O _{2n+2+δ} n=2, 3	^{199m} Hg	Argon flow	463	15
		Argon flow	473	25
		O ₂ flow	463	17
		O ₂ flow	473	25
		8 bar O ₂	473	18
		8bar O ₂	493	18
		25 bars O ₂	473	18
		25 bars O ₂	473	25
		40 bar O ₂	473	25
		152 bar O ₂	463	25
152 bar O ₂	533	25		

During this work different procedures have been followed to account for the different sample compositions. The annealing conditions used for the different compounds are summarized in table 2.4. For the RMnO₃ system post-implantation annealing at 973 K for 20 minutes in air is enough to remove the remaining implantation damages. Particularly for the Hg-based superconductors, due to the high hygroscopicity of these compounds, the sample transfer and all manipulations have been performed under controlled atmosphere. The sample transfer between the glove box and the implantation chamber was done in rough vacuum. All manipulations were performed inside a glove box under dry atmosphere. The post-implantation annealings were performed at 463-473 K under different atmospheres: in gas flow (argon or oxygen) or under pressurized oxygen. The annealings in gas flow were carried out using a flux furnace, after what the samples were enclosed and sealed inside purified copper sample containers, which were previously baked at 873 K, under 8×10^{-6} mbar vacuum for two hours. The thermal treatments under pressurized oxygen, up to 152 bar, were performed using a system equipped with 200 bar oxygen bottle connected to a stainless steel

sample container (shown in fig. 2.15(a)), which was cleaned using the same procedure applied to the copper containers. After annealing the samples were sealed inside the containers, under dry air at ambient pressure. For the specific cases where the effect of pressure during the measurement was studied, the temperature was lowered and the samples were kept under pressure.

$\gamma - \gamma$ PAC setup

After the post-implantation annealing, the samples are mounted in the center of the PAC spectrometers. Most of the present experiments have been performed using a highly efficient BaF₂ 6-detector PAC spectrometer as shown in fig. 2.15(b). This setup produces thirty spectra from the paired combinations, six from detectors at $\theta = 180^\circ$ and twenty four at $\theta = 90^\circ$. A second setup, with four detectors, has also been used. In this case 12 spectra are obtained: four from detectors at $\theta = 180^\circ$ and eight at $\theta = 90^\circ$.

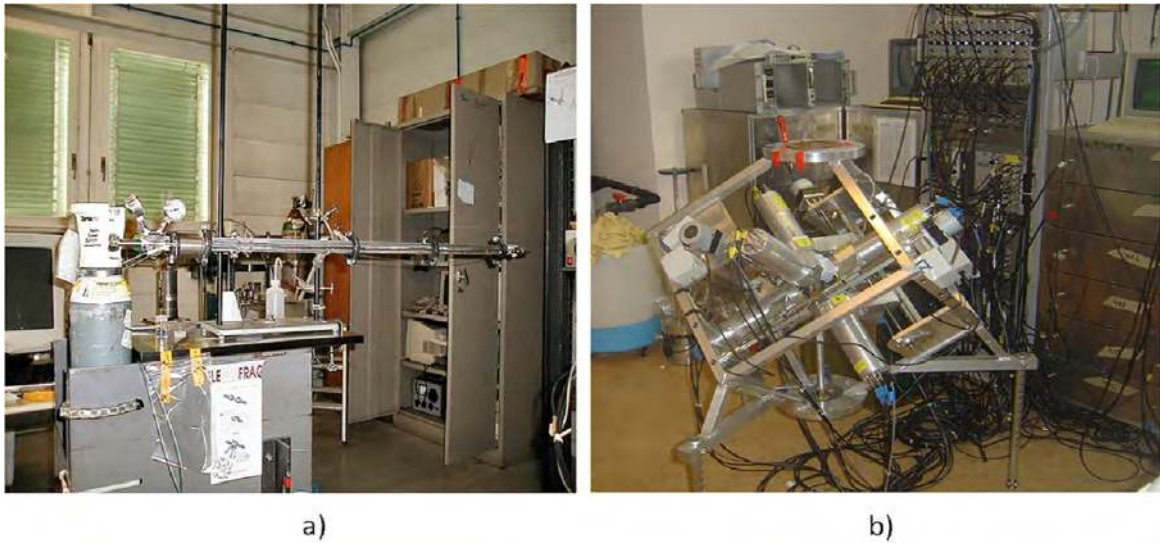


Figure 2.15: a) Picture of the system used for annealings under oxygen pressure. b) Picture of the six detector $\gamma - \gamma$ PAC spectrometer equipped with a refrigerator mounted in the centre of the detectors.

To cover a wide range of physical phenomena, the measurements have been performed from 10 K up to 1300 K. For low temperature measurements (from 10 K up to room temperature), the samples were cooled by a closed-cycle helium refrigerator equipped with a PID temperature controller. For the study of high temperature effects (from room temperature up to 1300 K), a

resistive furnace has been used. This system allows the use of different atmospheres such as O₂, N₂ and Ar. Both cryostat and furnace are mounted in such way that the sample is always at the center of the detector's ensemble.

Chapter 3

Local Probe Studies in Rare-earth Manganites

In this chapter the study of local distortions in magneto-electric rare-earth manganites (RMnO_3) is presented. The perturbed angular correlations (PAC) techniques has been applied to perform a systematic study of the evolution of the electric field gradients (EFG) as a function of the rare-earth ionic radius. The experimental data has been interpreted with *ab-initio* augmented plane wave (LAPW) calculations.

3.1 Hexagonal Rare-Earth Manganites

3.1.1 Structural and magnetic characterization

All polycrystalline samples of the RMnO_3 hexagonal system (R=Lu, Er, Y and Ho) have been synthesized via the urea sol-gel route at atmospheric pressure. The control of the quality of the samples has been performed by x-ray diffraction (XRD) in a 2θ range between 20° and 90° , at room temperature. Representative XRD patterns (experimental, calculated patterns and the reflections of the correspondent phases) have been shown on chapter 2. Analysis of the XRD data showed that, with the exception of LuMnO_3 (referenced as LuMO), the samples are chemically homogeneous. The crystalline structures and corresponding cell parameters have been obtained by refinement of the XRD data using the Le Bail method^[127] with the FullProf program^[128]. The XRD pattern matching allowed obtaining the crystallographic cell parameters for each sample, which are listed

in table 3.1. As expected from lanthanide contraction, both a and c lengths decrease with the decrease of the rare-earth ionic radius being the smallest values obtained for LuMnO₃.

Table 3.1: Hexagonal RMnO₃ structures and cell parameters obtained from XRD pattern matching.

Sample Reference	Crystalline Phase (%vol.)	Structure/ Space group	a Å	b Å	c Å	V_{unitcell} Å ³
LuMO	92(2)% LuMnO ₃	Hexagonal/ $P6_3cm$	6.0403(4)	6.0403(4)	11.3770(8)	359.483
	8(2)% Lu ₂ O ₃	Body centered cubic/ $Ia3$	10.3906(3)	10.3906(3)	10.3906(3)	1121.8220
ErMO	single phase ErMnO ₃	Hexagonal/ $P6_3cm$	6.1121(4)	6.1121(4)	11.4200(10)	369.471
YMO	single phase YMnO ₃	Hexagonal/ $P6_3cm$	6.1354(1)	6.1354(1)	11.3916(3)	371.363
HMO	single phase HoMnO ₃	Hexagonal/ $P6_3cm$	6.1429(2)	6.1429(2)	11.42656(5)	373.418

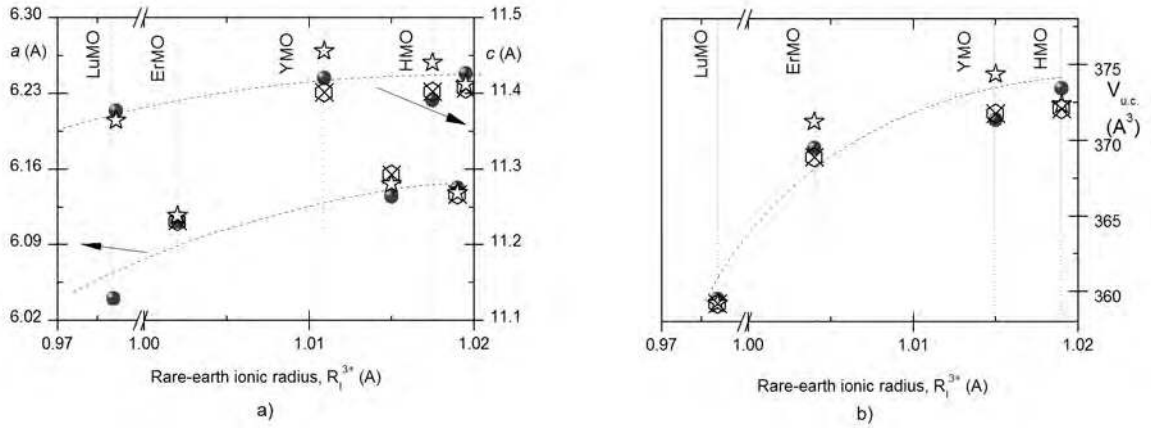


Figure 3.1: a) a and c cell parameters, and b) respective unit cell volumes as a function of the rare-earth ionic radius (R_I^{3+}) for the hexagonal RMnO₃ (R= Lu, Er, Y and Ho). The closed dots represent the values obtained in this work. For comparison unit cell values for polycrystalline (hexagons) and single-crystal (stars) samples taken from the literature are also included^[9,42–46]. Dashed lines are guides to the eye. The ionic radii have been taken from^[47].

Figure 3.1 shows the evolution of the obtained cell parameters and unit cell volumes with the rare-earth ionic radius (R_I^{3+}) together with a compilation of these values taken from the literature^[9,42–46]. The experimental values obtained in this work follow the expected trend of decrease of the unit cell volume with the reduction of R_I whereas there is a small deviation from the single crystal values, as expected due to the polycrystalline nature of the present samples. Nevertheless, the unit cell refinements show that the samples show a good agreement with the values reported in the literature for polycrystalline samples allowing to conclude about their high quality.

As a complement to structural characterization, magnetic susceptibility measurements have been performed. Analysis of the magnetization data allowed, as mentioned in chapter 2, to determine the Néel (T_N) and Curie-Weiss (θ_P) temperatures as well the ratio $|\theta_P|/T_N$ which is a measure of the geometrical frustration of the system^[73,106]. As a common procedure, θ_P was determined by fitting the high temperature linear dependence of the reciprocal susceptibility with a Curie-Weiss law and finding its interception with the temperature axis, which is in some cases difficult to obtain in the temperature range studied. A summary of the values obtained from the analysis of the susceptibility magnetic measurements is listed in table 3.2.

Figure 3.2 shows representative susceptibility, χ , field cooling curves as well as the inverse susceptibility curves (right side scale) for the hexagonal RMnO_3 series, obtained using 98 Oe applied magnetic field in a $10 < T < 380$ K temperature range.

Figure 3.2(a) shows the $\chi(T)$ and $1/\chi(T)$ curves for the sample with nominal composition LuMnO_3 . The sample shows a paramagnetic-antiferromagnetic transition with $T_N \sim 90$ K, which is in good agreement the values reported in the literature^[85]. However, the shape of the curve is somewhat different than the reported previously and a detailed analysis shows another transition at $T \sim 45$ K suggesting the remaining of a magnetic impurity (Mn_3O_4 with $T_C = 43$ K) in the sample, not detected by x-ray diffraction. One shall note that a ferromagnetic impurity content less than 0.05% is clearly visible in susceptibility measurements. Regarding the Curie-Weiss temperature, the obtained value ($\theta_P \sim -533$ K) is higher than the value reported by other authors^[85]. This difference might be due to the presence of the Mn_2O_3 impurity that could cause an amplification in the $1/\chi$ curve. Nevertheless, the absolute value of θ_P is much higher than T_N showing a high degree of magnetic frustration in the two-dimensional triangular Mn-O lattice^[106] as given by the high value obtained for the ratio $|\theta_P|/T_N$.

Figure 3.2(b) shows both χ and reciprocal χ as function of temperature for the sample ErMnO_3 . The sample exhibit a paramagnetic to antiferromagnetic transition at $T_N \sim 76$ K in good agreement with the values determined by other DC magnetization measurements^[85]. The curves show a slight deviation of magnetization below T_N without a clear magnetic transition and its reciprocal susceptibility shows an almost paramagnetic-like evolution. This behavior is due to the strong paramagnetism of Er^{3+} that masks the magnetic transition. Concerning $|\theta_P|$, the obtained value (~ 41 K) is smaller than T_N .

Table 3.2: Néel (T_N) and Curie-Weiss (θ_P) temperatures and $|\theta_P|/T_N$ ratio obtained for the hexagonal RMnO₃.

Sample Reference	T_N (K)	θ_P (K)	$ \theta_P /T_N$
LMO	90	-533	6
ErMO	76	-41	0.54
YMO	67	-526	8
HMO	76	-39	0.51

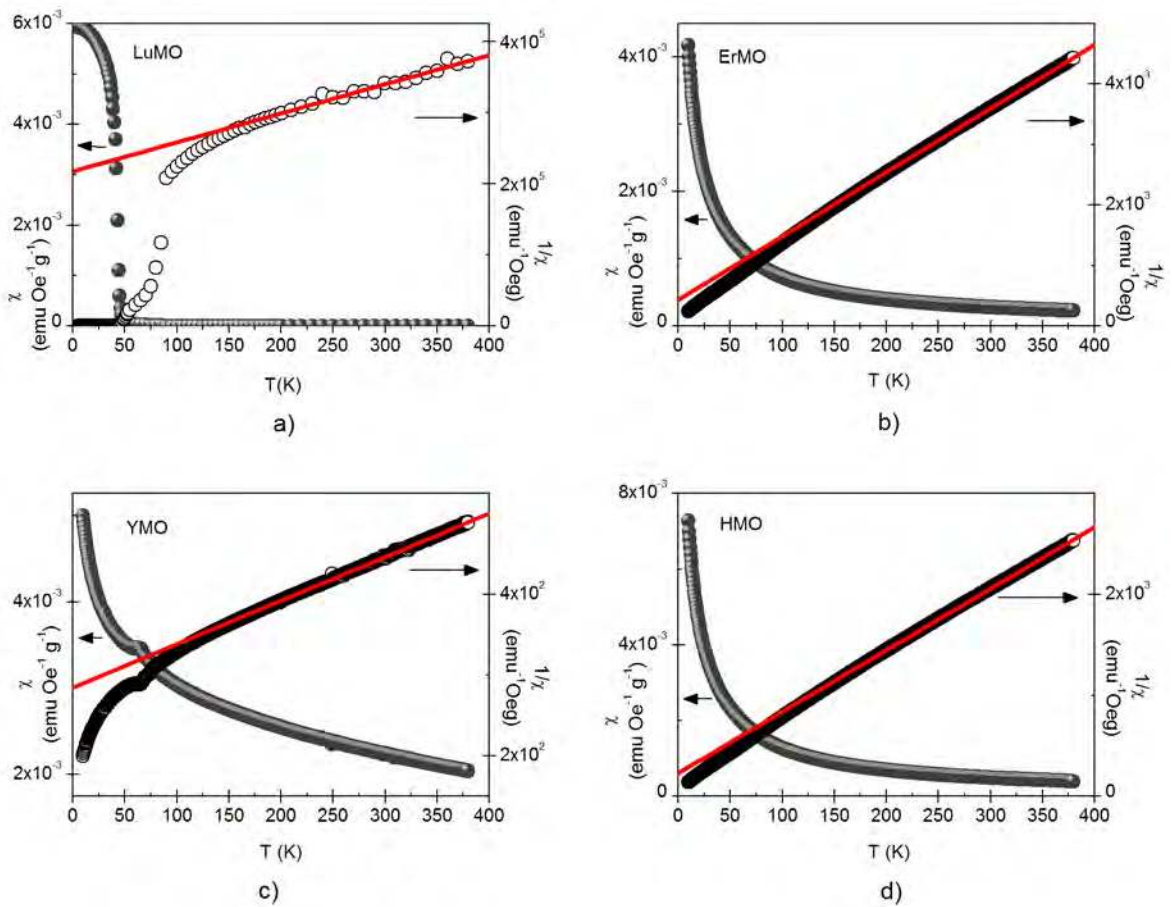
**Figure 3.2:** Field cooling magnetic susceptibilities as a function of temperature for the samples (nominal composition): a) LuMO (LuMnO₃), b) ErMO (ErMnO₃), c) YMO (YMnO₃) and HMO (HoMnO₃). Right side scale: inverse magnetic susceptibility for the same samples.

Fig. 3.2(c) depicts the thermal dependence of the magnetic susceptibility of YMnO₃ where the anomaly at the antiferromagnetic transition, $T_N \sim 67$ K, is evident from the curves. The

obtained value is in good agreement with the values reported in the literature for polycrystalline samples^[86]. Similarly to LuMnO₃ case, $|\theta_P|$ is much higher than T_N showing a high degree of geometric frustration ($|\theta_P|/T_N \sim 8$).

Figure 3.2(d) shows the $\chi(T)$ and $1/\chi(T)$ curves for HoMnO₃ where there is a similarity of these curves with the ones for ErMnO₃. Both plots have no clear magnetic transition although one can observe a deviation from the Curie-Weiss behavior for $T < T_N$. This behavior can be justified by the paramagnetism of Ho³⁺. Also, it has been reported a strong dependence of the susceptibility with the applied magnetic field, which for low fields can lead to a paramagnetic like curve. The obtained T_N (~ 76 K) and θ_P (~ -39 K) values are in good agreement with the ones reported in the literature^[85].

As a final remark, the hexagonal manganites used in this work follow the trend reported previously showing the high quality of the compounds. All samples crystallize in the hexagonal structure and present a paramagnetic-antiferromagnetic transition with Néel temperatures ranging between 67 and 90 K. One shall note that the different $\chi(T)$ curves are due to the different magnetic behavior exhibited by the different rare-earth ions.

3.1.2 EFG dependence on the rare-earth ionic radius

PAC experimental results at room temperature

A systematic study of the dependence of the electric field gradients (EFG) as a function of the rare-earth ionic radius (R_1^{3+}) is presented in this section. The perturbed angular correlations (PAC) experiments have been performed by implanting the hexagonal RMnO₃ (R= Lu, Er, Y and Ho) with ^{111m}Cd, following the procedure described in chapter 2. Afterwards the samples were annealed at 973 K in air for 20 minutes to recover from implantation damage. After the annealing, the experimental $R(t)$ spectra were measured in a temperature range from 10 K up to 573 K. The experimental results have been correlated with the corresponding crystallographic structures and magnetic data. Figure 3.3 shows representative experimental perturbation functions $R(t)$ (left) and corresponding Fourier transforms (right), measured at room temperature. The fits to each experimental PAC spectrum (continuous lines over $R(t)$) were calculated numerically by taking into account the hamiltonian for the nuclear quadrupole interaction^[166]. The best fit to each spectrum

was obtained considering that the ^{111}Cd probes interact with two different EFG distributions, which were assumed as Lorentzian-like. In the particular case of the sample LuMO, extra EFG distributions have been used to account for the presence of the Lu_2O_3 impurity in this sample (as observed by XRD). Previous studies in binary oxides^[184], with the same structure as Lu_2O_3 , showed the presence of two EFG distributions related with the two non-equivalent crystallographic sites of the metal-oxygen bond length. The presence of these contributions was assumed and fixed to improve the quality of the overall fit.

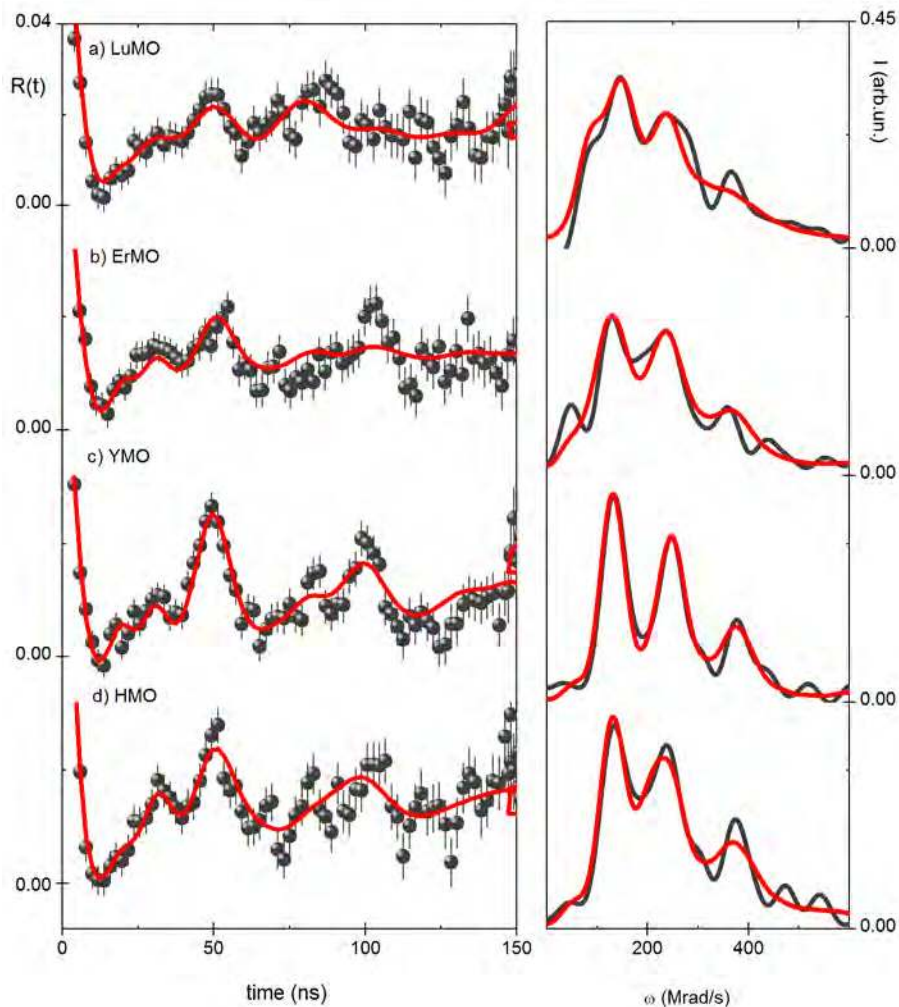


Figure 3.3: (Left) Representative room temperature $R(t)$ experimental functions and correspondent fits (represented as thicker lines over the $R(t)$ spectra) for the hexagonal RMnO_3 samples : a) LuMO (LuMnO_3), b) ErMO (ErMnO_3), c) YMO (YMnO_3) and d) HMO (HoMnO_3). (Right): Corresponding Fourier transforms.

Globally, the experimental $R(t)$ spectra depicted in figure 3.3 are quite similar and the small differences found on the Fourier transforms are due to the different rare-earth substitution. These spectra are characterized by the coexistence of two EFG distributions (named EFG_1 and EFG_2), which have been found in all compounds. The main EFG distribution (EFG_1) is given by $\sim 70(7)\%$ of the probe atoms interacting with it and it is characterized by $V_{zz1} \sim 65.5 \text{ V}/\text{\AA}^2$ ($\omega_1 \sim 125 \text{ Mrad/s}$) and an $\eta_1 \sim 0.2$. The EFG_2 distribution is given by a smaller fraction of probes (EFG_2 , $f_2 \sim 30(8)\%$) interacting with an EFG characterized by a $V_{zz2} \sim 102 \text{ V}/\text{\AA}^2$ ($\omega_2 \sim 187 \text{ Mrad/s}$) and $\eta_2 \sim 0.4$. A list of the EFG parameters obtained in these fits is summarized in table 3.3.

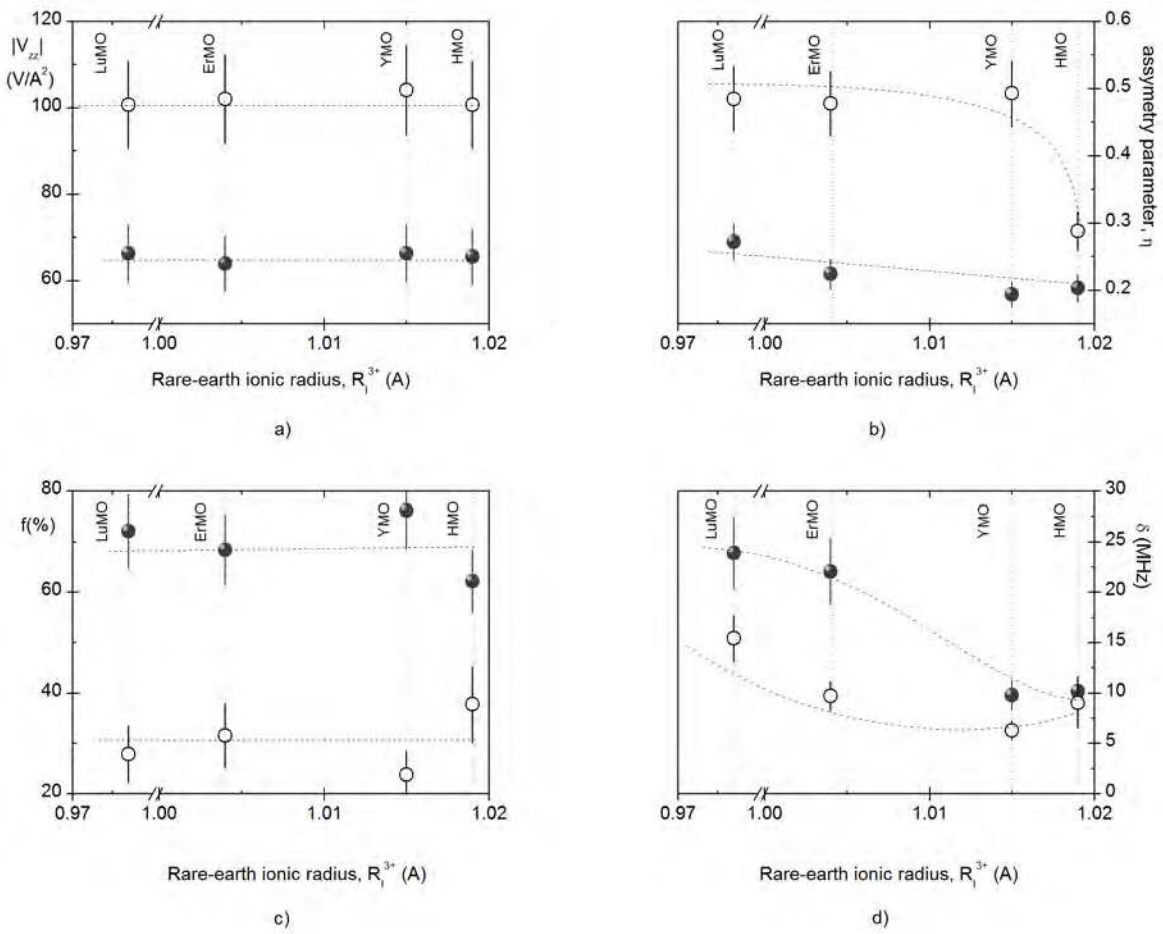


Figure 3.4: EFG parameters for measurements at room temperature: a) EFG principal component, V_{zz} , b) asymmetry parameter, η , c) fractions of probes interacting with each EFG distribution, f , and d) static attenuation parameter, δ , for EFG_1 (closed dots) and EFG_2 (open dots). The vertical lines indicate the ionic radius of each rare-earth element, which have been taken from^[47]. The dashed lines are guides to the eye.

Figure 3.4 shows the evolution of the EFG parameters (principal component of the EFG tensor,

Table 3.3: Room temperature EFG parameters for the hexagonal RMnO₃ samples. The indexes 1 and 2 refers to the two EFG distributions obtained from the fitting procedure.

Sample Reference	EFG ₁					EFG ₂				
	f ₁	ω ₁	V _{zz1}	η ₁	δ ₁	f ₂	ω ₂	V _{zz2}	η ₂	δ ₂
	%	Mrads ⁻¹	V/Å ²		MHz	%	Mrads ⁻¹	V/Å ²		MHz
LuMO	72	125	66	0.27	24	28	191	101	0.48	15
	±7	±10	±10	±0.04	±6	±6	±15	±15	±0.04	±6
ErMO	68	121	64	0.22	22	32	193	102	0.48	10
	±7	±11	±11	±0.03	±4	±6	±13	±13	±0.05	±6
YMO	76	125	66	0.19	9	24	197	104	0.49	6
	±8	±10	±10	±0.03	±3	±6	±14	±14	±0.05	±8
HMO	62	124	66	0.20	10	38	190	101	0.29	16
	±6	±10	±10	±0.03	±3	±8	±15	±15	±3	±5

V_{zz} ; the axial asymmetry parameter, η ; fraction of probes interacting with each EFG, f ; and the static attenuation parameter, δ) with the rare-earth ionic radius is plotted in figure 3.4. As one can observe, the two EFG distributions are distinct, as seen in the V_{zz} magnitudes. Both V_{zz1} and V_{zz2} present an indistinct evolution with the rare-earth substitution. The two local environments present different asymmetry parameters, being EFG₂ highly axially asymmetric, with the exception of HoMnO₃. Nevertheless, the dependence of this parameter with the rare-earth ionic radius shows a small trend to decrease when increasing the rare-earth ionic size.

Concerning the evolution of the fractions of probes interacting with each EFG distribution, alike V_{zz} , there is an indistinct dependence with the rare-earths size. On the other hand, the static attenuation parameters show a defined decrease while increasing the rare-earth size for both EFG₁ and EFG₂.

The existence of two experimental EFG distributions could be related with the two non-equivalent rare-earth crystallographic sites allowed by the non-centrosymmetric space group $P6_3cm$ (R(2a site) and R(4b site)), since the site multiplicities are comparable to the obtained EFG fractions. In addition, in previous PAC studies performed in manganites, the Cd atom was assigned to the A site in the structure^[12,158,181,185,186] giving consistence to the attribution of the two experimental EFG to the two non-equivalent rare-earth sites. One shall note that although one would expect nil asymmetry parameters according to the point symmetries of the sites, both

EFG distributions are non-axially symmetric.

Eventual changes in the rare-earth local environment induced by temperature have been studied by measuring the samples at different temperatures (573 K, 77 K and 10 K), covering the magnetic transition. The PAC experimental results will be presented in the following subsections.

PAC experimental results at 573 K

At 573 K, the hexagonal RMnO₃ series are in the ferroelectric and paramagnetic phases. Although macroscopically these compounds have the same behavior from room temperature to 573 K, it is of great interest to observe what happens at the local scale.

Figure 3.5 shows representative R(t) spectra and corresponding Fourier transforms for measurements at 573 K. A summary of the EFG parameters obtained in these fits is presented in table 3.4. Again the best fit to each spectrum was obtained considering that the ¹¹¹Cd probe atoms interact with two EFG distributions. One shall note that for LuMO sample, extra EFG distributions have been used accounting for the presence of Lu₂O₃ in the sample.

The R(t) spectra of figure 3.5 show larger differences than the ones found in the room temperature measurements. These differences are more noticeable in the smaller rare-earth compounds, LuMnO₃ and ErMnO₃, where the R(t) spectra are clearly more attenuated than the others. Nevertheless two EFG distributions have been found for all compounds. Similarly to room temperature measurements, a major EFG₁ distribution is found in coexistence with EFG₂. EFG₁ is still characterized by $V_{zz1} \sim 66 \text{ V}/\text{\AA}^2$ and it is given by 50 to 70% of the ¹¹¹Cd probe atoms interacting with it. The second distribution, EFG₂, is characterized by $V_{zz2} \sim 102 \text{ V}/\text{\AA}^2$ with a smaller fraction of probes (30-50%) interacting with it. One shall note that the V_{zz} values were found to be essentially the same as found at room temperature although the other EFG parameters show a different dependence with the ionic radius.

Figure 3.6 presents the R_I dependence of the EFG parameters as function of the rare-earth ionic radius. As referred previously, the V_{zz} values were found to be essentially the same as found for room temperature with an indistinct dependence on R_I for both EFG distributions. However, the asymmetry parameters shows a dependence of the rare-earth ionic radius unlike the small variations observed at room temperature. At 573 K, for the smaller rare-earth compounds (LuMnO₃ and ErMnO₃) the two EFG distributions were found to be highly asymmetric. Also,

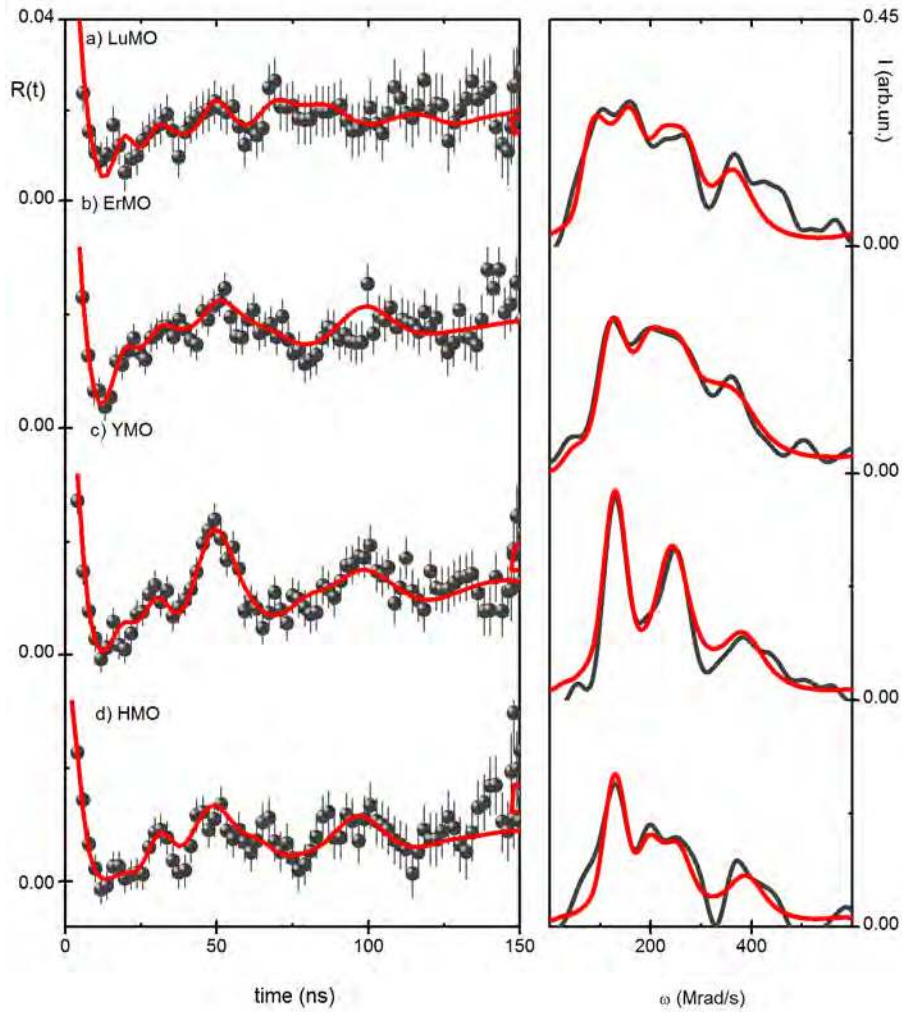


Figure 3.5: (Left) Representative $R(t)$ experimental functions and correspondent fits (thicker lines over the $R(t)$ spectra) measured at 573 K, for the hexagonal RMnO_3 samples: a) LuMO (LuMnO_3), b) ErMO (ErMnO_3), c) YMO (YMnO_3) and d) HMO (HoMnO_3). (Right) Corresponding Fourier transforms.

there is a decrease of the η values with the increase of the rare-earth ionic size. This result could be explained using structural considerations since one would expect a higher structural distortion associated to the accommodation of the structure due to the decrease of the rare-earth ionic size, in a similar manner as observed in the orthorhombic distortion. However, this trend was not observed at room temperature and since no structural distortion is known to occur in this temperature range, the present results suggest a different origin for this evolution of the η values. Furthermore, both fraction of probes interacting with each EFG and static attenuation coefficients show differences. These differences are larger in the smaller rare-earth compounds, where the two EFG distributions

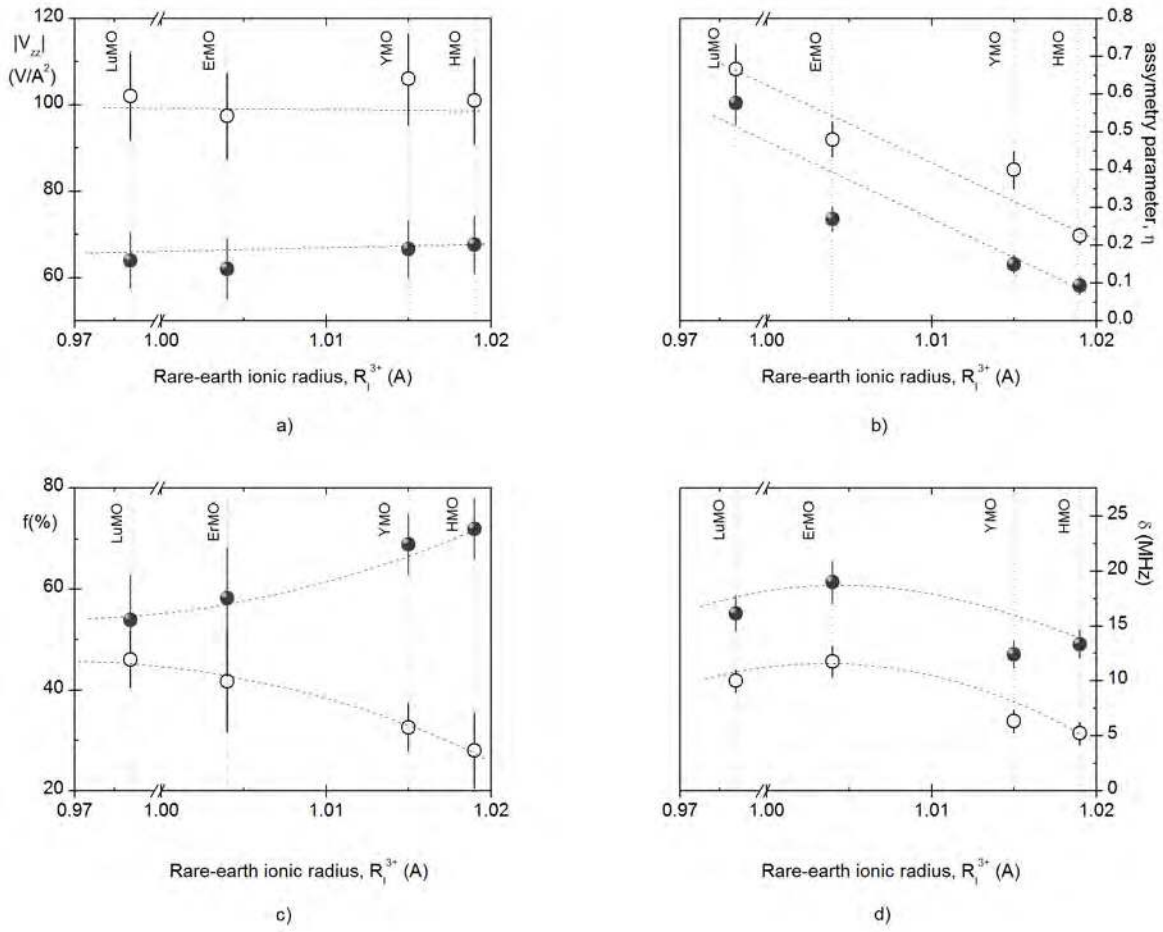


Figure 3.6: EFG parameters for measurements at 573 K: a) EFG principal component, V_{zz} , and b) asymmetry parameter, η , c) fractions of probes interacting with each EFG distribution, f , and d) static attenuation parameter, δ , for EFG₁ (closed dots) and EFG₂ (open dots). The vertical lines indicate the ionic radius of each rare-earth ion, which have been taken from^[47]. The dashed lines are guides to the eye.

were found to be in competition with $\sim 50\%$ of the ^{111}Cd probe atoms interacting with each EFG. Also, the attenuation coefficients are higher for LuMnO_3 and ErMnO_3 as clearly seen in the $R(t)$ spectra.

The different evolution of the EFG parameters at 573 K could be correlated with the ferroelectric transition temperature dependence with R_I^{3+} . For the smaller Lu and Er manganites, T_{FE} is reported to occur at lower temperatures than YMnO_3 and HoMnO_3 . The higher η and δ values, as well as the competing f_1 and f_2 for LuMnO_3 and ErMnO_3 suggest the appearance of local instabilities preceding the ferroelectric transition, in a temperature range of ~ 300 K lower than

the reported T_{FE} values.

Table 3.4: Electric field gradient parameters for the hexagonal $RMnO_3$ samples measured at 573 K. The indexes 1 and 2 refers to the two EFG distributions obtained from the fitting procedure.

Sample Reference	EFG ₁					EFG ₂				
	f_1	ω_1	V_{zz1}	η_1	δ_1	f_2	ω_2	V_{zz2}	η_2	δ_2
	%	Mrads ⁻¹	V/Å ²		MHz	%	Mrads ⁻¹	V/Å ²		MHz
LuMO	54	121	64	0.58	16	46	194	102	0.67	10
	±5	±10	±10	±0.02	±2	±5	±8	±8	±0.05	±3
ErMO	58	117	62	0.27	19	42	184	97	0.48	12
	±10	±5	±5	±0.02	±2	±4	±10	±10	±0.05	±4
YMO	69	126	67	0.15	12	31	200	106	0.40	6
	±5	±10	±10	±0.05	±2	±5	±10	±10	±0.08	±4
HMO	72	128	68	0.09	13	28	191	101	0.23	5
	±5	±10	±10	±0.02	±2	±5	±8	±8	±0.08	±5

PAC experimental results at 77 K

PAC measurements have been performed at liquid nitrogen temperature in order to study the rare-earth local environment near the magnetic transition temperatures. Magnetic measurements performed in the series of hexagonal $RMnO_3$ showed that at 77 K, $LuMnO_3$ is already in the antiferromagnetic phase, $ErMnO_3$ and $HoMnO_3$ are near the transition ($T_N \sim 76$ K for both compounds) while $YMnO_3$ is still in the paramagnetic phase ($T_N \sim 67$ K). Furthermore, no other transitions are known to occur at low temperature.

Figure 3.7 shows representative experimental perturbation functions $R(t)$ and corresponding Fourier transforms, measured at liquid nitrogen temperature, as function of the different rare-earth substitutions. Similarly to the previous cases, the best fit to each spectrum was obtained considering that the ^{111}Cd probe atoms interact with two EFG distributions, which were assumed as Lorentzian-like. A list of the obtained EFG parameters is summarized in table 3.5. The experimental $R(t)$ spectra present differences, which could be attributed to the different magnetic phase of each compound in this temperature although all spectra are more attenuated than the ones obtained at room temperature. $LuMnO_3$ is ordered antiferromagnetically below ~ 90 K, shows a different

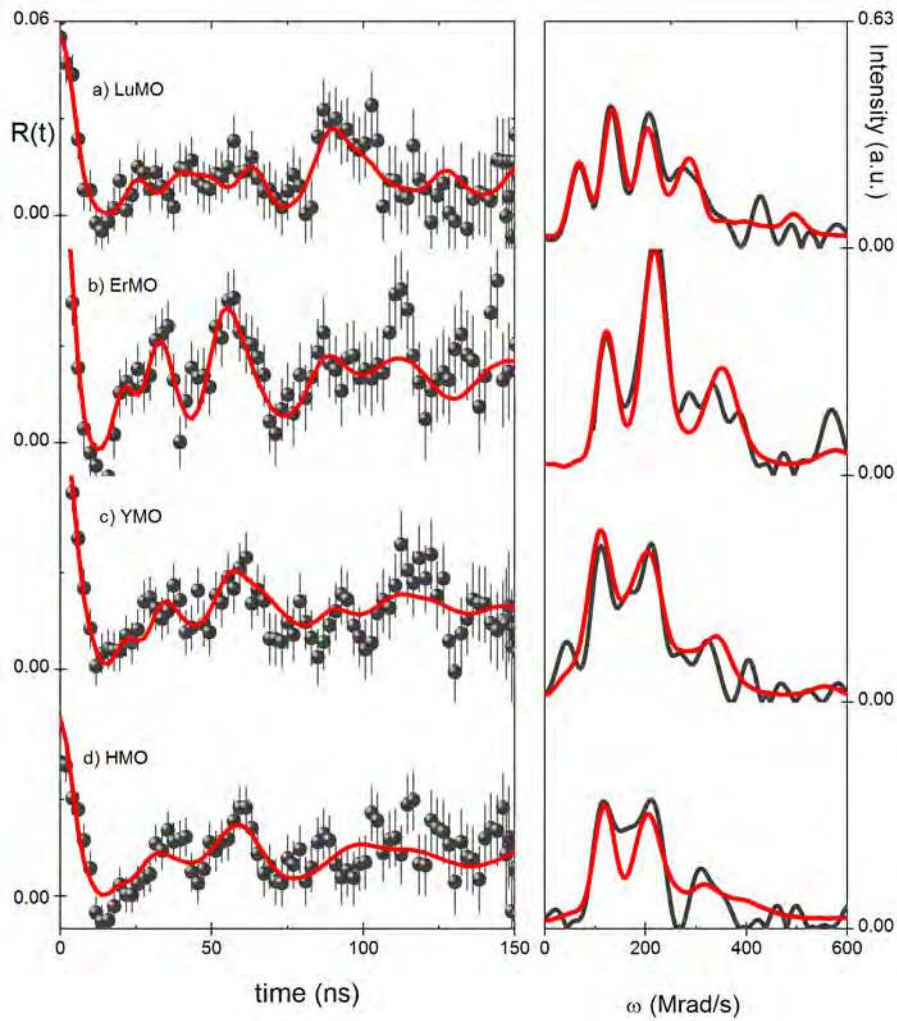


Figure 3.7: (Left) Representative $R(t)$ experimental functions and correspondent fits (thicker lines over the $R(t)$ spectra) measured at 77 K, for the hexagonal RMnO_3 samples: a) LuMO (LuMnO_3), b) ErMO (ErMnO_3), c) YMO (YMnO_3) and d) HMO (HoMnO_3). (Right) Corresponding Fourier transforms.

spectrum which is still characterized by the two EFG_1 and EFG_2 distributions. One shall note that the apparent splitting of the frequency triplets in the Fourier transform could suggest the presence of a magnetic hyperfine field (MHF) already at 77 K. However, the fitting procedures accounting for a combined (electrical and magnetic) interaction showed that the MHF is much smaller than the EFG contribution resulting only in a small perturbation in the quadrupolar frequency. This perturbation is revealed by the higher V_{zz1} value than the one found to be characterizing EFG_1 at room temperature.

Regarding ErMnO_3 and HoMnO_3 compounds, which are both in the vicinity of the magnetic

transition, one still observes the coexistence of EFG₁ and EFG₂. The R(t) spectra show essentially the same features although the Fourier transform show different characteristics. In particular for ErMnO₃ there is again an apparent splitting of the frequency triplets suggesting the presence of a MHF combined with a EFG distribution. However, similarly to HoMnO₃, the MHF is much smaller than the EFG contribution resulting in a small perturbation to the R(t) spectra.

YMnO₃ shows essentially the same EFG distributions found in the other compounds being the EFG parameters quite similar to the ones obtained at room temperature.

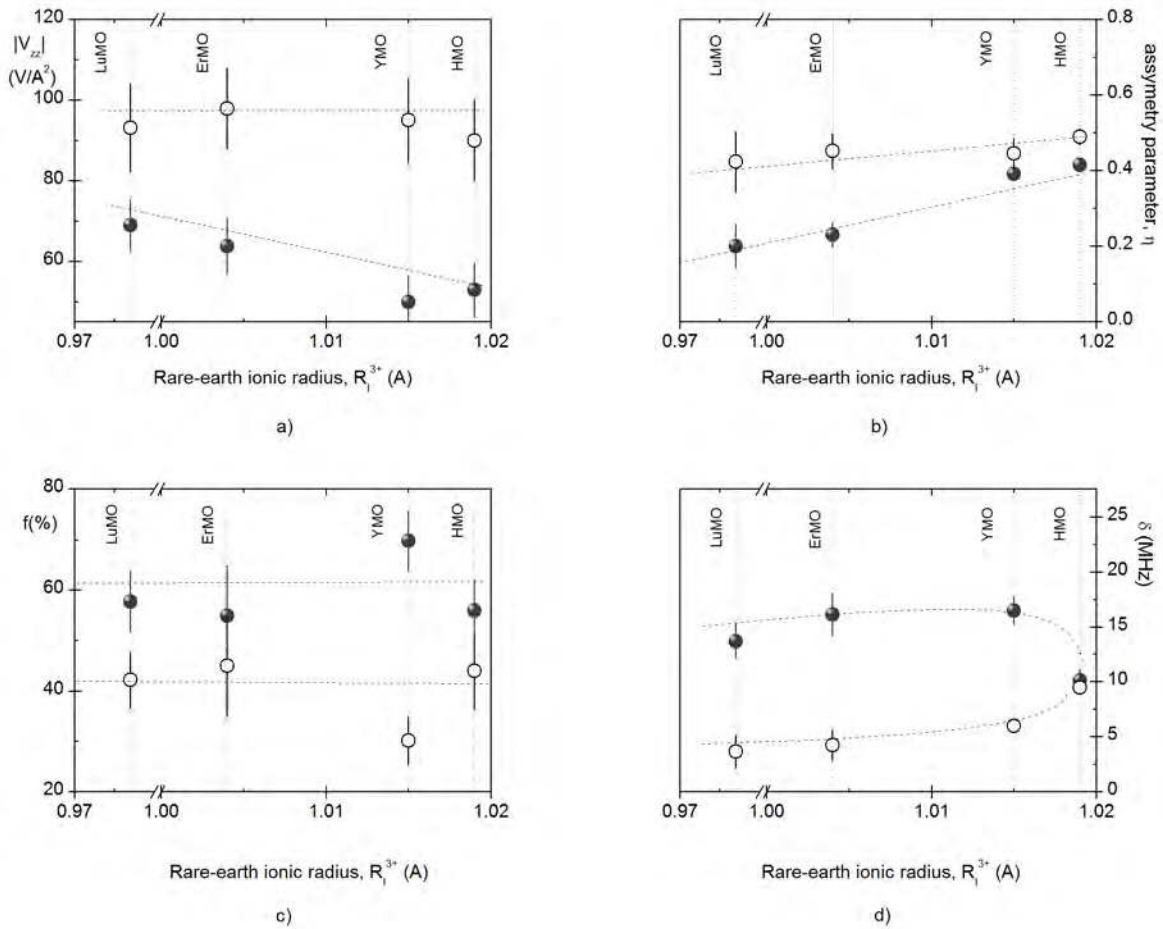


Figure 3.8: EFG parameters for measurements at 77 K: a) EFG principal component, V_{zz} , b) asymmetry parameter, η , c) fractions of probes interacting with each EFG distribution, f , and d) static attenuation parameter, δ , for EFG₁ (closed dots) and EFG₂ (open dots). The vertical lines indicate the ionic radius of each rare-earth element, which have been taken from^[47]. The dashed lines are guides to the eye.

Figure 3.8 depicts the evolution of the EFG parameters with the rare-earth ionic radius. Starting

Table 3.5: Electric field gradient parameters for the hexagonal RMnO₃ samples measured at 77 K. The indexes 1 and 2 refers to the two EFG distributions obtained from the fitting procedure.

Sample Reference	EFG ₁					EFG ₂				
	f ₁ %	ω ₁ Mrads ⁻¹	V _{zz1} V/Å ²	η ₁	δ ₁ MHz	f ₂ %	ω ₂ Mrads ⁻¹	V _{zz2} V/Å ²	η ₂	δ ₂ MHz
LuMO	58	131	69	0.20	14	42	176	93	0.42	4
	±6	±6	±6	±0.01	±2	±6	±11	±11	±0.09	±2
ErMO	55	121	64	0.23	16	45	185	101	0.45	4
	±4	±5	±5	±0.02	±2	±4	±10	±10	±0.05	±4
YMO	70	95	50	0.39	16	30	179	95	0.44	6
	±6	±7	±7	±0.03	±3	±6	±11	±11	±0.05	±3
HMO	56	100	53	0.42	10	44	170	90	0.49	9
	±5	±10	±10	±0.03	±3	±5	±10	±10	±0.05	±3

with the V_{zz} evolution, one can observe that there is an indistinct trend for EFG₂ while there is small decrease of V_{zz1} with the increase of the rare-earth ionic size. Both EFG distributions were still found to be non-axially symmetric ($\eta > 0$) with a slight trend for the increase of the η values with the rare-earth ionic size. For HoMnO₃ both local environments are highly asymmetric contrarily to the results obtained at room temperature.

Looking at the fraction of probes interacting with each EFG distribution, one can observe that for both EFG₁ and EFG₂, f_1 and f_2 have closer values. In particular for YMnO₃, f_1 and f_2 are more defined following the trend obtained at room temperature. The static attenuation parameters, δ_1 and δ_2 are essentially the same for all rare-earth although HoMnO₃ shows the less attenuated spectrum.

PAC experimental results at 10 K

At 10 K, all compounds of the hexagonal RMnO₃ series present antiferromagnetic order of the Mn³⁺ spins. Depending on the rare-earth substitution the magnetic susceptibility curves showed different behaviors which can be attributed to the magnetic behavior of each rare-earth element.

Figure 3.9 presents representative experimental perturbation functions $R(t)$ and respective Fourier transforms, measured at 10 K, as function of the different rare-earth substitutions. The

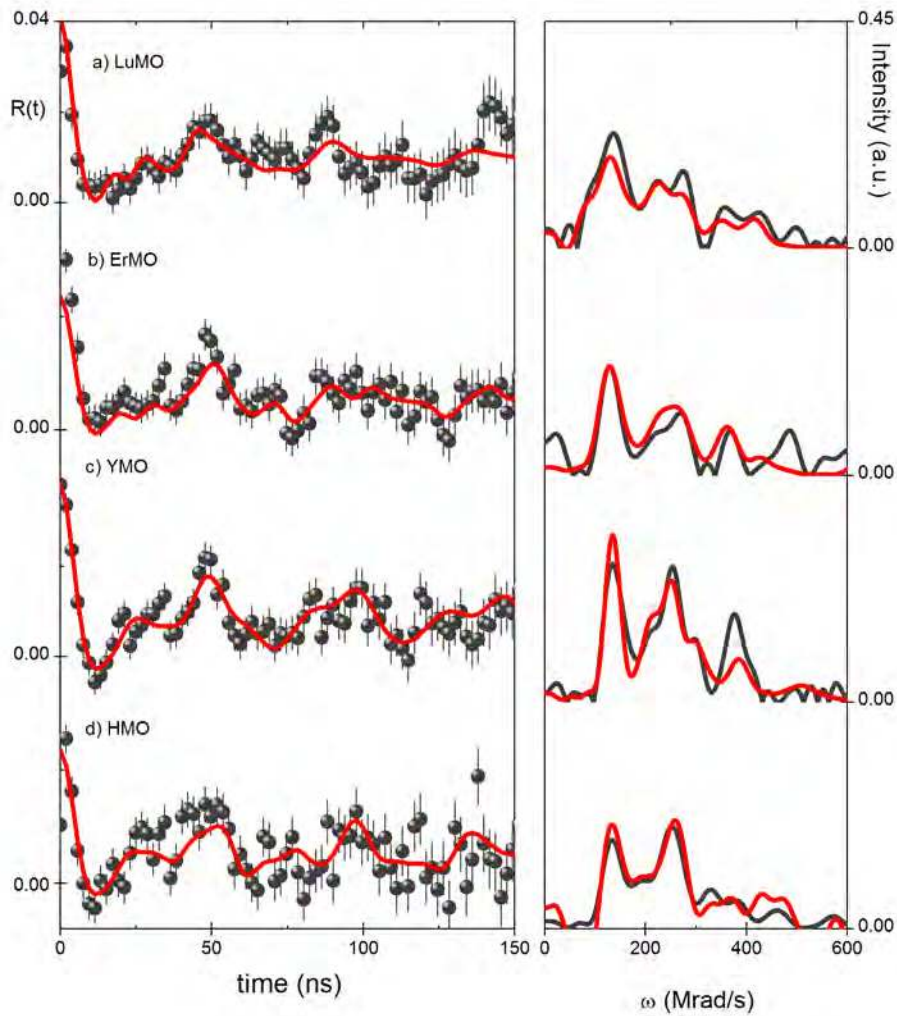


Figure 3.9: (Left) Representative $R(t)$ experimental functions and correspondent fits (thicker lines over the $R(t)$ spectra) measured at 10 K, for the hexagonal RMnO_3 samples: a) LuMO (LuMnO_3), b) ErMO (ErMnO_3), c) YMO (YMnO_3) and d) HMO (HoMnO_3). (Right): Corresponding Fourier transforms.

best fit to each spectrum was obtained, at a first step, considering that the ^{111}Cd probe atoms interact with two EFG distributions. A close inspection to the Fourier transforms shows a splitting of the frequency triplets suggesting the presence of a magnetic hyperfine field (MHF).

Different fitting models have been applied considering the presence of a magnetic hyperfine field. The first model considered the coexistence of two pure quadrupolar (electric) EFG distributions. This model proved to be not sufficient to obtain the best fits which better characterize these compounds. The second model assumed the presence of two combined interactions ($\text{EFG}_1 + \text{MHF}_1$ and $\text{EFG}_2 + \text{MHF}_2$). The resulting parameters showed the presence of one combined interaction with

Table 3.6: Electric field gradient parameters for the hexagonal RMnO₃ samples measured at 10 K. The indexes 1 and 2 refers to the two EFG distributions obtained from the fitting procedure.

Sample Reference	EFG ₁					EFG ₂ +MHF ₂					
	f ₁ %	ω ₁ Mrads ⁻¹	V _{zz1} V/Å ²	η ₁	δ ₁ MHz	f ₂ %	ω ₂ Mrads ⁻¹	V _{zz2} V/Å ²	η ₂	δ ₂ MHz	B _{hf} T
LuMO	73	118	62	0.31	20	27	215	113	0.52	9	0.7
	±8	±4	±4	±0.03	±4	±8	±11	±11	±0.07	±2	±0.3
ErMO	69	124	65	0.20	17	31	191	101	0.51	6	1.8
	±8	±4	±4	±0.02	±3	±8	±10	±10	±0.05	±2	±0.2
YMO	67	126	67	0.30	16	33	198	105	0.54	4	0.1
	±10	±10	±10	±0.02	±3	±10	±10	±10	±0.07	±1	±0.1
HMO	58	129	68	0.22	15	42	191	101	0.45	6	2
	±8	±7	±7	±0.02	±3	±8	±10	±10	±0.04	±2	±1

a quantifiable MHF while the second distribution presented a nil MHF. Following these results, the third and fourth models (denoted here as MI and MII) have been implemented accounting for the coexistence of a combined (electric and magnetic) with a pure quadrupolar interactions. In detail, MI presupposes that only the probes in the major fraction experience a MHF being EFG₁ combined with a magnetic distribution while the minor fraction would interact with a pure electrical distribution. MII has been applied considering that a minor fraction of probes would be experiencing a MHF, i.e. EFG₂ would be combined with a magnetic distribution whereas the major fraction of probes would be interacting with a pure electrical distribution. Both models have implemented showing that the best fit is obtained by using MII approach, which resulting fitting parameters are summarized in table 3.6. One shall note that the presence of combined interactions adds additional attenuation to the R(t) spectra limiting the accuracy of the EFG/MHF determination.

All compounds show the presence of a MHF, which intensity was found to be different for different rare-earth substitutions, as summarized in table 3.6. In particular, all samples show both LuMnO₃ and YMnO₃ (with diamagnetic rare-earths) present a main distribution (f₁ ~65(7)%), which is due to a pure quadrupole interaction. The secondary distribution (f₂ ~35(7)%) is due to a combined interaction accounting for the presence of a MHF. The magnitude of this MHF was found to be different for different rare-earth substitutions. The compounds with paramagnetic rare-

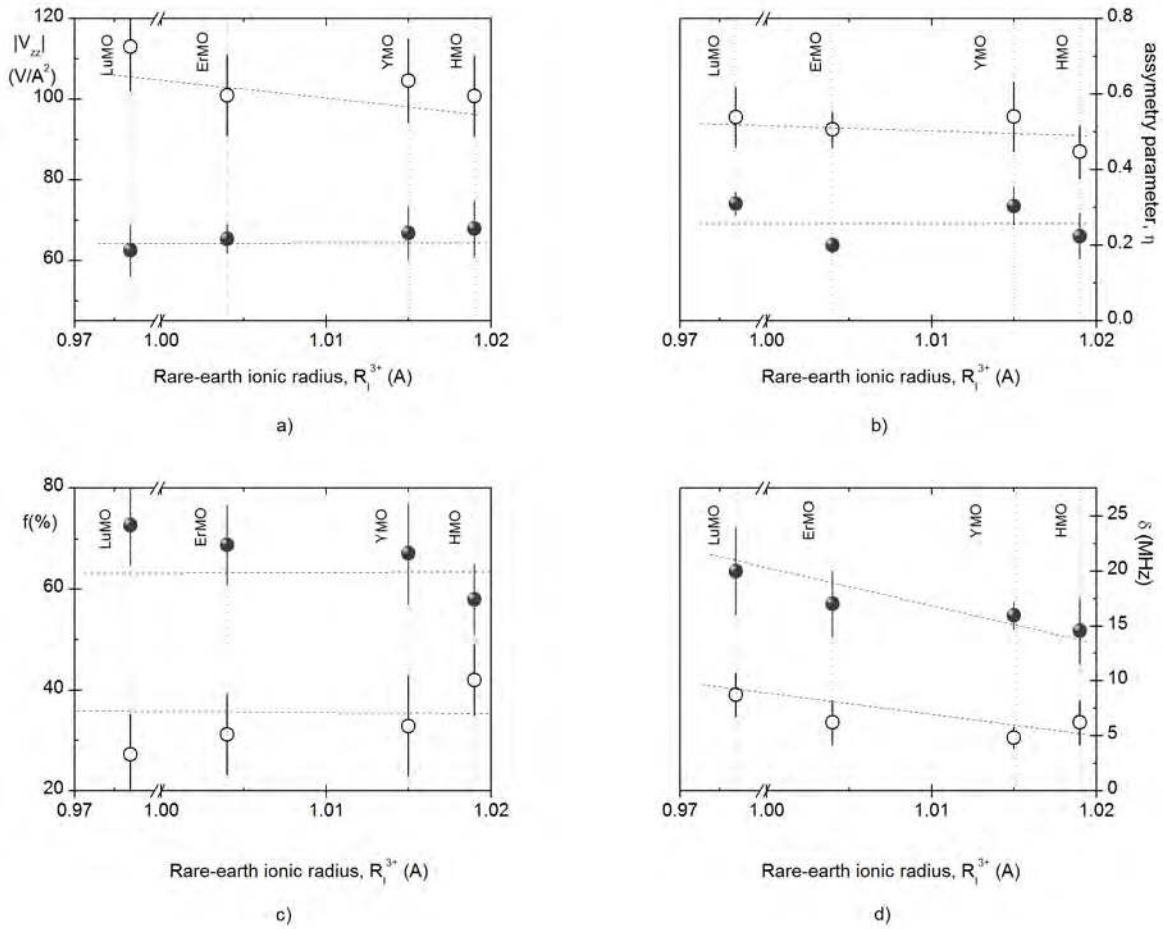


Figure 3.10: EFG parameters for measurements at 10 K: a) EFG principal component, V_{zz} , b) asymmetry parameters, η , c) fractions of probes interacting with each EFG distribution, f , and d) static attenuation parameter, δ , for EFG₁ (closed dots) and EFG₂ (open dots). The vertical lines indicate the ionic radius of each rare-earth element, which have been taken from^[47]. Dashed lines are guides to the eye.

earths, ErMnO₃ and HoMnO₃, show a higher MHF ($B_{hf} \sim 1.8(3)$ T) while the other compounds exhibit a very weak MHF (in the order of 0.1-0.7 T).

Figure 3.10 shows the evolution of the EFG parameters with the rare-earth ionic radius. Both V_{zz} , η and fractions of probes interacting with each EFG show an indistinct dependence with the rare-earth ionic radius. On the other hand, both f and δ show a decrease with the increase of the rare-earth size for both EFG distributions.

3.1.3 EFG dependence on temperature

Representative samples of the hexagonal RMnO_3 series have been selected to study in detail the temperature dependence of the EFGs. The ^{111}Cd PAC results have been complemented with measurements with ^{111}In . Due to its half-life (2.8 days), ^{111}In probe is very suitable to perform several measurements at different temperatures within a single implantation.

YMnO_3 and ErMnO_3 samples have been chosen to study the temperature dependence of the EFG parameters in a temperature range from 10 K up to 1300 K. The PAC experimental results will be presented separately for each sample in the following subsections.

YMnO_3 : EFG dependence on temperature

YMnO_3 crystallizes in the hexagonal structure with $P6_3cm$ space group at room temperature. Additionally, in its high temperature paraelectric state, YMnO_3 adopts the centrosymmetric space group $P6_3mmc$. Discrepancies in the ferroelectric transition temperatures reported in the literature suggested that this change in space group occurs at higher temperatures than the ferroelectric polarization^[94], which is reported to occur at ~ 950 (30) K^[82,90]. Indeed, structural studies showed that there are two distinct phase transitions at high temperatures for YMnO_3 as well as for all hexagonal RMnO_3 compounds^[94], being the structural transition some 300 K higher than the ferroelectric ordering temperature. Concerning the magnetic properties, YMnO_3 shows a paramagnetic-antiferromagnetic transition at $T_N \sim 67$ K. No other transitions are known to occur at low temperatures.

Figures 3.11 and 3.12 shows representative experimental $R(t)$ functions and respective Fourier transforms, for measurements performed at different temperatures from 10 up to 1296 K, trying to cover both magnetic and ferroelectric transitions. The fit to each experimental spectrum was obtained considering that the probe atoms interact with two EFG distributions for all temperatures, which were assumed to be Lorentzian-like. For simplicity the data will be divided according to high (from 293 K up to 1296 K) and low (from 10 K up to 293 K) temperature measurement intervals.

Figure 3.11 displays the $R(t)$ spectra obtained for measurements performed from room temperature (293 K) up to 1296 K. The plots show essentially the same features for all temperatures revealing that the ^{111}Cd probe atoms interact with two EFGs distributions (named EFG_1 and EFG_2

following the previous notations). Similarly to the results described for room temperature, a main EFG (EFG_1) was found affecting about 70(6)% of the probe atoms and it is characterized by a lower V_{zz1} and a non axially symmetric local environment ($\eta \sim 0.23$). The second EFG distribution, EFG_2 , is characterized by a higher V_{zz2} and a highly asymmetric local environment given by η values ranging between 0.50-0.62. This EFG_2 affects $\sim 30(8)\%$ of the probe atoms. Although there are

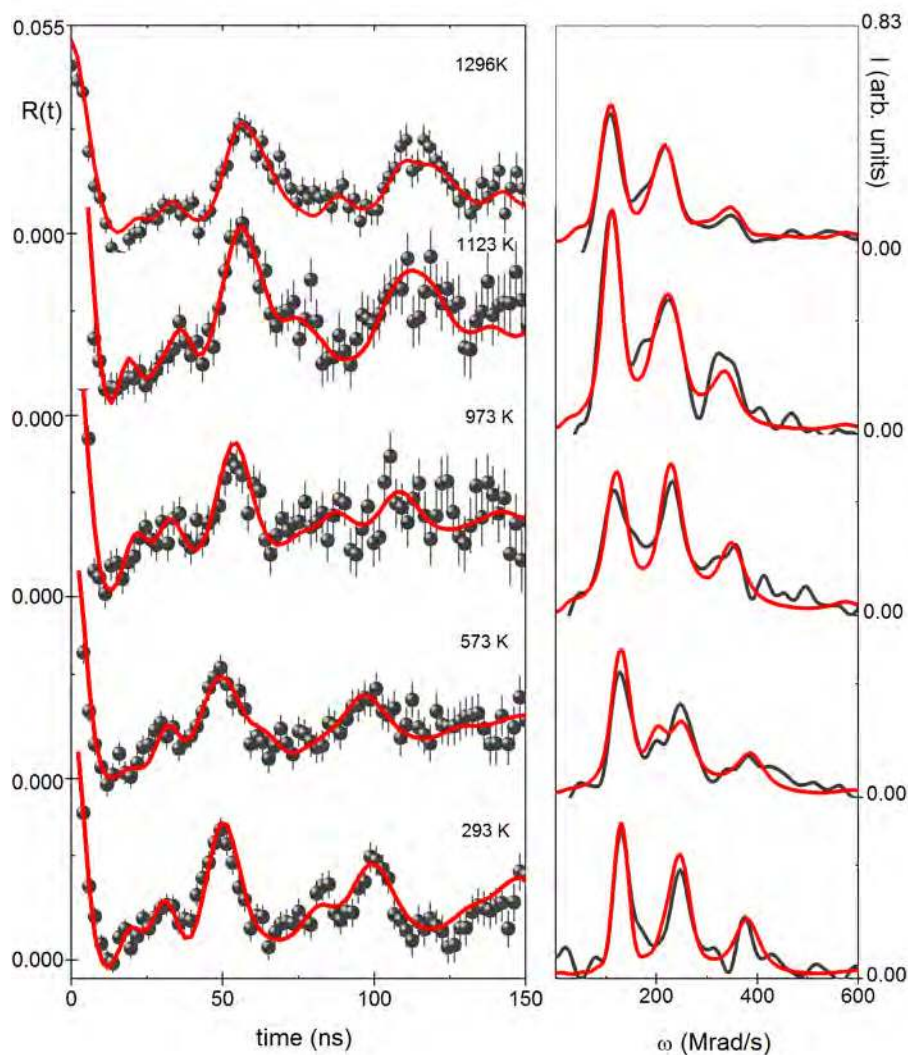


Figure 3.11: (Left) Representative $R(t)$ experimental functions and correspondent fits (thicker lines over the $R(t)$ spectra) measured from room temperature (293 K) up to 1296 K, for $YMnO_3$. (Right) corresponding Fourier transforms.

small differences in the $R(t)$ spectra with temperature, one shall note that there is a decrease on the main peak on the Fourier transforms with decreasing temperature hinting for an increase of the

attenuation parameter. This feature will be discussed later on together with the evolution of the other EFG parameters.

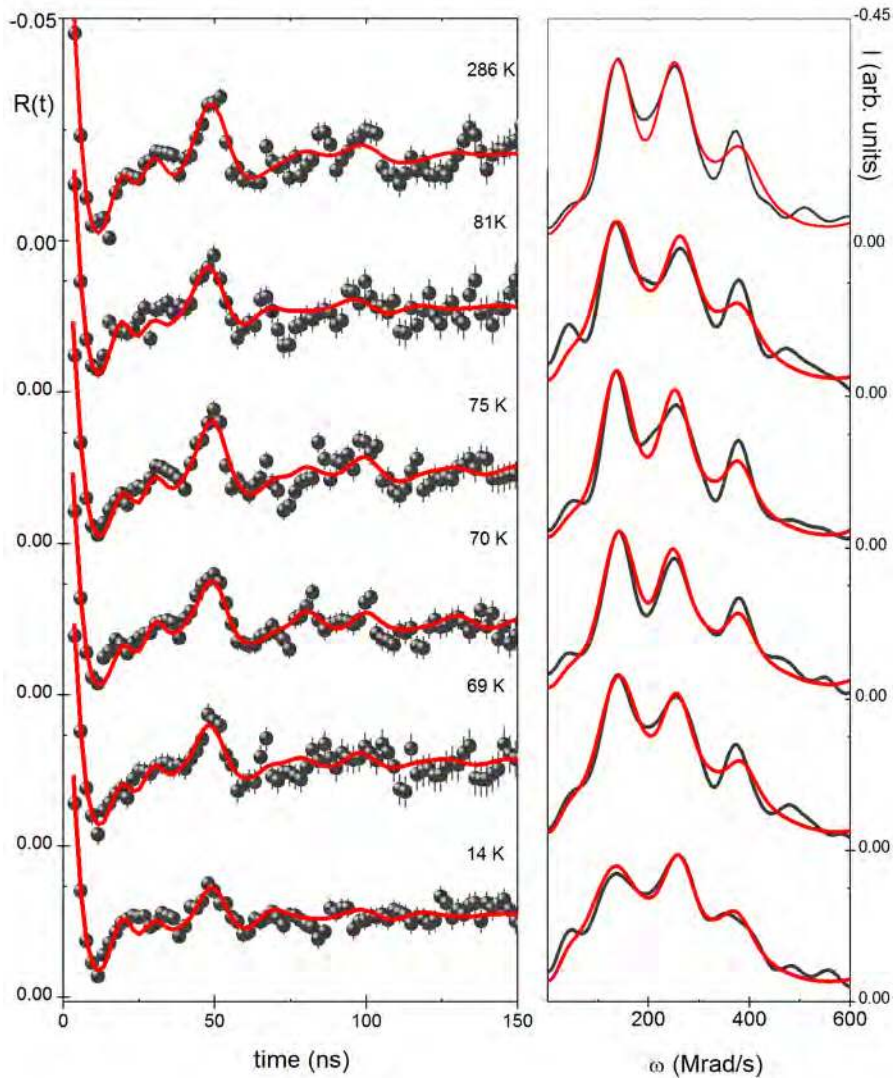


Figure 3.12: (Left) Representative $R(t)$ experimental functions and correspondent fits (thicker lines over the $R(t)$ spectra) measured from 14 K up to 286 K, for YMnO_3 . (Right) corresponding Fourier transforms.

Figure 3.12 shows the $R(t)$ spectra obtained for low temperature measurements. The plots show essentially the same features with the best fit to each spectrum being given by the interaction of the ^{111}Cd probe atoms with the same two EFG distributions obtained for the high temperature measurements. Once again, there is a decrease on the intensity of the frequency peaks in the Fourier transforms suggesting an increase of the attenuation of the spectra with decreasing temperature.

Moreover, the close inspection of the Fourier transforms hint for the presence of a small MHF at 14 K, as seen by the enlargement of the frequency peaks. The presence of a MHF ($B_{\text{hf}} \sim 0.1(2)$ T) has been accounted in the fitting procedure in the measurements at 14 and 10 K, in a combined quadrupolar and magnetic interaction ($\text{EFG}_2 + \text{MHF}_2$) as described for 10 K measurements.

Figure 3.13 shows the evolution of the EFG parameters with temperature for YMnO_3 . The resulting EFG parameters are summarized in table 3.7.

Table 3.7: Electric field gradient parameters for the hexagonal YMnO_3 sample as a function of temperature.

T(K)	EFG ₁					EFG ₂ +MHF ₂					B _{hf} T
	f ₁	ω ₁	V _{zz1}	η ₁	δ ₁	f ₂	ω ₂	V _{zz2}	η ₂	δ ₂	
	%	Mrads ⁻¹	V/Å ²		MHz	%	Mrads ⁻¹	V/Å ²		MHz	
1296	85±8	106±5	56±4	0.17±0.03	9±2	15±8	184±8	97±6	0.48±0.05	4±1	-
1206	85±8	117±8	62±6	0.23±0.04	16±3	15±8	170±8	90±8	0.48±0.05	7±2	-
1123	72±8	107±5	56±5	0.22±0.08	10±3	28±8	181±10	96±10	0.59±0.04	7±2	-
973	61±8	113±5	60±5	0.23±0.06	15±3	39±8	181±5	96±5	0.53±0.03	6±3	-
573	76±6	113±5	66±5	0.18±0.04	15±3	24±6	191±10	101±10	0.55±0.10	9±2	-
293	76±8	125±10	66±10	0.19±0.03	9±3	24±6	197±14	104±14	0.49±0.05	6±5	-
81	67±8	128±6	67±6	0.24±0.03	17±6	33±8	204±10	108±10	0.55±0.07	8±3	-
75	73±5	128±10	68±10	0.24±0.09	18±3	27±5	199±10	105±10	0.54±0.05	7±3	-
73	69±5	129±10	68±10	0.23±0.07	18±3	31±5	197±10	105±10	0.54±0.03	8±2	-
71	66±9	131±4	70±4	0.22±0.04	22±4	34±9	200±5	106±5	0.52±0.02	6±3	-
70	72±6	133±4	70±4	0.22±0.08	19±2	28±6	198±6	105±6	0.50±0.05	7±3	-
69	70±8	133±5	70±5	0.25±0.02	23±4	30±8	202±8	107±8	0.51±0.04	9±3	-
14	61±5	129±8	68±8	0.28±0.07	27±5	39±5	199±10	105±10	0.57±0.04	9±3	0.1±0.1

Starting with the EFG principal component, V_{zz} , one can observe that the magnitudes of both EFG principal components are quite distinct and decrease with increasing temperature. This trend has been also observed in perovskite systems^[12,186] and is frequently associated to an increase if the atomic vibrations and volumic thermal expansions (α) due to the increase of temperature. One shall note that the thermal expansion contribution is very small and shall not account alone for the V_{zz} temperature dependence (e.g., for LaMnO_3 α is approximately $1.2 \times 10^{-5} \text{ K}^{-1}$ ^[158]). The variation of V_{zz} with temperature has been calculated for both EFG distributions giving the values $\frac{1}{V_{zz}^{01}} \frac{\Delta V_{zz}^{01}}{\Delta T} \sim$

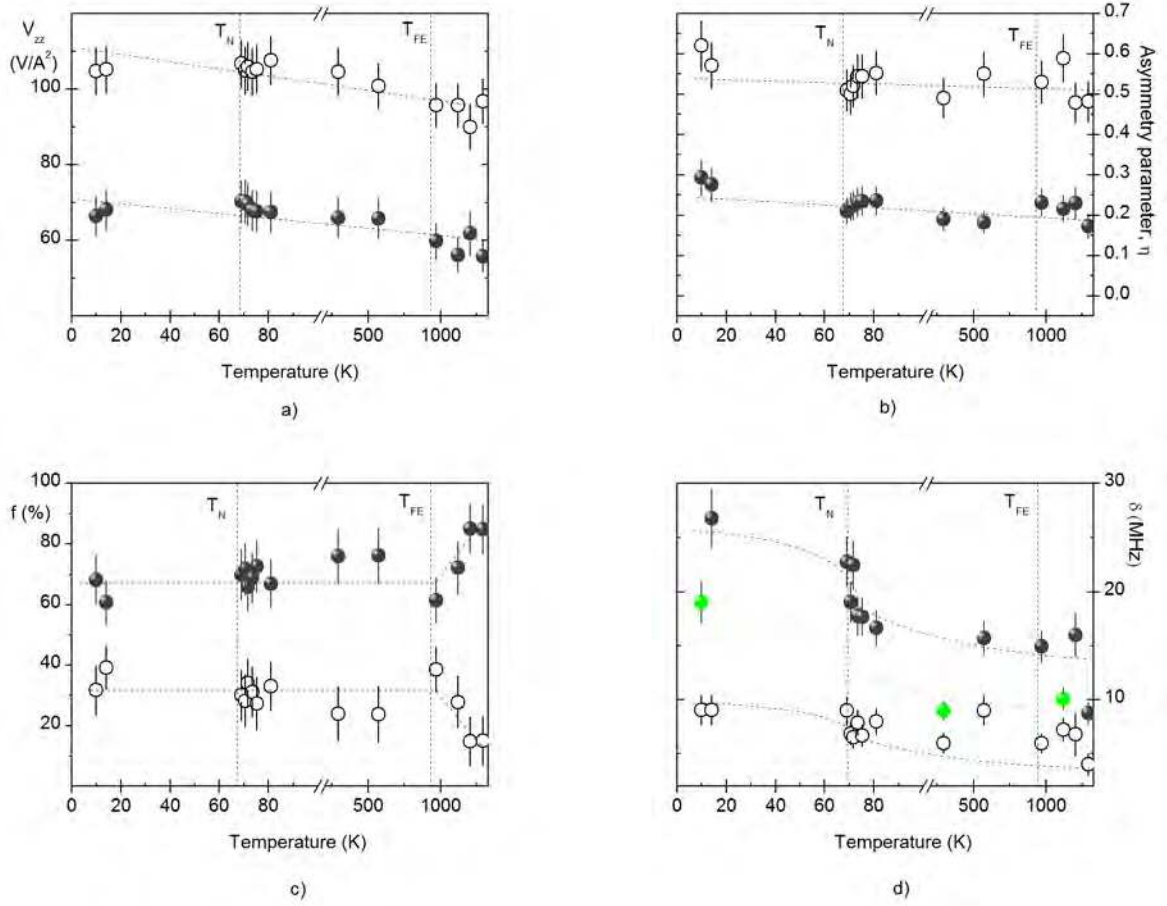


Figure 3.13: EFG parameters dependence with temperature for YMnO_3 : a) EFG principal component, V_{zz} , b) asymmetry parameter, η , c) fractions of probes interacting with each EFG distribution, f , and d) static attenuation parameter, δ . The vertical dashed lines indicate the ferroelectric (T_{FE}) and magnetic (T_{N}) transition temperatures.

$-1.8 \times 10^{-4} \text{ K}^{-1}$ and $\frac{1}{V_{zz}^{02}} \frac{\Delta V_{zz}^{02}}{\Delta T} \sim -9.9 \times 10^{-5} \text{ K}^{-1}$, which are one order of magnitude higher than the volumic thermal expansion. Regarding the asymmetry parameter η , this parameter is almost temperature independent with small variations within the error bars for both EFG distributions. The fractions (f) of probes interacting with each EFG distributions exhibit very subtle variations with temperature in the ferroelectric phase. At high temperatures (above $T_{\text{FE}} \sim 950 \text{ K}$) a strong dependence of this parameter is observed, being EFG₁ the dominant distribution. The obtained results hint that at temperatures above 1400 K, EFG₁ might be the only distribution observed in the compound. One shall note that, in this compound, the structural transition to the centrosymmetric space group is expected to occur at 1220 K^[94]. This space group allows only one non-equivalent

rare-earth site. The observed evolution of f_1 and f_2 gives consistence to the fact that the ^{111}Cd probe atoms sit in the rare-earth sites. Moreover, the present results hint for a change in the space group at higher temperatures than the one reported previously.

The attenuation parameters, which give the relative width of each EFG distribution, show a different behavior as function of temperature. Although the relative width of EFG₂ is relatively narrow and almost constant with temperature, for EFG₁ a broader distribution was found. Also, when decreasing temperature δ_1 increases in the region of the magnetic transition temperature, T_N , stabilizing around $\delta \sim 25$ MHz for $T < T_N$. One shall note that the EFG₁ data points obtained at 10, 293 and 1123 K (underlined as green dots in figure 3.13(d)) are out of the described trend line most likely due to the fact that these experiments have been performed in different experimental conditions. Nevertheless, considering only these data points one can observe the same dependence if δ_1 with temperature. The variation of δ_1 with temperature suggests the existence of a small perturbation due to the magnetic transition. Although one would expect that the magnetic ordering would lead to a coherent local environment, the present results show that there is only a broadening of the frequency lines.

As mentioned before, the existence of two EFG distributions for all temperature range could be related to the existence of the two non-equivalent rare-earth sites allowed by the $P6_3cm$ space group (R(2a site) and R(4b site)). Nevertheless, one shall remind that at high temperatures YMnO_3 is in the paraelectric phase and adopts the centrosymmetric space group $P6_3/mmc$, which allows only one non-equivalent Y site. Thus, assuming that the ^{111}Cd probe atoms are located at the rare-earth site, only one experimental EFG distribution is expected above the structural transition.

As already mentioned, reports in literature about the ferroelectric transition showed large discrepancies^[82,94] in the temperature values, suggesting that the space group change occurs at higher temperatures than the dipole ordering^[94]. In fact, works reported in the literature^[94] point to the the structural transition to occur around 1220 K, which is consistent with the existence of two EFG distributions at this temperature. Nevertheless, the present PAC results show that EFG₁ tends to be the only distribution at temperatures above 1400 K in agreement with the existence of only one rare-earth site allowed by the centrosymmetric space group. Also, these results show that the space group change occurs ~ 200 K higher than the values reported previously.

One shall note that in previous PAC studies performed in manganite systems, the Cd probe

atoms have been assigned to the A site in the structure^[12,181,185,186] in agreement to the assignment of the two low temperature experimental EFG to the two non-equivalent rare-earth sites.

ErMnO₃ EFG dependence on temperature

Similarly to the other hexagonal RMnO₃ compounds, ErMnO₃ crystallizes in the non centrosymmetric $P6_3cm$ space group in the hexagonal crystalline structure at room temperature. It was reported a structural transition to the centrosymmetric $P6_3/mmc$ space group at ~ 1310 K^[83]. Moreover, the electric dipole ordering, i.e., the transition from the paraelectric to the ferroelectric phase was reported to be at a lower temperature, $T_{FE} \sim 833$ K^[92]. Regarding the magnetic properties of ErMnO₃, this compound shows a transition to an antiferromagnetic ordering at $T_N \sim 76$ K^[85]. In ErMnO₃, due to the partially filled $4f$ shell of the rare-earth ion, the antiferromagnetic ordering of the Er³⁺ was reported to occur $T_{4f} \sim 5$ K^[107].

The PAC data have been measured from 10 K up to 1296 K. For simplicity the obtained results will be presented by high temperature (from 373 K up to 1296 K) and low temperature (from 10K up to room temperature) measurements. Alike YMnO₃, the best fit to each spectrum was obtained considering that the ¹¹¹Cd probe atoms interact with two EFG distributions (named EFG₁ and EFG₂ following the previous notations). The resulting fitting parameters are listed in table 3.8.

Figure 3.14 shows the R(t) spectra obtained for measurements performed at high temperatures. The spectra show essentially the same frequency triplets in this temperature range. The main fraction of probes ($f_1 \sim 60-80\%$) was found again to be interacting with EFG₁, which is characterized by an average $V_{zz1} \sim 63.5$ V/Å² and η_1 ranging between 0.2-0.3. A minor EFG₂ was also found being described by $V_{zz2} \sim 98$ V/Å² and $\eta_2 \sim 0.45$. Although EFG₁ and EFG₂ are coexisting in this temperature range, one shall note that the spectra obtained at 773 K and 833 K are more attenuated. Furthermore, the Fourier transforms show small changes in the intensities of the main frequency peaks suggesting small changes in the fractions of probe atoms interacting with each EFG distribution.

Figure 3.15 depicts the R(t) spectra obtained for low temperature measurements (from 10 K up to room temperature). Again, the same frequency triplets are present showing the coexistence of EFG₁ and EFG₂ in this temperature range. The Fourier transforms show some differences suggesting small variations of the EFG parameters. One shall note that, similarly to YMnO₃,

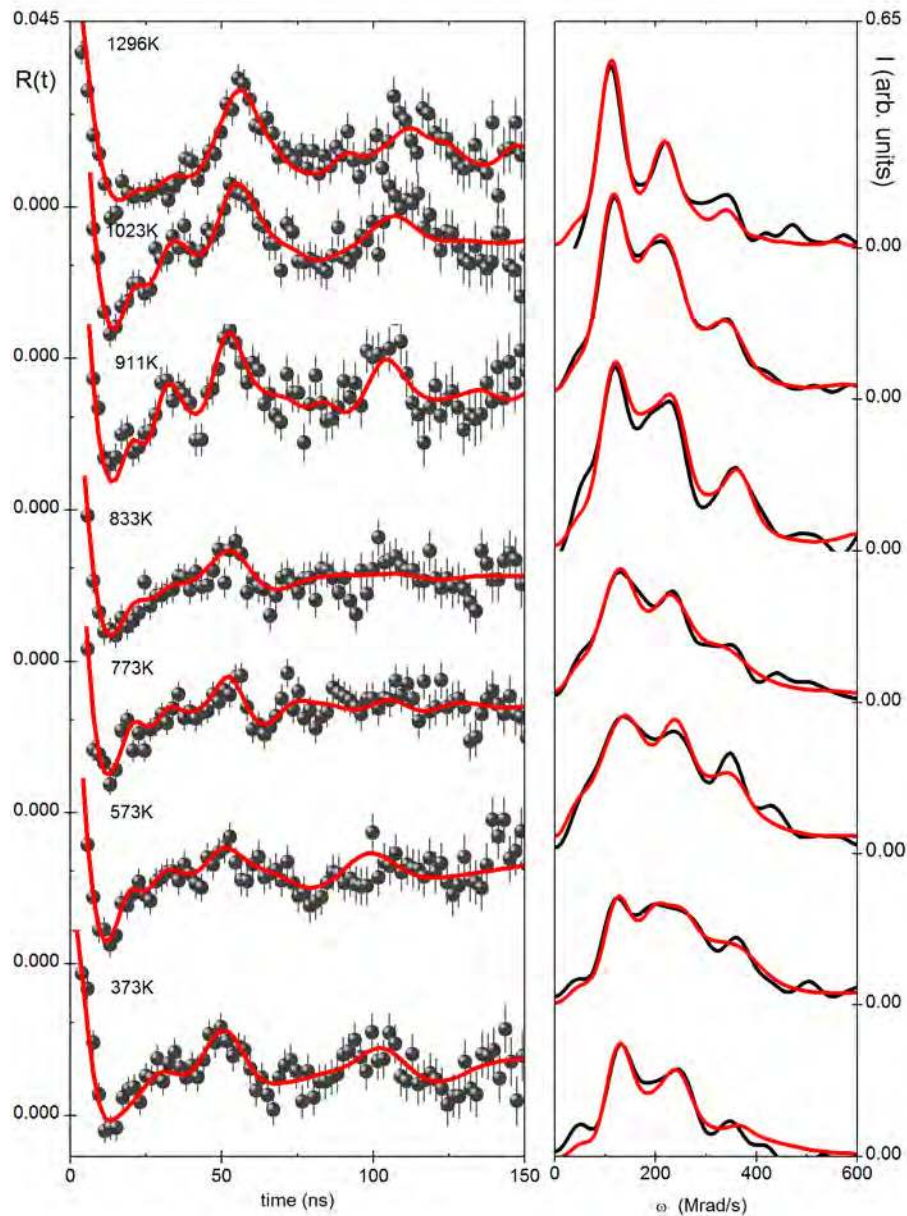


Figure 3.14: (Left) Representative $R(t)$ experimental functions and correspondent fits (thicker lines over the $R(t)$ spectra) measured from 373 K up to 1296 K, for ErMnO_3 . (Right) Corresponding Fourier transforms.

there is an increase of the attenuation of the spectra when decreasing temperature. Furthermore, the apparent splitting of the frequency triplets at 10 K has been accounted with the inclusion of a magnetic hyperfine field in the fitting procedure. At 10 K, the applied fitting model presupposes the coexistence of a pure quadrupolar distribution (EFG_1) with a combined quadrupolar and magnetic interaction ($\text{EFG}_2 + \text{MHF}_2$).

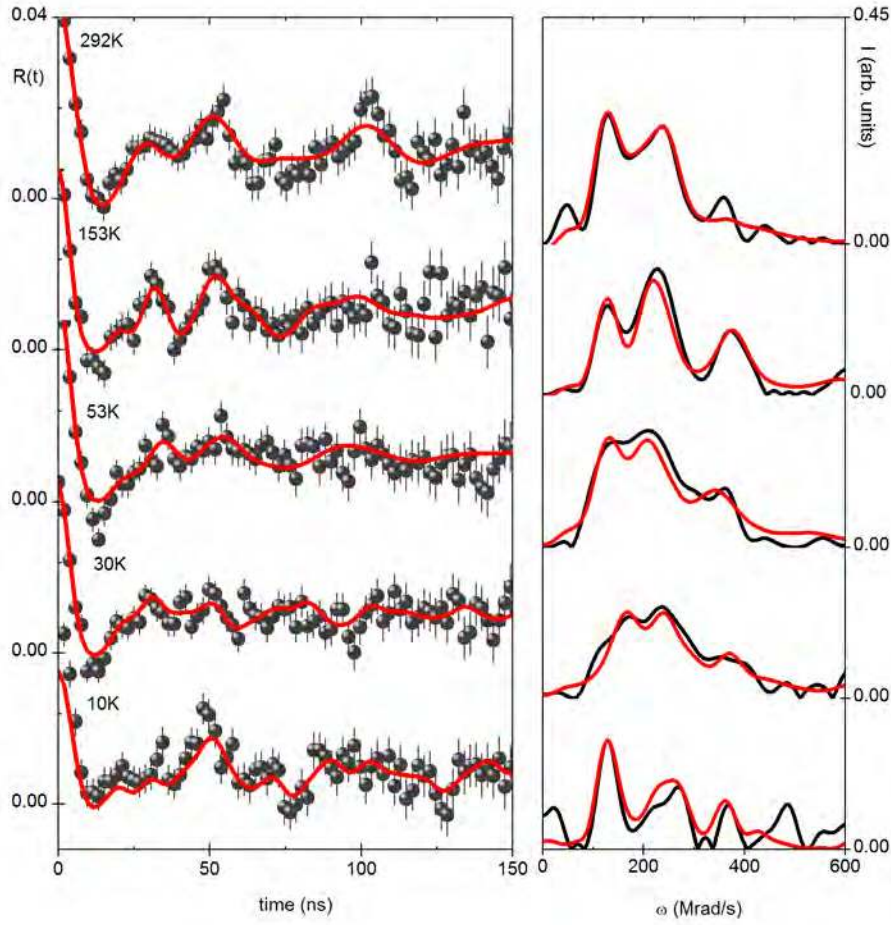


Figure 3.15: (Left) Representative $R(t)$ experimental functions and correspondent fits (thicker lines over the $R(t)$ spectra) measured from 10 K up to 292 K, for ErMnO_3 . (Right) Corresponding Fourier transforms.

Figure 3.16 shows the temperature dependence of the EFG parameters for ErMnO_3 , which are listed in table 3.8. As depicted in figure 3.16(a), the EFG principal component, V_{zz} shows a decrease on its magnitude with increasing temperature for both EFG_1 and EFG_2 following the trend observed in other perovskite systems^[12,181,185,186] and in YMnO_3 . This dependence has been associated to the increase of atomic vibrations and volumic thermal expansion due to the increase of temperature. However, this contribution is very small (in the order of $10^{-5} \text{ K}^{[158]}$) being about one order of magnitude smaller than the variation of V_{zz} with temperature ($\frac{1}{V_{zz}^{01}} \frac{\Delta V_{zz}^{01}}{\Delta T} \sim -9.5 \times 10^{-5} \text{ K}^{-1}$ and $\frac{1}{V_{zz}^{02}} \frac{\Delta V_{zz}^{02}}{\Delta T} \sim -6 \times 10^{-4} \text{ K}^{-1}$).

Concerning the evolution of the asymmetry parameter one observes a weak dependence of η_1 with temperature with small changes in its magnitude within the error bars. However, η_2 shows a

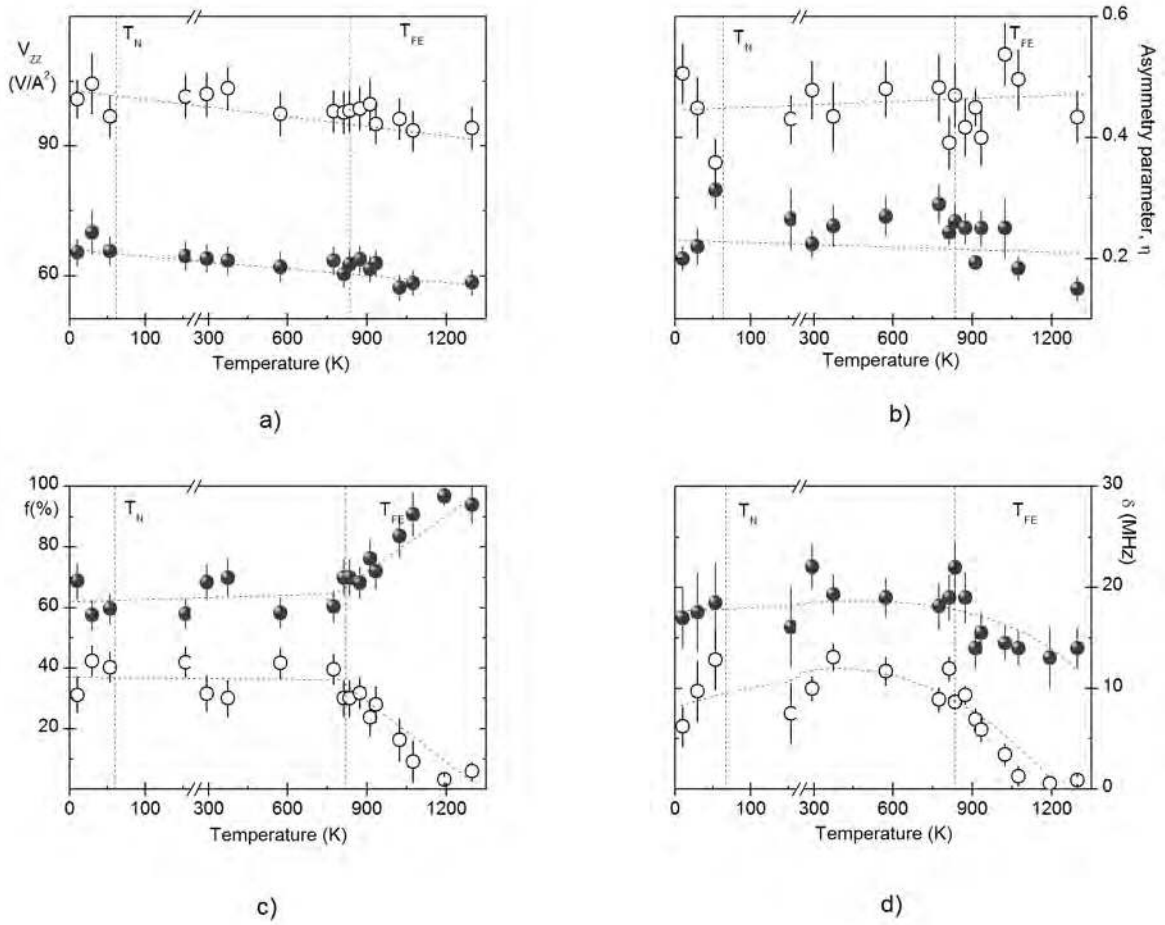


Figure 3.16: EFG parameters evolution with temperature for ErMnO_3 : a) EFG principal component, V_{zz} , b) asymmetry parameter, η , c) fraction of probes interacting with each EFG distribution, f , and d) static attenuation parameter, δ . The vertical dashed lines indicate the ferroelectric (T_{FE}) and magnetic (T_{N}) transition temperatures.

small increase with temperature.

The fractions of probes interacting with each EFG distribution show a dependence on temperature, above the ferroelectric transition. While for low temperatures there is a competition between the two EFG distributions, at high temperatures EFG₁ is the dominant distribution. One shall note that the structural transition is expected to occur at ~ 1310 K^[83], which is accompanied by a crystalline space group change that allows only one non-equivalent rare-earth site. In fact, the observed evolution of f_1 and f_2 is expected, if one assumes the location of the ^{111}Cd probe atoms at the rare-earth site. Nevertheless, the different local transition temperature of ErMnO_3 regarding YMnO_3 shall be attributed to the different ferroelectric ordering temperature range, which occurs

Table 3.8: Electric field gradient parameters for the hexagonal ErMnO₃ sample as a function of temperature.

T(K)	EFG ₁					EFG ₂					B _{hf}
	f ₁	ω ₁	V _{zz1}	η ₁	δ ₁	f ₂	ω ₂	V _{zz2}	η ₂	δ ₂	
	%	Mrads ⁻¹	V/Å ²			%	Mrads ⁻¹	V/Å ²		MHz	
1296	94±6	111±5	58±3	0.15±0.02	14±2	6±37	178±5	94±5	0.43±0.04	1±0.4	-
1073	91±7	110±3	58±3	0.18±0.02	17±3	9±7	177±5	94±5	0.50±0.05	1±0.5	-
1023	84±7	108±3	57±3	0.25±0.05	18±4	16±7	182±5	96±5	0.54±0.05	3±0.7	-
933	72±6	119±3	63±3	0.25±0.03	18±4	28±6	180±5	95±5	0.40±0.05	6±1	-
911	76±6	116±3	62±3	0.19±0.01	16±4	24±6	188±6	100±6	0.45±0.03	7±1	-
873	68±5	121±3	64±3	0.25±0.03	22±2	32±5	187±5	99±5	0.42±0.05	9±1	-
833	70±6	118±3	63±3	0.26±0.03	19±2	30±6	186±5	98±5	0.47±0.05	9±1	-
812	70±6	114±3	60±3	0.24±0.02	19±2	30±6	185±5	98±5	0.39±0.04	12±1	-
773	60±5	120±3	63±3	0.29±0.03	18±2	40±5	186±5	98±5	0.48±0.05	9±1	-
573	58±5	117±4	62±3	0.27±0.03	17±2	42±5	184±5	97±5	0.48±0.05	12±1	-
373	70±6	120±3	64±3	0.25±0.03	22±3	30±6	196±5	103±5	0.44±0.04	13±1	-
292	68±6	121±3	64±3	0.22±0.02	22±4	32±6	193±5	102±5	0.48±0.05	10±1	-
153	58±5	122±3	64±3	0.26±0.05	13±2	42±6	192±5	101±5	0.43±0.04	7±1	-
53	60±5	124±3	66±3	0.31±0.03	15±2	40±5	183±5	97±5	0.36±0.04	13±3	-
30	57±5	155±5	70±5	0.22±0.03	11±2	43±5	198±7	104±7	0.45±0.05	10±2	-
10	69±6	124±3	65±3	0.20±0.05	12±2	31±6	191±7	101±7	0.51±0.05	6±2	1.8±0.9

at lower temperatures for the former compound. Furthermore, the fact that about 90% of the probe atoms interacting with EFG₁ at 1296 K suggests that the structural transition occurs at ~ 1300 K. In fact, extrapolating the linear part of f_1 vs. temperature to 100%, one obtains a structural transition temperature of ~ 1300 K, being this value in agreement with the values reported in the literature^[82,83].

Figure 3.16(d) shows the evolution of the attenuation parameters, δ_1 and δ_2 with temperature. As observed in the R(t) spectra, there is a clear increase of these parameters with decreasing temperature. One shall note a subtle variation of these values up to 833 K, temperature value reported for the ferroelectric transition^[92]. These results suggest that, as expected, the dipole ordering is accompanied by the creation of a random distributed local environment, which orders when decreasing temperature as observed by a stabilization of the attenuation parameters.

3.1.4 EFG calculations in hexagonal RMnO₃

In order to extract maximum information and to fully understand the PAC experimental results, *ab-initio* calculations of the hyperfine parameters in the R1, R2 and Mn sites on the hexagonal lattice and, in a second step, with substitutional Cd in the same sites, have been performed. The relaxation of internal atomic positions has been also implemented to make a more accurate description of the EFG parameters. As described on chapter 2, the first step of these calculations was performed in pure hexagonal compounds using a set of lattice parameters taken from the literature^[42–44,73], to have the best precision on the atomic positions. A second step in the simulations has been performed by allowing the relaxation of the internal atomic positions values, which has been implemented by minimizing the atomic forces to values less than 5 mRy/a.u. The calculated EFG parameters are summarized in table 3.9.

Table 3.9: Augmented plane wave + local orbitals calculated EFG parameters in the rare-earth and manganese sites for the hexagonal RMnO₃. The first set of columns displays the simulations results with the unrelaxed structures while the second one shows the relaxed values.

Compound	EFG unrelaxed structure						EFG relaxed structure					
	(V/Å ²)						(V/Å ²)					
	V _{zz} (R1)	η(R1)	V _{zz} (R2)	η(R2)	V _{zz} (Mn)	η(Mn)	V _{zz} (R1)	η(R1)	V _{zz} (R2)	η(R2)	V _{zz} (Mn)	η(Mn)
LuMnO ₃	-19.4	0	142.5	0	-35.9	0.092	-8.8	0	134.8	0	-31.8	0.050
ErMnO ₃	-37.4	0	96.6	0	-57.1	0.118	-9.5	0	111.6	0	-52.8	0.006
YMnO ₃	5.5	0	96.6	0	-49.2	0.040	10.25	0	65.85	0	-42.82	0.080
HoMnO ₃	-12.5	0	71.1	0	-46.0	0.260	13.20	0	94.00	0	-42.10	0.011

Looking at the V_{zz} of the pure manganites, simulations with unrelaxed structures do not give similar results as with relaxed ones. With respect to the EFG in different rare-earth crystallographic sites, one can observe distinct values being V_{zz}(R1) < V_{zz}(R2). These differences are sufficiently large in order to be differentiated by the PAC measurements. The asymmetry parameters, before and after structural relaxation, are nil in the rare-earth sites as expected by site symmetry considerations in a hexagonal structure (3m(C_{3v}) and 3(C₃) for 2a and 4b sites, respectively). The Mn 4c site has monoclinic point symmetry, m(C_s) with an asymmetry parameter different from zero. Nevertheless, the local bipyramidal environments can be approximated by the trigonal symmetry where η can be approximated to zero, consistent with the calculated values in this

work^[10]. The EFG's dependence on the rare-earth ionic radius shows subtle changes without a specific tendency.

The simulation of the PAC experiments has been performed by inserting Cd atoms into the structure. The radius of the Cd augmented plane wave sphere is the same of the substituted atom. For each EFG calculation per crystallographic site (R1, R2 or Mn), the Cd was included in the structure by substitution at one of the sites in the unit cell, giving the formulas $R_{5/6}Cd_{1/6}MnO_3$ or $RCd_{1/6}Mn_{5/6}O_3$. Looking at the V_{zz} with substitutional Cd, displayed in table 3.10, the differences between the values obtained with unrelaxed and relaxed structures are slightly higher than those found in the pure structures. These differences are more pronounced at the Mn site. This can be understood since the insertion of Cd, with ionic radius about two times larger than the Mn one, can lead to an additional distortion in MnO_5 surroundings. Nevertheless, when comparing the simulated EFGs of pure and Cd substituted relaxed structures, and taking into account the Sternheimer coefficients, one realizes that the resulting values are in good agreement. This correlation suggests that the insertion of a Cd atom does not significantly modify the site local environment. Once again, the asymmetry parameter values are approximately zero.

Table 3.10: APW+lo calculated EFG parameters in the rare-earth and manganese sites with substitutional Cd ($x=1/6$) for the hexagonal $RMnO_3$. The first set of columns refers to the simulations with unrelaxed structures while the second one with relaxed crystalline structures.

Compound	EFG unrelaxed structure ($V/\text{\AA}^2$)						EFG relaxed structure ($V/\text{\AA}^2$)					
	$V_{zz}(R1)$	$\eta(R1)$	$V_{zz}(R2)$	$\eta(R2)$	$V_{zz}(Mn)$	$\eta(Mn)$	$V_{zz}(R1)$	$\eta(R1)$	$V_{zz}(R2)$	$\eta(R2)$	$V_{zz}(Mn)$	$\eta(Mn)$
LuMnO ₃	-10.9	0	44.1	0	-174.7	0.11	3.1	0	65.4	0	-197.7	0.05
ErMnO ₃	1.6	0	36.4	0	-180.1	0.09	10.6	0	55.6	0	-232.6	0.02
YMnO ₃	0.8	0	41.0	0	-186.7	0.06	13.8	0	66.1	0	-239.0	0.06
HoMnO ₃	13.8	0	34.1	0	-171.8	0.01	13.10	0	61.6	0	-211.7	0.02

A simpler and computationally faster way to obtain an electric field gradient estimation is the point charge model (PCM). In this method, the EFG is calculated by taking the ion cores as point charges located at the ions lattice sites, being an approximation for the lattice contribution to the EFG since it considers only its nominal charge. Again, different atoms are differentiated by the Sternheimer coefficient, γ_∞ ^[170,172]. EFG calculations in the compounds under study have been

performed at different positions from the point charge. PCM calculations have been performed with substitutional Cd in the R1, R2 and Mn sites on the hexagonal structure. The lattice parameters have been taken from the literature. In table 3.11, a comparison between the different calculations is presented, where a fair agreement is found between the APW+lo calculated EFG parameters and the PCM ones for all rare-earth and manganese sites.

Table 3.11: Calculated EFG parameters in the rare-earth and manganese sites using the APW+lo and PCM methods for the hexagonal RMnO₃.

Compound	APW+lo (V/Å ²)						PCM (V/Å ²)					
	V _{zz} (R1)	η(R1)	V _{zz} (R2)	η(R2)	V _{zz} (Mn)	η(Mn)	V _{zz} (R1)	η(R1)	V _{zz} (R2)	η(R2)	V _{zz} (Mn)	η(Mn)
LuMnO ₃	3.10	0	65.4	0	-197.7	0.05	11	0	54	0	-290	0.01
ErMnO ₃	10.6	0	55.6	0	-232.6	0.02	15	0	56	0	-220	0.01
YMnO ₃	13.8	0	66.1	0	-239.0	0.06	16	0	51	0	-221	0.02
HoMnO ₃	13.1	0	61.6	0	-211.7	0.02	35	0	47	0	-221	0.20

3.1.5 Discussion

Figure 4.17 shows the evolution of the experimental and simulated EFG results with the rare-earth ionic radius. The EFG parameters are listed in table 3.12. When comparing the calculations in the hexagonal compounds with the experimental results, one can observe that only one of the EFG distributions is in concordance with the calculated values, i.e., EFG₁ can be directly assigned to the R2 (4a site). For this EFG₁, the experimental asymmetry parameters are higher than the calculated (nil values) maybe due to the polycrystalline nature of the ceramic samples.

As referred previously, it would be tempting to assign the two EFG distributions to the different rare-earth crystallographic sites (R(2a site) and R(4b site)), since the site multiplicities (2:1) are comparable to the EFG fractions. Moreover, the Cd atoms have been assigned to the rare-earth site in other manganite systems^[12,181,185,186]. Nevertheless, the simulated results showed that the EFG at R1 site has a small V_{zz} being below the resolution limit of the present PAC experiments and one is not sensitive to it.

Additional information on the behavior of these two EFG distributions has been obtained by the study of the temperature dependence of the EFG parameters this series of compounds. Both

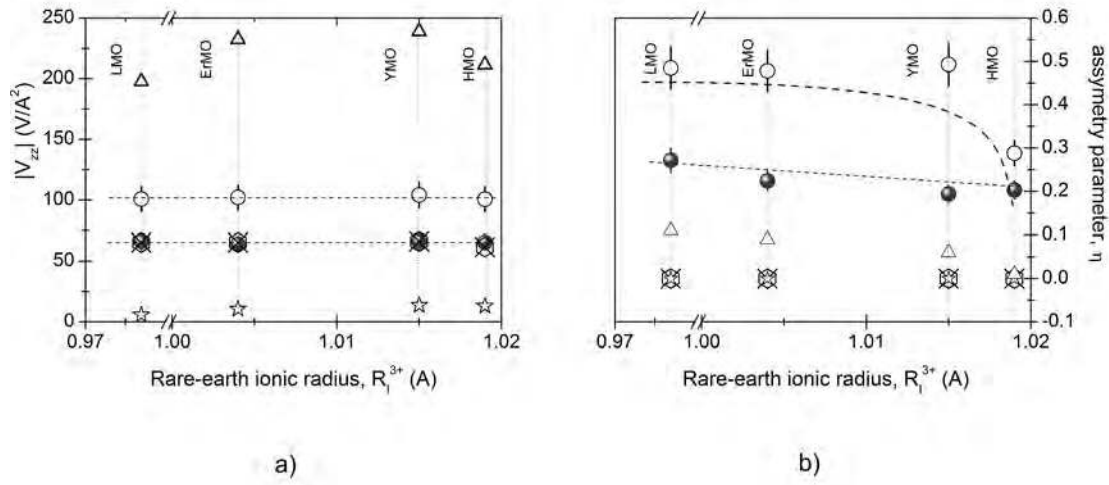


Figure 3.17: EFG parameters evolution with the rare-earth ionic radius: a) EFG principal component, V_{zz} , and b) asymmetry parameter, η , for the experimental EFG₁ (closed dots) and EFG₂ (open dots). The APW calculated EFG parameters for R1 (stars), R2 (hexagons) and Mn (triangles) sites are included for comparison.

EFG distributions show a similar evolution of V_{zz} with a decrease on its magnitude when increasing temperature due to atomic vibrations^[12,186]. The two EFG distributions were found coexisting in up to 1300-1500 K. Furthermore, the evolution of the fractions f_1 and f_2 in ErMnO₃ and YMnO₃ shows that EFG₁, here assigned to the rare-earth R(4a) site, is dominant above the ferroelectric transition and tends to vanish around the structural transition temperature. One shall remind that the existence of only EFG distribution above the structural transition is expected due to the high temperature space group symmetry.

Intriguingly, the experimental EFG₂ cannot be assigned either to regular R(2a) or the manganese sites, which calculated EFG parameters are very distinct from the experimental ones. Moreover, based on the high quality of the samples, the origin of EFG₂ cannot be attributed to impurities. Additionally, the presence of a magnetic hyperfine field suggest that the Cd probe atoms are not located at the Mn sites. The described results hint for the existence of subtle distortions around the R-O polyhedra, which are responsible for the measured EFG₂. Since EFG₁ can be directly assigned to the simulated R1 site, using the macroscopic crystalline structure, EFG₂ could be assigned to a randomly distributed distorted regions in the former matrix.

Table 3.12: Experimental and calculated EFG parameters in the rare-earth and manganese sites with substitutional Cd for the hexagonal RMnO₃.

Sample	Experimental				Calculated APW+lo					
	V _{zz2}	η ₂	V _{zz1}	η ₁	V _{zz} (R1)	η(R1)	V _{zz} (R2)	η(R2)	V _{zz} (Mn)	η(Mn)
LuMnO ₃	100.8	0.48	66.2	0.27	3.10	0	65.4	0	-197.7	0.05
ErMnO ₃	102.1	0.48	64.0	0.22	10.6	0	55.6	0	-232.6	0.02
YMnO ₃	104.2	0.49	66.2	0.19	13.8	0	66.1	0	-239.0	0.06
HoMnO ₃	100.7	0.29	64.5	0.20	13.1	0	61.6	0	-211.7	0.02

3.2 Orthorhombic Rare-Earth Manganites

3.2.1 Structural and magnetic characterization

The polycrystalline samples of the RMnO₃ with the bigger rare-earth elements (R=Nd, Sm, Eu, Gd and Tb) have been synthesized using the urea co-precipitation method. The purity of the samples has been investigated by x-ray diffraction (XRD) in a 2θ range between 20° and 90° at room temperature. The evaluation of the XRD data showed that all samples are single phase and crystallize in the orthorhombic structure with space group *Pbnm*. The corresponding cell parameters and unit cell volumes, as obtained by refinement of the XRD data using the Le Bail method^[127] with the FullProf program^[128], are listed in table 3.13.

Table 3.13: Orthorhombic RMnO₃ structures and cell parameters obtained from XRD pattern matching.

Sample Reference	Crystalline Phase (%Vol.)	Structure/ Space group	<i>a</i> Å	<i>b</i> Å	<i>c</i> Å	V _{unitcell} Å ³
GMO	single phase GdMnO ₃	Orthorhombic/ <i>Pbnm</i>	5.3131(1)	5.8567(1)	7.4279(2)	231.130
EuMO	single phase EuMnO ₃	Orthorhombic/ <i>Pbnm</i>	5.3385(1)	5.8477(1)	7.4516(2)	232.623(6)
SMO	single phase SmMnO ₃	Orthorhombic/ <i>Pbnm</i>	5.3556(4)	5.8166(5)	7.4846(6)	233.156(16)
NMO	single phase NdMnO ₃	Orthorhombic/ <i>Pbnm</i>	5.4102(8)	5.7231(9)	7.5764(11)	234.587(21)

Figure 3.18 shows the evolution of the obtained cell parameters with the rare-earth ionic radius (R_I³⁺) together with a compilation of these values taken from the literature^[44,48-50]. The experimental values obtained in this work follow the expected trend with a decrease on *a* and *c* constants with a decrease on the rare-earth ionic size, while the *b* parameter shows an inverse

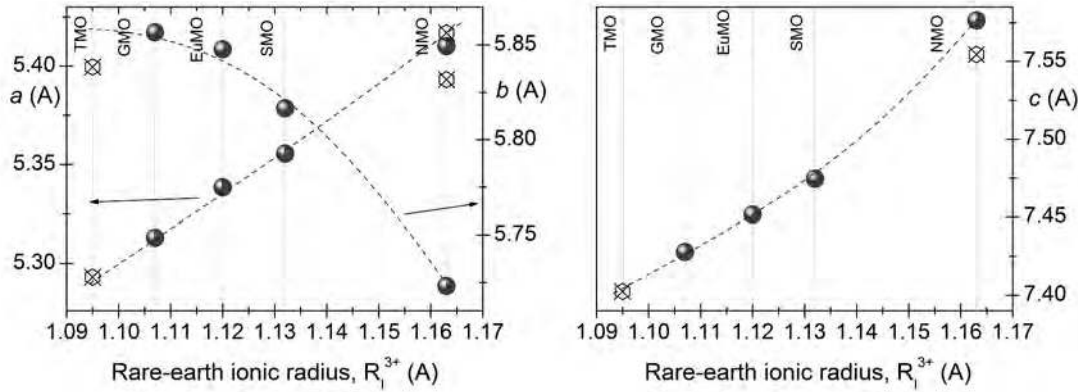


Figure 3.18: RMnO_3 ($R = \text{Tb, Gd, Eu, Sm}$ and Nd) cell parameters as a function of the rare-earth ionic radius (R_1^{3+}). The closed dots represent the values obtained in this work. For comparison cell parameter values for polycrystalline (hexagons) samples taken from the literature are also included^[44,48–50]. Dashed lines are guides to the eye. The ionic radii have been taken from^[47].

evolution. Due to the decrease of the rare-earth ionic radius, the MnO_6 octahedra tilt and buckle to accommodate the ion, known as the GdFeO_3 rotation, causing a decrease on a and c cell parameters. Furthermore, as expected from lanthanide contraction, the unit cell volume is known to decrease with the rare-earth ionic radius (R_1^{3+}).

As a complement to the structural characterization, magnetic susceptibility measurements have been also performed. Figure 3.19 depicts representative susceptibility (χ) curves as well as the reciprocal susceptibility obtained during the field cooling procedure with 98 Oe applied magnetic field in a $10 < T < 380$ K temperature range. Evaluation of the experimental magnetization data allowed determining the Néel (T_N) and the Curie-Weiss (θ_P) temperatures. As common procedure, θ_P was obtained by fitting the high temperature linear dependence of the reciprocal susceptibility with a Curie-Weiss law. A list of the values obtained by the analysis of magnetization data is summarized in table 3.14.

Figure 3.19(a) shows the susceptibility and reciprocal susceptibility curves for TbMnO_3 . This compound exhibits a transition at $T_N \sim 44$ K, which corresponds to an incommensurate sinusoidal antiferromagnetic ordering of the Mn^{3+} spins^[50]. An additional transition at ~ 8 K is also observed in which the Tb spins order. These values is in good agreement with the ones reported in the literature^[50]. The Curie-Weiss fitting of the high temperature linear dependence of the reciprocal

Table 3.14: Néel (T_N) and Curie-Weiss (θ_P) temperatures obtained for the orthorhombic RMnO_3 .

Sample	T_N	θ_P
Reference	(K)	(K)
TMO	44	-40
GMO	41	-40
EuMO	53	-88
SMO	69	-8
NMO	82	-6

susceptibility allowed the determination of θ_P which was found to be around -40 K.

Figure 3.19(b) shows the $\chi(T)$ and $1/\chi(T)$ curves for GdMnO_3 sample. The compound shows an antiferromagnetic ordering of the Mn spins at $T_N \sim 43$ K and a Curie-Weiss temperature θ_P of about -41 K. Both values are in excellent agreement with the temperatures reported in the literature^[187]. One shall note that the magnetic behavior of this compound is dominated by the strong paramagnetism of the Gd^{3+} ions, which might hinder the observation of further anomalies arising from the Mn^{3+} ordering^[187,188].

The magnetic behavior of SmMnO_3 is depicted in figure 3.19(c). The sharp transition at $T_N \sim 68$ K in the $\chi(T)$ curve is consistent with the onset of the A-type antiferromagnetic ordering of the Mn^{3+} ions^[187]. The fitting of the linear part of the $1/\chi$ curve shows a θ_P of ~ 8 K.

The thermal dependence of χ and reciprocal χ of NdMnO_3 is shown in figure 3.19(d). This compound undergoes a paramagnetic to a A-type antiferromagnetic transition at $T_N \sim 82$ K as given by the sharp transition in the $\chi(T)$ curve. Both T_N and θ_P (~ 6 K) were found to be in excellent agreement with the values reported in the literature^[189].

As a final comment, the orthorhombic manganites used in this work follow the trend reported previously showing the high quality of the compounds. All samples were found to be single phase and crystallize in the orthorhombic structure within the $Pbnm$ space group. Concerning the magnetic behavior, the measured $\chi(T)$ curves and respective transition temperatures are in good agreement with the reported in the literature giving consistence to the high quality of the compounds.

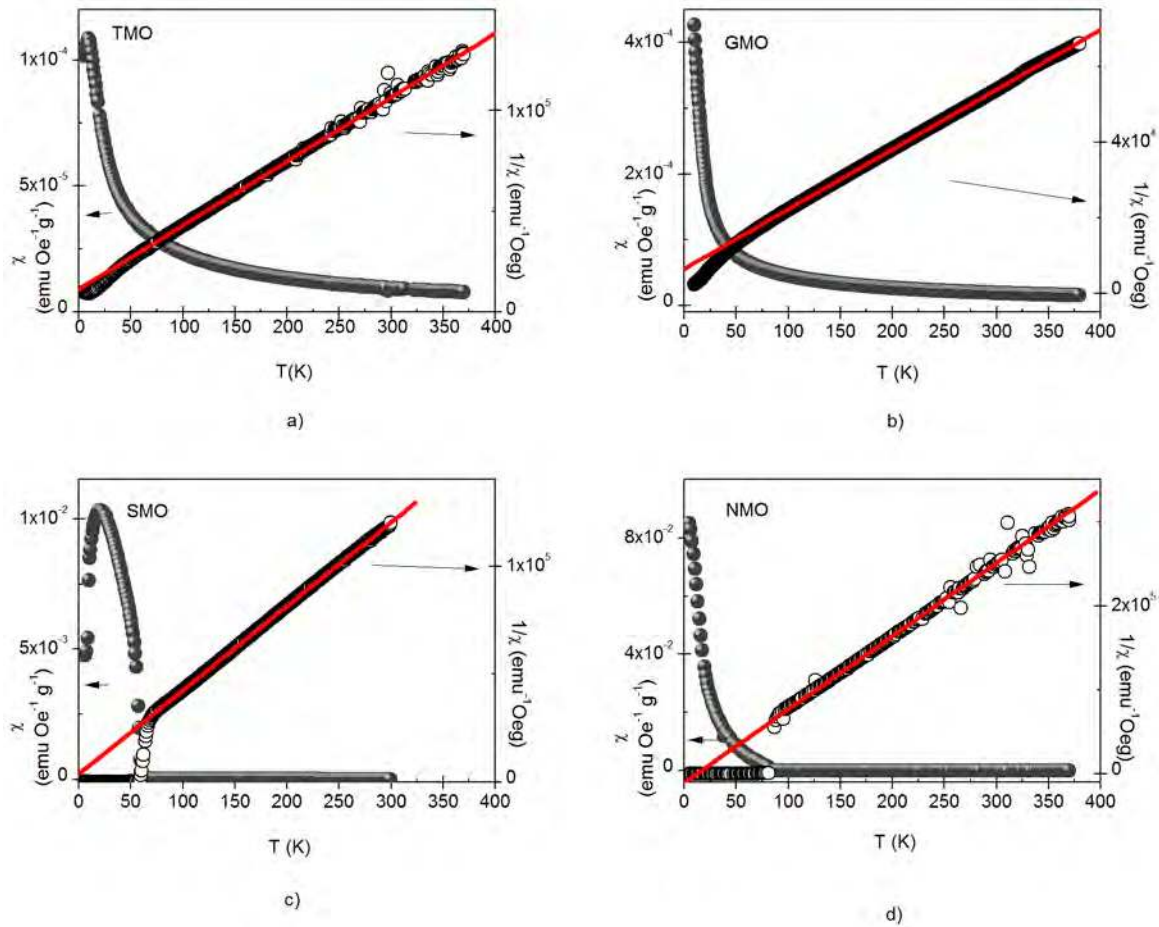


Figure 3.19: Field cooling magnetic susceptibilities as a function of temperature for the samples: a) TMO (TbMnO_3), b) GMO (GdMnO_3), c) SMO (SmMnO_3) and d) NMO (NdMnO_3). Right side scale: reciprocal magnetic susceptibility for the same samples.

3.2.2 EFG dependence on the rare-earth ionic radius

A systematic study of the dependence of the electric field gradients (EFG) on the rare-earth ionic radius was also performed for the orthorhombic series of rare-earth manganites. The experimental results have been correlated with the corresponding crystallographic structures, magnetic data and *ab-initio* calculations. Similarly to the hexagonal RMnO_3 series, the PAC experiments have been performed by implanting the orthorhombic RMnO_3 samples ($R=\text{Tb, Gd, Eu, Sm, and Nd}$) with ^{111}mCd with further annealing to remove implantation damage. In a first step, the experimental $R(t)$ spectra have been taken in a temperature range from 10 K up to 573 K.

PAC results at room temperature

Figure 3.20 shows representative room temperature experimental $R(t)$ spectra and corresponding fourier transforms. The best fit to each spectrum was obtained considering that the ^{111}Cd probes interact with two EFG distributions, which were assumed as Lorentzian-like.

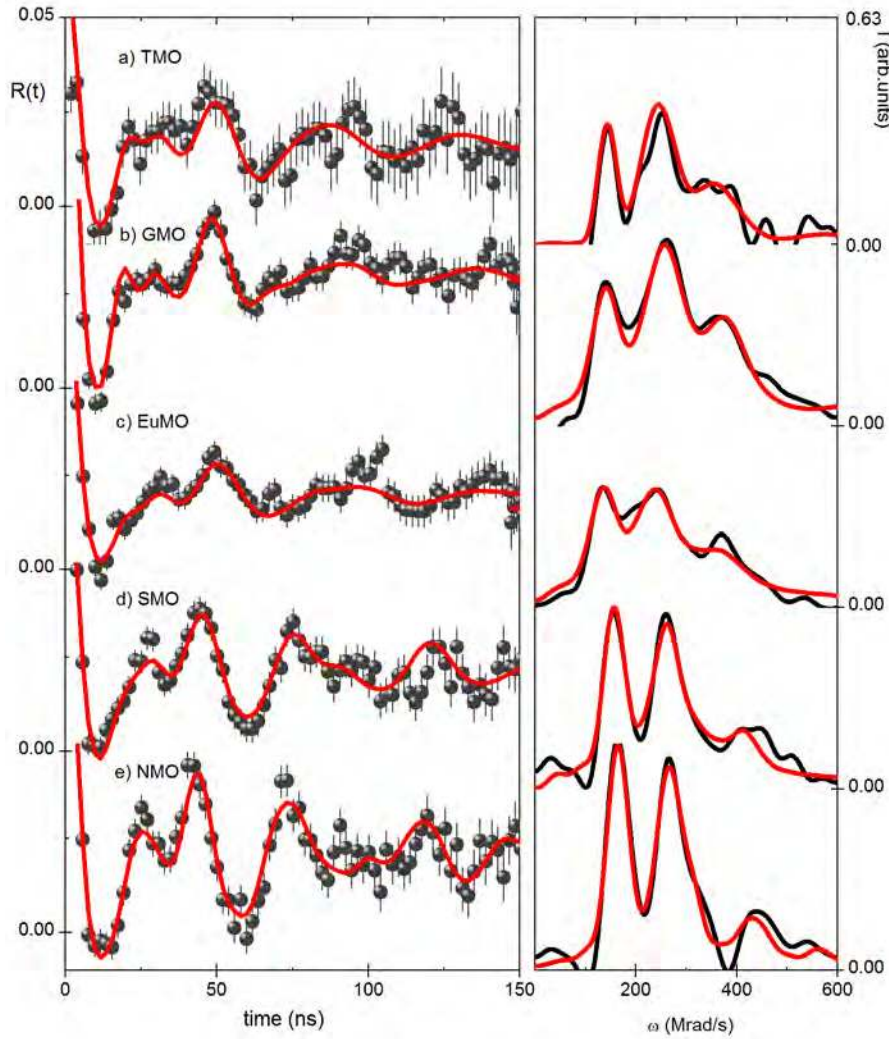


Figure 3.20: (Left) Representative room temperature $R(t)$ experimental functions and correspondent fits (thicker lines over the $R(t)$ spectra) for the orthorhombic RMnO_3 samples: a) TMO (TbMnO_3), b) GMO (GdMnO_3), c) EuMO (EuMnO_3), d) SMO (SmMnO_3) and e) NMO (NdMnO_3). (Right) Corresponding Fourier transforms.

Globally, the $R(t)$ spectra show essentially the same frequency triplets, being characterized by the coexistence of two EFG distributions in all compounds. Due to the similarity in the V_{zz} values, these two EFG distribution have been named EFG_1 and EFG_2 alike the EFG distributions found on the hexagonal RMnO_3 . Nevertheless, a close inspection to the spectra show that although V_{zz}

values are quite similar to the ones obtained for the hexagonal RMnO_3 , these two local environments are highly asymmetric. Here, EFG_1 is characterized by $V_{zz1} \sim 68(3) \text{ V}/\text{\AA}^2$ ($\omega_1 \sim 129(4) \text{ Mrad/s}$) and an asymmetry parameter ranging between 0.3 and 0.5. On the other hand, EFG_2 is described by $V_{zz2} \sim 98(5) \text{ V}/\text{\AA}^2$ ($\omega_2 \sim 185(9) \text{ Mrad/s}$) and η_2 ranging between 0.6 and 0.8. One shall note also a slight increase of the attenuation of the spectra for the smaller rare-earths. A list of the obtained EFG parameters is summarized in table 3.15.

Table 3.15: Electric field gradient parameters for the orthorhombic RMnO_3 samples measured at room temperature. The indexes 1 and 2 refers to the two EFG distributions obtained from the fitting procedure.

Sample Reference	EFG_1					EFG_2				
	f_1	ω_1	V_{zz1}	η_1	δ_1	f_2	ω_2	V_{zz2}	η_2	δ_2
	%	Mrads^{-1}	$\text{V}/\text{\AA}^2$		MHz	%	Mrads^{-1}	$\text{V}/\text{\AA}^2$		MHz
TMO	41	134	71	0.28	11	59	185	98	0.58	9
	± 5	± 7	± 7	± 0.04	± 2	± 5	± 10	± 10	± 0.06	± 1
GMO	41	126	67	0.33	10	59	198	104	0.64	8
	± 5	± 7	± 7	± 0.05	± 2	± 5	± 10	± 10	± 0.06	± 2
EuMO	39	124	66	0.31	8	61	185	98	0.58	11
	± 7	± 7	± 7	± 0.05	± 2	± 7	± 10	± 10	± 0.06	± 2
SMO	65	127	67	0.42	6	35	181	96	0.58	11
	± 5	± 7	± 7	± 0.06	± 1	± 5	± 9	± 9	± 0.06	± 2
NMO	74	133	70	0.48	7	26	173	92	0.80	11
	± 8	± 7	± 7	± 0.07	± 1	± 8	± 9	± 9	± 0.08	± 2

The evolution of the EFG parameters with the rare-earth ionic radius is plotted in figure 3.21. Unlike the hexagonal RMnO_3 , the orthorhombic compounds show a dependence of the EFG parameters with the rare-earth ionic radius. Nonetheless, the principal component of the EFG tensor, V_{zz} , show an indistinct trend for EFG_1 and a small increase on its values for EFG_2 , while varying the rare-earth ionic size.

As mentioned before, both EFG_1 and EFG_2 are characterized by highly asymmetric local environments as given by the high η values observed for all compounds. Moreover, as depicted in figure 3.21(b), the η values for both distributions show a trend to increase with the increase of the rare-earth ionic size.

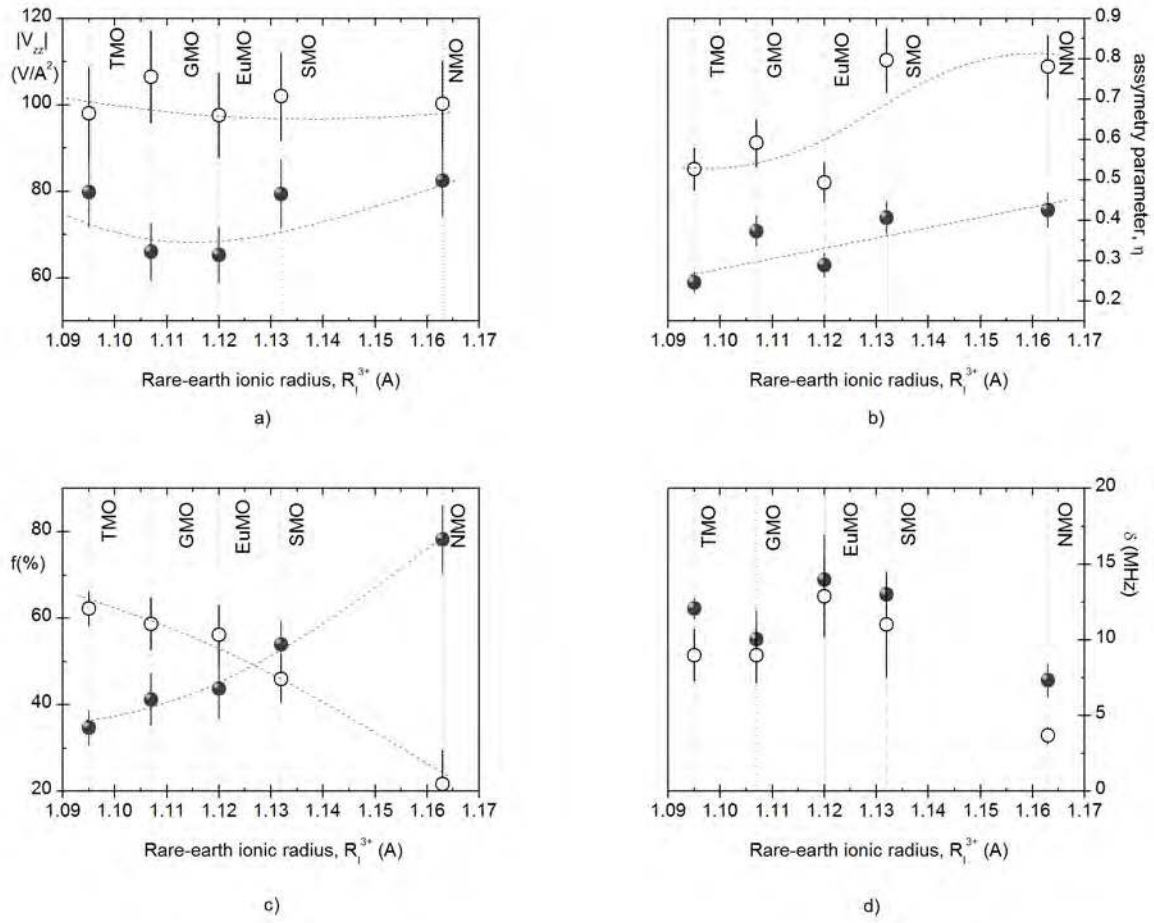


Figure 3.21: Room temperature EFG parameters for the orthorhombic RMnO_3 series: a) EFG principal component, V_{zz} , b) asymmetry parameter, η , c) fractions of probes interacting with each EFG, f , and d) static attenuation parameters, δ , for EFG₁ (closed dots) and EFG₂ (open dots). The vertical lines indicate the ionic radius of each rare-earth element, which has been taken from^[47]. The dashed lines are guides to the eye.

The most interesting trend is the one presented by the fraction of probes interacting with each EFG distribution, as depicted in figure 3.21(c). For the smaller rare-earths, Tb, Gd and Eu, the main fraction of probes was found to be interacting with the highly asymmetric EFG₂ although the two EFG distributions are found to be in competition ($f_1 \sim 40\%$ and $f_2 \sim 60\%$). For this ions, both f_1 and f_2 are almost constant. On the other hand, for the bigger cations (Sm and Nd) EFG₁ is found to be dominant with a small trend to increase for larger ionic sizes.

The attenuation parameters, δ_1 and δ_2 , show a different dependence on the ionic radius. Starting with δ_1 one can observe a very weak dependence with the rare-earth ionic size. On the other hand,

δ_2 shows a small trend to decrease with the increase of the rare-earth ionic size. One shall note also an inversion of the most attenuated EFG distribution coincidental with the inversion on the fraction of probes interacting with each EFG distribution.

Following structural considerations, the existence of two EFG distributions in the orthorhombic RMnO_3 could suggest the location of part of the ^{111}Cd probe atoms in other crystalline sites than the rare-earth ones. In fact, the $Pbnm$ space group allows only one rare-earth site suggesting that one of the experimental EFG distributions is due to the location of the probe atoms in other sites of the structure. The assignment of the second experimental EFG distribution shall be correctly done by performing EFG ab-initio calculations, which will be discussed later on. Additional information shall be given by the study of the EFG evolution at different temperatures, which will be presented in the next subsections.

PAC experimental results at 573 K

At 573 K, the orthorhombic RMnO_3 compounds are paramagnetic and paraelectric, similarly to room temperature. Eventual local changes as function of the rare-earth ionic radius have been studied at this temperature.

Figure 3.22 shows representative $R(t)$ spectra and corresponding Fourier transforms for measurements at 573 K. Again the best fit to each spectrum was obtained considering that the ^{111}Cd probe atoms interact with two EFG distributions. A list of the obtained EFG parameters is presented in table 3.16.

Globally, the $R(t)$ spectra present essentially the same frequency triplets for all rare-earth substitutions. Here EFG_1 is characterized by $V_{zz1} \sim 64(4) \text{ V}/\text{\AA}^2$ ($\omega_1 \sim 120(8) \text{ Mrad/s}$) and η ranging between 0.3 and 0.6. This EFG_1 distribution affects 28-81% of the probe atoms. On the other hand, EFG_2 is characterized by $V_{zz2} \sim 101(11) \text{ V}/\text{\AA}^2$ ($\omega_2 \sim 192(11) \text{ Mrad/s}$) and η_2 varying between 0.4 and 0.6. Alike room temperature, there is a trend to an increase of the attenuation of the $R(t)$ spectra for the smaller rare-earth ions. A close inspection to the Fourier transforms show larger differences than the ones found in the room temperature measurements, which are expected to be seen in the dependence of the EFG parameters with the rare-earth ionic size.

Figure 3.23 depicts the thermal dependence of the EFG parameters as function of the rare-earth ionic radius where one can observe an influence of this parameter on the obtained values.

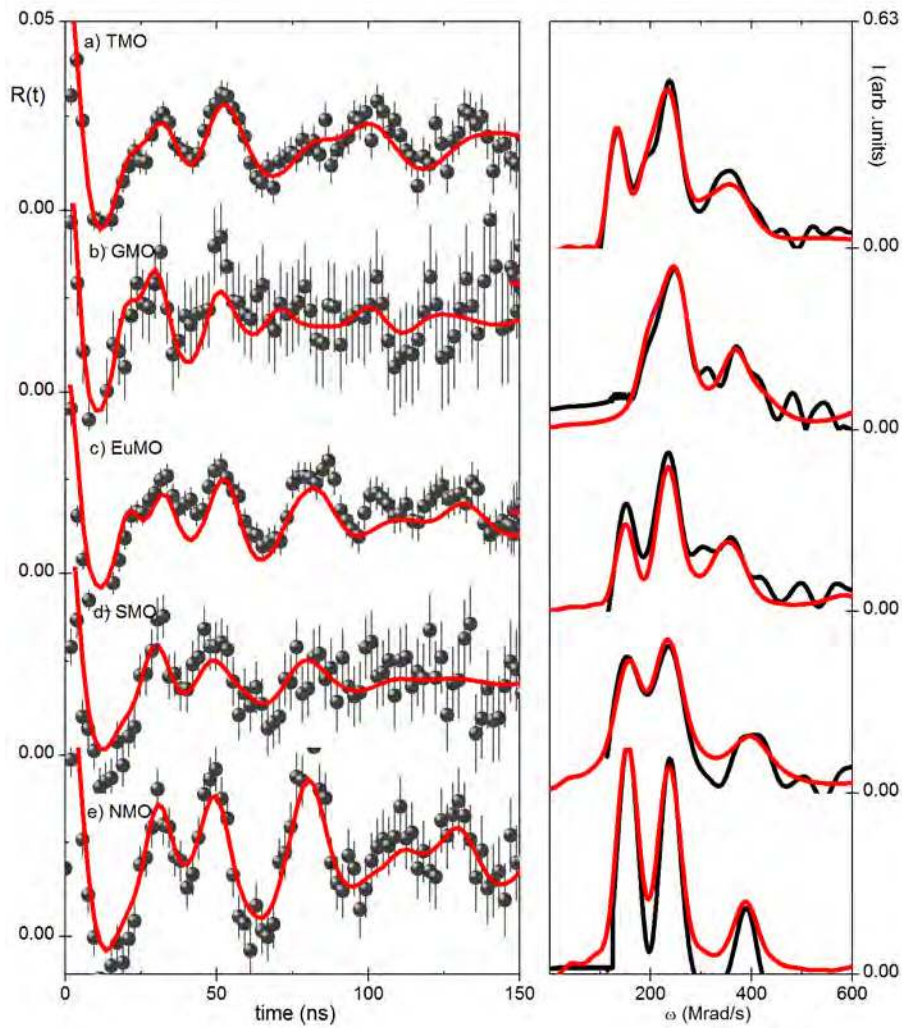


Figure 3.22: (Left) Representative $R(t)$ experimental functions and correspondent fits (represented as thicker lines over the $R(t)$ spectra) measured at 573 K, for the orthorhombic $RMnO_3$ samples: a) TMO ($TbMnO_3$), b) GMO ($GdMnO_3$), c) EuMO ($EuMnO_3$), d) SMO ($SmMnO_3$) and e) NMO ($NdMnO_3$). (Right) Corresponding Fourier transforms.

Nonetheless, the principal component of the EFG, V_{zz} , present a weak dependence on the rare-earth size.

Both EFG_1 and EFG_2 are characterized again by highly asymmetric local environments as given by the high η values observed for all compounds. Moreover, as depicted in figure 3.23(b), the η values for both EFG distributions show an interesting inversion. For the smaller rare-earth ions EFG_2 is found to be the most distorted local environment while for the larger rare-earth ions (Sm and Nd) EFG_1 is now responsible for the higher η values. For the latter compounds, the asymmetry

Table 3.16: Electric field gradient parameters for the orthorhombic RMnO₃ samples measured at 573 K. The indexes 1 and 2 refers to the two EFG distributions obtained from the fitting procedure.

Sample Reference	EFG ₁					EFG ₂				
	f ₁ %	ω ₁ Mrads ⁻¹	V _{zz1} V/Å ²	η ₁	δ ₁ MHz	f ₂ %	ω ₂ Mrads ⁻¹	V _{zz2} V/Å ²	η ₂	δ ₂ MHz
TMO	35	135	80	0.25	12	62	184	98	0.52	9
	±4	±8	±8	±0.03	±3	±4	±11	±11	±0.05	±2
GMO	41	125	66	0.37	10	59	201	106	0.59	9
	±6	±7	±7	±0.04	±2	±6	±11	±11	±0.06	±2
EuMO	44	124	65	0.29	14	56	185	98	0.49	13
	±7	±7	±7	±0.03	±3	±7	±10	±10	±0.05	±3
SMO	54	134	79	0.40	13	46	172	102	0.80	11
	±8	±8	±8	±0.05	±3	±8	±11	±11	±0.08	±3
NMO	78	139	82	0.42	7	22	169	100	0.78	4
	±9	±8	±8	±0.04	±1	±9	±10	±10	±0.08	±1

parameters of both EFG distributions are quite similar.

Concerning the evolution of the fractions of probes interacting with each EFG distribution, at room temperature there is an inversion of the main fraction. EFG₁ is found to be the dominant EFG distribution for the larger rare-earths while EFG₂ is the main EFG distribution for the smaller ions. This evolution is coincidental with the inversion observed in the attenuation parameters (δ₁ and δ₂), where EFG₁ is the most attenuated distribution for Sm and Nd manganites while EFG₂ is found to be the responsible for the attenuation for the smaller ions.

The coexistence of the two EFG distributions at 573 K suggest again the existence of part of the probes that are located mainly in distorted sites. This suggestion is somehow supported by the decrease on η₂ values observed for the biggest rare-earths together with the fact that EFG₂ tends to decrease with temperature.

PAC results at 10 K

At 10 K, all compounds of the orthorhombic RMnO₃ series are ordered antiferromagnetically although the type of ordering is quite different for different compounds. The study of the local

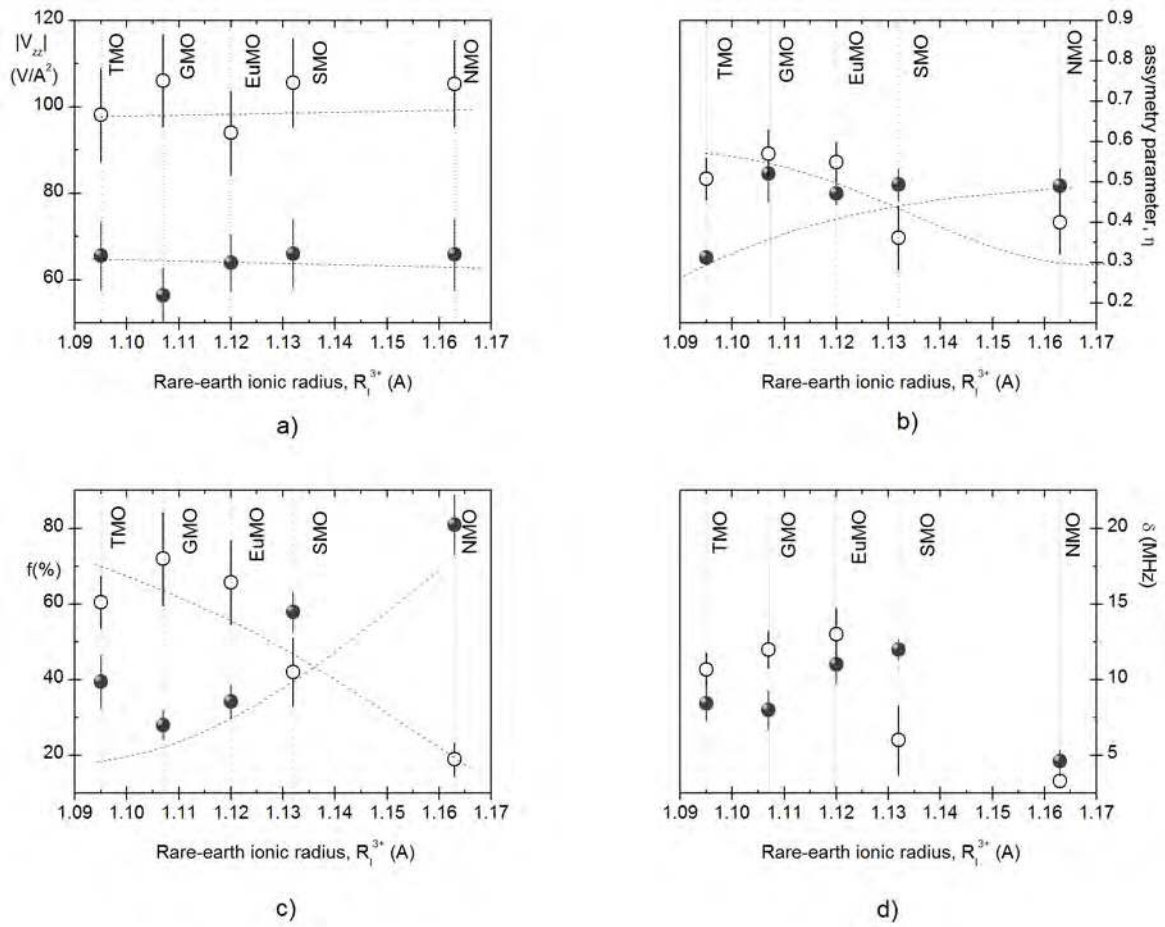


Figure 3.23: EFG parameters obtained at 573 K: a) EFG principal component, V_{zz} , b) asymmetry parameter, η , c) fractions of probes interacting with EFG distribution, f , and d) static attenuation parameter, δ , for EFG₁ (closed dots) and EFG₂ (open dots). The vertical lines indicate the ionic radius of each rare-earth element, which have been taken from^[47]. The dashed lines are guides to the eye.

environment at 10 K has been performed using the same procedure followed for room temperature measurements.

Figure 3.24 show representative $R(t)$ spectra and corresponding Fourier transforms obtained at 10 K, as a function of the different rare-earth substitution. The best fit to each spectrum was obtained, at a first step, considering that the ¹¹¹Cd probe atoms interact with two EFG distributions in a similar manner as proceeded for the room temperature analysis. However, a close inspection to the Fourier transforms suggest the presence of a magnetic hyperfine field (MHF).

Several fitting models have been applied considering the presence of a magnetic hyperfine

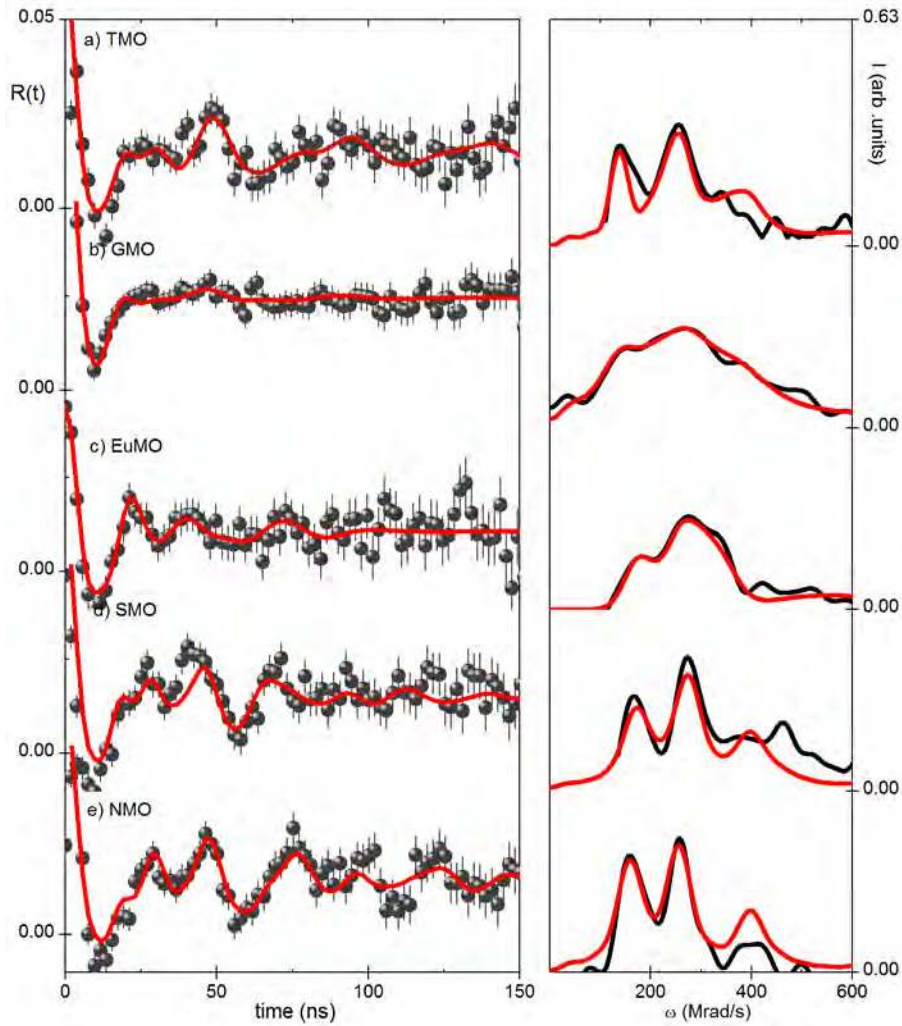


Figure 3.24: (Left) Representative $R(t)$ experimental functions and correspondent fits (thicker lines over the $R(t)$ spectra) measured at 10 K, for the orthorhombic RMnO_3 samples: a) TMO (TbMnO_3), b) GMO (GdMnO_3), c) EuMO (EuMnO_3), d) SMO (SmMnO_3) and e) NMO (NdMnO_3). (Right) Corresponding Fourier transforms.

field. The first model accounted for the coexistence of two pure quadrupolar (electric) EFG distributions. As expected from the shape of the Fourier transforms, this model was not sufficient to fully characterize the spectra. A second model assumed the coexistence of two combined interactions, considering the coexistence of $\text{EFG}_1 + \text{MHF}_1$ and $\text{EFG}_2 + \text{MHF}_2$. Once again, the resulting parameters showed that only of the distributions presented a quantifiable MHF. Therefore, the subsequent models considered that only one local environment would be in the presence of a MHF. In detail, the presence of a MHF has been accounted either in the first local environment (combined with EFG_1) or in the second one (combined with EFG_2). The best fits have been

obtained by using a combined EFG₂+MHF₂ in coexistence with a pure quadrupolar EFG₁ distribution, alike the procedure used in the analysis of the hexagonal RMnO₃. One shall note that the presence of combined interactions adds additional attenuation to the R(t) spectra, as observed in figure 3.24, limiting the accuracy of the EFG/MHF parameters determination.

All compounds show the presence of a MHF which intensity has been found to be quite similar in all orthorhombic RMnO₃ series, as listed in table 3.17. EFG₁ is characterized by an asymmetric local environment ($\eta_1 \sim 0.4$) with $V_{zz1} \sim 72(6)$ V/Å² ($\omega_1 \sim 136(11)$ Mrad/s). The second distribution is given by a combined electric and magnetic interaction EFG₂+MHF₂. EFG₂ is now characterized by $V_{zz2} \sim 109(8)$ V/Å² ($\omega_2 \sim 203(16)$ Mrad/s) and η_2 ranging between 0.45-0.6. With the exception of GdMnO₃, all compounds exhibit a very weak MHF ($B_{hf} \sim 0.3(1)$ T). The major local environment for GdMnO₃ (EFG₂+MHF₂) shows the presence of a magnetic hyperfine field of the order of 3 T.

Table 3.17: Electric field gradient parameters for the orthorhombic RMnO₃ samples measured at 10 K. The indexes 1 and 2 refers to the two EFG distributions obtained from the fitting procedure.

Sample Reference	EFG ₁					EFG ₂ +MHF ₂					
	f ₁	ω_1	V_{zz1}	η_1	δ_1	f ₂	ω_2	V_{zz2}	η_2	δ_2	B _{hf}
	%	Mrads ⁻¹	V/Å ²		MHz	%	Mrads ⁻¹	V/Å ²		MHz	T
TMO	44	128	68	0.43	14	56	187	99	0.55	16	0.1
	±7	±8	±8	±0.02	±1	±7	±11	±11	±0.05	±2	±0.1
GMO	38	124	66	0.37	12	62	220	120	0.50	13	3
	±4	±6	±6	±0.04	±2	±4	±11	±11	±0.06	±2	±0.8
EuMO	40	150	79	0.40	10	60	185	104	0.60	13	0.4
	±4	±7	±7	±0.04	±2	±4	±10	±10	±0.05	±3	±0.2
SMO	54	146	77	0.42	14	46	211	112	0.55	7	0.4
	±5	±8	±8	±0.04	±2	±5	±10	±10	±0.08	±2	±0.1
NMO	68	133	70	0.43	12	32	211	111	0.47	4	0.4
	±8	±8	±8	±0.04	±2	±8	±10	±10	±0.08	±1	±0.1

Figure 3.25 shows the thermal dependence of the EFG parameters with the rare-earth ionic radius. The main component of the EFG tensor, V_{zz} shows an indistinct trend with rare-earth ionic size, in a similar manner as observed for other temperatures. Both EFG distributions have been found to be non axially symmetric has given by the high η values. Moreover, there is a weak

dependence of these values with the ionic size of the rare-earths.

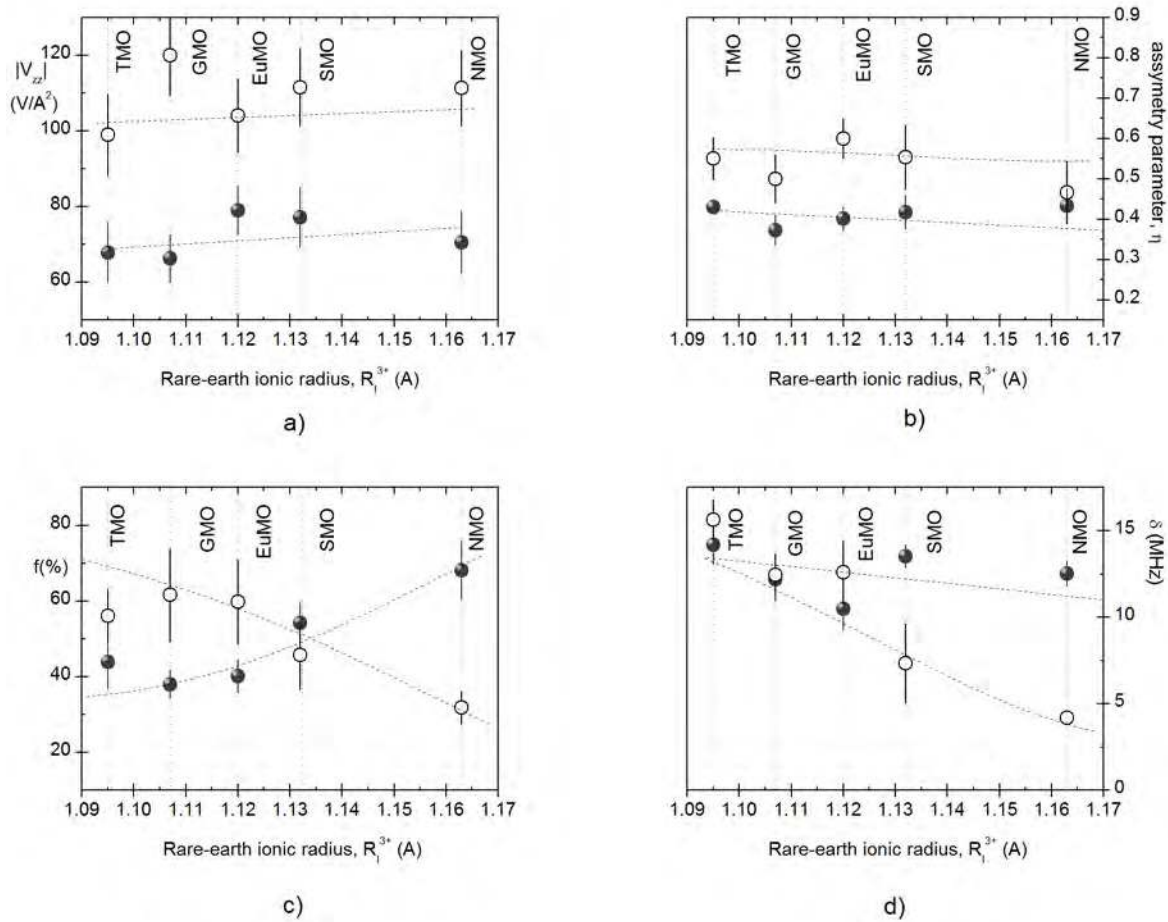


Figure 3.25: EFG parameters obtained at 10 K: a) EFG principal component, V_{zz} , b) asymmetry parameter, η , c) fractions of probes interacting with EFG distribution, f , and d) static attenuation parameter, δ , for EF G_1 (closed dots) and EF G_2 (open dots). The vertical lines indicate the ionic radius of each rare-earth element, which have been taken from^[47]. The dashed lines are guides to the eye.

Again the fractions of probes interacting with each EFG distribution show the same evolution observed for higher temperatures with an inversion of the main EFG distribution characterizing the compounds. EF G_1 is found again to be the dominant local environment for the bigger rare-earths. Unlike the previous results, the attenuation parameters show a different evolution. Here, δ_1 is almost independent of the rare-earth substitution. On the other hand, δ_2 decreases strongly with the increase of the rare-earth ionic size.

3.2.3 EFG dependence on temperature

A representative sample of the orthorhombic RMnO_3 series, EuMnO_3 , has been selected to study in detail the temperature dependence of the EFG parameters and eventually the existence of magnetic hyperfine fields. The data obtained with ^{111}Cd has been complemented with ^{111}In . The samples have been annealed at 973 K in air. The $R(t)$ spectra have been measured after annealing in a temperature interval between 10 K and 1100 K. The PAC results will be presented separately for each sample in the following subsections.

EuMnO_3 : EFG dependence on temperature

EuMnO_3 crystallizes in the orthorhombic structure in the $Pbnm$ space group without any structural changes with temperature. In addition, the $Pbnm$ allows one non-equivalent Eu site. This compound is reported to be non magnetoelectric^[65,114,188,190]. At room temperature, EuMnO_3 is paraelectric and paramagnetic. Lowering temperature, the compound undergoes a phase transition to an incommensurate antiferromagnetic phase (ICAFM) at ~ 50 K with a modulation wave vector directed along the b axis^[65,190], which corresponds to a collinear arrangement of competing exchange interactions between successive neighbor spins leading to a frustrated magnetic system. Another magnetic transition, into an A-type antiferromagnetic order at $T_1 \sim 43$ K, is reported^[65,114].

Figures 3.26 and 3.27 shows representative experimental $R(t)$ functions and respective Fourier transforms, for measurements performed at different temperatures from 10 K up to 973 K. Similarly to the procedure applied for fitting room temperature results, the fit to each experimental spectrum was obtained considering that the probe atoms interact with two EFG distributions, which were assumed as Lorentzian-like.

Figure 3.26 displays the $R(t)$ spectra obtained for measurements performed from room temperature up to 968 K. The plots show essentially the same frequency triplets in all temperature range with the best fit being given by the interaction of ^{111}Cd probe atoms with two EFG distributions. Similarly to room temperature results, described previously, a major EFG_2 was found affecting $\sim 57\text{-}70\%$ of the probes being characterized by $V_{zz2} \sim 87(11) \text{ V}/\text{\AA}^2$ ($\omega_2 \sim 165(10) \text{ Mrad/s}$) and η_2 ranging between 0.6 and 0.7. The minor EFG distribution, EFG_1 , is characterized by a lower $V_{zz1} (\sim 64(2) \text{ V}/\text{\AA}^2)$ and $\eta_1 \sim 0.4$. EFG_1 affect about 30-43% of the probe atoms.

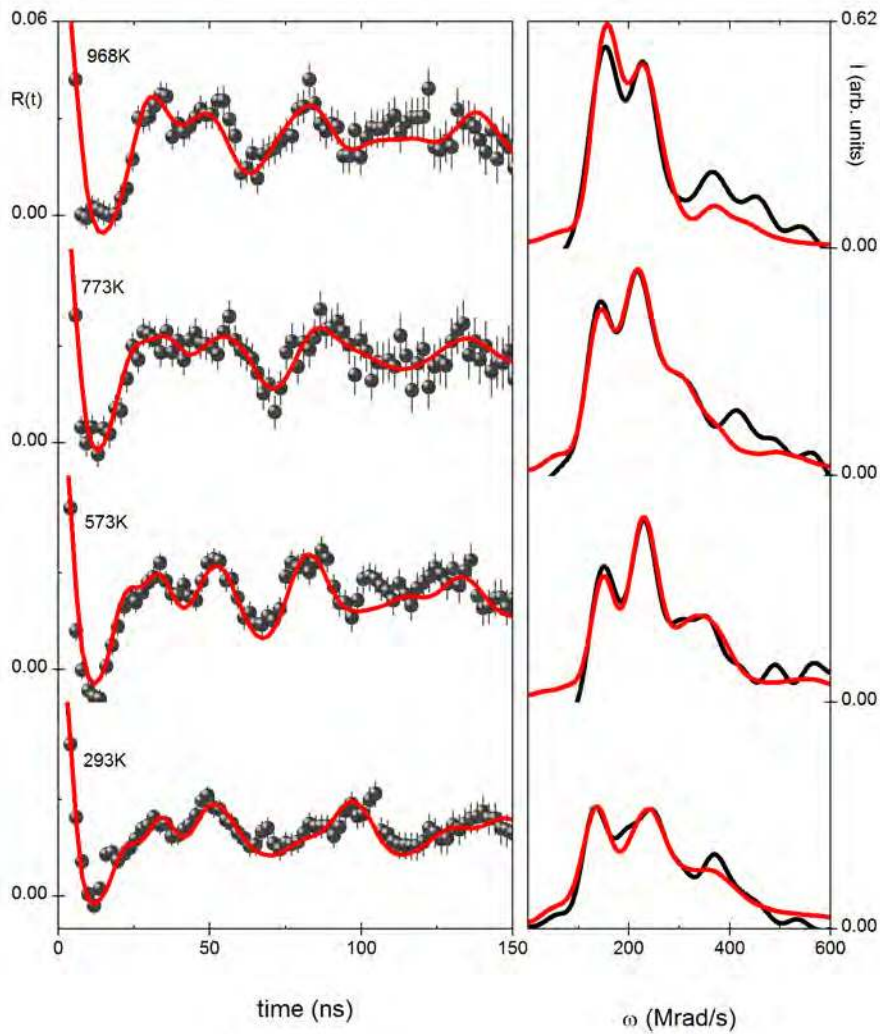


Figure 3.26: (Left) Representative $R(t)$ experimental functions and correspondent fits (thicker lines over the $R(t)$ spectra) for EuMnO_3 measured from room temperature up to 968 K. (Right) Corresponding Fourier transforms.

Figure 3.27 displays the $R(t)$ spectra obtained for measurements performed at low temperatures, below room temperature. Once again the spectra are characterized by the coexistence of two EFG distributions, alike the high temperature spectra. One shall note that there is an increase of the attenuation of the spectra while lowering temperature. Also, a close inspection to the Fourier transforms suggests the presence of a magnetic hyperfine field at 12 and 10 K. As described previously, a MHF has been included in the fitting procedure in the measurements at 12 and 10 K, in a combined quadrupolar and magnetic interaction ($\text{EFG}_2 + \text{MHF}_2$) resulting in a very weak MHF ($B_{\text{hf}} \sim 0.4$ T).

Figure 3.28 shows the thermal dependence of the EFG parameters with temperature for

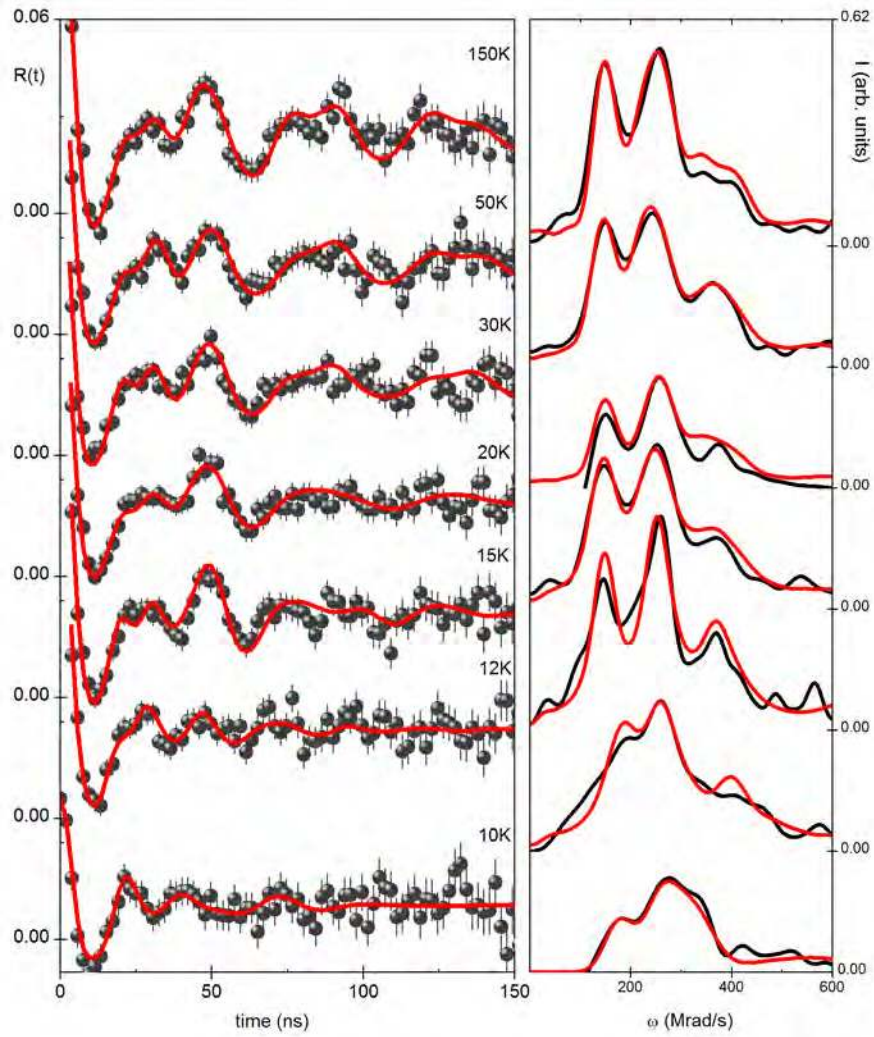


Figure 3.27: (Left) Representative $R(t)$ experimental functions and correspondent fits (thicker lines over the $R(t)$ spectra) for EuMnO_3 measured from 10 K up to 292 K. (Right) Corresponding Fourier transforms.

EuMnO_3 . The resulting EFG parameters are listed in table 3.18. Globally, one can observe a dependence of some EFG parameters with temperature. Starting with V_{zz} , one can see that the magnitude of both EFG principal components are quite distinct and clearly decrease when increasing temperature. This feature has been observed also for the hexagonal YMnO_3 and ErMnO_3 being associated to the increase of atomic vibrations. In order to see the contribution of the atomic vibrations, the V_{zz} variation with temperature has been calculated giving the values $\frac{1}{V_{zz}^{01}} \frac{\Delta V_{zz}^{01}}{\Delta T} \sim -6.63 \times 10^{-4}$ and $\frac{1}{V_{zz}^{02}} \frac{\Delta V_{zz}^{02}}{\Delta T} \sim -8.68 \times 10^{-4}$, which are one order of magnitude higher than the thermal volumic expansion ($\sim 10^{-5} \text{ K}^{-1}$).

Looking at the asymmetry parameters, two different dependencies have been found. While η_2

Table 3.18: Electric field gradient parameters for the orthorhombic EuMnO_3 sample as a function of temperature.

T(K)	EFG ₁					EFG ₂					B _{hf}
	f ₁	ω ₁	V _{zz1}	η ₁	δ ₁	f ₂	ω ₂	V _{zz2}	η ₂	δ ₂	
	%	Mrads ⁻¹	V/Å ²			%	Mrads ⁻¹	V/Å ²		MHz	
968	30±3	121±4	64±4	0.49±0.03	9±2	70±3	136±5	72±5	0.70±0.03	13±2	-
773	37±4	119±4	63±4	0.42±0.03	6±1	63±4	158±6	83±6	0.55±0.03	13±2	-
573	42±4	122±4	64±4	0.48±0.04	11±2	58±4	179±6	95±6	0.54±0.05	15±3	-
153	43±4	134±5	70±5	0.31±0.02	5±1	57±4	180±7	95±7	0.52±0.03	13±2	-
53	35±4	132±5	70±5	0.29±0.02	6±1	65±4	184±7	97±7	0.46±0.05	12±2	-
30	31±3	135±5	72±5	0.25±0.02	6±2	69±3	188±7	100±7	0.50±0.05	12±2	-
20	29±3	129±5	68±5	0.29±0.02	8±2	71±5	188±7	100±7	0.43±0.04	12±1	-
15	47±5	132±5	70±5	0.33±0.03	9±2	53±5	194±7	103±7	0.55±0.05	14±3	-
12	33±4	149±5	79±5	0.48±0.03	7±2	67±4	209±8	110±9	0.48±0.05	17±3	0.4±0.1
10	40±3	150±6	79±6	0.40±0.03	10±3	40±3	185±5	104±10	0.60±0.05	13±3	0.4±0.2

is almost temperature independent, η_1 increases with temperature reaching its maximum in values close to the ones characterizing EFG₂.

Both fractions of probes interacting with each EFG distribution and attenuation parameters show a dependence with temperature. Both parameters show an increase when decreasing temperature. This feature might be related with a local perturbation due the presence of magnetic hyperfine fields at low temperatures.

3.2.4 EFG calculations in orthorhombic RMnO_3

As referred previously, the coexistence of two EFG distributions in the orthorhombic RMnO_3 cannot be fully explained by the crystalline structure. Looking forward to extract maximum information and to fully understand the PAC experimental results, *ab-initio* calculations of the hyperfine parameters in the rare-earth and manganese sites in the orthorhombic lattice have been performed. In a first step, the calculations have been performed in pure orthorhombic compounds using a set of lattice parameters taken from the literature^[44,48,49], to have the best precision on the atomic positions. The relaxation of the internal atomic position values has been also implemented by

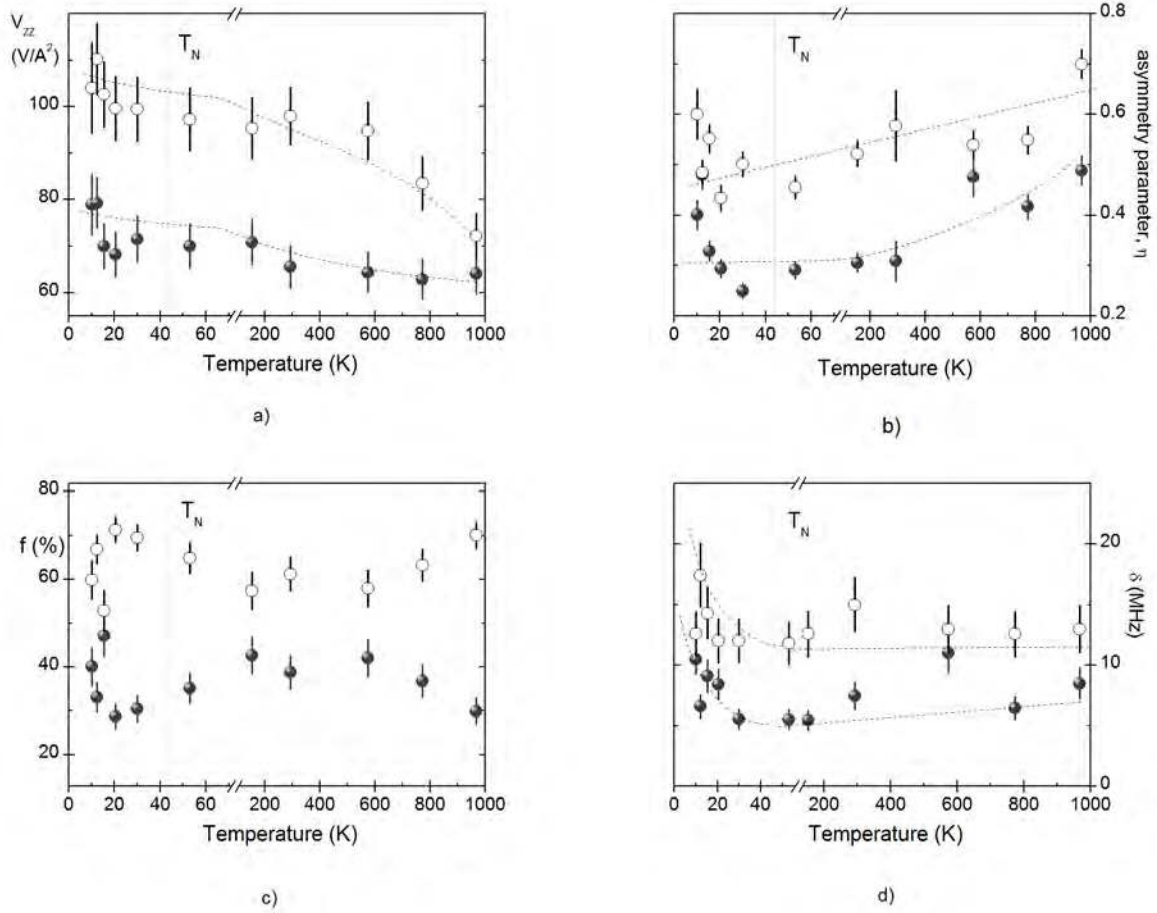


Figure 3.28: EFG parameters as a function of temperature for EuMnO₃: a) EFG principal component, V_{zz} , b) asymmetry parameter, η , c) fractions of probes interacting with each EFG, f , and d) static attenuation parameter, δ , for EFG₁ (closed dots) and EFG₂ (open dots). The vertical lines indicate the magnetic transition temperature, T_N . The dashed lines are guides to the eye.

minimizing the atomic forces to values less than 5 mRy/a.u. The calculated parameters are listed in table 3.19.

Looking at the V_{zz} of the pure manganites, simulations with unrelaxed structures do not give similar results to the relaxed ones. With respect with the values obtained at the rare-earth and manganese sites, one can observe that these values are quite distinct being the difference large enough to be differentiated by the PAC measurements. One shall note that V_{zz} at the rare-earth site has negative signal contrarily to the observed in the hexagonal compounds. Also the asymmetry parameters are different from zero in both sites.

Table 3.19: APW+lo calculated EFG parameters in the rare-earth and manganese sites for GdMnO₃ and EuMnO₃. The first set of columns displays the simulations results with the unrelaxed structures while the second one shows the relaxed values.

Compound	EFG unrelaxed structure				EFG relaxed structure			
	(V/Å ²)				(V/Å ²)			
	V _{zz} (R)	η(R)	V _{zz} (Mn)	η(Mn)	V _{zz} (R)	η(R)	V _{zz} (Mn)	η(Mn)
GdMnO ₃	-53.4	0.30	20	0.50	-53.5	0.33	18.4	0.48
EuMnO ₃	-57.9	0.40	96.6	0.60	-56.5	0.57	49.2	0.58

The simulation of the PAC experiments has been performed by inserting Cd atoms into the orthorhombic structure. The radius of the Cd augmented plane wave sphere is the same of the substituted atom. For each calculation per crystallographic site (rare-earth and manganese), the Cd was included by substitution at one of the sites of the unit cell giving the formulas R_{3/4}Cd_{1/4}MnO₃ or RCd_{1/4}Mn_{3/4}O₃. The resulting EFG parameters are listed in table 3.20.

Table 3.20: Calculated EFG parameters in the rare-earth and manganese sites with substitutional Cd (x=1/4) using APW+lo for GdMnO₃ and EuMnO₃. The first set of columns refers to the simulations with unrelaxed structures while the second one with relaxed crystalline structures.

Compound	EFG unrelaxed structure				EFG relaxed structure			
	(V/Å ²)				(V/Å ²)			
	V _{zz} (R)	η(R)	V _{zz} (Mn)	η(Mn)	V _{zz} (R)	η(R)	V _{zz} (Mn)	η(Mn)
GdMnO ₃	-30.4	0.10	10.2	0.30	-32.5	0.12	21.1	0.42
EuMnO ₃	-20.4	0.40	10.1	0.30	-37.9	0.42	23.2	0.56

Looking at the calculated EFG parameters after the insertion of the Cd atoms one can observe small differences between unrelaxed and relaxed structures. These differences are more pronounced at the manganese site. This result could be attributed to the fact that the insertion of Cd, with ionic radius about two times larger than the Mn one, could lead to additional distortion in the MnO₆ surroundings. Nonetheless, when comparing the simulated EFG parameters of the pure and Cd substituted one, and taking into account the Sternheimer coefficients^[171,172], it is possible to observe differences in the V_{zz} values. These are more pronounced at the manganese site, which can be again explained by the differences in the Cd and Mn ionic radius.

Point charge model (PCM) calculations have been also performed to give another estimate of

the EFG gradients at the rare-earth and manganese sites. Here the EFG was calculated with substitutional Cd in the rare-earth and Mn sites on the orthorhombic structure. The lattice parameters have been taken from the literature^[44,48,49]. A comparison between the different PCM and APW calculations is presented in table 3.21. A good matching between the calculated EFG parameters is found at the rare-earth site. However, at the manganese sites there are big discrepancies, which could be explained by the additional distortion created by the insertion of the Cd atom at the manganese sites.

Table 3.21: Calculated EFG parameters in the rare-earth and manganese sites using APW+lo and PCM methods for GdMnO₃ and EuMnO₃.

Compound	APW				PCM			
	(V/Å ²)				(V/Å ²)			
	V _{zz} (R)	η(R)	V _{zz} (Mn)	η(Mn)	V _{zz} (R)	η(R)	V _{zz} (Mn)	η(Mn)
GdMnO ₃	-32.5	0.12	21.1	0.42	-26.0	0.11	164	0.47
EuMnO ₃	-37.9	0.42	23.2	0.56	-29.0	0.35	169	0.44

3.2.5 Discussion

Figure 3.29 depicts the evolution of the experimental and simulated EFG results with the rare-earth ionic radius for the orthorhombic RMnO₃ series. The same EFG parameters are listed in table 3.22.

Table 3.22: Experimental and APW calculated EFG parameters in the rare-earth and manganese sites with substitutional Cd, for GdMnO₃ and EuMnO₃.

Sample	Experimental				Calculated APW			
	V _{zz} (R)	η(R)	V _{zz} (Mn)	η(Mn)	V _{zz} (R)	η(R)	V _{zz} (Mn)	η(Mn)
GdMnO ₃	64	0.37	106	0.59	-32.5	0.12	21.1	0.42
EuMnO ₃	65	0.29	98	0.49	-37.9	0.42	23.2	0.56

When comparing the calculations in the orthorhombic compounds with experimental results, one can observe that the V_{zz} values are in a fair agreement for one of the experimental distributions, i.e. EFG₁ can be directly assigned to the rare-earth sites. The η values are not coincident, with differences that can be attributed to defects and to the polycrystalline nature of the ceramic samples.

As referred previously, following structural considerations the existence of two experimental EFG

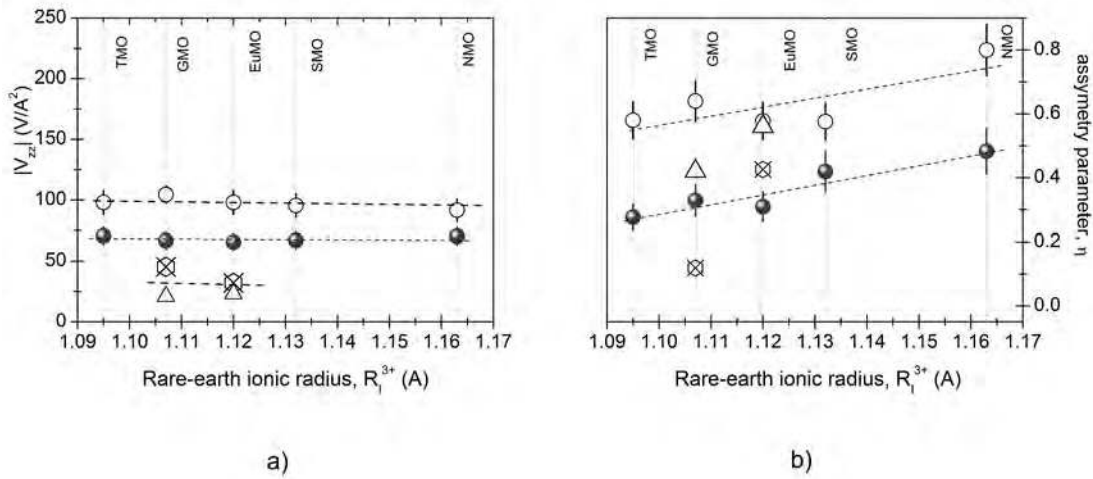


Figure 3.29: EFG parameters evolution with the rare-earth ionic radius at room temperature: a) EFG principal component, V_{zz} , and b) asymmetry parameter, η , for the experimental EFG₁ (closed dots) and EFG₂ (open dots). The APW calculated EFG parameters for the rare-earth (hexagons) and manganese (triangles) sites are included for comparison. The dashed lines are guides to the eye.

distributions in the orthorhombic samples suggest that part of the probe atoms are sitting in other sites of the structure than the rare-earth ones. However, as one can see from the comparison between calculated and experimental EFGs, the second distribution cannot be assigned to the manganese sites, where the differences in the V_{zz} values are very large. Also the fact that the major fraction of probes in the small orthorhombic compounds cannot be assigned to the regular rare-earth sites suggest the existence of distorted rare-earth sites. Moreover, the present results show that the crystalline structure as described by diffraction techniques is not enough to fully explain the origin of two local environments.

The EFG study across the series of orthorhombic and hexagonal manganites show the coexistence, at room temperature, of the two local environments for all compounds. Figure 3.30 shows the dependence of V_{zz} and η for the full series of hexagonal and orthorhombic compounds. For comparison, EFG experimental results for PrMnO_3 and CaMnO_3 ^[158] have been also included.

While for the orthorhombic ones there is a strong dependence of the EFG parameters with the rare-earth ionic radius, for the hexagonal compounds this dependence is very small. In these hexagonal compounds, one could assign the two EFG distributions to the different rare-earth crystallographic sites (R(2a site) and R(4b site)), since the site multiplicities (2:1) are comparable

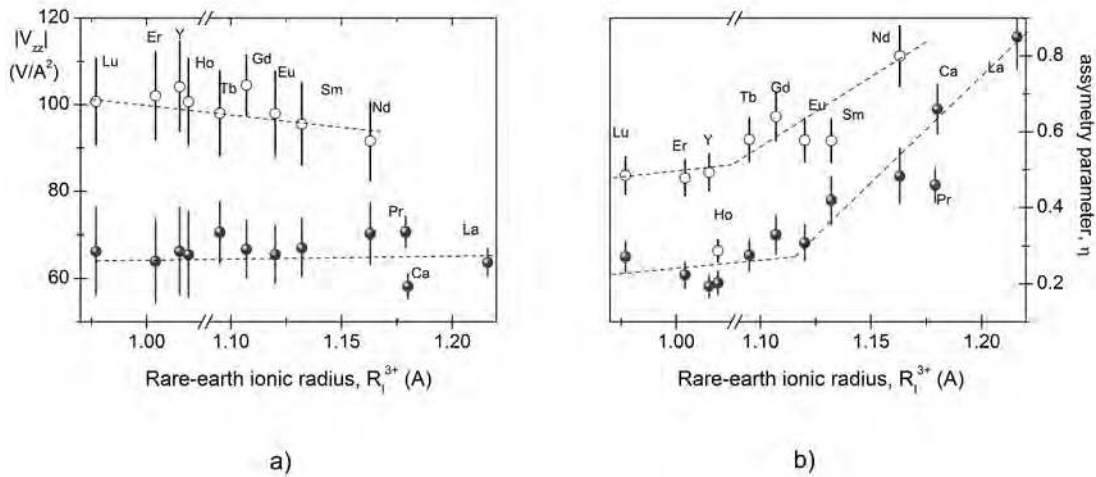


Figure 3.30: EFG parameters evolution with the rare-earth ionic radius for the hexagonal and orthorhombic RMnO_3 series: a) EFG principal component, V_{zz} , and b) asymmetry parameter, η , for the experimental EFG_1 (closed dots) and EFG_2 (open dots).

to the EFG fractions. Moreover, Cd has been assigned to the rare-earth site in other manganite systems^[12,181,186]. Additionally, the two local environments coexist up to the space group change temperature range. At these temperatures, EFG_1 is the dominant distribution and EFG_2 tends to vanish. Even though EFG_2 cannot be directly assigned either to regular R1 or Mn sites, which EFG calculated parameters are very distinct from the experimental ones, the PAC results suggest that this distribution is due to the existence of distorted rare-earth sites.

On the other side, in the orthorhombic compounds there is only one rare-earth crystallographic site and in all previous PAC studies the Cd atom was located at the A site on the structure^[12,186]. Also here, EFG_1 can be assigned to the rare-earth site which V_{zz} is in good agreement with the calculated and reported EFG values for other orthorhombic-based manganites like CaMnO_3 and PrMnO_3 ^[181]. PCM calculations give consistence to this assignment. However, the asymmetry parameter shows a distinct trend with an increase with the ionic radius reaching a maximum for SmMnO_3 and NdMnO_3 . It shall be mentioned here that in CaMnO_3 , the A site cation has divalent charge resulting in a different local environment when compared with RMnO_3 series though the crystalline structure is similar. The coexistence of two EFG experimental distributions, also in the orthorhombic compounds, is then very surprising assuming that the Cd is not going to the regular Mn site. The Cd location in the centre of the MnO_6 octahedra would be quite improbable since the

four shorter Mn-O bond lengths in small ionic radius orthorhombic manganites are smaller than those in the large ionic radius orthorhombic compounds (Pr and Ca). The temperature dependence of these two EFGs shows subtle variations. The origin of this second EFG₂ in the orthorhombic RMnO₃ is not clear and the described results show that the crystalline structure is not enough to explain the coexistence of two different local environments and its origin has to be found in more subtle and local grounds.

Following the EFG_{1,2} (V_{zz} and η) evolution across the rare-earth diagram one realizes that changes in the orthorhombic - hexagonal structure transition are due to the average lattice structure. According to PAC local observation this transformation is predominantly attributed to changes in the fraction of the local environments 1 (EFG₁) and 2 (EFG₂), and in the distortion degree (asymmetry parameter).

Chapter 4

Oxygen Ordering in Hg-based Superconductors

This chapter resumes the work performed to study the local ordering of oxygen at the Hg planes in the 2nd and 3rd members of the $\text{HgBa}_2\text{Ca}_{n-1}\text{Cu}_n\text{O}_{2n+2+\delta}$ superconducting family by using the perturbed angular correlations technique. The experimental results have been interpreted with the help of electric field gradient (EFG) *ab-initio* full potential augmented plane wave (FLAPW) calculations. Particular attention is given to the coexistence of different oxygen species at the Hg planes, which have been suggested earlier for other families of high temperature superconductors but no experimental nor theoretical evidence for its existence in the Hg-based cuprates family has been reported.

4.1 Local probe studies in $\text{HgBa}_2\text{CaCu}_2\text{O}_{6+\delta}$

4.1.1 Structural and magnetic characterization

The Hg-1212 polycrystalline samples, synthesized via the high pressure-high temperature method at 1.8 GPa and 1086K, crystallize in the tetragonal structure (space group P_4mmm). The lattice parameters refinement using the Le Bail method^[127] gave as result $a=b=3.869(8)\text{\AA}$ and $c=12.6746(6)\text{\AA}$. The extra oxygen content (δ) of 0.22(3) was inferred by comparison of structural data with those available in the literature for systems with controlled oxygen content^[52,55]. The samples are almost single phase with traces of CaHgO_2 (< 8% vol.) with hexagonal structure.

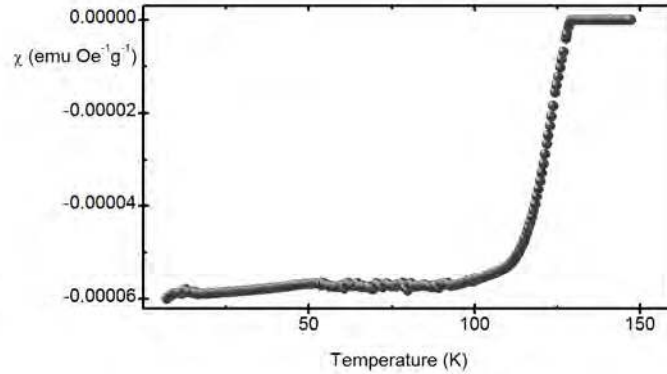


Figure 4.1: Temperature dependence of the magnetic susceptibility, χ , for the Hg-1212.

As a complement to structural characterization, magnetic susceptibility measurements have been performed using 50 Oe applied magnetic field in a $10 \text{ K} < T < 150 \text{ K}$ temperature interval. Figure 4.1 shows the susceptibility, χ , curves obtained in the Hg-1212 as-synthesized samples. The sharp drop in the susceptibility is characteristic of the good quality samples. The obtained onset critical temperature is 128 K, in good agreement with the previously reported values^[52,55]. One shall stress that the impurity found by XRD, CaHgO_2 , is diamagnetic and its presence will not be visible in magnetic susceptibility measurements. Nevertheless, the sharp transition shows that no other superconducting phases are present and the oxygen doping distribution is reasonably homogeneous in the as-synthesized Hg-1212 samples.

In hole-doped high T_C superconductors, the oxygen non-stoichiometry (δ) can be changed via suitable thermal treatments under oxidizing or reducing atmospheres. These thermal treatments are expected to lead to changes in both T_C and lattice parameters due to the insertion or removal of oxygen. To perform each PAC experiment, after implanting the samples with $^{199\text{m}}\text{Hg}$ probe atoms, each sample (consisting of about 10 mg of powder taken from the same as-synthesized batch) was further annealed under different atmosphere and temperature conditions that are summarized in table 4.1.

After the PAC measurements, XRD and magnetic measurements have been performed in order to control sample's properties. XRD pattern matching has been performed allowing the extraction of structural information including the crystalline structure and lattice constants. Similarly to the as-synthesized samples, the annealed samples are characterized by a dominant Hg-1212

Table 4.1: Preliminary annealing conditions upon oxygen doping of the Hg-1212 as-synthesized samples.

Sample Reference	Atmosphere	Temperature K	dwel time min
S0	as-synthesized		
S1	Argon Flow	463	20
S2	Argon Flow	463	15
S3	Argon Flow	473	25
S4	O ₂ Flow	463	17
S5	O ₂ Flow	473	25
S6	8 bar O ₂	473	18
S7	8 bar O ₂	493	18
S8	25 bar O ₂	473	18
S9	25 bar O ₂	473	25
S10	40 bar O ₂	463	25
S11	152 bar O ₂	463	25
S12	152 bar O ₂	533	25

tetragonal structure (92(4)% vol. Hg-1212) without strong changes in the lattice parameters. However, the sample annealed at 152 bar (sample S11) shows partial decomposition of the Hg-1212 tetragonal phase with an increase on the volume fraction of the secondary phase, CaHgO_2 , up to 30(8)% vol. For a better understanding of the influence of the post-implantation annealings on the crystalline parameters, a comparison between the present experimental lattice constants and literature values^[37,38,51–54] is presented in figure 4.2(a). Following the results reported in literature, for oxidizing atmospheres there is a decrease on both a and c parameters. The present results show that the post-implantation annealings led to small changes in the lattice parameters suggesting small changes in the doping of the samples. Although the annealing performed at 152 bar pressurized oxygen led to partial decomposition of the Hg-1212 crystalline phase, the lattice parameters of the superconducting phase are still in good agreement with the as-synthesized one.

Additional magnetization measurements were performed to determine the influence of the post-implantation annealing in the superconducting transition temperatures. The dependence of T_C on oxygen doping is plotted in figure 4.2(b) together with a compilation of values taken from the

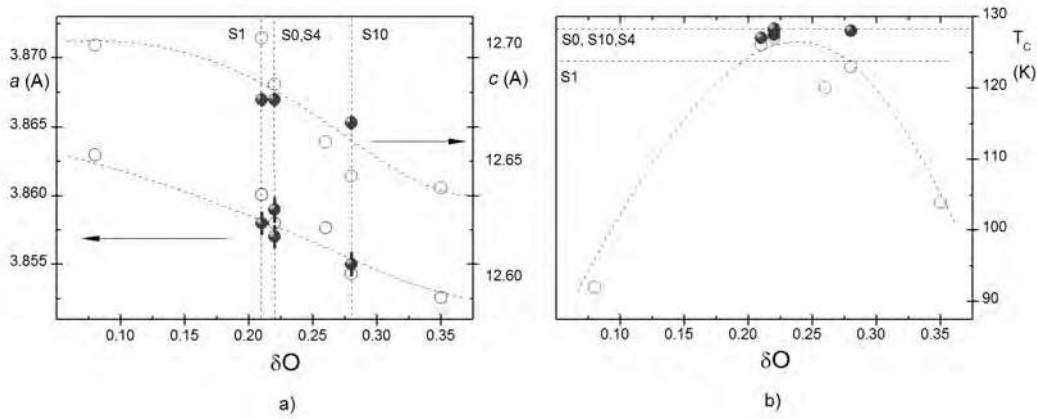


Figure 4.2: a) a and c cell parameters, and b) superconducting transition temperature, T_C , dependence on the extra oxygen content, O_δ , for Hg-1212 samples. The experimental values obtained in this work are represented by closed dots and the values taken from the literature^[37,38,51–54] by open dots. The vertical line indicate the values obtained per sample.

literature^[37,38,51–54]. Although one would expect a bigger influence of the different annealings on T_C , as reported in the literature, the present results show that the T_C 's are practically unchanged after the post-implantation short time annealings. These results hint that the in bulk oxygen content after synthesis prevails over the present doping procedures. The exception is the sample annealed at 152 bar oxygen pressure showing a diamagnetic behavior in all temperature range and loss of superconductivity hinting a possible overdoping of the Hg-1212 fraction.

4.1.2 Description of the experimental PAC results at room temperature

In this subsection, the study of the EFG behavior in Hg-1212 as function of different oxygen dopings is presented. The experimental data is correlated with *ab-initio* full potential augmented plane wave (FLAPW) calculations.

To perform the PAC experiments, Hg-1212 as-synthesized samples were implanted following the procedures described in chapter 2. To remove remaining implantation defects and to promote different oxygen doping contents, the samples were annealed under different atmospheres. After the annealings, the experimental $R(t)$ spectra were measured.

Figure 4.3 displays representative experimental perturbation functions $R(t)$ (left) and corresponding Fourier transforms (right), for samples annealed under different atmospheres and

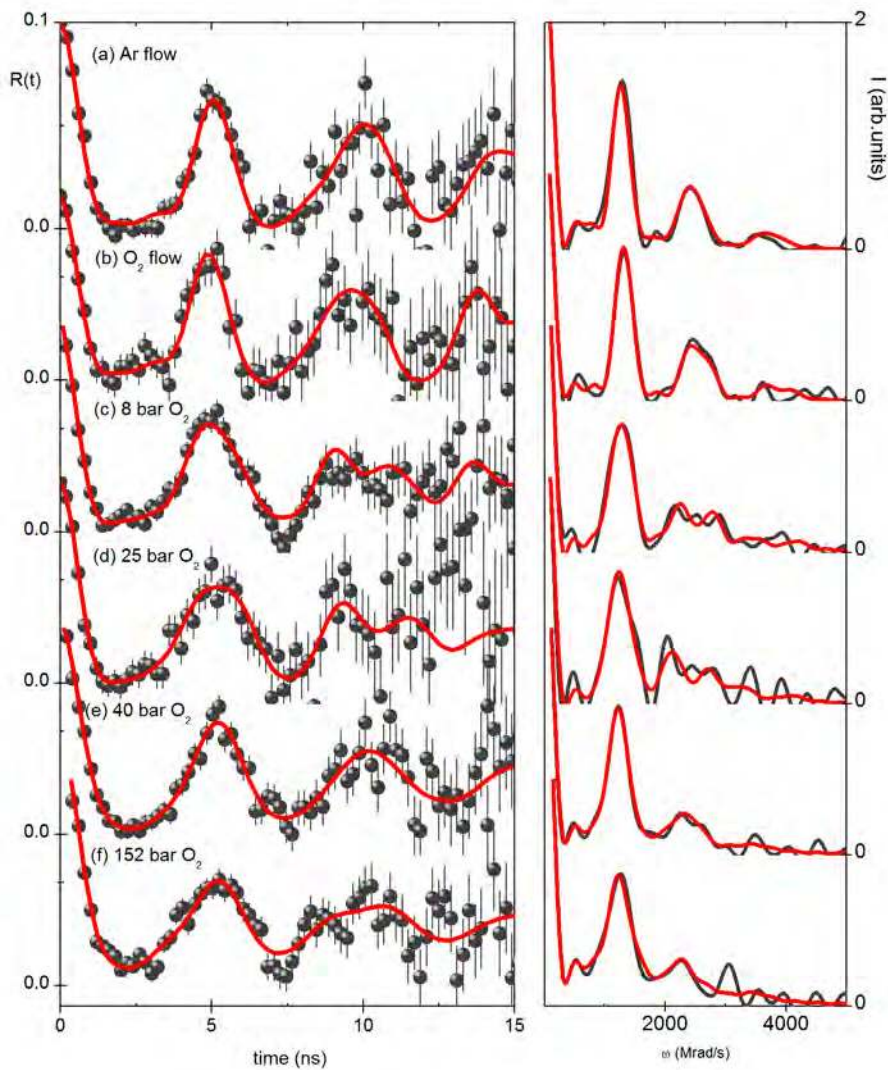


Figure 4.3: a)-f) (Left) Room temperature experimental perturbation functions, $R(t)$, and (Right) corresponding Fourier transforms for Hg-1212 samples. The thicker lines over the spectra are the fitting functions.

measured at room temperature. The high quality fits are shown by continuous lines in the $R(t)$ spectra and were calculated numerically by taking into account the hamiltonian for the nuclear quadrupole interaction^[166]. The resulting fitting parameters are summarized in table 4.2.

The fitting procedure used in this analysis took into account three EFG distributions per fit. A EFG_D distribution was included to account for the attenuation observed in all spectra and thus to improve the quality of the fits. This EFG_D is believed to be due to probes out of regular sites

Table 4.2: EFG fitting parameters of the experimental R(t) PAC functions measured at room temperature for Hg-1212 samples.

Sample Ref.	E1					E2					E3				
	f ₁ %	ν_{Q1} MHz	V_{zz1} V/Å ²	η_1	δ_1	f ₂ %	ν_{Q2} MHz	V_{zz2} V/Å ²	η_2	δ_2	f ₃ %	ν_{Q3} MHz	V_{zz3} V/Å ²	η_3	δ_3
S1	31	1392	854	0.01	0.02	69	1267	777	0.20	0.03	-	-	-	-	-
	±12	±70	±98	±0.01	±0.04	±10	±55	±89	±0.05	±0.03	-	-	-	-	-
S4	42	1441	884	0.09	0.01	63	1288	742	0.20	0.06	-	-	-	-	-
	±11	±72	±102	-	±0.03	±7	±64	±91	±0.03	±0.01	-	-	-	-	-
S6	37	1476	906	0	0.02	63	1209	742	0.20	0.06	-	-	-	-	-
	±6	±72	±104	-	±0.01	±6	±60	±85	±0.01	±0.02	-	-	-	-	-
S8	46	1444	886	0.09	0.05	54	1141	700	0.27	0.04	-	-	-	-	-
	±9	±72	±102	±0.01	±0.03	±10	±57	±80	±0.02	±0.04	-	-	-	-	-
S10	-	-	-	-	-	69	1212	744	0.21	0.10	31	788	484	0.86	0.03
	-	-	-	-	-	±10	±60	±85	±0.04	±0.07	±8	±40	±56	±0.03	±0.01
S11	-	-	-	-	-	69	1213	744	0.26	0.07	31	854	524	0.76	0.07
	-	-	-	-	-	±10	±60	±86	±0.01	±0.09	±8	±43	±60	±0.02	±0.03

(non-annealed sites) in the Hg-1212 lattice and/or in the secondary phase, CaHgO₂, present in the samples. A constant fraction of about 20 % of the probes was assumed to be responsible for EFG_D, which is characterized by $\nu_Q \sim 585(80)$ MHz and $\delta \sim 0.43(3)$. The asymmetry parameter, η_D , was set to zero since the attenuation is too important and does not allow determining it. Since this distribution is considered not to be representative of the regular Hg local environment in Hg-1212 phase, it will be excluded from the discussion. One shall point that on the following when E₁, E₂, E₃ are referred and/or discussed the sum of their relative fractions has been normalized to 100%.

Globally, the differences found in the experimental R(t) functions, as measured in the Hg-1212 phase, can be attributed to the different annealing conditions, under argon or oxygen gas flow, or under pressurized oxygen. When performing the annealing step at 473 K under argon flow, the spectrum of fig. 4.3(a) (sample S1) displays two electric field gradient distributions, named E1 and E2. The dominant distribution, E2, characterizes 69(10)% of the ^{199m}Hg probes and is described by $\nu_{Q2} = 1267(63)$ MHz and an asymmetry parameter, $\eta_2 = 0.21(1)$. Since there is a big similarity at the Hg planes for all members of this superconductor family and the EFG has a highly local sensitivity, one could refer to ref.^[58] to assign this non-axially symmetric distribution

as corresponding to ^{199}Hg nuclei placed in lattice sites with symmetry lower than tetragonal as a consequence of the existence of a single O_δ in the center of the Hg mesh. An axial symmetric distribution is also observed for 31(12) % of the probe atoms interacting with it. This EFG, named E1, is described by $\nu_{\text{Q1}} = 1392(70)$ MHz and a nil asymmetry parameter. This distribution is also consistent with the results reported in refs.^[57,58] corresponding to $^{199\text{m}}\text{Hg}$ nuclei placed on regular sites of the Hg-1212 lattice without O_δ or other point defects in their nearest neighborhood.

Figure 4.3(b) shows the result of the measurement performed on sample S4, after annealing in oxygen flow. Once again, a main EFG distribution (58(7)% of the $^{199\text{m}}\text{Hg}$ probes) was found to be interacting with a non-axially symmetric EFG (E2), as found in the argon flow annealing case. Most likely, this result shows that the doping during the synthesis still prevails over the present annealing procedure. A fraction of 42(11)% of the probes was found to be O_δ free as revealed by the axially symmetric EFG (E1).

Figures 4.3(c) to (f) present the results obtained after annealing in pressurized oxygen. The data show essentially two distinct results depending on the applied pressures. For lower pressures, up to 25 bars (samples S6 and S8), the same frequency triplets are found as in the previous experiments under argon and oxygen flow. The results only show slight changes in the fractions of ^{199}Hg probe nuclei interacting with E1 and E2: 54-63 % of Hg atoms interact with E2 and 37-46% of Hg atoms still do not have any O_δ in their neighborhood (E1). When higher pressures were applied strong changes were observed, as shown in figures 4.3(e) and 4.3(f) relative to samples S10 and S11. E2 is still the dominant EFG as in previous cases, assigned to 69(10)% of the Hg atoms interacting with a distribution characterized by $\nu_{\text{Q2}} \sim 1212(60)$ MHz and $\eta_2 \sim 0.25(4)$. However, a new and highly asymmetric EFG (named E3), is observed being characterized by $\nu_{\text{Q3}} \sim 800(40)$ MHz and $\eta_3=0.8-0.9$ that affects 31(8)% of the Hg atoms. E3 is not explained by any of the calculated configurations reported so far in the literature^[57,58] and hints the existence of a different oxygen configuration in the Hg planes that requires new O_δ configurations to be simulated.

The effect of high oxygen pressure during the measurement has been also investigated^[191]. To test this effect, after annealing at 152 bar oxygen pressure, the temperature was lowered and the samples were kept under 152 bar oxygen pressure during the PAC measurement. This result was further compared with the one obtained in the measurement at atmospheric pressure. Figure 4.4 displays the $R(t)$ functions (left) and corresponding fourier transforms (right) for measurements at

atmospheric pressure and under 152 bar pressurized oxygen. The resulting fit parameters are listed in table 4.3.

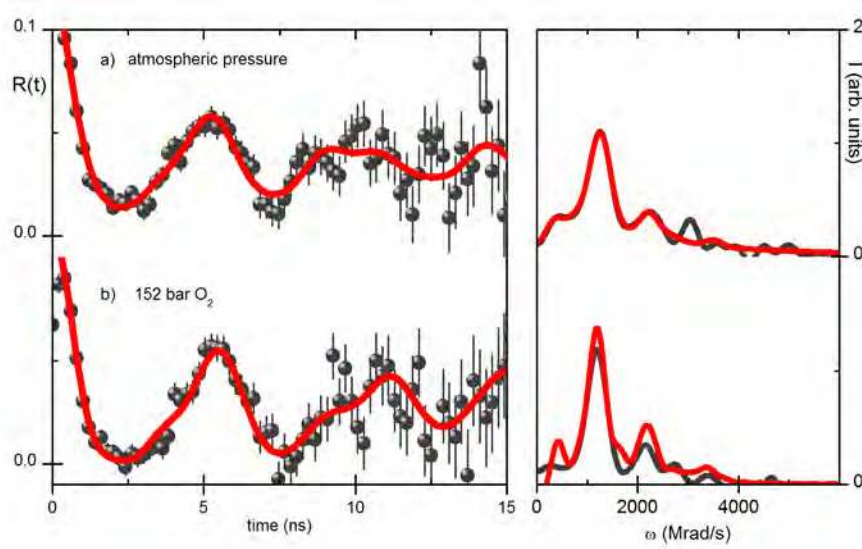


Figure 4.4: (Left) Room temperature experimental perturbation functions, $R(t)$, and (Right) corresponding Fourier transforms, for measurements performed at: a) atmospheric pressure and b) under 152 bar pressurized oxygen. The thicker lines over the spectra are the fitting functions.

Table 4.3: EFG fitting parameters of the experimental $R(t)$ functions for room temperature measurements as function of high oxygen pressure for Hg-1212 samples.

Sample Reference	Preliminary Annealing Conditions	Measurement Conditions	E_2					E_3				
			f_2 %	ν_{Q2} MHz	$ V_{zz} _2$ $V/\text{\AA}^2$	η_2	δ_2	f_3 %	ν_{Q3} MHz	$ V_{zz} _3$ $V/\text{\AA}^2$	η_3	δ_3
S11	Pressurized O_2 (152 bar)	Atmospheric	69	1213	744	0.26	0.07	31	854	524	0.76	0.07
		Pressure	± 16	± 60	± 86	± 0.01	± 0.01	± 8	± 43	± 60	± 0.02	± 0.03
S12	Pressurized O_2 (152 bar)	152 bar	83	1175	721	0.24	0.06	17	904	555	0.69	0.06
			± 5	± 60	± 60	± 0.06	± 0.01	± 4	± 70	± 50	± 0.05	± 0.03

The analysis of the data showed again two representative EFG distributions. The experiment performed at atmospheric pressure (fig. 4.4(a)), as described previously, shows a dominant non-symmetric EFG (denoted as E_2) in coexistence with a highly asymmetric EFG distribution (named E_3). The measurement performed under 152 bar pressurized oxygen, displayed in fig. 4.4(b), shows essentially the same EFG distributions. However, the fractions of probes interacting with

E2 and E3 were found to be slightly different. A dominant fraction of 83(5)% was found to be interacting with E2, which is characterized by $\nu_{Q2}=1175(70)$ MHz and $\eta_2=0.24(6)$. Similarly to the atmospheric pressure measurement, the highly asymmetric E3 was also found and is characterized by $\nu_{Q3}=904(70)$ MHz and $\eta_3=0.69(5)$. E3 affects here 17(4)% of the $^{199\text{m}}\text{Hg}$ probe atoms. One shall stress that one would expect that the measurement under high pressure would lead to strong changes in the fractions of probes interacting with the different EFGs, due to the continuous doping. The slight increase of the fraction of probes interacting with E2 for the measurement under high pressure together with the fact that Hg-1212 as opposed to the 1st member, Hg-1201, can trap more oxygen, gives consistence to the idea of a new oxygen ordering scenario. Furthermore, one shall call the attention to the fact that such high local oxygen concentrations have not been reported or calculated for Hg-1201 [57].

4.1.3 Description of the experimental PAC results in the superconducting state

To further study possible changes of the O_δ configurations at low temperature, below the T_C of the raw samples, measurements in liquid nitrogen have been performed. Representative experimental $R(t)$ spectra (left) and their respective Fourier analysis (right) are displayed in figure 4.5 being the resulting fitting parameters also summarized in table 4.4. Essentially, the experimental results show the same type of EFG distributions as found in the room temperature measurements. Also here the same fitting procedure has been applied. Figure 4.5(a) shows the experimental PAC results as

Table 4.4: EFG fitting parameters of the experimental $R(t)$ PAC functions measured at 77 K for Hg-1212 samples.

Sample Ref.	E1					E2					E3				
	f_1 %	ν_{Q1} MHz	V_{zz1} $\text{V}/\text{\AA}^2$	η_1	δ_1	f_2 %	ν_{Q2} MHz	V_{zz2} $\text{V}/\text{\AA}^2$	η_2	δ_2	f_3 %	ν_{Q3} MHz	V_{zz3} $\text{V}/\text{\AA}^2$	η_3	δ_3
S2	38	1392	854	0.01	0.02	62	1164	757	0.31	0.09	-	-	-	-	-
	± 15	± 70	± 98	± 0.01	± 0.04	± 12	± 55	± 88	± 0.08	± 0.01	-	-	-	-	-
S9	24	1474	886	0.09	0.05	76	1178	723	0.20	0.02	-	-	-	-	-
	± 9	± 74	± 102	± 0.01	± 0.03	± 11	± 58	± 83	± 0.01	± 0.01	-	-	-	-	-
S10	-	-	-	-	-	83	1262	774	0.28	0.12	17	828	508	0.74	0.06
	-	-	-	-	-	± 10	± 62	± 90	± 0.01	± 0.03	± 9	± 42	± 58	± 0.09	± 0.01
S12	-	-	-	-	-	67	1151	706	0.16	0.15	33	818	502	0.98	0.01
	-	-	-	-	-	± 8	± 56	± 81	± 0.04	± 0.03	± 9	± 41	± 58	± 0.08	± 0.01

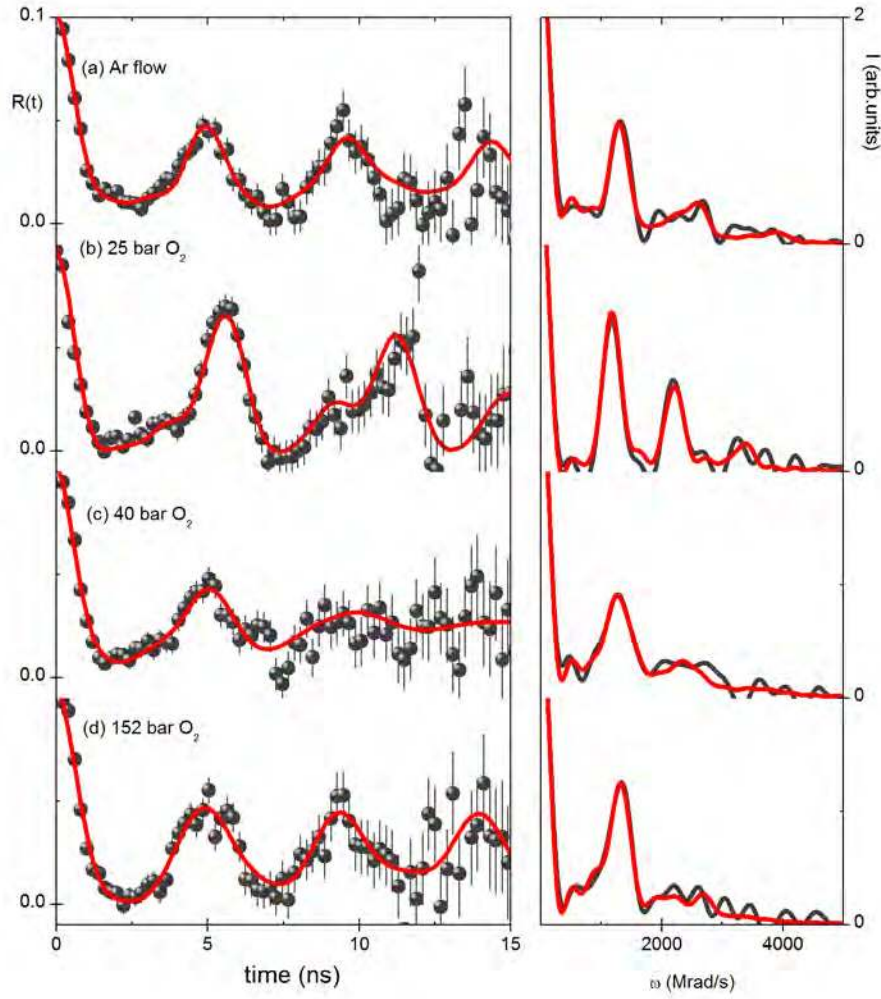


Figure 4.5: a)-d) (Left) Experimental perturbation functions, $R(t)$, and (Right) corresponding Fourier transforms for measurements performed at 77 K in Hg-1212 samples. The thicker lines over the spectra are the fitting functions.

measured at 77 K for the sample S2 annealed in argon flow revealing the same frequency triplets as found in the room temperature measurement. The main EFG (E2, $f_2=62(8)\%$) is described by $\nu_{Q2}=1164(55)$ MHz and an axial asymmetry parameter $\eta_2=0.31(6)$, slightly higher than the one characterizing this EFG at room temperature. An axially symmetric EFG (E1) was also found, for 38(10)% of the probe Hg atoms and is characterized by $\nu_{Q1}=1392(70)$ MHz and $\eta=0.01(1)$.

Fig. 4.5(b) shows $R(t)$ data for the sample S9, annealed at 25 bars pressurized oxygen, where one can observe two EFGs. The dominant EFG (E2) corresponds to 76(11)% of the probes interacting with a non axial symmetric distribution characterized by $\nu_{Q2}=1178(58)$ MHz and $\eta_2=0.20(1)$. About 24% of the probe ^{199m}Hg nuclei are free of O_δ as revealed by the axially symmetric EFG

(E1) characterized by $\nu_{Q1}=1454(74)$ MHz and $\eta_1=0$.

When higher pressures were applied (figs. 4.5(c) and (d), referring to samples S10 and S12, respectively) the new and highly asymmetric EFG (E3) appears as observed in the room temperature measurements. E3 affects now 17-33% of the probes, depending on the annealing oxygen pressure. At 77 K, E3 parameters are not much different from the room temperature measurements with $\nu_{Q3} \sim 820(41)$ MHz and a high asymmetry parameter ($\eta_3 \sim 1$) in the specific case of the sample annealed at 152 bars. In these measurements the dominant EFG (E2) is described by $\nu_{Q2}=1151-1262$ MHz, $\eta \sim 0.16-0.28$ that affects about 67-83% of the probes.

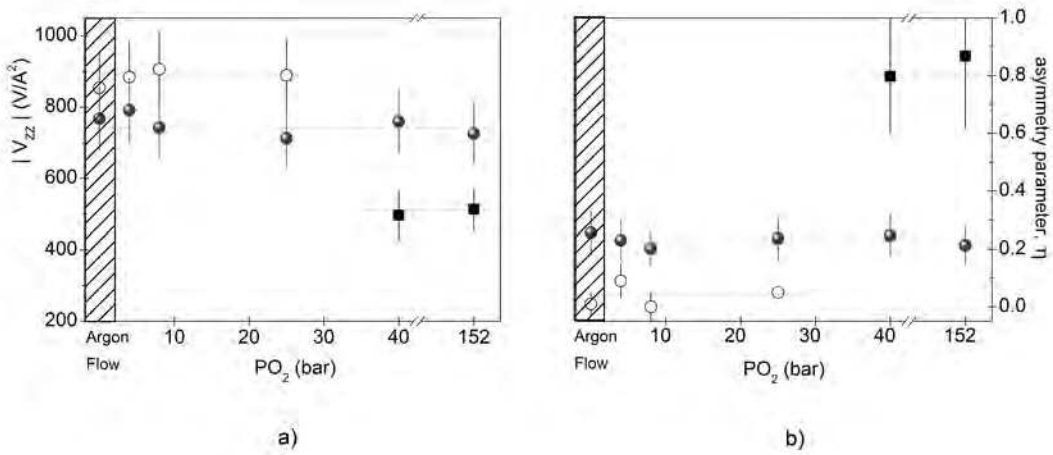


Figure 4.6: a) Principal component of each EFG tensor, V_{zz} , and b) asymmetry parameter, η , as a function of the preliminary annealing atmosphere. The obtained EFG are represented by open dots (E1), closed dots (E2) and closed squares (E3).

Table 4.5: Mean values per EFG triplet, obtained by averaging room temperature and 77 K EFG parameters.

E1				E2				E3			
ν_{Q1}	V_{zz1}	η_1	δ_1	ν_{Q2}	V_{zz2}	η_2	δ_2	ν_{Q3}	V_{zz3}	η_3	δ_3
MHz	$\text{V}/\text{\AA}^2$			MHz	$\text{V}/\text{\AA}^2$			MHz	$\text{V}/\text{\AA}^2$		
1440	883	0.04	0.035	1215	750	0.23	0.067	822	504	0.84	0.05
± 72	± 102	± 0.05	± 0.03	± 60	± 86	± 0.04	± 0.03	± 14	± 50	± 0.04	± 0.01

The PAC measurements performed at room temperature and 77 K show equivalent results, mainly depending from the previous annealing treatment. Due to this similarity, average EFG parameters for E1, E2 and E3 were calculated and are summarized also on table 4.5. Figure

4.6 plots the experimental EFG parameters (principal EFG component, V_{zz} , and the asymmetry parameter, η , as a function of the oxygen doping, dependent here on the annealing atmosphere. Based only on the experimental data and previous literature results some conclusions can be already drafted. The compound presents non uniform oxygen distribution in which different oxygen doped regions are found coexisting. In more detail, the annealing in argon flow was not sufficient to reduce the initial, as-synthesized, O_δ content. The PAC results revealed a dominant EFG distribution, E2, which hints a diluted concentration of interstitial O_δ in the Hg planes. The annealings in oxygen flow and at oxygen pressures up to 25 bars maintained the system unchanged. When higher oxygen pressures were applied, 40 and 152 bars, there is no more evidence for Hg atoms free of O_δ in their neighborhood (no evidence for E1) and a highly asymmetric EFG appears that hints to a new O_δ configuration at higher concentrations, that will be discussed after presenting experimental results for Hg-1223.

4.2 Local probe studies in $\text{HgBa}_2\text{Ca}_2\text{Cu}_3\text{O}_{8+\delta}$

4.2.1 Structural and magnetic characterization

The polycrystalline Hg-1223 samples, synthesized via the high pressure-high temperature method as described in chapter 2, crystallize in the tetragonal structure. Based on the tetragonal symmetry of the space group P_4mmm , the refined lattice constants were found to be $a=3.85133(12)$ Å and $c=15.83355(20)$ Å in good agreement with the values reported in the literature^[40]. The extra oxygen content (δ) of 0.25(3) was inferred by comparison of the structural data with those available in the literature for systems with controlled oxygen content^[26,39,40,55,56]. The samples are almost single phase although a small content of CaHgO_2 ($< 5(3)\%$ vol.) was also found.

Complementary information on the sample's quality has been obtained using magnetic susceptibility measurements. Figure 4.7 shows the susceptibility, χ , curves obtained in the as-synthesized Hg-1223 samples using 50 Oe applied magnetic field in a $10 \text{ K} < T < 150 \text{ K}$ temperature interval. The sharp drop in the susceptibility is characteristic of the good quality of the samples showing that no other superconducting phases are present. Furthermore, the onset critical temperature, T_{Conset} , of 132 K is in excellent agreement with the previously reported values^[26,39,40,55,56]. Once again, the presence of CaHgO_2 in the samples, due to its diamagnetic behavior, is not visible in the

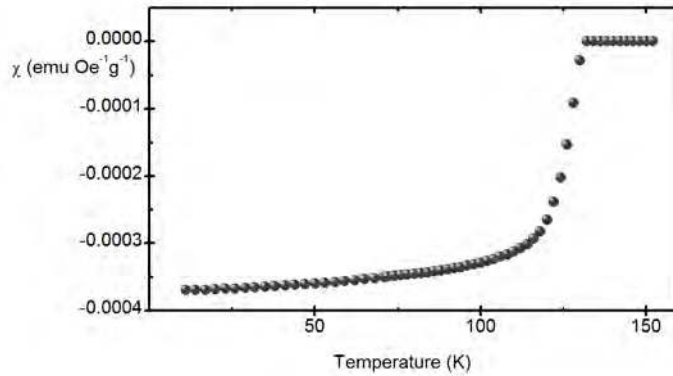


Figure 4.7: Temperature dependence of the magnetic susceptibility, χ , for Hg-1223.

magnetic measurements.

Similarly to the procedure used to study the oxygen ordering in Hg-1212, Hg-1223 samples were annealed under different atmospheres aiming the change on their oxygen concentration and, eventually, its ordering at the Hg planes. After implanting the samples with $^{199\text{m}}\text{Hg}$ ions, annealings under different atmosphere and temperature conditions have been performed. The conditions used in each annealing are summarized in table 4.6. One shall note that the samples have different references according to the different annealings although these have been taken from the same batch of the as-synthesized Hg-1223.

Table 4.6: Preliminary annealing conditions upon oxygen doping of the Hg-1223 as-synthesized samples.

Sample Reference	Atmosphere	Temperature K	dwel time min
S13	as-synthesized		
S14	Argon Flow	463	20
S15	O ₂ Flow	475	18
S16	25 bar O ₂	473	18
S17	40 bar O ₂	463	25
S18	152 bar O ₂	463	25
S19	152 bar O ₂	533	25

Post-annealing XRD and magnetic measurements have been performed in order to control sam-

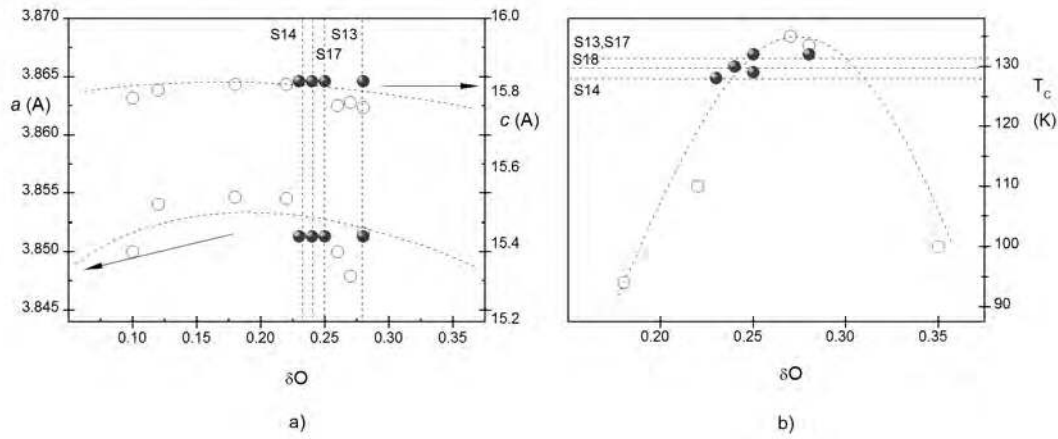


Figure 4.8: a) a and c cell parameters, and b) superconducting transition temperature, T_C , dependence on the extra oxygen content, δO , for Hg-1223 samples. The experimental values obtained in this work are represented by closed dots while the literature values by open dots [26,39,40,55,56]. The vertical lines represent the experimental values per sample. The dashed lines are guides to the eye.

ple's properties and to extract information about the effectiveness of doping. XRD measurements showed that all samples crystallize in the tetragonal phase with slight changes in the cell parameters as seen in figure 4.8(a). The obtained a and c cell parameters are compared with the same values taken from the literature [26,39,40,55,56]. Moreover, these results show the same evolution as the ones obtained for Hg-1212 with a decrease of both a and c parameters for an increase on oxygen doping. One shall stress that the small changes in the lattice constants of the annealed samples show that the oxygen content of the as-synthesized samples was, alike for Hg-1212, practically unchanged. This was also confirmed by magnetic measurements where no changes in $T_{C\text{onset}}$ have been observed after subjecting the samples to different reducing or oxidizing atmospheres as depicted in figure 4.8(b). An effective reducing annealing should lead to a decrease on T_C , which was not observed for the samples annealed in argon flow.

4.2.2 Description of the PAC experimental results at room temperature

The study of the EFG behavior in Hg-1223 as function of different oxygen dopings is presented in this subsection. Following the procedure applied in used for Hg-1212, Hg-1223 samples were implanted with $^{199\text{m}}\text{Hg}$ and annealed. After the annealings, the experimental perturbation functions, $R(t)$, have been measured.

Figure 4.9 shows representative $R(t)$ functions (left) and corresponding fourier transforms (right)

for samples annealed under different atmospheres and measured at room temperature. The high quality fits are shown by continuous lines over the $R(t)$ spectra and were calculated numerically by taking into account the hamiltonian for the nuclear quadrupole interaction^[166] and the resulting fitting parameters are summarized in table 4.7.

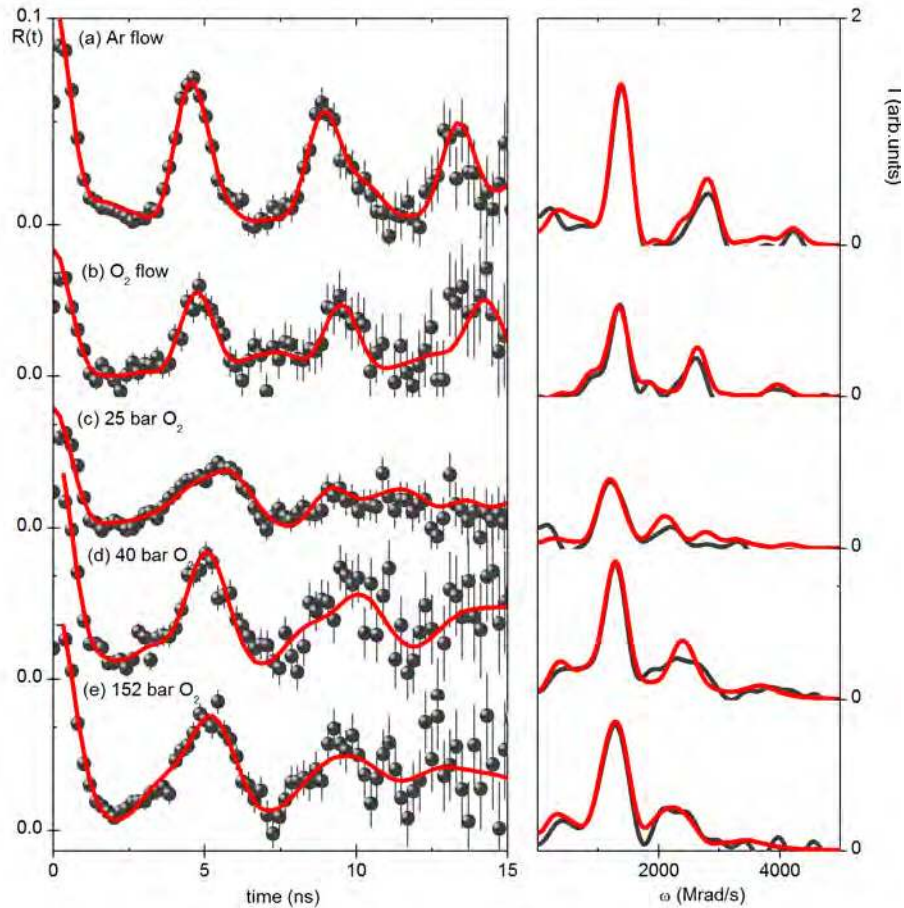


Figure 4.9: a)-e) (Left) Room temperature experimental perturbation functions, $R(t)$, and (Right) corresponding Fourier transforms as a function of the annealing atmospheres for Hg-1223. The thicker lines over the spectra are the fitting functions.

Alike Hg-1212 case, the fitting procedure used in this analysis also took into account three EFG distributions. A EFG distribution (also denoted here as EFG_D) was included to account for the attenuation observed in all spectra and thus to improve the quality of the fits. EFG_D is believed to be due to probes in the secondary phase present in the Hg-1223 samples and /or out of regular sites

(non-annealed sites) in the Hg-1223 lattice. A constant fraction of about 10(4)% of the probes was assumed to be interacting with EFG_D which is characterized by $\nu_D \sim 360(60)$ MHz and $\delta \sim 0.36(6)$. The asymmetry parameter was again set to zero due to its irrelevance here. This distribution is considered not to be representative of the regular Hg environment in the Hg-1223 phase and it will not be included in the following discussion being the sum of E₁, E₂, E₃ fractions, referred further on the discussion, normalized to 100%.

Looking at figure 4.9, the differences found in the room temperature experimental R(t) functions for Hg-1223 can be associated to the different annealing conditions, under argon or oxygen flow or under pressurized oxygen. The annealing performed in argon flow, plotted in figure 4.9(a) (sample S15), shows that the Hg probe atoms interact with two EFG distributions, which EFG parameters are similar to the ones observed for Hg-1212. For this reason, the notation used in the EFG distributions observed in Hg-1212 samples will be kept for Hg-1223 samples. The dominant EFG (E1) is due to an axially symmetric distribution, which is given by 72(10)% of the probe atoms and is described by $\nu_{Q1} = 1495(50)$ MHz and a nil asymmetry parameter. According to refs.^[57,58], this E1 distribution corresponds to ^{199m}Hg nuclei placed in sites of the Hg-1223 lattice without O_δ or other point defects in their neighborhood. An non axially symmetric EFG distribution (E2) is also observed for 30(15)% of the probe atoms and it is characterized by $\nu_{Q2} = 1309(100)$ MHz and an asymmetry parameter $\eta_2 = 0.11$. Considering that the Hg planes in this series of superconductors are quite similar, one could refer again to^[58] to attempt assigning this E2 distribution to ^{199m}Hg probe nuclei sitting in lattice sites with symmetry lower than tetragonal as a consequence of the existence of a single O_δ at the centre of the Hg mesh.

Figure 4.9(b) presents the result of the measurement performed on sample S15, after annealing in oxygen flow. A dominant EFG distribution (69(9)% of the ^{199m}Hg probes) was found to be interacting with the axially symmetric E1, as found in the argon flow annealing case. This result shows the doping efficiency of the present oxygen flow annealing is still too low not leading to changes on the oxygen doping. Alike the argon flow annealing, E1 was found to be in coexistence with the non-axially symmetric E2 as given by 31(11)% of the ^{199m}Hg probe nuclei.

Figures 4.9(d) to (e) show the effect of high oxygen pressure annealings on Hg-1223 samples. The data show distinct results from the gas flow annealings, being the obtained EFGs dependent on the applied pressures. For lower oxygen pressures, up to 25 bar (figure 4.9(c)), the same frequency

Table 4.7: EFG fitting parameters of the experimental $R(t)$ PAC functions measured in Hg-1223 samples at room temperature.

Sample Ref.	E1					E2					E3				
	f_1 %	ν_{Q1} MHz	V_{zz1} $\text{V}/\text{\AA}^2$	η_1	δ_1	f_2 %	ν_{Q2} MHz	V_{zz2} $\text{V}/\text{\AA}^2$	η_2	δ_2	f_3 %	ν_{Q3} MHz	V_{zz3} $\text{V}/\text{\AA}^2$	η_3	δ_3
S14	72	1495	917	0.01	0.015	28	1309	803	0.11	0.03	-	-	-	-	-
	± 10	± 50	± 100	± 0.01	± 0.005	± 15	± 100	± 92	± 0.09	± 0.01	-	-	-	-	-
S15	69	1400	859	0.09	0.01	31	924	567	0.30	0.10	-	-	-	-	-
	± 9	± 74	± 102	± 0.01	± 0.03	± 11	± 58	± 83	± 0.01	± 0.01	-	-	-	-	-
S16	21	1473	904	0.01	0.05	79	1132	695	0.26	0.07	-	-	-	-	-
	\pm	\pm	\pm	\pm	\pm	± 10	± 62	± 90	± 0.01	± 0.03	-	-	-	-	-
S17	-	-	-	-	-	87	1287	790	0.25	0.07	13	796	488	0.68	0.07
	-	-	-	-	-	± 5	± 80	± 80	± 0.05	± 0.03	± 3	± 100	± 80	± 0.10	± 0.03
S18	-	-	-	-	-	70	1151	706	0.16	0.15	30	818	502	0.98	0.01
	-	-	-	-	-	± 8	± 56	± 81	± 0.04	± 0.03	± 9	± 41	± 58	± 0.08	± 0.01

triplets are found as in the experiments under gas flow. However, the fraction of probes interacting with each EFG is inverted being now the dominant EFG distribution (79(10)% of the probes) the one given by $^{199\text{m}}\text{Hg}$ probe nuclei interacting with the non-axially symmetric E2. E2 is still found in coexistence with the axially symmetric E1. When higher oxygen pressures were applied, strong changes were observed as depicted in the spectra of figure 4.9(d) and (e) relative to samples S17 and S18. The non-axially symmetric E2 is the dominant EFG distribution on both cases as given by $\sim 78(8)\%$ of the probes interacting with it. Similarly to the results obtained for Hg-1212 samples annealed at high oxygen pressures, the highly asymmetric E3 is also found in Hg-1223 samples, being characterized by $\nu_{Q3} \sim 800(30)$ MHz and $\eta_3 \sim 0.7-0.9$ affecting $\sim 21(9)\%$ of the Hg probe atoms. As referred for Hg-1212, E3 cannot be assigned to any of the calculated configurations reported so far in the literature^[57,58] suggesting the existence of a different oxygen configuration in the Hg planes.

The effect of high oxygen pressure during the measurement has been also investigated in Hg-1223 samples. This effect has been studied following the same procedure used in Hg-1212 samples, by keeping the oxygen pressure at 152 bar during the PAC measurement at room temperature. This result was compared with the one obtained in the measurement at atmospheric pressure.

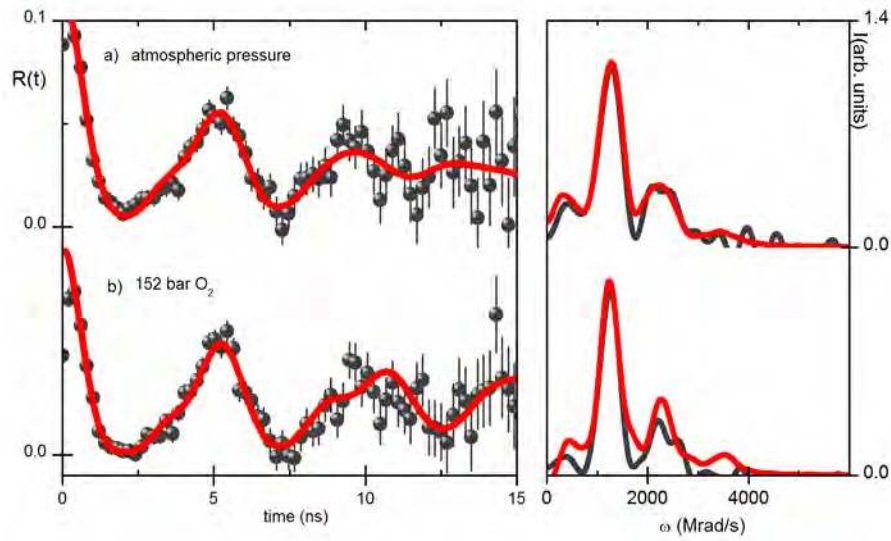


Figure 4.10: (Left) Room temperature experimental perturbation functions, $R(t)$, and (Right) corresponding Fourier transforms for measurements performed in Hg-1223 at: a) atmospheric pressure and b) under 152 bar pressurized oxygen. The thicker lines over the spectra are the fitting functions.

Figure 4.10 shows the $R(t)$ functions and corresponding fourier transforms for measurements at atmospheric pressure and under 152 bar oxygen pressure being the resulting fitting parameters summarized in table 4.8. Alike for the atmospheric pressure measurement, the data obtained under 152 bar pressurized oxygen shows two representative EFG distributions. Once again, the dominant non-axially symmetric E2 affects 78(10)% of the ^{199m}Hg probe nuclei. E2 is still found in coexistence with the highly asymmetric E3, which is given by 22(7)% of the probes. Although one could expect stronger changes of the fractions of the probes interacting with each EFG due to the continuous doping, it was observed a slight decrease of the fraction of probes interacting with E3, similarly to the results obtained with Hg-1212. It is well accepted that Hg-1223 can trap more oxygen than Hg-1212, what would in principle lead to differences in the Hg local environment due to different oxygen concentrations. Nevertheless, the present results suggest again for the existence of a different oxygen ordering, which justifies the similar results obtained in both Hg-1212 and Hg-1223 under high oxygen pressure.

Table 4.8: EFG fitting parameters of the experimental $R(t)$ functions for room temperature measurements as function of high oxygen pressure for Hg-1223 samples.

Sample Reference	Preliminary Annealing Conditions	Measurement Conditions	E ₂					E ₃				
			f ₂ %	ν_{Q2} MHz	$ V_{zz} _2$ V/Å ²	η_2	δ_2	f ₃ %	ν_{Q3} MHz	$ V_{zz} _3$ V/Å ²	η_3	δ_3
S18	Pressurized O ₂ (152 bar)	Atmospheric Pressure	70	1213	744	0.26	0.07	31	854	524	0.76	0.07
			±16	±60	±86	±0.01	±0.01	±8	±43	±60	±0.02	±0.03
S19	Pressurized O ₂ (152 bar)	152 bar	78	1225	752	0.27	0.06	22	904	555	0.69	0.05
			±10	±70	±60	±0.05	±0.02	±7	±70	±50	±0.02	±0.02

4.2.3 Description of the PAC experimental results in the superconducting state

Eventual changes on the O_δ configurations at low temperature, below T_C of the Hg-1223 raw samples, have been studied by performing measurements in liquid nitrogen. Representative experimental $R(t)$ spectra and respective Fourier transforms are plotted in figure 4.11. The resulting fitting parameters are summarized in table 4.9.

Looking at figure 4.11, one can observe the same type of EFG distributions as found in the room temperature measurements. One shall recall that the EFG parameters have been obtained using the same fitting procedure used for the room temperature measurements. The annealing in argon flow (figure 4.11(a)) shows essentially the same EFG distributions in approximately the same relative fractions as obtained for the room temperature with the $^{199\text{m}}\text{Hg}$ neighborhood being due to a oxygen diluted environment being the axially symmetric E1 the dominant EFG distribution. Figures 4.11(b) and (c) show the spectra obtained after annealing under high oxygen pressure, at 40 and 152 bar pressurized oxygen respectively. Similarly to the results obtained at room temperature, the dominant EFG distribution is given by $\sim 78\%$ of the probe atoms, which were found interacting with the non-axially symmetric E2. Once again, E2 was found in coexistence with the highly asymmetric E3, which affects $\sim 21\%$ of the probes. In both cases, the Hg local environment was found to be not free from oxygen. Alike Hg-1212, the PAC results obtained for Hg-1223 at 77 K do not differ strongly from the room temperature ones allowing the calculation of average EFG values.

Figure 4.12 shows the experimental EFG parameters as a function of the oxygen doping, dependent on the annealing atmosphere, where one can observe the coexistence of two EFG distributions for all studied cases.

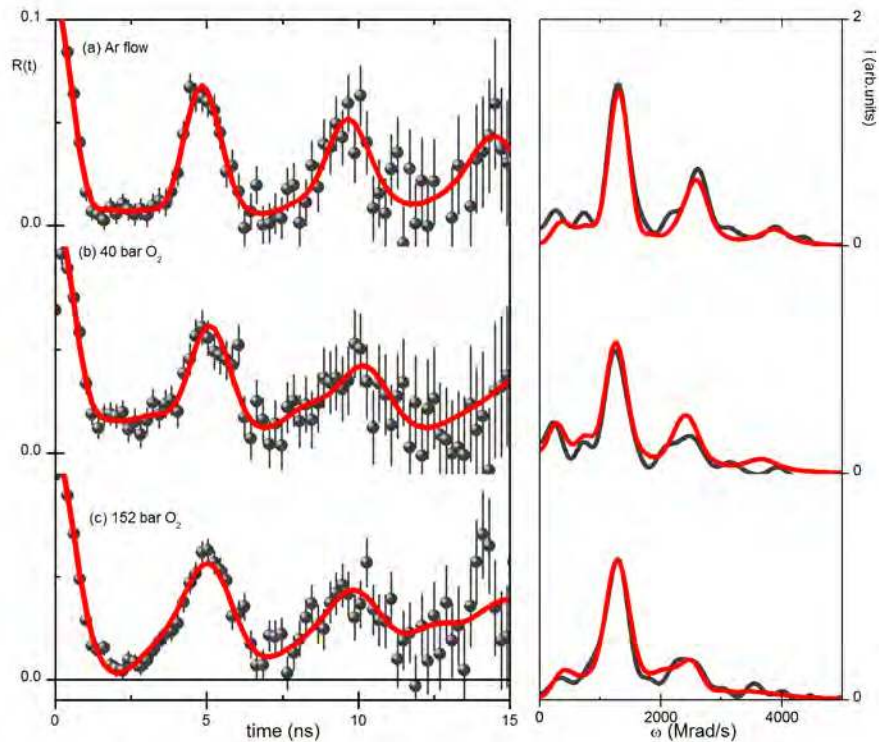


Figure 4.11: a)-c) (Left) Experimental perturbation functions, $R(t)$, and (Right) corresponding Fourier transforms as a function of the annealing atmospheres for Hg-1223 as measured at 77 K. The thicker lines over the spectra are the fitting functions.

Based on the experimental data obtained for Hg-1223, some conclusions can be drafted. The Hg-1223 compound presents a non uniform oxygen distribution as given by the coexistence of different EFG distributions. The annealing in argon flow led to an almost oxygen free Hg environment although a small fraction of probe atoms was found in the vicinity of oxygen. This result suggests a better mobility of the oxygen atoms in Hg-1223 regarding Hg-1212. The annealing in oxygen flow was not sufficient to dope the system, being once again the Hg local environment mainly free of oxygen. On the other hand, the doping under oxygen pressure led to changes in the system with an oxygen diluted environment for lower pressures. For high oxygen pressures, the Hg atoms are not free from oxygen in their vicinity and the existence of a highly asymmetric EFG distribution suggest a new oxygen configuration, which appears only at high concentrations.

Table 4.9: EFG fitting parameters of the experimental R(t) PAC functions measured in Hg-1223 samples at 77 K.

Sample Ref.	E1					E2					E3				
	f_1 %	ν_{Q1} MHz	V_{zz1} V/Å ²	η_1	δ_1	f_2 %	ν_{Q2} MHz	V_{zz2} V/Å ²	η_2	δ_2	f_3 %	ν_{Q3} MHz	V_{zz3} V/Å ²	η_3	δ_3
S14	80	1380	847	0.08	0.05	20	1293	794	0.20	0.07	-	-	-	-	-
	±10	±80	±100	±0.01	±0.01	±10	±100	±90	±0.08	±0.01	-	-	-	-	-
S17	-	-	-	-	-	86	1290	791	0.15	0.07	14	796	488	0.55	0.07
	-	-	-	-	-	±10	±100	±100	±0.05	±0.02	±10	±90	±100	±0.04	±0.03
S18	-	-	-	-	-	71	1212	744	0.42	0.01	29	790	490	0.81	0.13
	-	-	-	-	-	±10	±100	±98	±0.08	±0.01	±109	±60	±60	±0.08	±0.02

4.3 EFG simulations

To fully grasp the PAC experimental results and extract the maximum information, EFG *ab-initio* calculations have been performed using the code Wien2K^[175] via the full potential augmented plane wave method (FLAPW) with the generalized gradient approximation^[179] (GGA) for the density functional. The crystalline structure parameters (lattice constants and atomic positions), required as input information in FLAPW, have been taken from neutron diffraction experiments^[51,182] accounting for different oxygen dopings. The values for the undoped case ($\delta O=0$) were obtained by extrapolation. To illustrate different O_δ doping configurations, various Hg-1212 supercells have been constructed assuming the composition $Hg_mBa_{2m}Ca_mCu_{2m}O_{6m+n}$. Following earlier works^[57,58], the simulations here implemented describe different configurations of single O_δ atoms all sitting within the Hg planes, including also particular ones where the dopant is represented by a dumbbell $O_{2\delta}$ molecule with the symmetry axis parallel to *c*-axis at the centre of the Hg mesh. Only O_δ or $O_{2\delta}$ configurations which provide relevant information for the explanation and discussion of the experimental data are reported here. One shall stress that the aim of the different supercells is to provide the understanding of which local configurations of O_δ or $O_{2\delta}$ can originate the measured EFGs at the Hg site. It has been shown on previous works^[57,58] that the first neighbor contribution dominates the EFG allowing to infer the organization of O_δ atoms/dumbbells in the neighborhood of the ^{199m}Hg probing nuclei. With these considerations in mind one shall further note that in each different supercell volume a nominal oxygen dopant local concentration can be assigned.

Figure 4.13 illustrates a schematic view of the built supercells projected along the *c* axis onto the

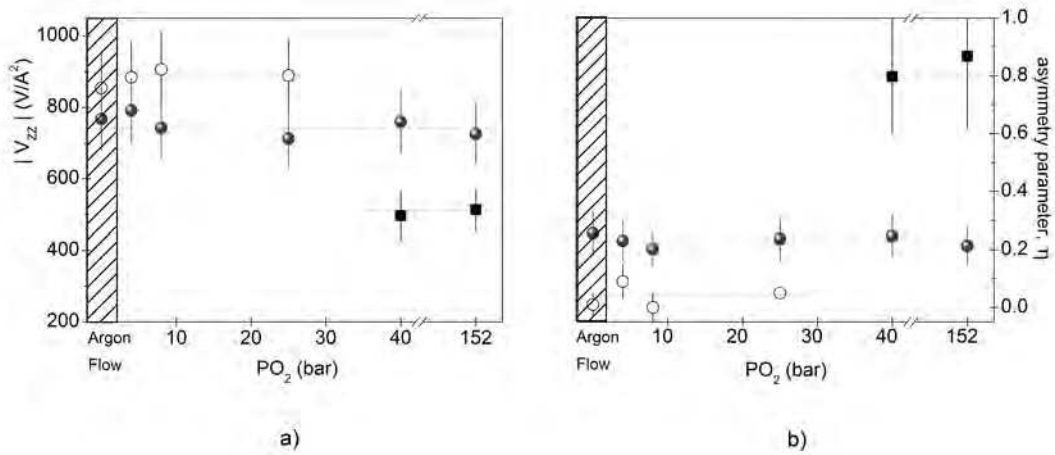


Figure 4.12: a) Principal component of the EFG tensor, V_{zz} , and b) asymmetry parameter, η , as a function of the annealing atmosphere for Hg-1223. The obtained EFG are represented by open dots (E1), closed dots (E2) and closed squares (E3).

Hg planes. The shaded regions represent the ab plane of the supercells used in the simulations. Since similar configurations were used for both O_δ and $O_{2\delta}$ cases, only one set of pictures is represented. The resulting EFG parameters found for Hg and for all other atoms in each supercell are summarised in tables 4.10 and 4.11 addressing for both O_δ and $O_{2\delta}$ cases, respectively.

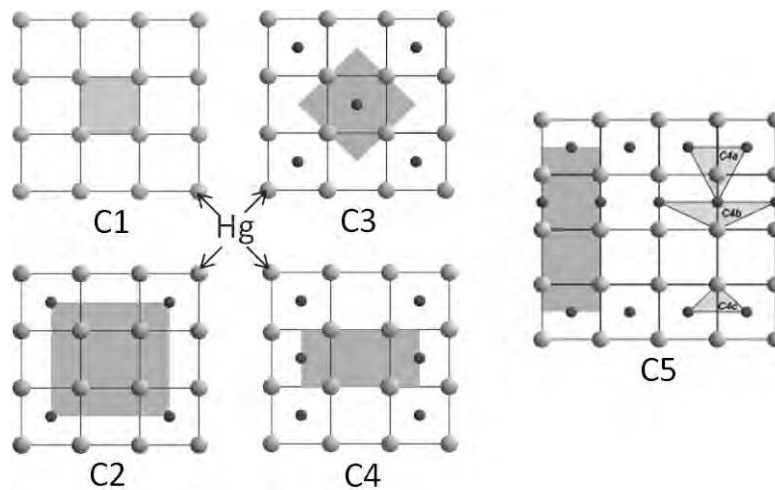


Figure 4.13: Representation of the Hg planes of Hg-1212 as viewed along the c axis. Shaded regions represent the different supercells used into the FLAPW simulations with different O_δ concentrations ($\delta= 0$ to 0.66).

Fig. 4.13-C1 shows the undoped supercell with $m=1$ and $n=0$, where there are no dopant oxygen

in the neighborhood of Hg atoms. This supercell has the highest $|V_{zz}|_{C1}$ at the Hg site and nil asymmetry parameter due to the tetragonal symmetry.

In order to calculate the effect of the single O_δ doping in the Hg planes, four doped supercells have been constructed with nominal δ of 0.25, 0.50 and 0.66. Fig. 4.13-C2 shows the supercell (m=4, n=1) where Hg atoms interact with one single dopant oxygen, which is located in the center of the Hg mesh. C2 shows a non symmetric EFG with a lower $|V_{zz}|_{C2} \sim 562 \text{ V}/\text{\AA}^2$ and a highly distorted local environment given by $\eta_{C2} = 0.7$. Figs. 4.13-C3 and 4.13-C4 display two local configurations (m=2 and n=1 supercells) existing for Hg atoms interacting with two O_δ , both having the same nominal concentration $\delta=0.50$. Even if these two configurations have the same nominal δ , the different oxygen rearrangement causes changes in the EFG parameters. The supercell C3 represents O_δ arranged in a checkerboard-like pattern where the Hg- O_δ bonds make 180° . In this case, $|V_{zz}|_{C3} = 572 \text{ V}/\text{\AA}^2 \sim |V_{zz}|_{C2}$ and $\eta_{C3} = 0.66$ is slightly lower than η_{C2} . The simulation represented by the supercell C4 corresponds to the situation where O_δ is distributed along interstitial rows parallel to the b axis and the Hg- O_δ bonds make 90° . C4 has a lower $|V_{zz}|_{C4} = 496 \text{ V}/\text{\AA}^2$ than the previous cases and an almost nil asymmetry parameter $\eta_{C4} \sim 0.02$.

Fig. 4.13-C5 (m=3, n=3) shows a supercell with three non equivalent Hg atoms leading to different EFG parameters. C5 was created to understand if under O_δ high concentrations, interstitial Hg-Hg bonds could be occupied. This supercell shows quite diverse $|V_{zz}|$ and η values depending on the non-equivalent Hg atoms. The atom noted as C5a has a $|V_{zz}|_{C5a} = 598 \text{ V}/\text{\AA}^2$ comparable to the values presented by C2 and C3 configurations; however the axial asymmetry parameter, $\eta_{C5a} = 0.08$, is almost nil. The Hg atom denoted as C5b has a highly asymmetric local environment with $\eta_{C5b} = 0.7$ though its $|V_{zz}|_{C5b} = 548 \text{ V}/\text{\AA}^2$ is also in the same range of C2, C3 and C5a. The third non-equivalent Hg atom (C5c) has the smallest $|V_{zz}|_{C5c} = 86 \text{ V}/\text{\AA}^2$ and an axially symmetric local environment revealed by $\eta_{C5c} \sim 0.09$. It is further pointed that interstitial O_δ along Hg-Hg bonds alone is not stable. Therefore, the C5 supercell was designed as the simplest distribution of O_δ that could stabilize the oxygen dopant in the Hg-Hg bonds.

The configurations C2, C3 and C4, now denoted by C2*, C3* and C4*, have been further used assuming the location of a $O_{2\delta}$ dumbbell molecule instead of a single O_δ in the Hg planes. As expected, the insertion of a molecule in the Hg planes led to changes in the EFG's at the Hg site regarding single O_δ cases. The C2* supercell shows a configuration where Hg atoms interact with one

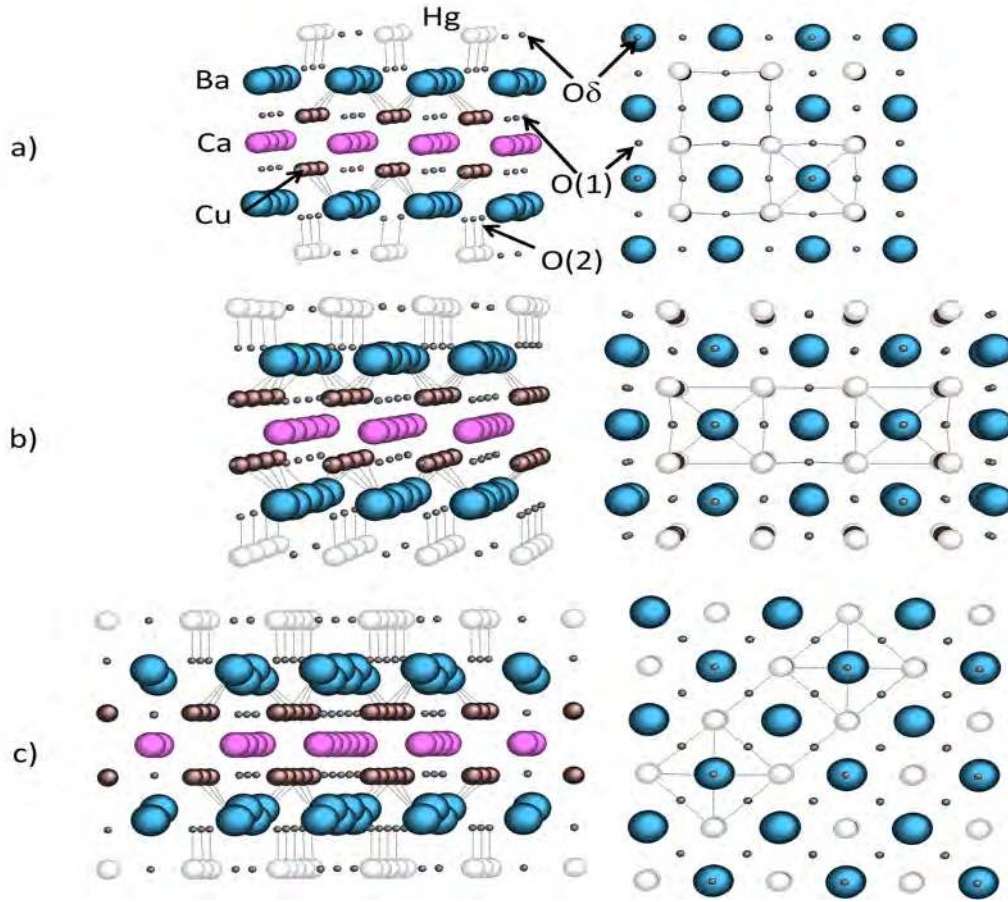


Figure 4.14: Artistic view of the Hg-1212 supercell structures C2, C3 and C4, as obtained from the FLAPW calculations, which were used to calculate the EFGs: (Left) projections of the lattice along the c axis and (Right) projections along the plane perpendicular to the c axis.

$O_{2\delta}$ dumbbell, with local nominal $\delta=0.5$, that is located at the centre of the Hg mesh. Differently from C2, this configuration originates a slightly non axially-symmetric EFG with $|V_{zz}|_{C2^*}=694 \text{ V/\AA}^2$ and $\eta_{C2^*}=0.16$. The two local configurations C3* and C4* have now nominal local $\delta=1$. C3* reproduces the checkerboard-like pattern although the resulting EFG parameters are different from C3 with $|V_{zz}|_{C3^*}=662 \text{ V/\AA}^2$ and $\eta_{C3^*}=0.33$. In the C4* configuration, the Hg atoms interact with oxygen dumbbells distributed along rows parallel to the c axis. In this case, an axially symmetric EFG with $|V_{zz}|_{C4^*}=670 \text{ V/\AA}^2$ and $\eta_{C4^*}=0.05$ is found.

Figure 4.14 shows a three dimensional (3D) artistic view of the relaxed C2, C3 and C4 supercells to help visualizing these atomic shifts. The atomic relaxation resulting from the C2*, C3* and

Table 4.10: Calculated EFG parameters for all atoms on the relaxed Hg-1212+ single O_6 supercells. The inserted figures show the Hg planes of different supercells, presented as shadowed regions. Light/dark symbols represent Hg/O atoms.

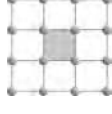
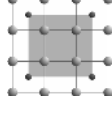
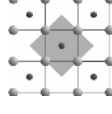
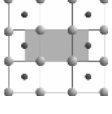
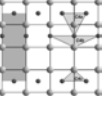
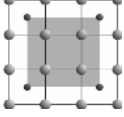
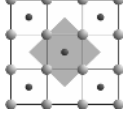
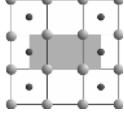
										
	Supercell C1		Supercell C2		Supercell C3		Supercell C4		Supercell C5	
	$\delta O=0$		$\delta O=0.25$		$\delta O=0.50$		$\delta O=0.50$		$\delta O=0.66$	
	V_{zz}	η	V_{zz}	η	V_{zz}	η	V_{zz}	η	V_{zz}	η
	$V/\text{\AA}^2$		$V/\text{\AA}^2$		$V/\text{\AA}^2$		$V/\text{\AA}^2$		$V/\text{\AA}^2$	
Hg_a	-734.96	0	-561.81	0.734	-572.39	0.661	-496.39	0.023	-598.78	0.080
Hg_b	-	-	-	-	-	-	-	-	-547.74	0.703
Hg_c	-	-	-	-	-	-	-	-	86.23	0.091
Ba_a	-	-	-100.75	0	97.16	0	-79.74	0.036	-66.54	0.220
Ba_b	55.33	0	82.50	0.098	-	-	100.01	0.007	32.51	0.435
Ba_b'	-	-	88.35	0	-89.14	0	-	-	127.45	0.425
Ca_a	-9.54	0	-12.74	0	-14.40	0	-15.89	0.427	-14.38	0.945
Ca_b	-	-	-14.53	0	-14.56	0	-14.74	0.312	-21.74	0.356
Ca_c	-	-	-13.37	0.6010	-	-	-	-	-14.19	0.271
Cu_a	-8.66	0	-	-	-	-	-	-	-47.52	0.012
Cu_b	-	-	-52.98	0.006	-	-	-	-	-58.77	0.030
Cu_c	-	-	-	-	-60.86	0.027	-	-	-53.28	0.003
Cu_d	-	-	-	-	-	-	-63.42	0.032	-	-
O(1)_a	128.50	0.307	149.58	0.219	145.76	0.199	-	-	156.22	0.272
O(1)_b	-	-	152.20	0.219	-	-	151.50	0.214	153.66	0.320
O(1)_c	-	-	-	-	-	-	155.08	0.220	151.99	0.200
O(1)_d	-	-	-	-	-	-	147.31	0.020	151.82	0.325
O(1)_e	-	-	-	-	-	-	-	-	155.19	0.245
O(1)_f	-	-	-	-	-	-	-	-	155.90	0.212
O(1)_g	-	-	-	-	-	-	-	-	186.55	0.042
O(1)_h	-	-	-	-	-	-	-	-	150.91	0.107
O(1)_i	-	-	-	-	-	-	-	-	146.76	0.021
O(2)_a	140.68	0	140.44	0.143	-	-	-	-	-	-
O(2)_b	-	-	-	-	-	-	-	-	-	-
O(2)_c	-	-	-	-	155.30	0.214	-	-	-	-
O(2)_d	-	-	-	-	-	-	147.31	0.020	204.72	0.198
O(3)_a	-	-	-90.72	0	-137.98	0	-	-	-	-
O(3)_b	-	-	-	-	-	-	-	-	-122.72	0.631
O(3)_c	-	-	-	-	-	-	-87.46	0.801	-	-

Table 4.11: Calculated EFG parameters for all atoms on the relaxed Hg-1212+ O_{2δ} dumbbells supercells. The inserted figures show the Hg planes of different supercells, presented as shadowed regions. Light/dark symbols represent Hg/O atoms.

						
	Supercell C2*		Supercell C3*		Supercell C4*	
	$\delta O=0.25$		$\delta O=0.50$		$\delta O=0.50$	
	V_{zz}	η	V_{zz}	η	V_{zz}	η
	$V/\text{\AA}^2$		$V/\text{\AA}^2$		$V/\text{\AA}^2$	
Hg_a	-694.40	0.156	-661.98	0.327	-669.48	0.049
Ba_a	-193.84	0	87.38	0	117.55	0.533
Ba_b	104.20	0	-	-	-180.88	0.206
Ba_b'	73.80	0.622	-147.72	0	-	-
Ca_a	-11.82	0	-11.66	0	-12.45	0.993
Ca_b	-11.83	0.934	-	-	7.80	0.174
Ca_c	-4.03	0	2.54	0	-	-
Cu_b	-39.29	0.002	-	-	-	-
Cu_c	-	-	-43.92	0.024	-	-
Cu_d	-	-	-	-	-49.21	0.027
O(1)_a	147.75	0.241	-	-	-	-
O(1)_b	146.85	0.235	152.28	0.220	152.85	0.159
O(1)_c	-	-	-	-	153.39	0.195
O(1)_d	-	-	-	-	154.80	0.196
O(2)_b	142.99	0.122	-	-	-	-
O(2)_c	-	-	130.35	0.032	-	-
O(2)_d	-	-	-	-	140.26	0.086
O(3)_a	228.62	0	-	-	-	-
O(3)_b	-	-	207.83	0	-	-
O(3)_c	-	-	-	-	208.86	0.064

C4* supercells are not presented since they are smaller than the single O_δ cases. The structural relaxation has a major effect on the barium and apical oxygen sites ($O(2)$), where strong shifts in the c -axis are observed due to the placement of O_δ in the interstitial sites of the Hg mesh.

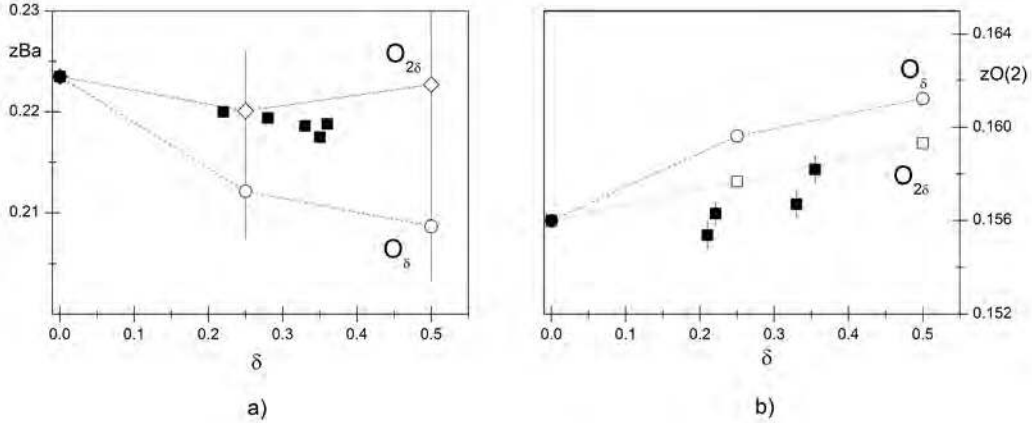


Figure 4.15: Plot of relative z coordinates for: a) barium and b) apical oxygen as a function of dopant oxygen, δ . The data includes values reported in the literature^[37,52,55] (dark symbols) and from FLAPW calculations for different supercells with single O_δ (open dots) and with $O_{2\delta}$ dumbbell molecules (open squares). The calculated values are normalized to the neutron powder diffraction ones for the undoped case.

The effect of structural relaxation in the relative z coordinates for barium and apical oxygen along the c -axis as calculated for the different configurations as function of δ is plotted in figure 4.15, together with available data taken from the literature. When non equivalent atomic positions exist for barium, the points represent the average calculation accounting the multiplicity of the non-equivalent atoms. For completeness of the discussion, the parameters of C* configurations are included keeping in mind that the true local dopant oxygen concentration of these supercells is obtained by multiplying δ by two due to the dumbbell configuration. Some conclusions can be already drafted based on the calculated data, which will help later on the interpretation of the experimental data. The present calculations have been performed for different $O_\delta/O_{2\delta}$ doping configurations, considering both unrelaxed and relaxed supercells. The relaxation of the atomic positions was done in a self-consistent way by minimizing atomic forces, which has important effects on some of the atomic internal parameters. In detail, the structural relaxation has a major effect on the barium and apical oxygen sites ($O(2)$), where strong shifts in the c -axis are observed

due to the placement of O_δ in the interstitial sites of the Hg mesh. This effect can be explained in the frame of an ionic picture where positive Ba ions are more attracted to the Hg doped layer while the apical oxygen atoms are further repelled. Consequently, the EFG at the Hg site was found to be largely affected from one configuration to the other depending essentially on the symmetry and local relaxations.

The simulations with the oxygen dumbbell molecule show less asymmetric local environments than the ones obtained with single O_δ atoms. On the other hand, the $|V_{zz}|$ magnitude shows an increase when compared with the single O_δ values though all $|V_{zz}|$ are quite similar, ranging between $670 \text{ V}/\text{\AA}^2$ and $700 \text{ V}/\text{\AA}^2$. Following again an ionic picture, the existence of a molecule sharing less charge than a single O_δ causes smaller shifts in the barium and apical oxygen positions leading to a smaller variations on $|V_{zz}|$ and η .

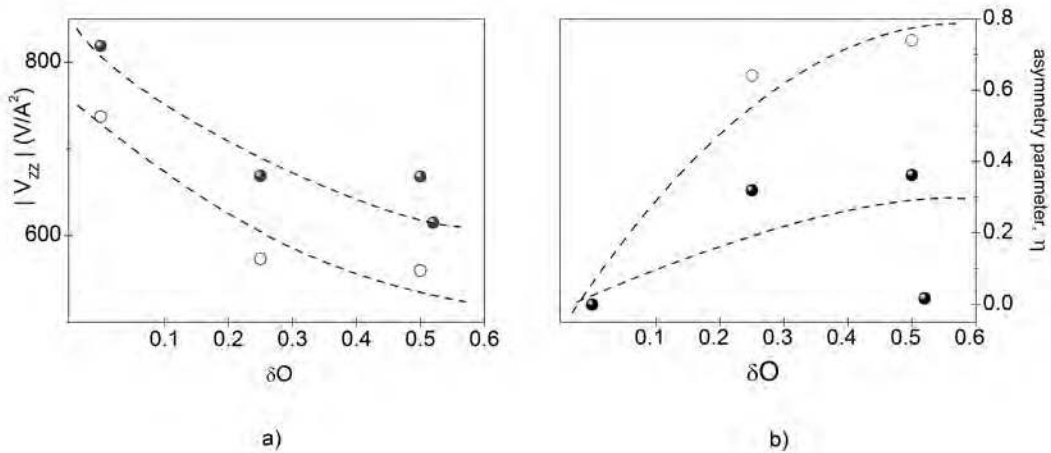


Figure 4.16: a) Evolution of the principal component of the EFG tensor, V_{zz} , and b) asymmetry parameter, η , with oxygen doping obtained from FLAPW calculation for different Hg-1201 supercells. The closed dots refer to unrelaxed structures^[57,58] and the open dots to the relaxed structures.

One shall stress that the present results are essentially different from the ones reported on the single layer compound (Hg-1201)^[57] since structural relaxation could not be performed due to software limitations. To confirm the importance of the relaxation of the atomic positions, calculations on Hg-1201 have been repeated allowing the atoms to move. Figure 4.16 shows the influence of the structural relaxation on the EFG parameters of Hg-1201 as function of oxygen doping for supercells accounting for single O_δ atoms. The structural relaxation in Hg-1201 also

leads to large changes in the EFG parameters, which were found to be much different from the reported previously^[57] and in very good agreement with the ones obtained for Hg-1212.

4.4 Discussion

When comparing the average experimental EFG parameters ($|V_{zz}|$ and η) with the simulated ones at the Hg sites (summarized in tables 4.10 and 4.11), it is possible to observe a good matching for some cases of the simulated configurations. Due to the similarity of the obtained EFG parameters on both Hg-1212 and Hg-1223 samples, the average EFG values of E1, E2 and E3 will be used in the comparison between experimental and calculated data.

Figure 4.17 plots the experimental and simulated EFG values obtained for O_δ and $O_{2\delta}$ cases, respectively, for clearness of the discussion. The axially symmetric experimental distribution E1 is assigned to Hg atoms in regular sites of the lattice without dopant oxygen or other defects in their neighborhood, corresponding to the EFG calculated within the C1 configuration. This EFG has the highest $|V_{zz}|$ and a nil asymmetry parameter in agreement with previous reports on Hg-1201^[57,58]. Still $|V_{zz}|_{C1}$ is smaller than the one observed experimentally though the nil asymmetry parameter allows the correct assignment to the C1 configuration.

The non-axially symmetric EFG distribution E2 can be assigned to C2* or C3* configurations where both experimental and simulated EFG parameters are in good agreement. Both C2* and C3* configurations have similar $|V_{zz}|$ parameters although the experimental η privileges the C2* configuration. This result evidences that the $O_{2\delta}$ molecules might be competing with single O_δ atoms when doping these compounds. One shall point that only single O_δ atoms were reported for Hg-1201^[57], but in that work the determinant factor for the EFG parameters calculation, i.e., structural relaxation could not be taken into account in the simulations, as referred previously. Additionally, the existence of $O_{2\delta}$ molecules was not there considered. In the present C2* configuration each Hg atom interacts with a oxygen dumbbell molecule which is located in interstitial sites in the centre of the Hg mesh with relative coordinates $(\pm 1/2, \pm 1/2, z_{Hg})$.

The highly asymmetric experimental distribution E3 presents EFG parameters which in a direct comparison with the calculated data could be assigned to more than one configuration. C4 and C4* configurations of O_δ or $O_{2\delta}$ that would correspond to stripe-like ordering of the dopants do

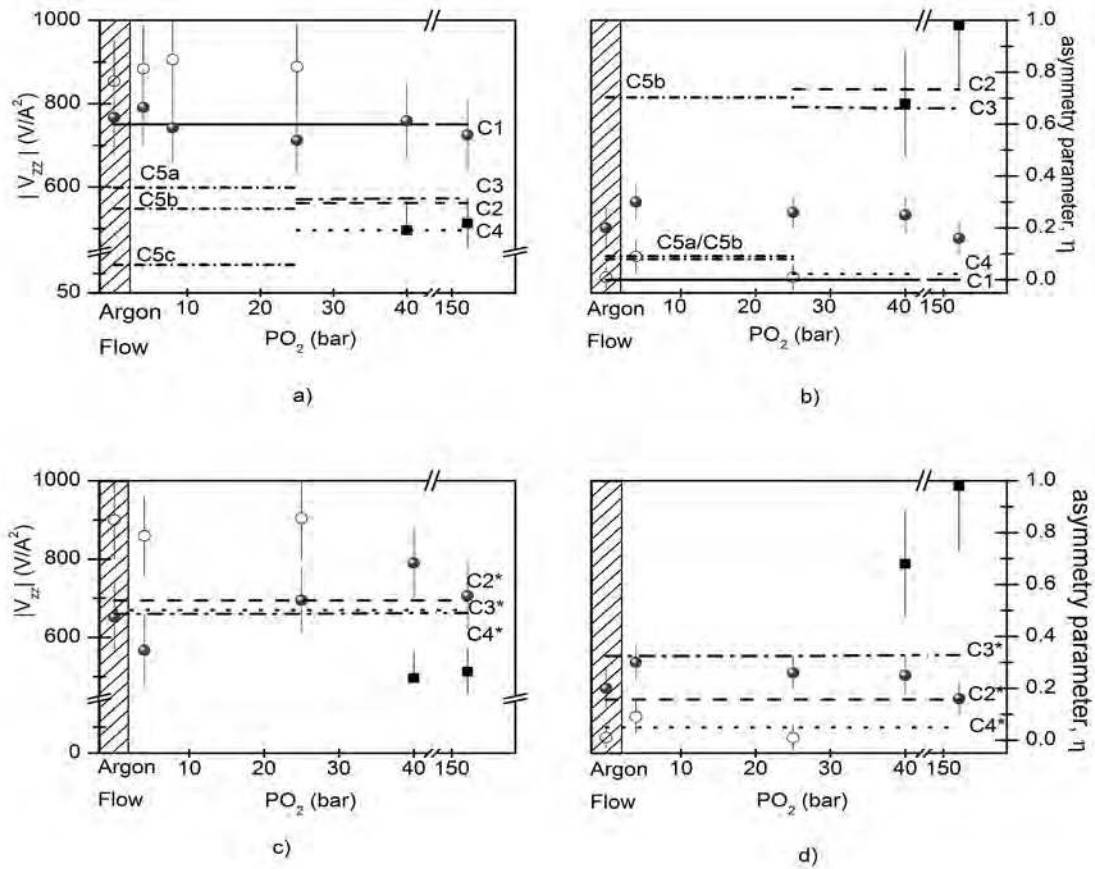


Figure 4.17: Experimental and simulated EFG parameters: a), c) principal component of the EFG tensor, V_{zz} ; and b), d): asymmetry parameter, η . The calculated EFG parameters for (top) Hg-1212+single O_δ and (bottom) Hg-1212+dumbbells $O_{2\delta}$ supercells are represented by the horizontal lines.

not find experimental equivalent. The good matching between the experimental and simulated $|V_{zz}|$ and η is found for C2, C3 and C5 configurations where only single O_δ atoms play a role. Starting with C5 supercell, at a first sight, one of the three non-equivalent Hg atoms (C5b) could explain the experimental distribution E3. However, the present simulations have shown that the C5b configuration is not a stable alone, without O_δ in adjacent cells. Therefore the other two EFGs generated by C5a and C5c should be experimentally observed. However the fitting analysis has excluded these two EFGs; consequently the full C5 configuration is excluded what agrees with the assumption that dopant O_δ atoms cannot occupy interstitial Hg-Hg bonds. In fact, the location of O_δ atoms in the Hg-Hg bonds was found to be energetically stable only in the cases of partial

substitution of Hg by Cu^[32,192].

Looking now to C2 and C3 configurations, the direct comparison between simulated and experimental EFG parameters is not sufficient to clearly assign one of these configurations. Therefore, an estimation of the dopant concentration, δ_{PAC} , within the ^{199m}Hg probing sample region will be performed. It is well known that T_{C} reaches its maximum value for an optimal value of oxygen doping (δ_{opt}) being this value approximately equal to 0.22^[37,52,55,193] and 0.27^[39,193], for Hg-1212 and Hg-1223 respectively. Moreover, the maximum dopings (δ_{max}) reported for these compounds is $\sim 0.30(3)$ ^[37,52,55,193]. From XRD measurements, the present samples after synthesis have $\delta(\text{Hg-1212})=0.22(3)$ and $\delta(\text{Hg-1223})=0.25(3)$, values that are in good agreement with the optimal doping for these compounds. After PAC experiments, the oxygen abundances can be quite different. To infer δ_{PAC} from the PAC E1, E2 and E3 fractions, the number of single O_{δ} or $\text{O}_{2\delta}$ dumbbells interacting with the probing nuclei is considered. The EFG calculations showed that E2 accounts for the Hg atoms that have single $\text{O}_{2\delta}$ dumbbell (C2*) in their neighborhood. Since each molecule can be *seen* by four Hg atoms, the corresponding δ_{PAC} abundance is given by $\delta_{\text{PAC}}(\text{C2}^*) = f_2/2$. Two abundances can be calculated depending on the assignment of E3 to either C2 or C3 configurations. Assuming on one hand that each Hg atom has only one O_{δ} in its neighborhood (C2), the corresponding PAC abundance shall be given by $\delta_{\text{PAC}}(\text{C2}) = f_3/4$. On the other hand, if each Hg atom is surrounded by two O_{δ} , in a checkerboard configuration (C3), the abundance will be given by $\delta_{\text{PAC}}(\text{C3}) = f_3/2$. The total δ_{PAC} per sample is thus given by the sum of all contributions, assuming either C2 or C3 configurations coexisting with C2*. Assuming the coexistence of both C2* and C3, with estimated $\delta_{\text{PAC}} \sim 0.5$, the local doping abundances are well above the reported dopant concentration limit allowed for Hg-1212, i.e. $\delta \sim 0.35$. Contrarily, the coexistence of C2* and C2 configurations leads to $\delta_{\text{PAC}} \sim 0.4$ more compatible with the reported dopant concentrations for Hg-1212 and Hg-1223. Although the coexistence of C2 and C2* are privileged for the majority of the experiments, one shall stress that in Hg-1223 under 152 bar oxygen the higher η_2 suggest a possible checkerboard ordering of $\text{O}_{2\delta}$ dumbbells (C3* configuration) in coexistence with C2 configuration, induced by the high oxygen pressure. Due to the particular case of the ^{199m}Hg implantation process, PAC technique is sensitive to regions near the surface on samples that can be inhomogeneously doped. Local dopant concentrations, as estimated from the PAC fractions, must be interpreted within the limited number of the dopant configurations here reported. Moreover,

the present results suggest the existence of $O_{2\delta}$ molecules coexisting with single O_δ atoms what has not been yet reported experimentally nor theoretically, with different local ordering for different compounds.

These experiments hint the break of the $O_{2\delta}$ dumbbell upon oxygen pressure increase. This further suggests that single O_δ and $O_{2\delta}$ have different solubilities. The dynamics of this process might be related with the atomic mobility, with the charge of the dopant and with the number of available copper planes in this type of compounds. Additionally, these should be short range effects since the ordering cannot build up coherently too far without originating deformed superlattices which would be seen by diffraction techniques. In fact, in the numerous neutron diffraction and X-ray scattering studies performed in the Hg-based series^[30,31,39,51,55,122] there was no indication or suggestion of the existence of molecules at the Hg planes. In fact, the main focus of those studies was concerned to the location of the interstitial oxygen which has been reported as sitting at the centre of the Hg mesh ($1/2, 1/2, z_{\text{Hg}}$) in agreement with the position found in the present work.

Besides the main focus on the location of O_δ in the Hg planes, the diffraction techniques present other limitations which can inhibit the observation of different oxygen species. A common problem was related to the high thermal factor obtained for Hg, which has been attributed to Hg substitution^[31] or to the high absorption cross-section of Hg for neutrons^[122]. Furthermore, it was suggested that the high thermal factors could hint for the existence of a different defect or instability although no experimental evidence for its nature was found. In addition, a non uniform dopant distribution, as found in this work, complicates the analysis via techniques that make use of coherence or average oxygen concentration such as neutron powder diffraction (NPD). Nevertheless, to confirm the possibility of $O_{2\delta}$ measurement using diffraction techniques, NPD patterns have been simulated assuming the presence of single O_δ atoms and $O_{2\delta}$ dumbbells in C2 and C2* configurations. Figure 4.18 shows both simulated NPD patterns together with experimental data obtained for Hg-1212 at room temperature^[59]. The comparison between the simulated and experimental data shows that all Hg-1212 reflections are present although there are differences in the intensities that can be attributed to the low statistics of the measurement. On the other hand, the simulated spectra with single O_δ and with $O_{2\delta}$ dumbbells gave essentially the same result showing that when using diffraction techniques different oxygen species cannot be differentiated. This result confirms the limitation of diffraction techniques in the observation of different oxygen

species, which have been assumed in single atom form in the numerous structural reports in the Hg-based series of superconductors. Furthermore, these results confirm the possibility of the existence of $O_{2\delta}$ dumbbells in coexistence with single O_δ atoms.

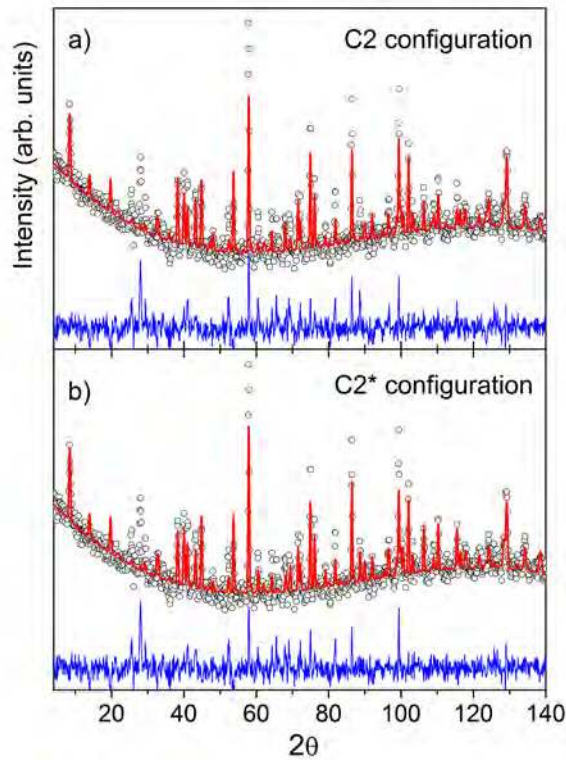


Figure 4.18: Neutron powder diffraction simulated spectra for: a) relaxed structure according to C2 configuration, and b) relaxed structure according to C2* configuration. The open dots represent the experimental data taken from^[59] and the line at the bottom represents the difference.

At a first sight the existence of $O_{2\delta}$ in competition with O_δ in the Hg planes could seem a justification for the systematic differences reported between the measured atomic dopant concentration and the number of holes created at the copper planes^[29,30]. However, these differences have been attributed to the existence of monovalent oxygen^[29] showing that the ionic model is inappropriate to describe the hole doping mechanism. Nevertheless, those results do not exclude the presence of $O_{2\delta}$ molecules at the Hg planes since it has been already suggested the presence of superoxide molecules (O_2^-) in $La_2CuO_{4+\delta}$ ^[123,194]. However there is not in FLAPW an unique way to assign separate charge density regions to each atom, i.e., to clearly define the spacial confinement of charge of an ion not allowing the confirmation of the existence of monovalent oxygen species as

reported^[29,194]. It shall be stressed that the calculations clearly showed that the charge transferred by the $O_{2\delta}$ molecules to the copper planes is much smaller than the one transferred by single O_δ atoms. Techniques like EPR, IR spectroscopy and mass spectrometry could be sensitive to the existence of low concentration oxygen anomalies but its detection and characterization in the Hg-based superconductors is quite difficult due to its high reactivity and easy decomposition. On the other hand, the PAC technique combined with powerful simulation techniques of atomic modelling provide unique ways to characterize nanoscopic phenomena which could not be unveiled in other ways. These studies would be ideally continued on single crystals where the orientation could be used to compare with the oxygen configuration models.

Chapter 5

Conclusions and Perspectives

The main results and conclusions of each chapter have been already presented and discussed. Here, a brief summary of these conclusions will be presented in a more general perspective. Some suggestions for future research are also proposed.

The quality of the synthesized samples is of great importance and the presence of impurities may lead to ambiguity in the interpretation of the experimental results. Hence, a big effort has been made in this work in order to develop and optimize the synthesis parameters of the studied systems. Therefore, all samples presented in this thesis have been the result of a systematic study of the optimal conditions to obtain pure and homogeneous samples. The sol-gel method, within the urea co-precipitation route, has been applied successfully in the production of polycrystalline rare-earth manganites and of Ba-Ca-Cu-O precursor powders. In the later case, this sol-gel route has been applied successfully for the first time in this work allowing the preparation of high purity powders in shorter processing times. Additionally, the use of mechanical induced reactions via high pressure methods has been also employed in the synthesis of Hg-based superconductors family, where a systematic study of the synthesis conditions has been performed.

Then, the combination of bulk characterization and nuclear techniques proved to be extremely useful to address the issues related with local distortions and dopants ordering in two representative families of strongly correlated electron systems, namely the rare-earth manganites and Hg-based superconductors.

First, a systematic study of the bulk properties has been performed via structural and magnetic characterization in order to obtain detailed knowledge on the macroscopic properties of the studied

systems. This information is crucial to engage on a atomic scale study of strongly correlated electron systems.

The local scale information has been obtained using the perturbed angular correlations technique to measure the electrical field gradients at the rare-earth sites in the RMnO_3 manganites, and at the Hg sites in the Hg-based superconductors series.

The PAC study of the EFG at the rare-earth sites in a series of hexagonal and orthorhombic RMnO_3 has been performed via the ^{111}Cd probe state. In the hexagonal RMnO_3 (R=Lu, Er, Y, and Ho) series, two experimental EFG distributions were found. *Ab-initio* EFG calculations showed that only one of the experimental EFG distributions can be assigned to the regular rare-earth sites whereas the second distribution cannot be assigned to the regular rare-earth or manganese sites. The temperature dependence of the EFG parameters showed that the two EFG distributions coexist up to the structural transition temperature range. Above the ferroelectric transition temperature, a continuous increase of the regular rare-earth site EFG distribution up to 100% is observed, that seems to occur near the reported structural transition. Therefore, these results suggest that the second EFG distribution might be due to distorted rare-earth sites.

In the orthorhombic RMnO_3 (R=Tb, Gd, Eu, Sm, and Nd) series, the coexistence of two experimental EFG distributions was also found. Following symmetry considerations, only one EFG distribution is allowed in the regular rare-earth sites. *Ab-initio* EFG calculations confirmed that the lower frequency EFG distribution is assigned to the rare-earth sites while the second EFG distribution cannot not be assigned to the regular rare-earth or manganese sites. Furthermore, the evolution of EFG distributions showed a strong dependence with the rare-earth ionic radius. The origin of the second EFG is not clear and the PAC results show that the crystalline structure is not sufficient to explain the coexistence of local environments in the orthorhombic RMnO_3 .

The EFG study across the series of hexagonal and orthorhombic manganites show that the changes in the hexagonal-orthorhombic structure are predominantly attributed to changes in the fraction of the local environments and in the distortion degree (asymmetry parameter).

The oxygen ordering at the Hg planes in Hg-based superconductors has been studied via the measurement of the EFG at the Hg sites. The EFGs have been studied as function of oxygen doping on the Hg planes, above and below T_C . For all studied cases, the experimental results showed that at a local scale there is non-uniform oxygen distribution. A series of *ab-initio* EFG calculations

allowed to infer that at low oxygen concentrations, regions without oxygen coexist with regions where $O_{2\delta}$ dumbbell molecules are located at the centre of the Hg mesh. On the other hand, at high oxygen concentrations, $O_{2\delta}$ dumbbell molecules coexist with single O_δ atoms occupying the centre of the Hg mesh. The present results hint for the coexistence of differently charged $O_{2\delta}$ and O_δ , which role on the systematic differences reported between effectiveness of charge doping and dopant concentration is not clear.

Perspectives

The present work opened several perspectives for future research in both representative families of strongly correlated electron systems. In this context, a summary of topics for future work are presented:

A complementary local scale study in the magneto-electric manganites system should be performed in order to verify the nature of the distortions observed at the rare-earth sites using other local probe techniques as for example pair distribution function.

The high temperature EFG dependence in the hexagonal manganites and its relation with the debated intermediate high temperature phase should be extended to the entire series in order to study the influence of the rare-earth ionic radius in the formation of this high temperature phase. Indeed, measurements at high temperature are crucial to clarify the discrepancies reported between the ferroelectric and structural transitions temperatures.

The PAC studies in the orthorhombic $RMnO_3$ can be also extended with the metastable small rare-earth compounds, which are expected to give considerable insights in the origin and stability of the possible rare-earth local distortion.

Concerning the high temperature superconductors, the PAC measurements in Hg-based single crystals should give additional information on the non uniform dopant distribution at a local scale could confirm the observation of oxygen dumbbell molecules at the Hg planes.

List of Articles

In the course of this study, several contributions were made to the scientific community: 3 scientific published papers, 16 oral presentations and 6 poster presentations. The list of accepted and published publications originating directly from this work is the following:

1. "*Oxygen ordering in the high T_C superconductor $HgBa_2CaCu_2O_{6+\delta}$ as revealed by perturbed angular correlation*", T.M. Mendonça, J.G. Correia, H. Haas, P. Odier, P.B. Tavares, M.R. da Silva, A.M.L. Lopes, A.M. Pereira, J.N. Gonçalves, J.S. Amaral, C. Darie, J.P. Araujo, Physical Review B 84, 094524 (2011)

2. "*The Urea Combustion Method in the Preparation of Precursors for High- T_C Single Phase $HgBa_2Ca_2Cu_3O_{8+\delta}$ Superconductor*", T.M. Mendonça, P.B. Tavares, J.G. Correia, A.M.L. Lopes, J.P. Araujo, Physica C 471, 1643 (2011)

3. "*Perturbed angular correlations studies in the $HgBa_2CaCu_2O_{6+\delta}$ high T_C superconductor*", T.M. Mendonça, J.G. Correia, H. Haas, P. Odier, P.B. Tavares, M.R. da Silva, A.M.L. Lopes, C. Darie, J.P. Araujo, Journal of Superconductivity and Novel Magnetism 24, 1153 (2011)

4. "*Perturbed angular correlations investigations on $YMnO_3$ multiferroic manganite*", T.M. Mendonça, A.M.L. Lopes, J.N. Gonçalves, J.G. Correia, P.B. Tavares, V.S. Amaral, C. Darie, J.P. Araujo, Hyperfine Interactions 197, 83 (2010)

Nevertheless, several collaborations and satellite works also took place, originating related publications:

1. "*Local Distortions in multiferroic $AgCrO_2$ triangular spin lattice*", A.M.L. Lopes, G.N.P. Oliveira, T.M. Mendonça, J. Agostinho Moreira, A. Almeida, J.P. Araújo, V.S. Amaral, J.G. Correia, Physical Review B 84, 014434 (2011)

2. "*Magnetoelectric $AgCrO_2$: A new local insight given by PAC*", G.N.P. Oliveira, A.M.L.

Lopes, T.M. Mendonça, J.P. Araujo, J. Agostinho Moreira, A. Almeida, V.S. Amaral, J.G. Correia, *Hyperfine Interactions* 197, 123 (2010)

3. "*Single crystal growth of BiMnO₃ under high pressure-high temperature*", P. Toulemonde, C. Darie, C. Goujon, M. Legendre, T. Mendonça, M. Álvarez-Murga, V. Simonet, P. Bordet, P. Bouvier, J. Kreisel, M. Mezouar *High Pressure Research* 29:4, 600 (2009)

4. "*Direct evidence for Sb as a Zn site impurity in ZnO*", U. Wahl, J.G. Correia, T. Mendonça, S. Decoster, *Applied Physics Letters* 94, 261901 (2009)

5. "*Spin phonon coupling and magnetoelectric properties: EuMnO₃ versus GdMnO₃*", W.S. Ferreira, J. Agostinho Moreira, A. Almeida, M.R. Chaves, J.P. Araújo, J.B. Oliveira, J.M. Machado Da Silva, M.A. Sá, T.M. Mendonça, P. Simeão Carvalho, J. Kreisel, J.L. Ribeiro, L.G. Vieira, P.B. Tavares, S. Mendonça, *Physical Review B* 79, 054303 (2009)

6. "*Dielectric and magnetic properties of ReMnO₃ (Re=Gd, Eu)*", W.S. Ferreira, J. Agostinho Moreira, A. Almeida, J.P. Araújo, T.M. Mendonça, P. Tavares, P. Simeão and S. Mendonça, *Ferroelectrics* 366, 17 (2008)

Bibliography

- [1] K.A. Müller and G. Bednorz. *Phase separation in cuprate superconductors*. World Scientific, Singapore, 1993.
- [2] M. Imada, A. Fujimori, and Y. Tokura. Metal-insulator transitions. *Reviews of Modern Physics*, 70:1039–1263, 1998.
- [3] E. Dagotto. Complexity in strongly correlated electronic systems. *Science*, 309:257–262, 2005.
- [4] A. Bianconi and N.L. Saini. Nanoscale lattice fluctuations in cuprates and manganites. *Structural Bond*, 114:287–330, 2005.
- [5] G.H. Jonker and J.H. Van Santen. Ferromagnetic compounds of manganese with perovskite structure. *Physica XVI*, 3:337–349, 1950.
- [6] E.O. Wollan and W.C. Koehler. Neutron diffraction study of the magnetic properties of the series of perovskite-type compounds $[(1-x)\text{La},x\text{Ca}]\text{MnO}_3$. *Physical Review*, 100:545–563, 1955.
- [7] X. Fabréges, S. Petit, I. Mirebeau, S. Pailhès, L. Pinsard, A. Forget, M.T. Fernández-Díaz, and F. Porcher. Spin lattice coupling, frustration and magnetic order in multiferroic RMnO_3 . *Physical Review Letters*, 103:067204 (4pp.), 2009.
- [8] W.S. Choi, D.G. Kim, S.S.A. Seo, S.J. Moon, D. Lee, J.H. Lee, H.S. Lee, D.-Y. Cho, Y.S. Lee, P. Murugavel, J. Yu, and T.W. Noh. Electronic structures of hexagonal RMnO_3 (R=Gd, Tb, Dy, and Ho) thin films: optical spectroscopy and first principle calculations. *Physical Review B*, 77:045137 (7pp.), 2008.

- [9] X. Fabrèges, I. Mirebeau, P. Bonville, S. Petit, G. Lebras-Jasmin, A. Forget, G. André, and S. Pailhès. Magnetic order in YbMnO_3 studied by neutron diffraction and Mössbauer spectroscopy. *Physical Review B*, 78:214422 (8pp), 2008.
- [10] H.A. Salama, G.A. Stewart, D.H. Ryan, M. Elouneq-Jamroz, and A.V.J. Edge. A Mössbauer spectroscopy investigation of h- YbMnO_3 . *Journal of Physics: Condensed Matter*, 20:255213 (7pp.), 2008.
- [11] H.J. Lewtas, T. Lancaster, P.J. Baker, S.J. Blundell, and D. Prabhakaram. Local magnetism and magnetoelectric effect in HoMnO_3 studied with muon-spin relaxation. *Physical Review B*, 81:014402 (6pp.), 2010.
- [12] A.M.L. Lopes, J.P. Araujo, V.S. Amaral, J.G. Correia, Y. Tomioka, and Y. Tokura. New phase transition in the $\text{Pr}_{1-x}\text{Ca}_x\text{MnO}_3$ system: evidence for electrical polarization in charge ordered manganites. *Physical Review Letters*, 100:155702(4 pp.), 2008.
- [13] J.G. Bednorz and K.A. Müller. Possible High T_C Superconductivity in the Ba-La-Cu-O System. *Zeitschrift fuer Physics B - Condensed Matter*, 64:189–193, 1986.
- [14] K.I. Kugel, A.L. Rakhmanov, A.O. Sboychakov, F.V. Kusmartev, N. Poccia, and A. Bianconi. A two-band model for the phase separation induced by the chemical mismatch pressure in different cuprate superconductors. *Superconducting Science and Technology*, 22:014007 (7pp), 2009.
- [15] F.V. Kusmartev and M. Saarela. About two component physics of HTSC. *Journal of Superconductivity and Novel Magnetism*, 22:155–163, 2009.
- [16] S. Pathak, V.B. Shenoy, M. Randeria, and N. Trivedi. Competition between antiferromagnetic and superconducting states, electron-hole doping asymmetry, and Fermi-surface topology in high temperature superconductors. *Physical Review Letters*, 102:027002 (4pp), 2009.
- [17] T. Honma and P.H. Hor. Unified electronic phase diagram for hole-doped high T_C cuprates. *Physical Review B*, 77:184520 (16pp), 2008.
- [18] J.E. Hirsch. Hole superconductivity. *Physics Letters A*, 134:451–454, 1989.

- [19] A.N. Pasupathy, A. Pushp, K.K. Gomes, C.V. Parker, J. Wen, Z. Xu, G. Gu, S. Ono, Y. Ando, and A. Yazdani. Electronic origin of the inhomogeneous pairing interaction in the high- T_C superconductor $\text{Bi}_2\text{Sr}_2\text{CaCu}_2\text{O}_{8+\delta}$. *Science*, 320:196–201, 2008.
- [20] K. McElroy, J. Lee, J.A. Slezak, D.-H. Lee, H. Eisaki, S. Uchida, and J.C. Davis. Atomic-scale sources and mechanism of nanoscale disorder in $\text{Bi}_2\text{Sr}_2\text{CaCu}_2\text{O}_{8+\delta}$. *Science*, 309:1048–1052, 2005.
- [21] A. Yazdani. Visualizing pair formation on the atomic scale and the search for the mechanism of superconductivity in high- T_C cuprates. *Journal of Physics: Condensed Matter*, 21:164214 (9pp), 2009.
- [22] A. Damascelli, D. Hussain, and Z.X. Shen. *Review of Modern Physics*, 75:473, 2003.
- [23] K. Ishida, K. Yoshida, T. Mito, Y. Tokunaga, Y. Kitaoka, K. Asayama, A. Nakayama, J. Shimoyama, and K. Kishio. Pseudogap behavior in single crystal $\text{Bi}_2\text{Sr}_2\text{CaCu}_2\text{O}_{8+\delta}$ probed by Cu NMR. *Physical Review B*, 58:R5960, 1998.
- [24] Y. Itoh, J. Machi, S. Adachi, A. Fukuoka, K. Tanabe, and H. Yasuoka. *J. Phys. Soc. Jpn.*, 67:312, 1998.
- [25] M. Fratini, N. Poccia, A. Ricci, G. Campi, M. Burghammer, G. Aeppli, and A. Bianconi. Scale-free structural organization of oxygen interstitials in $\text{La}_2\text{CuO}_{4+y}$. *Nature*, 466:841–844, 2010.
- [26] A. Schilling, M. Cantoni, J.D. Gui, and H.R. Ott. Superconductivity above 130 K in the Hg-Ba-Ca-Cu-O system. *Nature*, 363:56–58, 1993.
- [27] D. Rybicki, J. Haase, M. Greven, G. Yu, Y. Li, Y. Cho, and X. Zhao. Spatial inhomogeneities in single crystal $\text{HgBa}_2\text{CuO}_{4+\delta}$ from ^{63}Cu NMR spin and quadrupole shifts. *Journal of Superconductivity and Novel Magnetism*, 22:179–183, 2009.
- [28] C. Ambrosch-Draxl and E.Ya. Sherman. Inhomogeneity effects in oxygen-doped $\text{HgBa}_2\text{CuO}_4$. *Physical Review B*, 74:024503 (6pp.), 2006.

- [29] D.J. Singh and W.E. Pickett. Unconventional oxygen doping behavior in $\text{HgBa}_2\text{Ca}_2\text{Cu}_3\text{O}_{8+\delta}$. *Physical Review Letters*, 73:476–479, 1994.
- [30] E. Pellegrin, J. Fink, C.T. Chen, Q. Xiong, Q.M. Lin, and C.W. Chu. Experimental hole densities in $\text{HgBa}_2\text{Ca}_{n-1}\text{Cu}_n\text{O}_{2n+2+\delta}$ compounds from near-edge x-ray absorption spectroscopy. *Physical Review B*, 53:2767–2772, 1996.
- [31] Q. Huang, J.W. Lynn, Q. Xiong, and C.W. Chu. Oxygen dependence of the crystal structure of $\text{HgBa}_2\text{CuO}_{4+\delta}$ and its relation to superconductivity. *Physical Review B*, 52:462–470, 1995.
- [32] V.L. Aksenov, A.M. Balagurov, V.V. Sikolenko, V.G. Simkin, V.A. Alyoshin, E.V. Antipov, A.A. Gippius, D.A. Mikhailova, S.N. Putilin, and F. Bouree. Precision neutron-diffraction study of the high- T_C superconductor $\text{HgBa}_2\text{CuO}_{4+\delta}$. *Physical Review B*, 55:3966–3973, 1997.
- [33] P. Raghavan, E.N. Kaufmann, R.S. Raghavan, E.J. Ansaldo, and R.A. Naumann. Sign and magnitude of the quadrupole interaction of ^{111}Cd in noncubic metals: Universal correlation of ionic and electronic field gradients. *Physical Review B*, 13, nř7:2835–2847, 1976.
- [34] S. Blundell. *Magnetism in Condensed Matter*. Oxford University Press, 2001.
- [35] T. Kimura, T. Goto, H. Shintani, K. Ishizaka, T. Arima, and Y. Tokura. Magnetic control of ferroelectric polarization. *Nature*, 426:55–58, 2003.
- [36] M. Tachibana, T. Shimoyama, H. Kawaji, T. atake, and E. Takayama-Muromachi. Jahn-Teller distortion and magnetic transitions in perovskite RMnO_3 (R=Ho, Er, Tm, Yb and Lu). *Physical Review B*, 75:144425, 2007.
- [37] E.V. Antipov, J.J. Capponi, C. Chailout, O. Chmaissem, S.M. Loureiro, M. Marezio, S.N. Putilin, A. Santoro, and J.L. Tholence. Synthesis and neutron powder diffraction study of the superconductor $\text{HgBa}_2\text{CaCu}_2\text{O}_{6+\delta}$ before and after treatment. *Physica C*, 218:348–355, 1993.
- [38] S.M. Loureiro, E.V. Antipov, J.L. Tholence, J.J. Capponi, O. Chmaissem, Q. Huang, and M. Marezio. Synthesis and structural characterization of the 127 K $\text{HgBa}_2\text{CaCu}_2\text{O}_{6.22}$ superconductor. *Physica C*, 217:253–264, 1993.

- [39] J.L. Wagner, B.A. Hunter, D.G. Hinks, and J.D. Jorgensen. Structure and superconductivity of $\text{HgBa}_2\text{Ca}_2\text{Cu}_3\text{O}_{8+\delta}$. *Physical Review B*, 51:15407–15414, 1995.
- [40] A.R. Armstrong, W.I.F. David, I. Gameson, P.P. Edwards, J. J. Capponi, P. Bordet, and M. Marezio. Crystal structure of $\text{HgBa}_2\text{Ca}_2\text{Cu}_3\text{O}_{8+\delta}$ at high pressure (to 8.5 GPa) determined by powder neutron diffraction. *Physical Review B*, 52:15551–15557, 1995.
- [41] P. Odier, A. Sin, P. Toulemonde, A. Bailly, and S. Le Floch. Synthesis of mercury cuprates. *Superconducting Science and Technology*, 13:1120–1128, 2000.
- [42] J.-S. Zhou, J.B. Goodenough, J.M. Gallardo-Amores, E. Moran, M.A. Alario-Franco, and R. Caudillo. Hexagonal versus perovskite phase of manganite RMnO_3 (R=Y, Ho, Er, Tm, Yb, Lu). *Physical Review B*, 74:014422 (7pp), 2006.
- [43] B.B. Van Aken, A. Meetsma, and T.T.M. Palstra. Hexagonal ErMnO_3 . *Acta Crystallographica Section E*, 57:38–40, 2001.
- [44] A. Muñoz, J.A. Alonso, M.J. Martínez-Lope, M.T. Casais, J.L. Martínez, and M.T. Fernández-Díaz. Magnetic structure of hexagonal RMnO_3 (R=Y, sc): thermal evolution from neutron powder diffraction data. *Physical Review B*, 62:9498–9510, 2000.
- [45] J. Park, U. Kong, S.I. Choi, J.-G. Park, C. Lee, and W. Jo. Magnetic structures of ErMnO_3 . *Applied Physics A*, 74:S802–S804, 2002.
- [46] E. Galstyan, B. Lorenz, K.S. Martirosyan, F. Yen, Y.Y. Sun, M.M. Gospodinov, and C.W. Chu. Magnetic hysteretic phenomena in multiferroic HoMnO_3 single crystals and polycrystals with nano- and micrometer particle size. *Journal of Physics: Condensed Matter*, 20:325241 (7pp), 2008.
- [47] R.D. Shannon. Revised effective ionic radii and systematic studies of interatomic distances in halides and chalcogenides. *Acta Crystallographica Section A*, 32:751–767, 1976.
- [48] J.A. Alonso, M.J. Martínez-Lope, M.T. Casais, and M.T. Fernández-Díaz. Evolution of the Jahn-Teller distortion of MnO_6 octahedra in RMnO_3 perovskites (R= Pr, Nd, Dy, Tb, Ho, Er, Y): a neutron diffraction study. *Inorganic chemistry*, 39:917, 2000.

- [49] T. Mori, N. Kamegashira, K. Aoki, T. Shishido, and T. Fukuda. Crystal growth and crystal structures of the LnMnO_3 perovskites: $\text{Ln}=\text{Nd, Sm, Eu}$ and Gd . *Materials Letters*, 54: 238–243, 2002.
- [50] J.M. Chen, T.L. Chou, J.M. Lee, S.A. Chen, T.S. Chan, T.H. Chen, K.T. Lu, W.T. Chuang, H.-S. Sheu, S.W. Chen, C.M. Lin, N. Hiraoka, H. Ishii, K.D. Tsuei, and T.J. Yang. Pressure-induced structural distortion of TbMnO_3 : a combined x-ray diffraction and x-ray absorption spectroscopy study. *Physical Review B*, 79:165110 (7pp.), 2009.
- [51] P.G. Radaelli, J.L. Wagner, B.A. Hunter, M.A. Beno, G.S. Knapp, J.D. Jorgensen, and D.G. Hinks. Structure, doping and superconductivity in $\text{HgBa}_2\text{CaCu}_2\text{O}_{6+\delta}$ ($T_C < 128\text{K}$). *Physica C*, 216:29–35, 1993.
- [52] A. Kareiva, J. Barkauskas, and S. Mathur. Oxygen content and superconducting properties of Hg-based superconductors synthesized by sol-gel method. *Journal of Physics and Chemistry of Solids*, 61:789–797, 2000.
- [53] S.N. Putilin, E.V. Antipov, and M. Marezio. Superconductivity above 120 K in $\text{HgBa}_2\text{CaCu}_2\text{O}_{6+\delta}$. *Physica C*, 212:266–270, 1993.
- [54] M. Paranthaman and B.C. Chakoumakos. Crystal chemistry of $\text{HgBa}_2\text{Ca}_{n-1}\text{Cu}_n\text{O}_{2n+2+\delta}$. *Journal of Solid State Chemistry*, 122:221–230, 1996.
- [55] O. Chmaissem, L. Wessels, and Z.Z. Sheng. Synthesis and characterization of $\text{HgBa}_2\text{Ca}_{n-1}\text{Cu}_n\text{O}_{2n+2+\delta}$ ($n=1,2$, and 3). *Physica C*, 230:231–238, 1994.
- [56] M. Paranthaman. Single step synthesis of bulk $\text{HgBa}_2\text{Ca}_2\text{Cu}_3\text{O}_{8+\delta}$. *Physica C*, 222:7–12, 1994.
- [57] J.G. Correia, J.P. Araujo, S.M. Loureiro, P. Toulemonde, S. Le Floch, P. Bordet, J.J. Capponi, R. Gatt, W. Tröger, B. Ctortekca, T. Butz, H. Haas, J.C. Marques, J.C. Soares, and the ISOLDE Collaboration. Local O_δ probing in the high T_C superconductor $\text{HgBa}_2\text{CuO}_{4+\delta}$. *Physical Review B*, 61:11769–11775, 2000.
- [58] J.G. Correia, H. Haas, V.S. Amaral, A.M.L. Lopes, J.P. Araujo, S. Le Floch, P. Bordet, E. Rita, J.C. Soares, W. Tröger, and the ISOLDE Collaboration. Atomic ordering of the

- fluorine dopant in the $\text{HgBa}_2\text{CuO}_{4+\delta}$ high- T_C superconductor. *Physical Review B*, 72:144523 (10pp), 2005.
- [59] *ILL database*.
- [60] S. Jin, T.H. Tiefel, M. McCormack, R.A. Fastnacht, R. Ramesh, and L.H. Chen. Thousandfold change in resistivity in magnetoresistive La-Ca-Mn-O films. *Science*, 264:413–415, 1994.
- [61] W. Eerenstein, N.D. Mathur, and J.F. Scott. Multiferroic and magnetoelectric materials. *Nature*, 442:759–765, 2006.
- [62] C. Martin, A. Maignan, M. Hervieu, and B. Raveau. Magnetic phase diagrams of $\text{L}_{1-x}\text{A}_x\text{MnO}_3$ manganites (L=Pr,Sm; A=Ca,Sr). *Physical Review B*, 60:12191–12199, 1999.
- [63] H. Schmid. Multiferroic magnetoelectrics. *Ferroelectrics*, 162:665–685, 1994.
- [64] N. Hur, S. Park, P.A. Sharma, J.S. Ahn, S. Guha, and S.-W. Cheong. Electric polarization reversal and memory in a multiferroic material induced by magnetic fields. *Nature*, 429:392–395, 2004.
- [65] T. Kimura, G. Lawes, and A.P. Ramirez. Electric polarization rotation in a hexaferrite with long wavelength magnetic structures. *Physical Review Letters*, 94:137201 (4 pp.), 2005.
- [66] Y. Yamasaki, S. Miyasaka, Y. Kaneki, J.-P. He, T. Arima, and Y. Tokura. Magnetic reversal of the ferroelectric polarization in a multiferroic spinel oxide. *Physical Review Letters*, 96:207204(4 pp.), 2006.
- [67] M. Gajek, M. Bibes, S. Fusil, K. Bouzehouane, J. Fontcuberta, A. Barthelemy, and A. Fert. Tunnel junctions with multiferroic barriers. *Nature Materials*, 6:296–302, 2007.
- [68] D.I. Khomskii. Multiferroic: different ways to combine magnetism and ferroelectricity. *Journal of Magnetism and Magnetic Materials*, 306:1–8, 2006.
- [69] M. Fiebig. Revival of the magnetoelectric effect. *Journal of Physics D: Applied Physics*, 38:R123–R152, 2005.

- [70] S.-W. Cheong and M. Mostovoy. Multiferroics: a magnetic twist for ferroelectricity. *Nature Materials*, 6:13–20, 2007.
- [71] R. Ramesh and N.A. Spaldin. Multiferroics: progress and prospects in thin films. *Nature Materials*, 6:21–29, 2007.
- [72] H. Schmid. Some symmetry aspects of ferroics and single phase multiferroics. *Journal of Physics: Condensed Matter*, 20:434201–434220, 2008.
- [73] S. Lee, A. Pirogov, M. Kang, K.-H. Jang, M. Yonemura, T. Kamiyama, S.-W. Cheong, S.-W. Gozzo, N. Shin, H. Kimura, Y. Noda, and J.-G. Park. Giant magneto-elastic coupling in multiferroic hexagonal manganites. *Nature*, 451:805–808, 2008.
- [74] J.P. Velev, S.S. Jaswal, and E.Y. Tsymlal. Multi-ferroic and magnetoelectric materials and interfaces. *Philosophical Transactions of the Royal Society A*, 369:3069–3097, 2011.
- [75] D. Khomskii. Classifying multiferroics: mechanisms and effects. *Physics*, 2:20 (8pp.), 2009.
- [76] N. Hur, I.K. Jeong, M.F. Hundley, S.B. Kim, and S.-W. Cheong. Giant magnetoelectric effect in multiferroic HoMnO_3 with a high ferroelectric transition temperature. *Physical Review B*, 79:134120 (4pp.), 2009.
- [77] J. Wang, J.B. Neaton, H. Zheng, V. Nagarajan, S.B. Ogale, B. Liu, D. Viehland, V. Vaithyanathan, D.G. Schlom, U.V. Waghmare, N.A. Spaldin, K.M. Rabe, M. Wuttig, and R. Ramesh. Epitaxial BiFeO_3 multiferroic thin film heterostructures. *Science*, 299:1719–1722, 2003.
- [78] G. Lawes and G. Srinivasan. Introduction to magnetoelectric coupling and multiferroic films. *Journal of Physics D: Applied Physics*, 44:243001 (23pp.), 2011.
- [79] Y. Wang, X. Lu, Y. Chen, F. Chi, S. Feng, and X. Liu. Hydrothermal synthesis of two perovskite rare-earth manganites, HoMnO_3 and DyMnO_3 . *Journal of Solid State Chemistry*, 178:1317, 2005.
- [80] L.-L. Zhu, Y. Chen, K.-K. Huang, G.H. Zhang, W.-W. Hu, H.-M. Yuan, H.B. Chang, and S.-H. Feng. Hexagonal and orthorhombic perovskite phases of ErMnO_3 and TmMnO_3 from hydrothermal systems. *Chemical Research Chinese Universities*, 26 (5):707–711, 2010.

- [81] L.J. Wang, S.M. Feng, J.L. Zhu, Q.Q. Liu, Y.C. Li, X.D. Li, J. Liu, and C.Q. Jin. Structure transition of multiferroic hexagonal TmMnO_3 compound under high pressure. *High Pressure Research*, 30 (2):258–264, 2010.
- [82] Th. Lonkai, D.G. Tomuta, U. Amann, J. Ihringer, R.W.A. Hendrix, D.M. Többens, and J.A. Mydosh. Development of the high temperature phase of the hexagonal manganites. *Physical Review B*, 69:134108 (10pp.), 2004.
- [83] S.C. Abrahams. Ferroelectricity and structure in the YMnO_3 family. *Acta Crystallographica Section B*, 57:485–490, 2001.
- [84] R. Kajimoto, H. Sagayama, K. Sasai, T. Fukuda, S. Tsutsui, T. Arima, K. Hirota, Y. Mitsui, Yoshizawa, A.Q.R. Baron, Y. Yamasaki, and Y. Tokura. Unconventional ferroelectric transition in the multiferroic compound TbMnO_3 revealed by the absence of an anomaly in c -polarized phonon dispersion. *Physical Review Letters*, 102:247602 (4pp.), 2009.
- [85] K. Yoshii and H. Abe. Magnetic properties of LnMnO_3 ($\text{Ln}=\text{Ho}$, Er , Tm , Yb and Lu). *Journal of Solid State Chemistry*, 165:131–135, 2002.
- [86] D.G. Tomuta, S. Ramakrishnan, G.J. Nieuwenhuys, and J.A. Mydosh. The magnetic susceptibility, specific heat and dielectric constant of hexagonal YMnO_3 , LuMnO_3 and ScMnO_3 . *Journal of Physics: Condensed Matter*, 13:4543–4552, 2001.
- [87] B.B. Van Aken. *Structural response to electronic transitions in hexagonal and ortho-manganites*. PhD thesis, Gröningen University, 2001.
- [88] I. Gelard, C. Dubourdieu, S. Pailhès, S. Petit, and Ch. Simon. Neutron diffraction study of hexagonal manganite YMnO_3 , HoMnO_3 and ErMnO_3 epitaxial films. *Applied Physics Letters*, 92:232506 (3pp.), 2008.
- [89] B.B. Van Aken, A. Meetsma, and T.T.M. Palstra. Hexagonal LuMnO_3 revisited. *Acta Crystallographica Section E*, 57:101–103, 2001.
- [90] A.S. Gibbs, K.S. Knight, and P. Lightfoot. High-temperature phase transitions of hexagonal YMnO_3 . *Physical Review B*, 83:094111 (9pp.), 2011.

- [91] H.L. Yakel, W.C. Koehler, E.F. Bertaut, and E.F. Forrat. On the crystal structure of the manganese(III) trioxides of the heavy lanthanides and yttrium. *Acta Crystallographica*, 16: 957–962, 1963.
- [92] G.A. Smolenskii and I.E. Chupis. Ferroelectromagnets. *Sov. Phys. Usp.*, 25:475–493, 1982.
- [93] T.A. Tyson, T. Wu, H.Y. chen, J. Bai, and K.H. Ahn. Measurements and ab initio molecular dynamics simulations of the high temperature ferroelectric transition in hexagonal RMnO₃. *Journal of Applied Physics*, 110:084116 (10pp.), 2011.
- [94] G. Nenert, M. Pollet, S. Marinel, G.R. Blake, A. Meetsma, and T.T.M. Palstra. Experimental evidence for an intermediate phase in multiferroic YMnO₃. *Journal of Physics: Condensed Matter*, 19:466212 (9pp), 2007.
- [95] A. Filippetti and N.A. Hill. Coexistence of magnetism and ferroelectricity in perovskites. *Physical Review B*, 65:195120 (11pp.), 2002.
- [96] B.B. Van Aken, T.M. Palstra, A. Filippetti, and N.A. Spaldin. The origin of ferroelectricity in magnetoelectric YMnO₃. *Nature Materials*, 3:164–170, 2004.
- [97] T. Katsufuji, M. Masaki, A. Machida, M. Moritomo, K. Kato, E. Nishibori, M. Takata, M. Sakata, and K. Ohoyama. Crystal structure and magnetic properties of hexagonal RMnO₃ (R=Y, Lu, and Sc) and the effect of doping. *Physical Review B*, 66:134434 (8pp.), 2002.
- [98] C.J. Fennie and K.M. Rabe. Ferroelectric transition in YMnO₃ from first principles. *Physical Review B*, 72:100103(R) (4pp.), 2005.
- [99] S.C. Abrahams. Atomic displacements at and order of all phase transitions in multiferroic YMnO₃ and BaTiO₃. *Acta Crystallographica Section B*, 65:450–457, 2009.
- [100] Th. Lonkai, D. Hohlwein, J. Ihringer, and W. Prandl. The magnetic structures of YMnO_{3-δ} and HoMnO₃. *Applied Physics A*, 74:S843–S845, 2002.
- [101] A. Muñoz, J.A. Alonso, M.J. Martínez-Lope, M.T. Casáis, J.L. Martínez, and M.T. Fernández-Díaz. Evolution of the magnetic structure of hexagonal HoMnO₃ from neutron powder diffraction data. *Chemistry of Materials*, 13:1497–1505, 2001.

- [102] M. Fiebig, C. Degenhart, and R.V. Pisarev. Interaction of frustrated magnetic sublattices in ErMnO_3 . *Physical Review Letters*, 88:027203 (4pp.), 2002.
- [103] V. Skumryev, M.D. Kuz'min, M. Gospodinov, and J. Fontcuberta. Anisotropic paramagnetic response of hexagonal RMnO_3 . *Physical Review B*, 79:212414 (4pp.), 2009.
- [104] B. Lorenz, A.P. Litvinchuk, M.M. Gospodinov, and C.W. Chu. Field-induced reentrant novel phase and a ferroelectric-magnetic order coupling in HoMnO_3 . *Physical Review Letters*, 92:087204 (4pp.), 2004.
- [105] D. Talbayev, A.D. LaForge, S.A. Trugman, N. Hur, A.J. Taylor, R.D. Averitt, and D.N. Basov. Magnetic exchange interaction between rare-earth and Mn ions in multiferroic hexagonal manganites. *Physical Review Letters*, 101:247601 (4pp.), 2008.
- [106] A.P. Ramirez. *Geometrical frustration. Handbook of Magnetic Materials*. Amsterdam: North-Holland/Elsevier, 2001.
- [107] M. Fiebig, Th. Lottermoser, M.K. Kneip, and M. Bayer. Correlation between magnetic and electrical orderings in multiferroic manganites. *Journal of Applied Physics*, 99:08E302 (5pp.), 2006.
- [108] H.W. Binks, H. Fjellvag, and A. Kjekshus. Synthesis of metastable perovskite-type YMnO_3 and HoMnO_3 . *Journal of Solid State Chemistry*, 129:334–340, 1997.
- [109] J.-S. Zhou and J.B. Goodenough. Universal octahedral-site distortion in orthorhombic perovskite oxides. *Physical Review Letters*, 94:065501 (4pp.), 2005.
- [110] V.M. Goldschmidt. *Geochemistry*. Oxford University Press, 1928.
- [111] J. Rodríguez-Carvajal, M. Hennion, F. Moussa, and A.H. Moudden. Neutron-diffraction study of the Jahn-Teller transition in stoichiometric LaMnO_3 . *Physical Review B*, 57:R3189–R3192, 1998.
- [112] T. Arima, Y. Tokunaga, T. Goto, H. Kimura, Y. Noda, and Y. Tokura. Collinear to spiral spin transformation without changing the modulation wavelength upon ferroelectric transition in $\text{Tb}_{1-x}\text{Dy}_x\text{MnO}_3$. *Physical Review Letters*, 96:097202 (4pp.), 2006.

- [113] M. Kenzelmann, A.B. Harris, S. Jonas, C. Broholm, J. Schefer, S.B. Kim, C.L. Zhang, S.-W. Cheong, O.P. Vajk, and J.W. Lynn. Magnetic inversion symmetry breaking and ferroelectricity in TbMnO_3 . *Physical Review Letters*, 95:087206 (4pp.), 2005.
- [114] T. Goto, T. Kimura, G. Lawes, A.P. Ramirez, and Y. Tokura. Ferroelectricity and giant magnetocapacitance in perovskite rare-earth manganites. *Physical Review Letters*, 92:257201 (4pp.), 2004.
- [115] J. Hemberger, F. Schrettle, A. Pimenov, P. Lunkenheimer, V.Yu. Ivanov, A.A. Mukhin, A.M. Balbashov, and A. Loidl. Multiferroic phases of $\text{Eu}_{1-x}\text{Y}_x\text{MnO}_3$. *Physical Review B*, 75:035118 (8pp.), 2007.
- [116] Y. Kamihara, T. Watanabe, M. Hirano, and H. Hosono. Iron-based layered superconductor $\text{La}[\text{O}_{1-x}\text{F}_x]\text{FeAs}$ ($x=0.05-0.12$) with $T_C=26$ K. *Journal of the American Chemical Society*, 130:3296–3297, 2008.
- [117] X.H. Chen, T. Wu, G. Wu, R.H. Liu, H. Chen, and D.F. Fang. Superconductivity at 43 K in $\text{SmFeAsO}_{1-x}\text{F}_x$. *Nature*, 453:761–762, 2008.
- [118] M. Rotter, M. Tegel, and D. Johrendt. Superconductivity at 38 K in the iron arsenide ($\text{Ba}_{1-x}\text{K}_x\text{Fe}_2\text{As}_2$). *Physical Review Letters*, 101:107006 (4pp.), 2008.
- [119] E.V. Antipov, A.M. Abakumov, and S.N. Putilin. Chemistry and structure of Hg-based superconducting Cu mixed oxides. *Superconducting Science and Technology*, 15:R31–R49, 2002.
- [120] P.G. Radaelli, M. Perroux, M. Marezio, S. de Brion, J.L. Tholence, Q. Huang, and A. Santoro. Synthesis and properties of a cuprate superconductor containing double mercury-oxygen layers. *Science*, 265:380–383, 1994.
- [121] N. Barisic, Y. Li, X. Zhao, Y.-C. Cho, G. Chabot-Couture, G. Yu, and M. Greven. Demonstrating the model nature of the high temperature superconductor $\text{HgBa}_2\text{CuO}_{4+\delta}$. *Physical Review B*, 78:054518 (7pp.), 2008.
- [122] Q. Huang, J.W. Lynn, R.L. Meng, and C.W. Chu. Crystal structure of annealed and as-prepared $\text{HgBa}_2\text{CaCu}_2\text{O}_{6+\delta}$ superconductors. *Physica C*, 218:356–364, 1993.

- [123] K.H. Lee and R. Hoffmann. Oxygen interstitials in superconducting La_2CuO_4 : their valence state and role. *Journal of Physics and Chemistry A*, 110:609–617, 2006.
- [124] A.M. Abakumov, V.L. Aksenov, V.A. Alyoshin, E.V. Antipov, A.M. Balagurov, D.A. Mikhailova, S.N. Putilin, and M.G. Rozova. Effects of fluorination on the structure and superconducting properties of the Hg-1201 phase. *Physical Review Letters*, 80:385–388, 1998.
- [125] V.K. Pecharsky and P.Y. Zavalij. *Fundamentals of Powder Diffraction and Structural Characterization of Materials*. Springer, New York, 2009.
- [126] W.H. Zachariasen. *Theory of X-ray Diffraction in Crystals*. Dover Publications, New York, 1967.
- [127] A. LeBail, H. Duroy, and J.L. Fourquet. *Materials Research Bulletin*, 23:447, 1988.
- [128] J. Rodriguez-Carvajal. Recent Advances in Magnetic Structure Determination by Neutron Diffraction. *Physica B: Condensed Matter*, 192:55–69, 1993.
- [129] Detailed information concerning the experimental setup is available online in <http://www.qdusa.com>.
- [130] J.A.M. Santos. *Magnetismo e fenómenos de transporte com comportamento não-convencional*. PhD thesis, Universidade do Porto, Portugal, 2006.
- [131] R. Roy. Aids in Hydrothermal Experimentation: II, Methods of Making Mixtures for Both 'Dry' and 'Wet' Phase Equilibrium Studies. *Journal of the American Ceramic Society*, 39:145–146, 1956.
- [132] R. Roy. Gel Route to Homogeneous Glass Preparation. *Journal of the American Ceramic Society*, 52:344, 1969.
- [133] L.L. Hench and J.K. West. The sol-gel process. *Chemical Review*, 90:33–72, 1990.
- [134] W. Glaubitt, W. Watzka, H. Scholz, and D. Sporn. Sol-gel processing of functional and structural ceramic oxide fibers. *Journal of Sol-Gel Science and Technology*, 8:29–33, 1997.
- [135] S.N.B. Hodgson and L. Weng. Processing and characterization of sol-gel glasses and powders in the system $\text{TeO}_2\text{-TiO}_2$. *Journal of Materials Science*, 37:3059–3066, 2002.

- [136] M.N. Rahaman. *Ceramic Processing and Sintering*. Marcel Dekker Inc., New York, 2003.
- [137] R.C. Buchanan. *Ceramic Materials for Electronics: Processing, Properties and Applications*. Marcel Dekker Inc., New York, 2004.
- [138] W.D. Kingery. *Ceramic Fabrication Processes*. Technology Press of Massachusetts Institute of Technology, 1968.
- [139] J.K. Kim, S.S. Kim, and W.-J. Kim. Sol-gel synthesis and properties of multiferroic BiFeO₃. *Materials Letters*, 59:4006–4009, 2005.
- [140] N. Das, R. Majumbar, A. Sen, and H.S. Maiti. Nanosized bismuth ferrite powder prepared through sonochemical and microemulsion techniques. *Materials Letters*, 61:2100–2104, 2007.
- [141] V. Samuel, S.C. Navale, A.D. Jadhav, A.B. Gaikwad, and V. Ravi. Synthesis of ultrafine BiMnO₃ particles at 100°C. *Materials Letters*, 61:1050–1051, 2007.
- [142] G. Dezanneau, A. Sin, H. Roussel, H. Vincent, and M. Audier. Synthesis and characterization of La_{1-x}MnO_{3±δ} nanopowders prepared by acrylamide polymerisation. *Solid State Communications*, 121:133–137, 2002.
- [143] M. López-Quintela R.D. Sanchez J. Rivas S.B. Oseroff C. Vázquez-Vázquez, M.C. Blanco. Characterization of La_{0.67}Ca_{0.33}MnO_{3+δ} particles prepared by the sol-gel route. *Journal of Materials Chemistry*, 8:991–1000, 1998.
- [144] J. Sfeir, S. Vaucher, P. Holtappels, U. Vogt, H.-J. Schindler, J. Van herle, E. Suvorova, P. Buffat, D. Perret, N. Xanthopoulos, and O. Bucheli. Characterization of perovskite powders for cathode and oxygen membranes made by different synthesis routes. *Journal of the European Ceramic Society*, 25:1991–1995, 2005.
- [145] A. Sin, P. Odier, and M. Nuñez-Regueiro. Sol-gel processing of precursor for high-T_c superconductors: influence of rhenium on the synthesis of Ba₂Ca₂Cu₃O_x. *Physica C*, 330: 9–18, 2000.
- [146] T.M. Mendonça, P.B. Tavares, J.G. Correia, A.M.L. Lopes, and J.P. Araujo. The urea combustion method in the preparation of precursors for high T_C single phase HgBa₂Ca₂Cu₃O_{8+δ} superconductor. *Physica C*, 471:1643–1646, 2011.

- [147] A. Kareiva and I. Bryntse. A novel synthesis route to the Hg-containing superconductor $\text{HgBa}_2\text{CaCu}_2\text{O}_{6+\delta}$ partly based on the sol-gel technique. *Journal of Materials Chemistry*, 5(6):885–887, 1995.
- [148] R.B. Penland, S. Mizushima, C. Columba Curran, and J.V. Quagliano. Infrared absorption spectra of inorganic coordination complexes. X. Studies of some metal-urea complexes. *Journal of the American Ceramic Society*, 70:1575, 1957.
- [149] R.J. Hemley and N.W. Ashcroft. The revealing role of pressure in the condensed matter sciences. *Physics Today*, pages 26–32, 1998.
- [150] D.P. Kozlenko, I. Mirebeau, J.-G. Park, I.N. Goncharenko, S. Lee, J. Park, and B.N. Savenko. High-pressure-induced spin-liquid phase of multiferroic YMnO_3 . *Physical Review B*, 78:054401 (5 pp.), 2008.
- [151] P. Toulemonde, C. Darie, C. Goujon, M. Legendre, T. Mendonça, M. Alvarez-Murga, V. Simonet, P. Bordet, P. Bouvier, J. Kreisel, and M. Mezouar. Single crystal growth of BiMnO_3 under high pressure-high temperature. *High Pressure Research*, 33:274–277, 2009.
- [152] T.M. Mendonça. Síntese de supercondutores da família $\text{HgBa}_2\text{Ca}_{n-1}\text{Cu}_n\text{O}_{2n+2+\delta}$ ($n=2$ e 3): novos métodos de preparação dos precursores. Master’s thesis, Universidade do Porto, 2006.
- [153] J.P. Araujo. *Local Probe and Bulk Properties Studies on Highly Correlated Electron Systems: High T_c Superconductors and CMR Magnetic Oxides*. PhD thesis, University of Porto, Portugal, 2002.
- [154] J. Christiansen. *Hyperfine Interactions of Radioactive Nuclei*. 1983.
- [155] J.G. Correia. *Aplicações da Técnica de Correlações Angulares Perturbadas $e-\gamma$ no Isolde-CERN*. PhD thesis, Universidade de Lisboa, Portugal, 1993.
- [156] H. Frauenfelder and R.M. Steffen. *Alpha, Beta and Gamma-ray Spectroscopy*. 1968.
- [157] E.B. Karlsson. *Solid State Phenomena: As Seen by Muons, Protons and Excited Nuclei*. 1995.
- [158] A.M.L. Lopes. *Local Probe Studies on Lattice Distortions and Electronic Correlations in Manganites*. PhD thesis, Universidade de Aveiro, Portugal, 2006.

- [159] G. Schatz and A. Weidinger. *Nuclear Condensed Matter Physics: Nuclear Methods and Applications*. 1996.
- [160] P.W. Martin and K. Skov. In-111 transferrin labeling studied by perturbed angular correlations. *Journal of Nuclear Medicine*, 19:1171–1174, 1978.
- [161] R.M. Beihn and G.A. Digenis. Noninvasive dissolution measurement using perturbed angular correlation. *Journal of Pharmaceutical Sciences*, 70:1324–1328, 1981.
- [162] L. Hemmingsen, K.N. Sas, and E. Danielsen. Biological Applications of Perturbed Angular Correlations of gamma-ray Spectroscopy. *Chemical Review*, 104:4027–4061, 2004.
- [163] T. Butz. Analytic Perturbation Functions for Static Interactions in Perturbed Angular Correlations of gamma-rays. *Hyperfine Interactions*, 52:189–228, 1989.
- [164] R.S. Hager and E.C. Seltzer. *Internal Conversion Tables: Part II - Directional and Polarization. Particle Parameters for Z=30 to Z=103, Nuclear Data Tables, vol.4*. 1968.
- [165] N. Barradas. *Sistemas magnéticos baseados em cobalto*. PhD thesis, Universidade de Lisboa, Portugal, 1994.
- [166] N.P. Barradas, M. Rots, A.A. Melo, and J.C. Soares. Magnetic anisotropy and temperature dependence of the hyperfine fields of ^{111}Cd in single-crystalline cobalt. *Physical Review B*, 47:8763–8768, 1993.
- [167] M. Forker. The problematic of the derivation of the electric field gradient asymmetry parameter from TDPAC measurements or Mössbauer spectroscopy in imperfect crystal lattices. *Nuclear Instruments and Methods*, 106:121–126, 1973.
- [168] E.N. Kaufmann and R.J. Vianden. The electric field gradient in noncubic metals. *Review Modern Physics*, 51:161–214, 1979.
- [169] A.C. Beri, T. Lee, T.P. Das, and R.M. Sternheimer. Theory of nuclear quadrupole interactions in ionic iron-group compounds: role of antishielding effects. *Hyperfine Interactions*, 4:509–514, 1978.

- [170] S. Edvarsson and M. Klintonberg. Role of the electrostatic model in calculating rare-earth crystal-field parameters. *Journal of Alloys and Compounds*, 275-277:230–233, 1998.
- [171] F.D. Feiock and W.R. Johnson. Atomic susceptibilities and shielding factors. *Physical Review*, 187 (1):39–50, 1969.
- [172] R.P. Gupta and S.K. Sen. Sternheimer shielding-antishielding. II. *Physical Review A*, 8 (3): 1169–1172, 1973.
- [173] P.C. Schmidt, K.D. Sen, T.P. Das, and A. Weiss. Effect of self-consistency and crystalline potential in the solid state on nuclear quadrupole Sternheimer antishielding factors in closed-shell ions. *Physical Review B*, 22 (9):4167–4179, 1980.
- [174] D. Wiarda, M. Uhrmacher, A. Bartos, and K.P. Lieb. Electric field gradients at ^{111}Cd in binary oxides. *Journal of Physics: Condensed Matter*, 5:4111–4124, 1993.
- [175] P. Blaha, K. Schwarz, P. Sorantin, and S.B. Trickey. Full potential, linearized augmented plane wave programs for crystalline systems. *Computer Physics Communications*, 59:399–415, 1990.
- [176] P.E. Blöchl. Projector augmented-wave method. *Physical Review B*, 50:17953–17979, 1994.
- [177] P. Blaha, P. Dufek, K. Schwarz, and H. Haas. Calculation of electric hyperfine interaction parameters in solids. *Hyperfine Interactions*, 97:3–5, 1996.
- [178] P. Blaha, K. Schwarz, W. Faber, and J. Luitz. Calculations of electric field gradient in solids: how theory can complement experiment. *Hyperfine Interactions*, 126:389–395, 2000.
- [179] J.P. Perdew, K. Burke, and M. Ernzerhof. Generalized gradient approximation made simple. *Physical Review Letters*, 77 (18):3865–3868, 1996.
- [180] Blaha, P. and Schwarz, K. and Madsen, G.K.H. and Kvasnicka, D. and Luitz, J. *Wien2K - an augmented plane wave + local orbitals program for calculating crystal properties*, www.wien2k.at.

- [181] J.N. Gonçalves, H. Haas, A.M.L. Lopes, V.S. Amaral, and J.G. Correia. First principle calculations of hyperfine parameters on the Ca manganites with substitutional Cd-modeling of a PAC experiment. *Journal of Magnetism and Magnetic Materials*, 322:1170–1173, 2010.
- [182] B.A. Hunter, J.D. Jorgensen, J.L. Wagner, P.G. Radaelli, D.G. Hinks, H. Shaked, and R.L. Hitterman. Pressure induced structural changes in superconducting $\text{HgBa}_2\text{Ca}_{n-1}\text{Cu}_n\text{O}_{2n+2+\delta}$ ($n=1, 2, 3$) compounds. *Physica C*, 221:1–10, 1994.
- [183] E. Kugler, D. Fiander, B. Johnson, H. Haas, A. Przewloka, H.L. Ravn, D.J. Simon, and K. Zimmer. The new CERN-ISOLDE on-line mass-separator facility at the PS-Booster. *Nuclear Instruments and Methods in Physics Research B*, 70:41–49, 1992.
- [184] L.A. Errico, M. Rentería, A.G. Bibiloni, and G.N. Darriba. Temperature dependence of the EFG at Cd-doped Lu_2O_3 : How *abinitio* calculations can complement PAC experiments. *Physica Status Solidi*, 10:3576–3580, 2005.
- [185] J.P. Araujo, A.M.L. Lopes, T.M. Mendonça, E. Rita, J.G. Correia, V.S. Amaral, and The ISOLDE Collaboration. Electric field gradient studies on $\text{La}_{1-x}\text{Cd}_x\text{MnO}_{3+\delta}$ system. *Hyperfine Interactions*, 158:347–351, 2004.
- [186] A.M.L. Lopes, J.P. Araujo, J.J. Ramasco, V.S. Amaral, R. Suryanarayanan, and J.G. Correia. Percolative transition on ferromagnetic insulator manganites: uncorrelated to correlated polaron clusters. *Physical Review B*, 73:100408 (4pp.), 2006.
- [187] Y. Chen, H. Yuan, G. Li, G. Tian, and S. Feng. Crystal growth and magnetic property of orthorhombic RMnO_3 ($R=\text{Sm-Ho}$) perovskites by mild hydrothermal synthesis. *Journal of Crystal Growth*, 305:242–248, 2007.
- [188] W.S. Ferreira, J. Agostinho Moreira, A. Almeida, M.R. Chaves, J.P. Araújo, J.B. Oliveira, J.M. Machado Da Silva, M.A. Sá, T.M. Mendonça, P. Simeão Carvalho, J. Kreisel, J.L. Ribeiro, L.G. Vieira, P.B. Tavares, and S. Mendonça. Spin-phonon coupling and magnetoelectric properties: EuMnO_3 versus GdMnO_3 . *Physical Review B*, 79:054303 (10pp.), 2009.

- [189] T. Chatterji, B. Ouladdiaf, and D. Bhattacharya. Neutron diffraction investigation of the magnetic structure and magnetoelastic effects in NdMnO₃. *Journal of Physics: Condensed Matter*, 21:306001 (5pp.), 2009.
- [190] T. Arima, T. Goto, Y. Yamasaki, S. Miyasaka, K. Ishii, M. Tsubota, T. Inami, Y. Murakami, and Y. Tokura. Magnetic-field-induced transition in the lattice modulation of colossal magnetoelectric GdMnO₃ and TbMnO₃ compounds. *Physical Review B*, 72:100102 (4pp.), 2005.
- [191] T.M. Mendonça, J. G. Correia, H. Haas, P. Odier, P.B. Tavares, M.R. da Silva, A.M.L. Lopes, C. Darie, and J.P. Araujo. Perturbed Angular correlations studies in the HgBa₂CaCu₂O_{6+δ} high T_C superconductor. *Journal of Superconductivity and Novel Magnetism*, 24:1153–1156, 2011.
- [192] X. Zhang, W.H. Lu, and C.K. Ong. Similarity of structural changes in HgBa₂CuO_{4+δ} induced by extra oxygen and by high pressure. *Journal of Physics and Chemistry of Solids*, 60:1675–1682, 1999.
- [193] A. Fukuoka, A. Tokiwa-Yamamoto, Y. Itoh, R. Usami, S. Adachi, and K. Tanabe. Dependence of T_C and transport properties on the Cu valence in HgBa₂Ca_{n-1}Cu_nO_{2n+2+δ} (n=2,3) superconductors. *Physical Review B*, 55:6612–6620, 1997.
- [194] J.W. Rogers, N.D. Shin, J.E. Schirber, and E.L. Venturini. Identification of a superoxide in superconducting La₂CuO_{4+δ} by X-ray photoelectron spectroscopy. *Physical Review B*, 38:5021–5024, 1988.